STUDY OF PROFILE CONTROL AND SUPRATHERMAL ELECTRON PRODUCTION WITH LOWER HYBRID WAVES

F.X. Söldner, M. Brambilla, F. Leuterer, M. Münich

IPP III/111

May 1986

MAX-PLANCK-INSTITUT FÜR PLASMAPHYSIK

8046 GARCHING BEI MÜNCHEN

MAX-PLANCK-INSTITUT FÜR PLASMAPHYSIK

GARCHING BEI MÜNCHEN

STUDY OF PROFILE CONTROL AND SUPRATHERMAL ELECTRON PRODUCTION WITH LOWER HYBRID WAVES

F.X. Söldner, M. Brambilla, F. Leuterer, M. Münich

IPP III/111 May 1986

This work was performed in the frame of an Article 14-Contract between

The JET JOINT UNDERTAKING,
The European Atomic Energy Community
and
Euratom/IPP Association on Fusion
(Project Leader: F.X. Söldner)
Contract No. JJ5/9009

Die nachstehende Arbeit wurde im Rahmen des Vertrages zwischen dem Max-Planck-Institut für Plasmaphysik und der Europäischen Atomgemeinschaft über die Zusammenarbeit auf dem Gebiete der Plasmaphysik durchgeführt.

Table of Contents

I. Introduction

The crucial role of the plasma current profile for the energy confinement in tokamaks has been revealed by a number of experimental and theoretical contributions during the last years. MHD-stability depends strongly on the form of the current distribution. Optimisation of the current profile therefore seems to be a prerequisite for the achievement of good confinement and high beta values. With inductive current drive, however, the current distribution is always determined by the local electrical conductivity and therefore subject to all changes of the electron temperature profile due to additional heating. A dramatic consequence of this coupling of $j(r)$ and $T_e(r)$ is seen with high power ICRF heating on JET where the central energy deposition leads to giant sawteeth with modulation of the central electron temperature by up to 50 % /II.1/. An independent external control of current and heat deposition profiles therefore would be highly desirable.

Complete decoupling of the current and electron temperature profiles could be attained on the other hand with non-inductive current drive by directional LH waves /II.2/. This allowed to stabilise sawtooth oscillations in OH- /II.3,4/ and NBI-heated discharges resulting in improved confinement /II.5/.

In this study the coupling of LH waves to suprathermal electrons, the LH current drive efficiency and the mechanism for sawtooth stabilisation will be discussed. A wide data base has been obtained by the LH experiments on Alcator C, ASDEX, FT; JFT-2M, JIPPT-IIU, Petula, PLT, Versator, WT II during the last years and important aspects as the scaling of global current drive efficiency are satisfactorily described by theory. We mainly rely here on experimental results from ASDEX and comparison with theoretical calculations by Fisch and Karney.

With extrapolation to JET parameters a LH system is proposed which could provide significant control of the current profile and suppression of sawteeth on JET.

II. Suprathermal Electron Production by Lower Hybrid Waves

Lower Hybrid waves are launched in all present day experiments by grill-type antennae. The grill coupler on ASDEX consists of 8 waveguides each of which is fed by one klystron and therefore individually controllable in amplitude and phase. This allows for high flexibility in the wave spectrum (c.f. III.3). Typical spectra for LH heating and current drive are shown in Fig. II.1. LH waves at f_o = 1.3 GHz were applied up to P_{LH} = 1.1 MW with pulse lenghts up to 1.5 s.

Two different regimes of plasma-wave interaction are found in all LH experiments. At low density suprathermal electrons are produced which absorb the rf power. Above a density threshold absorption of the LH waves by the ions and formation of high energy ion tails begins. The transition between both regimes occurs on ASDEX at densities $\bar{n}_e = 2 - 3 \times 10^{13}$ cm^{-3} as seen from Fig. II.2. The critical density $\bar{n}_c$ for the various experiments is well explained theoretically by the balance between power deposition on the electrons and on the ions as shown in Fig. II.3 taken from ref. /6/. An empirical scaling of the critical density $\bar{n}_c$ with the frequency f_o of the launched LH-waves

$$\bar{n}_c \sim f_o^2$$

is obtained from comparing different experiments with different transmitter frequencies as well as different frequencies on the same machine (PLT: 0.8/2.45 GHz, Petula: 1.25/3.7 GHz). The highest densities in the electron regime were obtained on Alcator C: $\bar{n}_c \approx 1.5 \times 10^{14}$ cm^{-3} with f_o = 4.6 GHz.

In the electron regime the ECE-emission increases strongly upon injection of LH waves and the ECE spectra are dominated by nonthermal components. The spectra during LH-current drive have the same shape as during suprathermal OH discharges in the slideaway regime /II.7/ and no difference is found for LH-current drive applied in a thermal or a nonthermal target plasma as shown in Fig. II.4. Similar parameters for the suprathermal electron tail are derived for all three cases: $n_{e,t}/\bar{n}_e \lesssim 5 \times 10^{-2}$, $E_t \approx 50 - 100$ keV.

This suggests that the same mechanism might determine the final steady state form of the tail electron distribution both in OH- and LH-suprathermal plasmas.

The evolution of the electron distribution can be directly seen from soft X-ray spectra. This diagnostics has been widely used for LH experiments on PLT /II.8/ and Alcator C /II.9/. Typical spectra from ASDEX are shown in Figs. II.5 and II.6. It should be noted that the same distribution with $E_{max} \approx 400$ keV is formed when starting with a small seed of runaway electrons (Fig. II.5) or with a thermal distribution (Fig. II.6). From the soft X-ray spectra the electron distribution function can be reconstructed. A plateau is formed at high energies, as seen from Fig. II.7, with boundaries corresponding to the extension of the accessible part of the $N_{\parallel}$-spectrum. With the distribution function determined at different radii, radial profiles of the electron population at fixed energies can be derived. Figure II.8 shows that the profile becomes flatter for higher electron energies. The radial density profile of the suprathermal electrons therefore is broader than the density profile of the bulk electrons.

In the presence of a dc toroidal electric field the LH-generated fast electrons can be further accelerated and may run away if they attain velocities above the critical velocity for runaway formation. A drastic effect is expected if the critical velocity lies within the LH wave spectrum and electrons then are directly accelerated by the LH up to runaway velocities /II.10/. This is demonstrated in experiments with different wave spectra on ASDEX with a nonnegligible residual electric field present. The temporal evolution of the loop voltage U_1 for normal current drive ($+\pi/2$), opposite current drive ($-\pi/2$) and LH heating with $\bar{N}_{\parallel} = 2$ ($00\pi\pi$ ...) and $\bar{N}_{\parallel} = 4$ ($0\pi0\pi$ ...) is shown in Fig. II.9. Only a small drop of U_1 results from opposite current drive and LH heating with $0\ \pi\ 0\pi$... . The maximum LH phase velocity in both cases exceeds the critical velocity. With LH-current drive and LH-heating at $0\ 0\ \pi\pi$ the loop voltage drops to about 25 % of the OH value. The critical velocity then for the remaining small dc electric field is well above the highest LH phase velocity. Figures II.10 and II.11 show the behaviour of the hard X-ray emission for the 4 different LH spectra. A strong increase with a long time constant of ~200 ms typical for runaway-build up is observed in the case of a large dc electric field ($-\pi/2$, $0\ \pi\ 0\pi$ ...) while a much lower saturated level in X-ray radiation is reached in the case of a small dc electric field ($+\pi/2$, $00\pi\pi$ ...) with a short time constant of ~50 ms typical for the establishment of a suprathermal slideaway distribution. The formation of a runaway electron distribution with opposite current drive was also noted on PLT /II.8/. High resolution X-ray spectroscopy was used on ASDEX to determine the role of the electric field on the generation of fast electrons /II.11/. The fractional

population of tail electrons n_t is shown in Fig. II.12 for LH-heating and LH-current drive at the same LH-power. Up to a factor 6 more fast electrons are produced in the case of LH heating where the residual electric field is larger.

Summarizing the results on suprathermal electron production the following points should be stated:

- Suprathermal electrons are produced by stationary (LHH) and propagating (LHCD) LH waves below the critical density for onset of LH-power absorption on the ions.
- With LH application at U_1 0 the electron tail extends up to maximum energies about an order of magnitude below the maximum runaway energies.
- The fast electrons have a broader radial density profile than the bulk electrons.
- In the presence of a strong residual dc toroidal electric field the generation of suprathermal electrons can be strongly enhanced. An acceleration to runaway energies is possible.

References

/II.1/ Jacquinot, et al., Plasma Physics and Controlled Fusion 28, 1 (1986).

/II.2/ K.McCormick, et al., 12th European Conf. on Controlled Fusion and Plasma Physis, Budapest, 1985, Vol. I, p. 199.

/II.3/ J.E. Stevens, et al., in Ref. /2/, Vol. II, p. 192.

/II.4/ F. Parlange, et al., in Ref. /2/, Vol. II, p. 172.

/II.5/ F.X. Söldner, et al., 13th European Conf. on Controlled Fusion and Plasma Physics, Schliersee, 1986, Vol. II, p. 319.

/II.6/ J.G. Wegrowe, G. Tonon, IAEA Tech. Meeting on Non-Inductive Current Drive in Tokamaks, Culham, 1983, Vol. II, p. 343.

/II.7/ G. Fußmann, et al., Phys. rev. Lett. 47, 1004 (1985).

/II.8/ J. E. Stevens, et al., Nuclear Fusion, Vol. 25, 1529 (1985).
S. v. Goeler, et al., Nuclear Fusion, Vol. 25, 1515 (1985).

/II.9/ S. Texter, internal report PFC/RR-85-24, MIT, Cambridge (1986)

/II.10/ V.S. Chan, et al., in Ref. /5/, Vol. II, p. 382.

/II.11/ R. Bartiromo, et al., in Ref. /5/, Vol. II, p. 335.

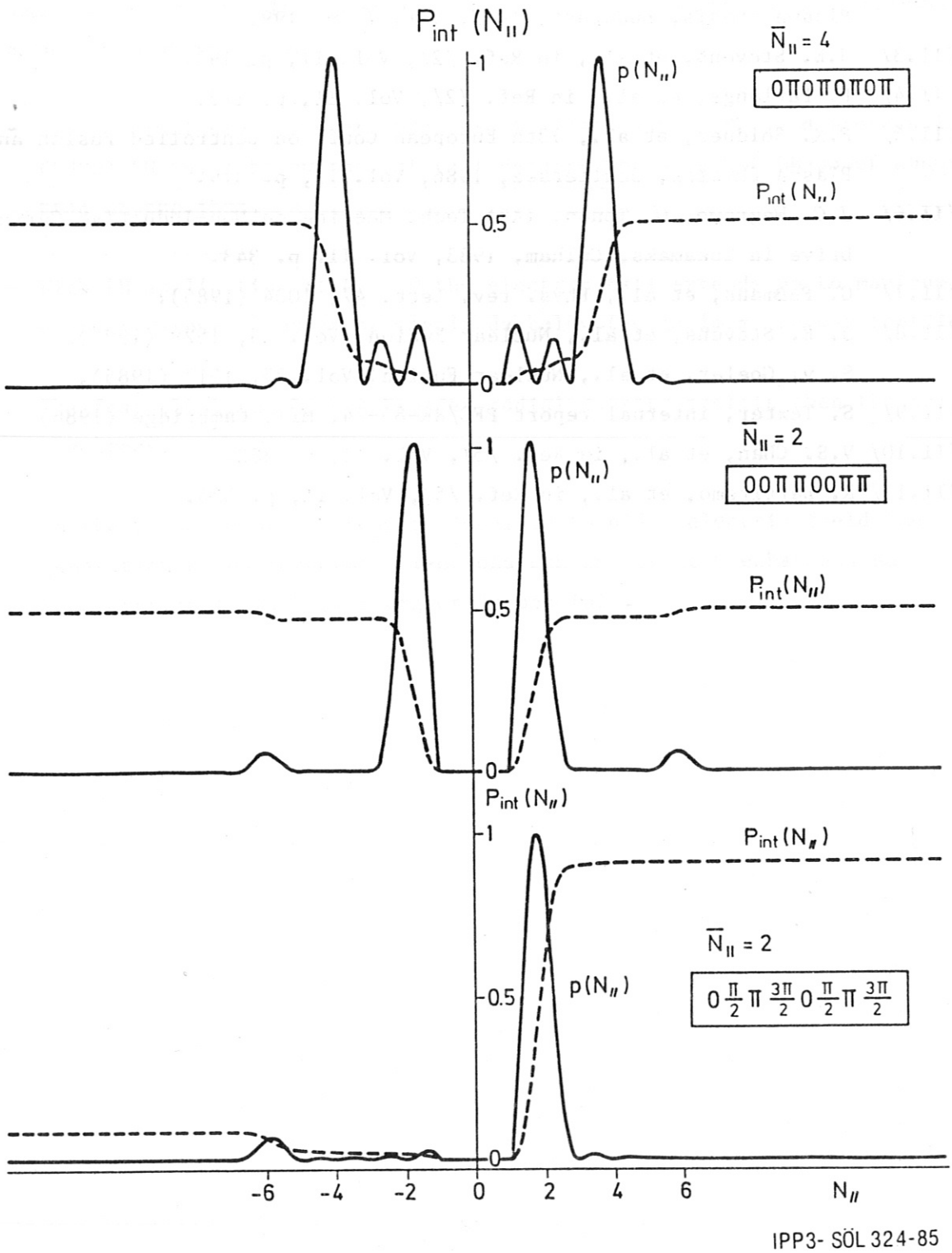

Fig. II.1: LH wave spectra of the 8-waveguide grill antenna on ASDEX

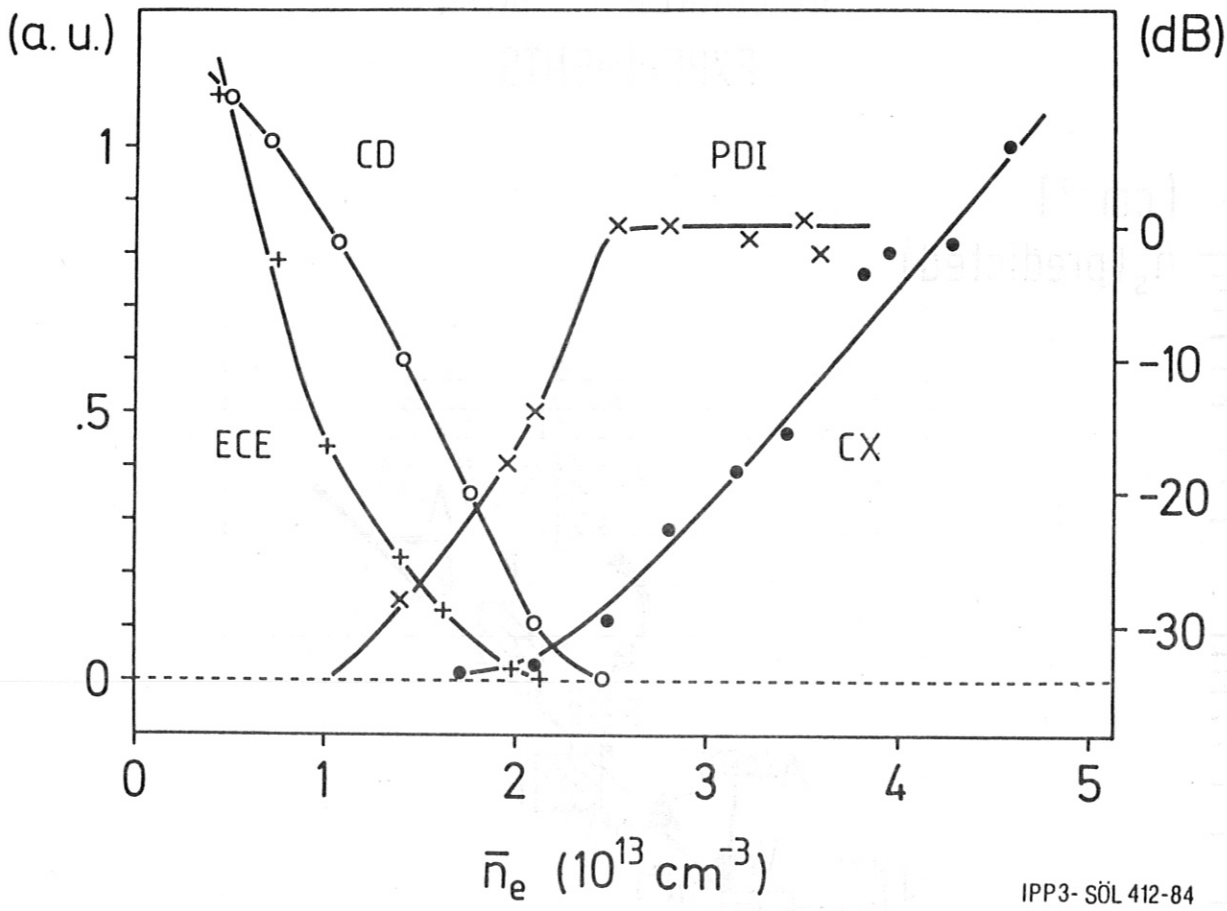

Fig. II.2: Density dependence of LH effects in H_2 plasmas

ECE: Amplitude of suprathermal electron cyclotron emission at $2.5\omega_{ce}$

CD: Current drive rate $\dot{I}_p^{RF} - \dot{I}_p^{OH}$

PDI: Amplitude of 2nd sideband in the parametric decay spectrum

CX: Flux of $\perp$-ions at E = 8.65 keV.

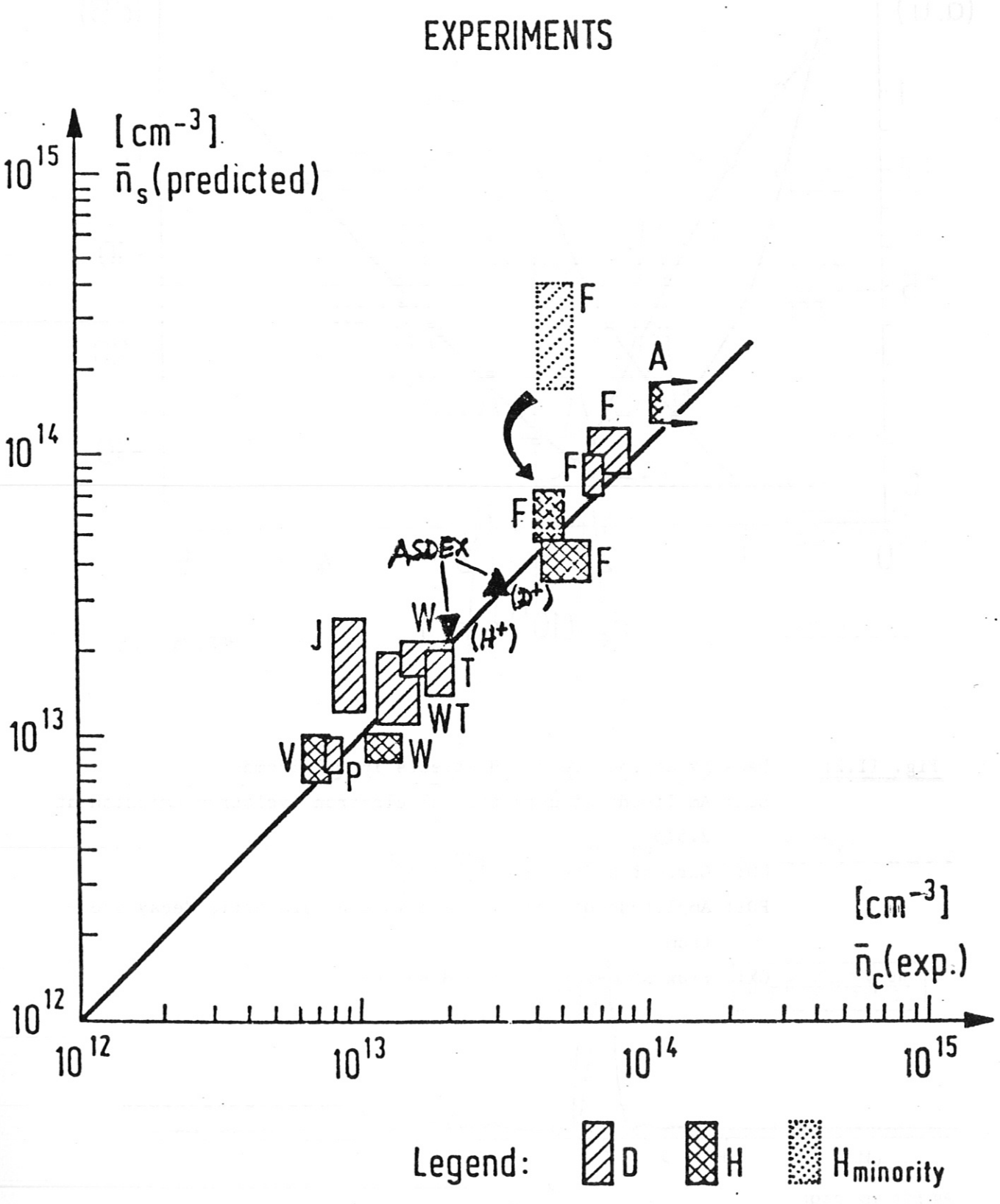

Fig. II.3: Theoretical switch-over density $\bar{n}_s$ from electron to ion absorption of LH waves versus upper density limit $\bar{n}_c$ in LH-current drive experiments from ref. /II.6/.

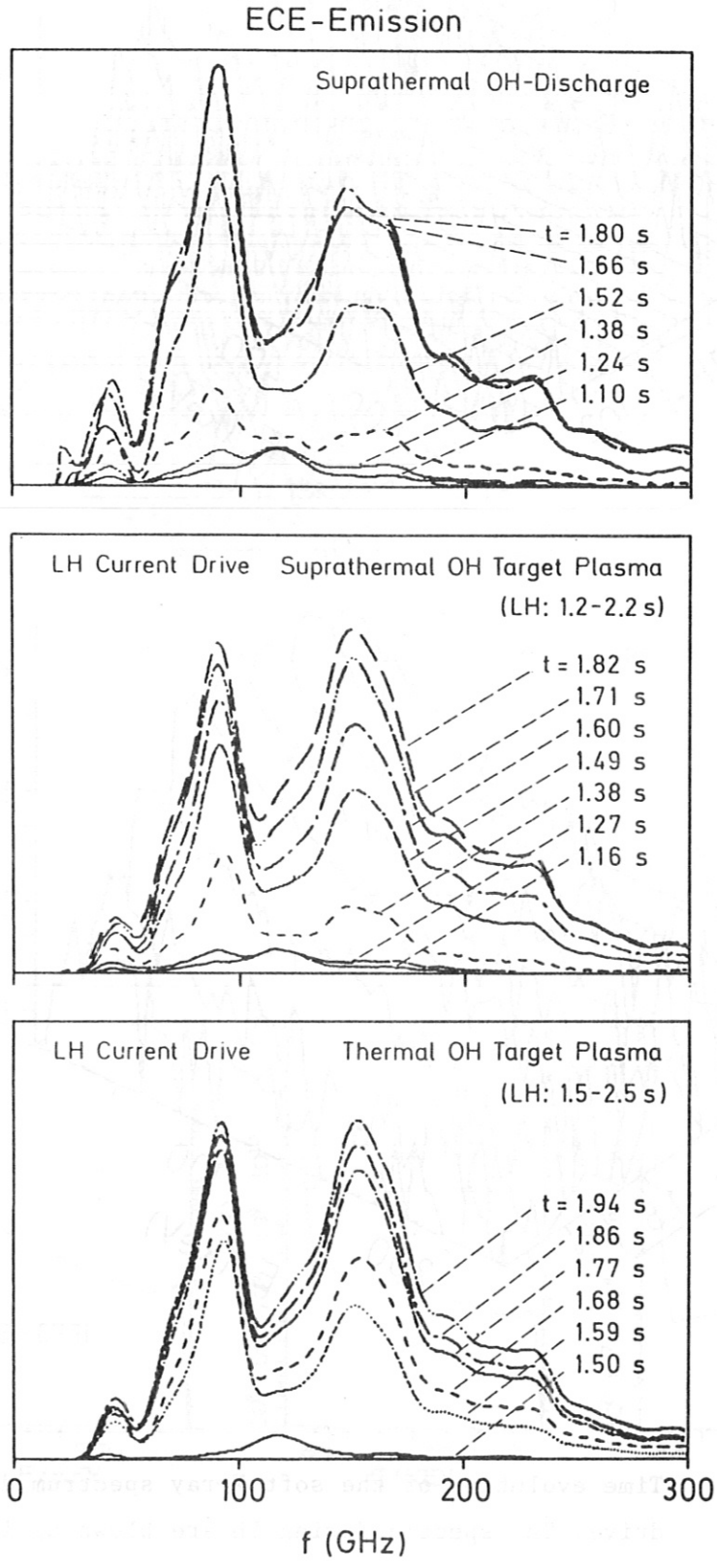

Fig. II.4: ECE spectra during a suprathermal OH discharge and during LH-current drive in thermal and suprathermal target plasmas.

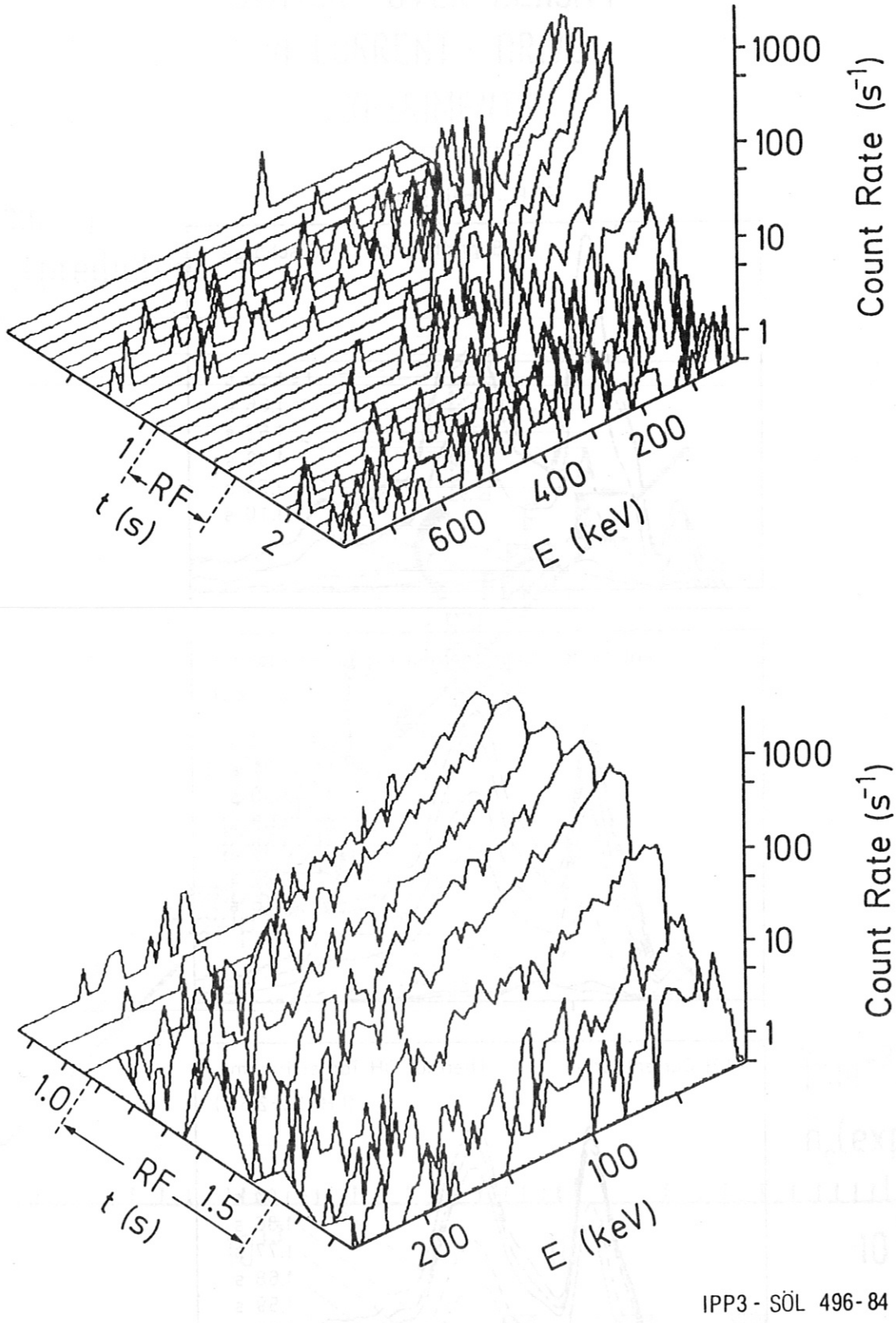

Fig. II.5: Time evolution of the soft X-ray spectrum during LH-current drive. The spectra during LH are blown up in the lower plot.

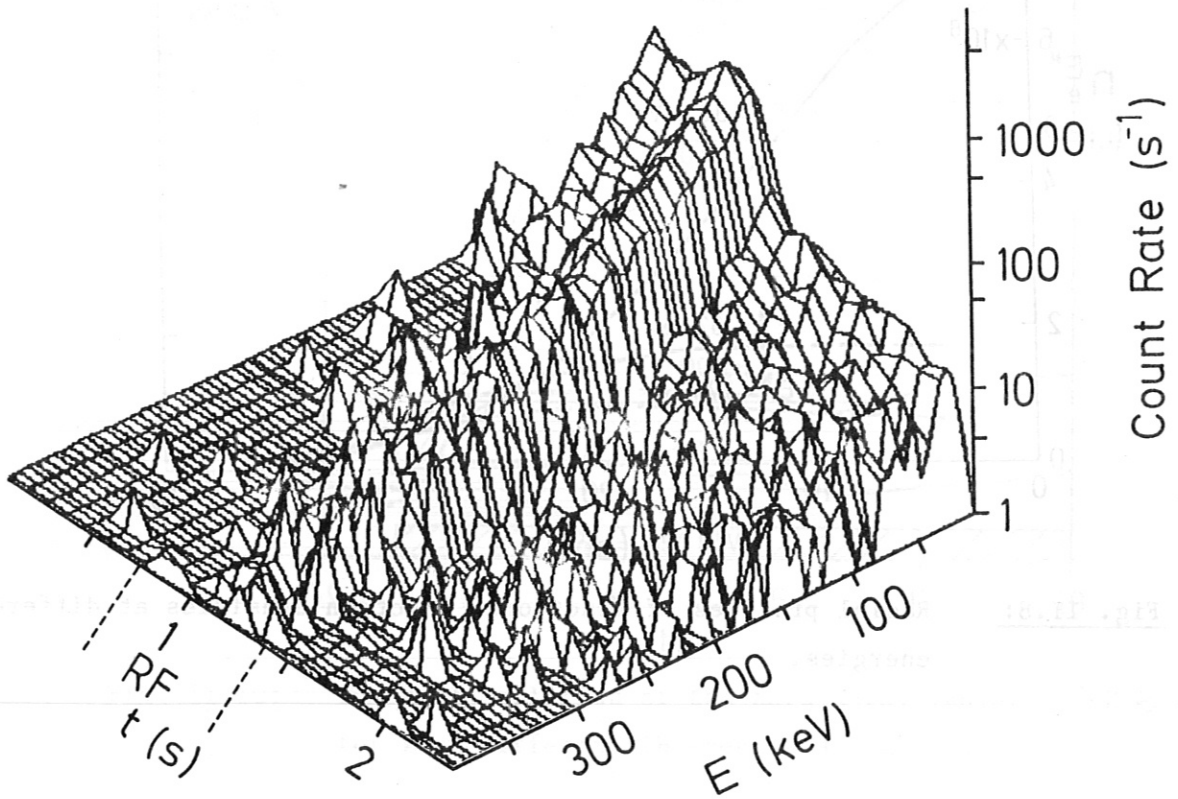

Fig. II.6: Formation of nonthermal soft x-ray spectra during LH-current drive.

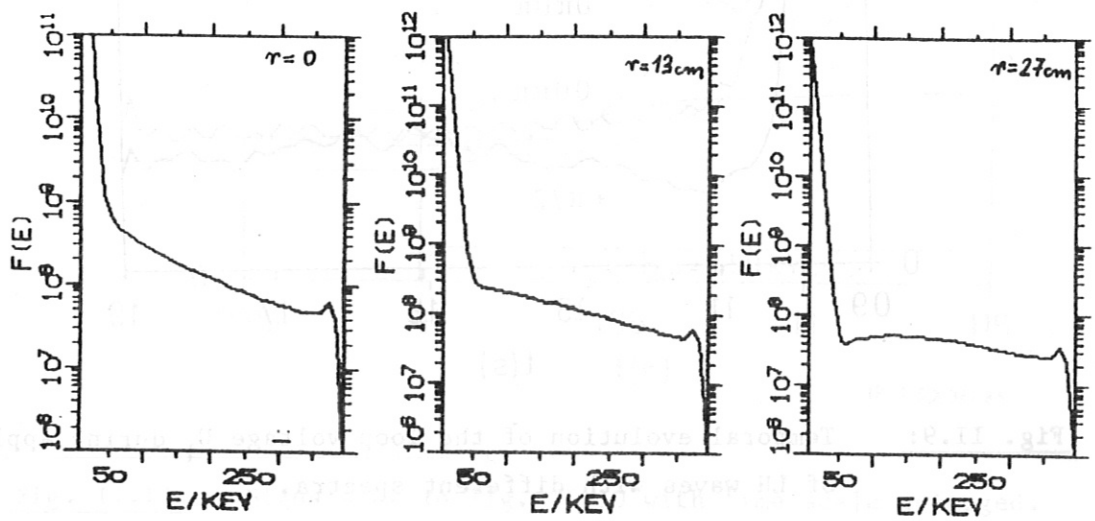

Fig. II.7: Electron distribution function at different radii from soft X-ray spectra during LH-current drive.

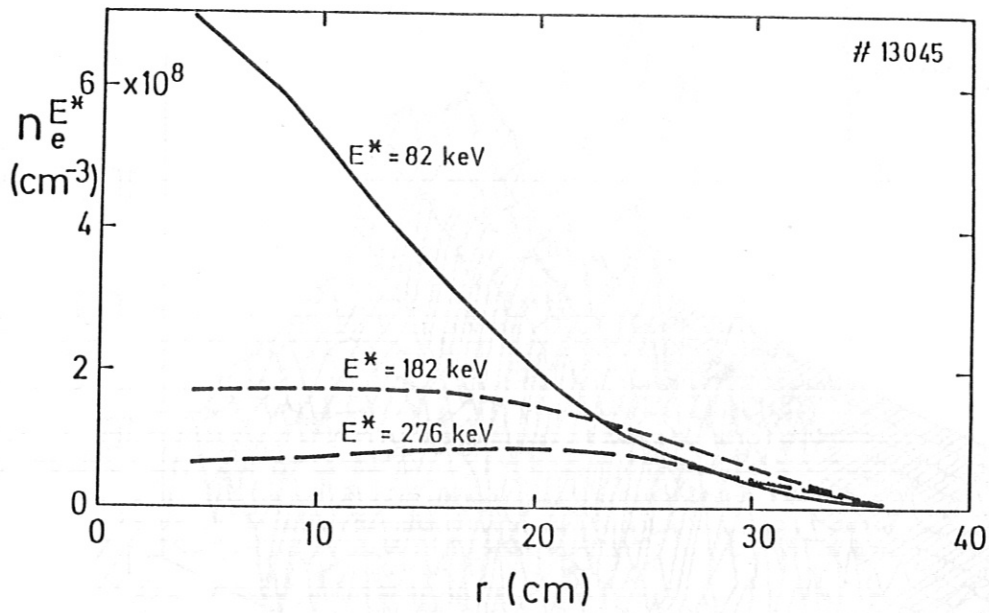

Fig. II.8: Radial profiles of fractional electron densities at different energies.

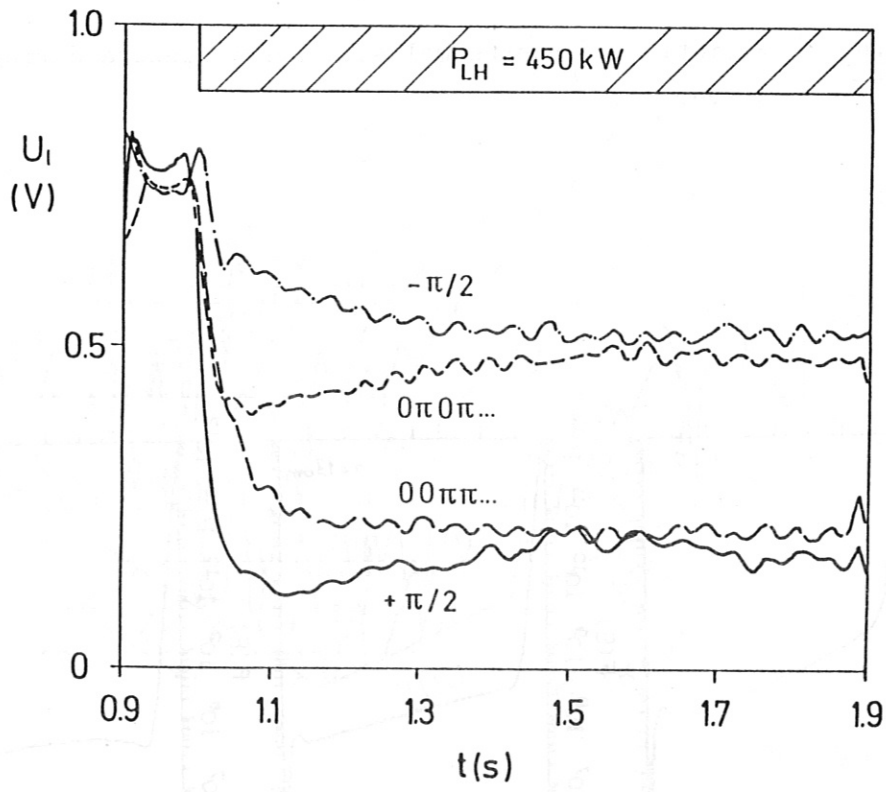

Fig. II.9: Temporal evolution of the loop voltage U_1 during application of LH waves with different spectra.

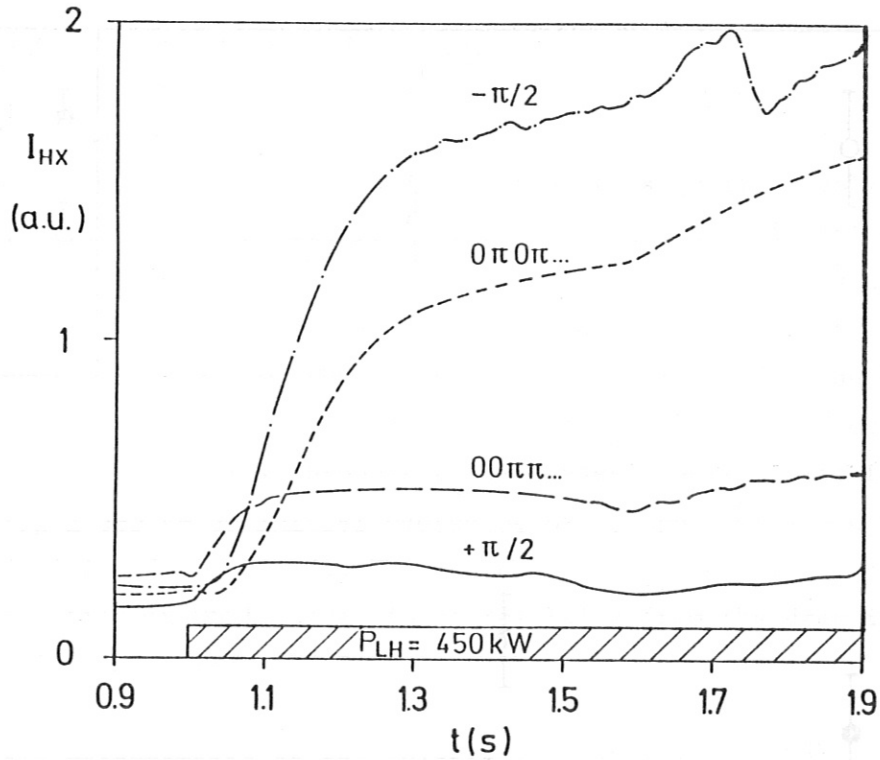

Fig. II.10: Temporal evolution of the hard X-ray radiation (E $\gtrsim$ 300 keV) for four different LH spectra as in Fig. II.9.

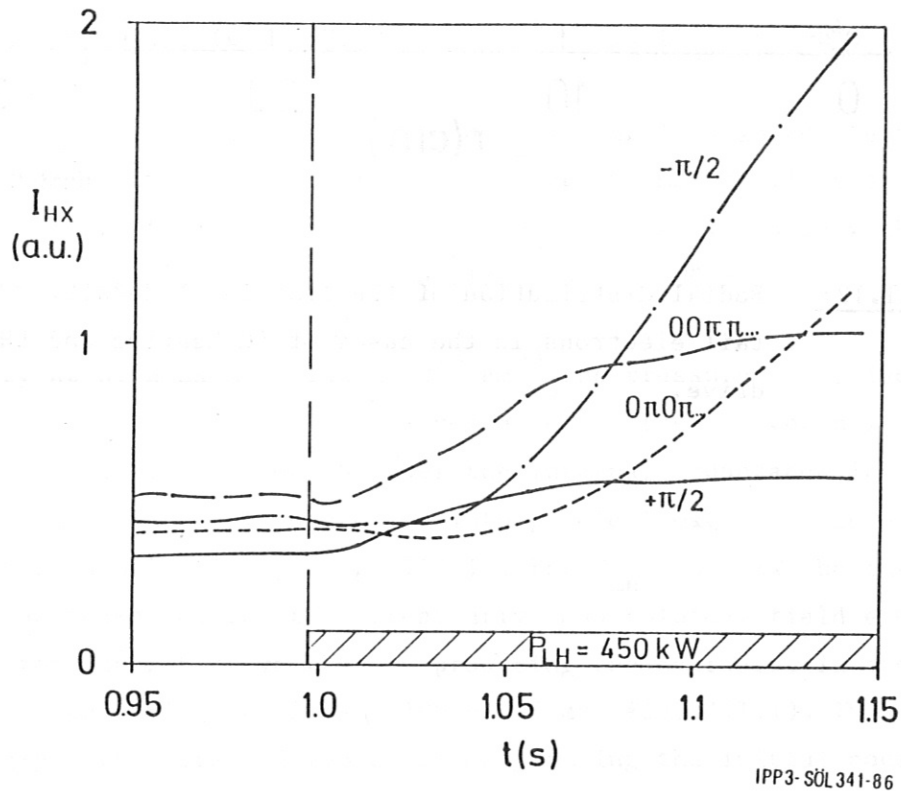

Fig. II.11: Signals as in Fig. II.10 with time scale enlarged.

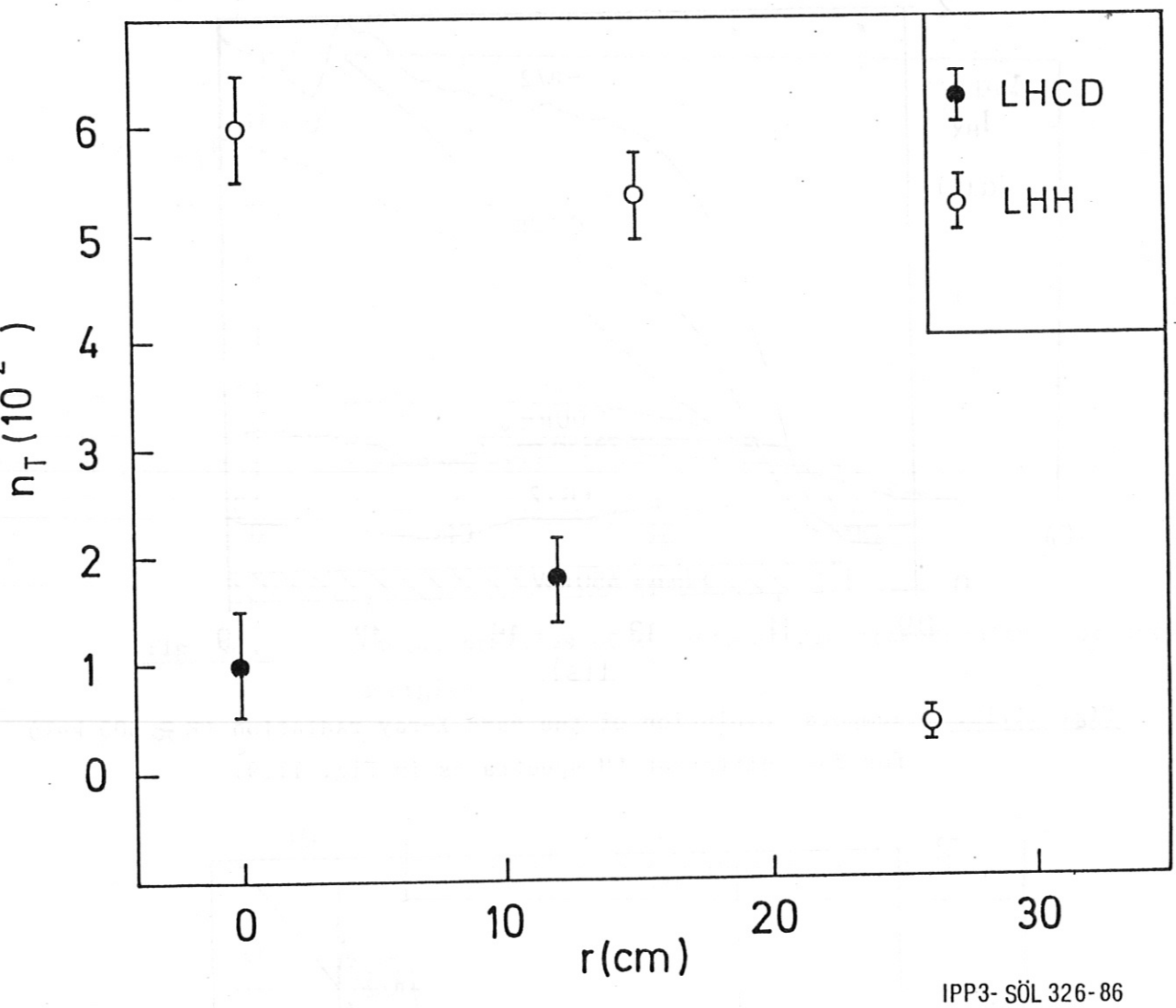

Fig. II.12: Radial distribution of the fractional density of high energy tail electrons in the cases of LH heating and LH current drive.

III. Lower Hybrid Current Drive Efficiency

1. Transient behaviour

Launching of directional LH wave spectra leads to a qualitatively different time behaviour of the loop voltage U_1 than the injection of stationary LH waves. With symmetric spectra U_1 drops smoothly to its steady-state value while asymmetric current drive spectra may lead to an overshoot of the loop voltage drop at the begin of the rf pulse. The dynamics of U_1 during LH current drive is shown for an LH-power scan at $\bar{n}_e = 1.6 \times 10^{13}$ cm^{-3} on ASDEX in Fig. III.1. At low LH-power U_1 decreases slowly to its final value while for $P_{LH} \geq 385$ kW an initial overshoot of U_1 upon switch-on of the rf is slowly diminished afterwards. The overshoot increases with increasing P_{LH}. The reduction in Ohmic power input resulting from the drop in loop voltage is plotted in Fig. III.2.

From magnetic measurements of the quantities $\beta_p^{equ} + l_i/2$ (β_p^{equ} = poloidal beta from equilibrium) and $\beta_p^{\perp}$ ($\beta_p^{\perp}$ = diamagnetic poloidal beta) the internal inductance l_i can be derived with:

$$\beta_p^{equ} + l_i/2 - \beta_p^{\perp} = 1/2\,(\beta_p^{\perp} + \beta_p'') + l_i/2 - \beta_p^{\perp} = 1/2\,(l_i + (\beta_p''-\beta_p^{\perp})$$

If the pressure is isotropic $\beta_p'' = \beta_p^{\perp}$ and l_i is obtained immediately. If $\beta_p'' \neq \beta_p^{\perp}$, the changes in l_i and in pressure anisotropy may still be separated from their different time constants: $\beta_p'' - \beta_p^{\perp}$ changes typically within ~50 ms while the change of l_i takes place within a few 100 ms.

At a density as high as $\bar{n}_e = 1.6 \times 10^{13}$ cm^{-3} the pressure stays isotropic and a change in $(\beta_p^{equ} - l_i/2) - \beta_p^{\perp}$ gives directly the change in l_i. This is plotted in Fig. III.3. At low LH-power the internal inductance increases. Therefore LH-wave energy is converted into poloidal magnetic field energy and U_1 decreases only slowly (Fig. III.1). For $P_{LH} \geq 385$ kW the internal inductance decreases during LH current drive and poloidal field energy is dissipated for current drive thereby producing the overshoot in the drop of the loop voltage during the first 100 - 200 ms (Fig. III.1). This leads to the seemingly high current drive efficiency during the initial nonstationary phase. The sometimes reported high current drive or current ramp-up efficiencies at the rf begin or in short pulse experiments may be due to such beneficial inductance effects.

The time constant for the change of the internal inductance depends on plasma density. The time when the overshoot in the U_1 drop is maximum ($\tau(U_1^{min})$) can be taken as a measure for it. It is well fitted by a $1/\bar{n}_e^{\,2}$-dependence as shown in Fig. III.4. The absolute amount of the change in l_i does nearly not depend on density. This is seen from the difference between initial and final drop in Ohmic power input which remains nearly independent on density at

$$\Delta P_{OH} = P_{dL/dt} \approx 65 \text{ kW}$$

as seen from Figs. III.5, III.6.

The sign of l_i-changes depends on the LH-power. At low power l_i increases, therefore the current profile steepens, while at higher rf powers the observed decrease in l_i has to be related to a broadening of the current profile. The different behaviour of the hard X-ray emission in the two regimes indicates formation of runaway electrons at low LH-power ($\leq$190 kW) and generation of a suprathermal slide-away distribution for $P_{LH} \geq 385$ kW. At low power the critical runaway velocity again lies within the range of the LH spectrum. Therefore we have to conclude that the position of the critical velocity with respect to the range of phase velocities covered by the LH wave spectrum not only determines the form of the electron distribution which develops but also the form of the current distribution. With a runaway distribution a current profile more peaked than the OH profile can be adjusted while a broader current profile is established by a current carrying slide-away distribution.

2. Combined stationary OH/LH-Current Drive

A nonlinear increase of the current drive rate with LH power and a saturation at high P_{LH} has been observed in several experiments /II.1-3/. The reduction in OH-power by replacing OH-current drive by LH-current drive is shown in Fig. III.7 for scaling studies on ASDEX. Only at low LH-power and at low density high conversion rates of rf-power can be obtained. The ratio of reduction in OH-power to net radiated LH-power becomes 1 only for $\bar{n}_e \leq 1.2 \times 10^{13}$ cm^{-3} and $P_{LH} \lesssim 250$ kW as seen from Fig. III.8. Complete current drive with $-\Delta P_{OH}^{LH}/P_{OH}^{OH} = 1$ with power conversion rates $-\Delta P_{OH}^{LH}/P_{LH} \approx 1$ is possible only for $\bar{n}_e \leq 0.5 \times 10^{13}$ cm^{-3}. In this parameter range high current drive efficiencies with $\eta > 1$ are obtained where

$$\eta = \frac{\bar{n}_e \, I_p \, R}{P_{LH}} \cdot \frac{-\Delta P_{OH}^{LH}}{P_{OH}^{OH}} \cdot$$

This means that the LH improves the OH-current drive efficiency by increasing the electrical conductivity through generation of suprathermal electrons. The savings in OH power with LH-current drive can be seen from Fig. III.10 in function of density.

3. Comparison with theory

3.1 Current drive efficiency of directional LH wave spectra

In ASDEX the current drive experiments have been performed in two different modes of operation /III.4,5/. In the first mode the primary current I_{OH} in the OH-transformer was kept constant and the plasma current I_p was allowed to change with time. In the second mode of operation I_p was kept constant by means of a feedback control acting on the primary of the OH transformer, thus changing the primary current rate of change, $\dot{I}_{OH}$, as soon as the RF-power is switched on.

Since for most applications only the second mode of operation is of interest, we describe here only these experiments. Switching on the RF-power we get an rf driven current I_{RF} in the plasma. The feedback system reacts in such a way as to generate a dc-electric field in the plasma which is necessary to maintain a constant total plasma current $I_p = I_{Ind} + I_{RF}$. (I_{Ind} is the inductively driven part of the current). Thus if $0 < I_{RF} < I_p$ we get a reduction of the loop voltage below its ohmic value, for $I_{RF} = I_p$ the loop voltage becomes zero, and for $I_{RF} > I_p$ the loop voltage is negative. The loop voltage is generated by a corresponding temporal change in the primary current, $\dot{I}_{OH}$,

$$\dot{I}_{OH} = \frac{-1}{\tau_p} \cdot (I_p - I_{RF}) \cdot L_p/M \qquad (1)$$

with $\tau_p = L_p/R_p$ = characteristic time of the plasma, and M = mutual inductance between primary coil and the plasma. Measurements of $\dot{I}_{OH}$ as a function of RF-power or density are shown in Figs. III.11 and III.12, where we see

that at low density and high RF-power $\dot{I}_{OH}$ becomes positive (corresponding to negative loop voltage), thus recharging the OH-transformer /III.4/.

From the points $\dot{I}_{OH} = 0$, i.e. where a stationary current is maintained by RF-power alone, we obtain a relation between the RF driven current and the launched RF power, which agrees fairly good with theoretical calculations /III.6,7/:

$$I_{RF} = \eta \cdot \mu \cdot g \cdot P_{RF}/(\bar{n}_e \cdot R \cdot \gamma) \qquad (2)$$

where

$$\eta = 11.5 \cdot \frac{3.82 + 0.176\ Z_{eff}}{5 + Z_{eff}}$$

$$\gamma = n_e/\bar{n}_e$$

$$\mu = P_{RF,abs}/P_{RF}$$

$$g(N_{"}) = \left((N_{"_1}/N_{"_2})^2-1\right)/\left(N_{"_1}^2 \ln (N_{"_1}/N_{"_2})\right)$$

with this separation of coefficients we can identify a figure of merit which is independent of machine- and plasma parameters. To derive this equation homogeneous current density and power absorption profiles were assumed, as well as an $N_{"}$-spectrum of rectangular shape with the upper and lower boundaries $N_{"_1}$ and $N_{"_2}$, respectively. For the comparison with the experiment we set $N_{"_2} = N_{"acc}$ which is determined in a raytracing code for propagation to the central region of the plasma, and which depends upon density and magnetic field. Given $N_{"acc}$ $(\bar{n}_e)$ we then calculate which is the fraction of the launched RF-power available for interaction with the current carrying electrons. The result is approximated by $\mu = (1-\bar{n}_{e_{12}}/30)$ for the case of a D_2-plasma and $B_o = 2.2$ T. Furthermore we use $\gamma = 1.25$ and $N_{"_1} = 2.75$, as launched at the boundary of the plasma. With these assumptions, the experimental and theoretical results agree within a factor of 2 - 2.5 as shown in Fig. III.13.

For the cases $\dot{I}_{OH} \neq 0$, our measurements can be well understood in terms of theories for LH-curent drive in the presence of a dc-electric field. For our comparison we use the results of N. Fisch /III.8,9/ for the case of a small electric field, which may still apply to our experiment. In this

theory, the enhancement of the plasma conductivity due to the suprathermal electron velocity distribution generated by the RF-fields is calculated, yielding when combined with equ. (1) a current rate of change

$$\dot{I}_{OH} = \frac{-1}{\tau_{po}} \cdot \frac{I_{po} - I_{RF}}{1 + b \cdot I_{RF}/\bar{n}_e} \cdot \frac{L_p}{M}$$

Here τ_{po} is the characteristic time without RF-power, I_{RF} is taken from eq. (2) with the experimental value for η, $b = \alpha w^2/(q\ e\ v_{the}\ \bar{n}_e)$, where α is a function of Z_{eff}, q is the plasma cross-section, and $w^2 = v^2/v_{the}^2$ refers to resonant electrons. In the experiment τ_{po} is found to depend on density and for the calculation we approximate it by $\tau_{po} = 60/(30 + \bar{n}_e)$, sec, 10^{12} cm^{-3}. A reasonable fit to the experimental data is obtained for $b = 0.03 \times 10^{13}$ cm^{-3} kA^{-1}, as shown in Figs. III.14 and III.15. This seems a plausible value, which is calculated, assuming $Z_{eff} = 3$, $w^2 = 300$ and $T_e = 1$ keV. For these curves we assumed a constant electron temperature. In recent current drive experiments we observed a linear rise in electron temperature as a function of the RF-power which, however, can by far not account for the enhancement of the conductivity.

From the experimental and the theoretical curves we see that the enhanced conductivity leads to a saturation in the current ramp-up or recharging rates as a function of RF-power and also to a maximum in the recharging rate as a function of density. Towards higher density the decreasing accessibility limits the power available for electron interaction. This is corroborated by experiments at higher magnetic field where the accessibility is improved and the current drive efficiency increased consistently with equ. (3). Figure III.16 shows this comparison. In hydrogen, as shown in Fig. III.17, curent drive effects disappear already at a lower density than in deuterium plasmas /III.1/, although the accessibility should be better. This is due to the onset of an interaction with fast ions near $\bar{n}_e = 2 \times 10^{13}$ cm^{-3} which reduces the power available for current drive, imposing a density limit.

3.2 Influence of the $N_{\parallel}$-spectrum on the efficiency

The experiments shown in Figs. III.11 to III.17 have all been done with a phase of $\Delta\varphi = \pi/2$ between successive waveguides of the grill. By changing the phase, we vary the form of the wave spectrum as shown in Fig. III.18. In the comparison with theory we have then to change the factors μ, g and b, respectively. Moreover, approaching $\Delta\varphi = \pi$ we have also to take into

account the fraction of power at negative $N_{\parallel}$ which leads to opposite current drive, although at reduced efficiency because of the high $N_{\parallel}$. Assuming that the contributions of each side of the $N_{\parallel}$-spectrum to the current drive and to the conductivity are additive we may write equ. (3) in the form

$$\frac{\dot{I}_{OH,RF}}{\dot{I}_{OH,OH}} = \frac{1 - \frac{I_{RF,+}}{I_p} + \frac{I_{RF,-}}{I_p}}{1 + b_+ + \frac{I_{RF,+}}{\bar{n}_e} + b_- \frac{I_{RF,-}}{\bar{n}_e}} \qquad (4)$$

A comparison between experiment and a calculation based on this equation is shown in Fig. III.19 and confirms that current drive is most efficient at the lowest phase, i.e. at low $N_{\parallel}$, as expected from equ. (2). In the ASDEX experiment phases less than $\Delta\varphi = 75^{o}$ could not be used because of too high nonacessible power leading to enhanced plasma-wall interaction and to increased reflection. According to the calculation, however, we should then anyhow expect a lower efficiency due to diminishing accessibility.

3.3 Influence of the width of the LH spectrum on the efficiency

Superimposing in the grill waveguides field patterns of different $N_{\parallel}$-spectra, we can generate $N_{\parallel}$-spectra of different shape and width by varying the field amplitudes /III.10/. One set of spectra used in the ASDEX experiments is shown in Fig. III.20. These spectra have been launched all with the same total power of 400 kW. With the narrowest spectrum C1, corresponding to a usual grill phasing of $\Delta\varphi = \pi/2$ and used as the reference case, we achieved just $\dot{I}_{OH} = 0$ at $\bar{n}_e = 6 \times 10^{12}$ cm^{-3}. With all of the wider spectra we always got $\dot{I}_{OH} < 0$ as shown in Fig. III.21. We consistently found that the more power is shifted to higher $N_{\parallel}$, the less efficient was the observed current drive. In Fig. III.22 we show for the various spectra C_n the fraction of power which would be necessary, if launched with the narrow reference spectrum C1, to obtain the same current drive, i.e. the same $\dot{I}_{OH}$ as with spectrum C_n. We again find from this experiment that current drive is most efficient when $N_{\parallel}$ is low and the line is narrow. We also find that for these spectra the function g in eq. (2), which takes into account only the boundaries $N_{\parallel 1}$ and $N_{\parallel 2}$ of the spectra, is only a poor approximation. The detailed shape of the spectrum should rather be considered.

4. LH-Current Drive combined with NBI

The scaling of current drive efficiency with temperature is of great interest for the extrapolation to JET parameters with large additional heating power. In OH-discharges the electron temperature can be varied only to a

limited extent without changing the conditions for wave propagation considerably (e.g. by increasing the plasma current). Therefore LH-current drive was combined with NBI of up to P_{NI} = 3.4 MW on ASDEX.

With neutral beam injection alone, the Ohmic power input decreases with increasing beam power in the case of NBI-co-injection (all beams are oriented tangentially in the same direction). This is due both to an increase of the electrical conductivity and to a contribution from beam driven currents. In the case of NBI-counter-injection the Ohmic power increases, partly due to the observed accumulation of impurities in the plasma centre. With NBI and superposed LH-current drive the additional drop in Ohmic power due to the LH is smaller than with LH-current drive in an OH-target plasma as shown in Fig. III.23. The reduction in OH power $-\Delta P_{OH}$ is plotted for two LH powers versus NBI power in Fig. III.24. A possible explanation for part of the degradation of LH-current drive efficiency with NBI heating could be the increase of the electrical conductivity σ_{el} in the beam heated plasma. An increase in σ_{el} leads also to the observed saturation of the current drive efficiency with P_{LH} for LH-current drive in an OH-target plasma (c.f. Figs. III.7-9). For comparison therefore with the characteristics $P_{OH} = f(P_{LH})$ from parameter studies in OH plasmas, the drop in Ohmic power $-\Delta P_{OH}^{LH}$ is calculated which would be obtained if the same power P_{LH} as in the NBI experiments is applied to an Ohmic target plasma with the same starting value of P_{OH} as obtained in the beam heated plasma.This calculated drop $-\Delta P_{OH}^{LH}$ can be written as:

$$-\Delta P_{OH}^{LH} = P_{OH}^{NI} - P_{OH}^{LH}(P'_{LH}),\ P'_{LH} = P_{LH}(P_{OH}^{NI}) + P_{LH}.$$

The calculated drop $-\Delta P_{OH}^{LH}$ is plotted in Fig. III.25 versus the measured drop $-\Delta P_{OH}^{LH+NI}$ in the combined operation LHCD/NBI. A large part of the degradation could in fact be explained by saturation effects due to the increase in electrical conductivity. Additional reduction of the current drive efficiency may be due to the observed absorption of LH power by fast beam ions /III.11/. This depletion of LH power by fast ions has certainly to be taken into account in all combinations of LH-current drive with additional heating methods which produce fast ions (NBI, ICRH minority heating).

References

/III.1/ F. Leuterer, et al., 10th Int. Conf. on Plasma Physics and Contr. Nuclear Fusion Research, London, 1984, Vol. I, p. 597.

/III.2/ Y. Uesugi, et al., Nuclear Fusion, Vol. 25, 1623 (1985).

/III.3/ C. Gormezano, et al., 13th European Conf. on Controlled Fusion and Plasma Physics, Schlierse, 1986, Vol. II, p. 311.

/III.4/ F. Leuterer, et al. Phys. Rev. Lett 55, 75, (1985).

/III.5/ F. Leuterer, et al., "Application of RF-waves to tokamak Plasmas", Varenna 1985, Vol. II, p. 633.

/III.6/ C. Karney, N. Fisch, Phys. Fluids 22, 1817 (1979).

/III.7/ G. Tonon, D. Moulin, Conf. "Heating in Toroidal Plasmas", Rome 1984, Vol. II, p. 1343.

/III.8/ N. Fisch, Phys. Fluids 28, 245, (1985).

/III.9/ F. Leuterer, et al., EPS-Conference, Budapest 1985, Vol. II, p. 240 and Plasma Phys. and Contr. Fus., Vol. 27, 1399 (1985).

/III.10/F. Leuterer, et al., EPS-conference, Schliersee 1986, Vol. II, p. 409.

/III.11/F. Ryter, et al., in Ref. /3/, Vol. I, p. 101.

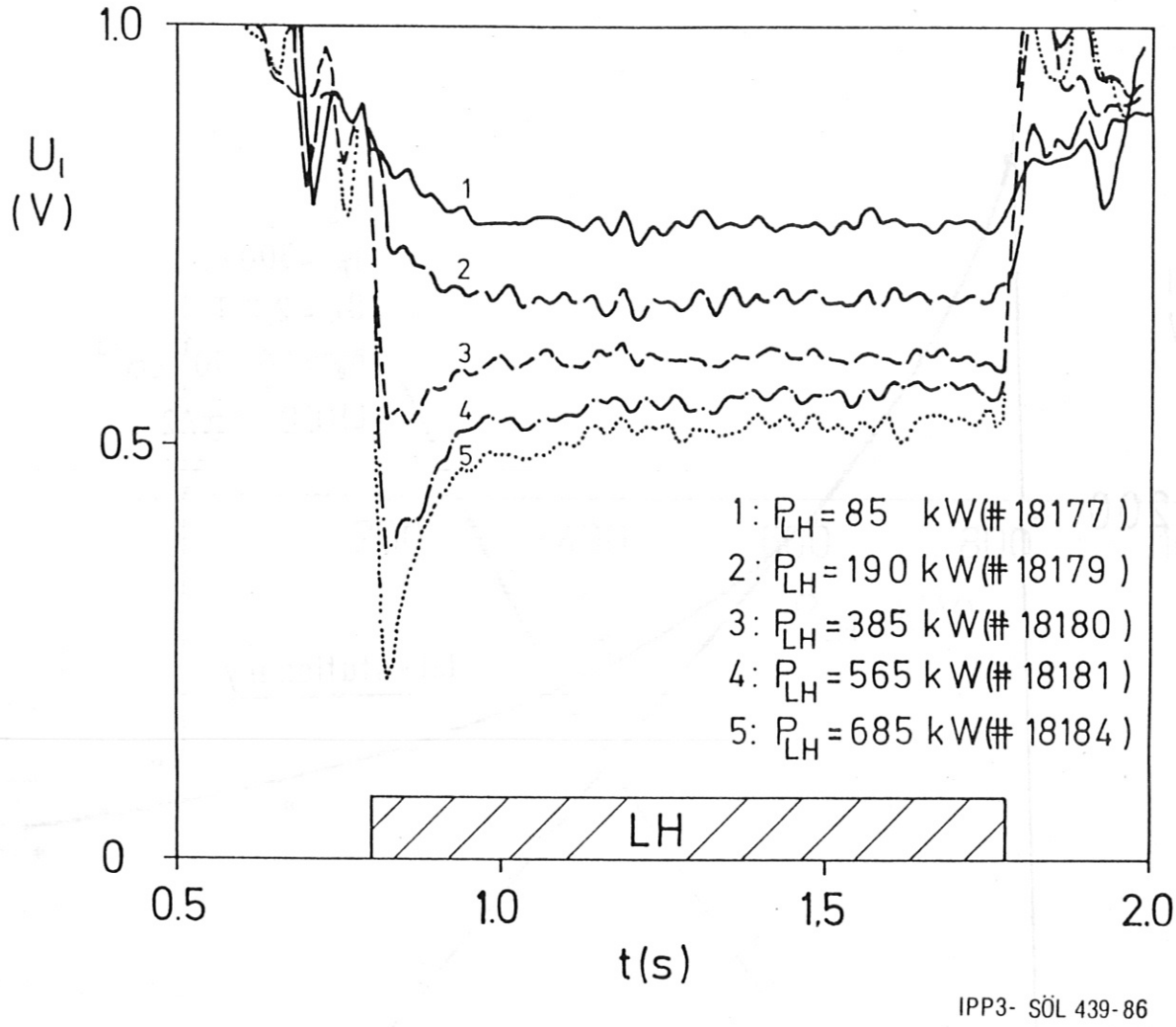

Fig. III.1: Temporal evolution of the loop voltage U_l during LH-current drive for a P_{LH}-scan at $\bar{n}_e = 1.6 \times 10^{13}$ cm^{-3}.

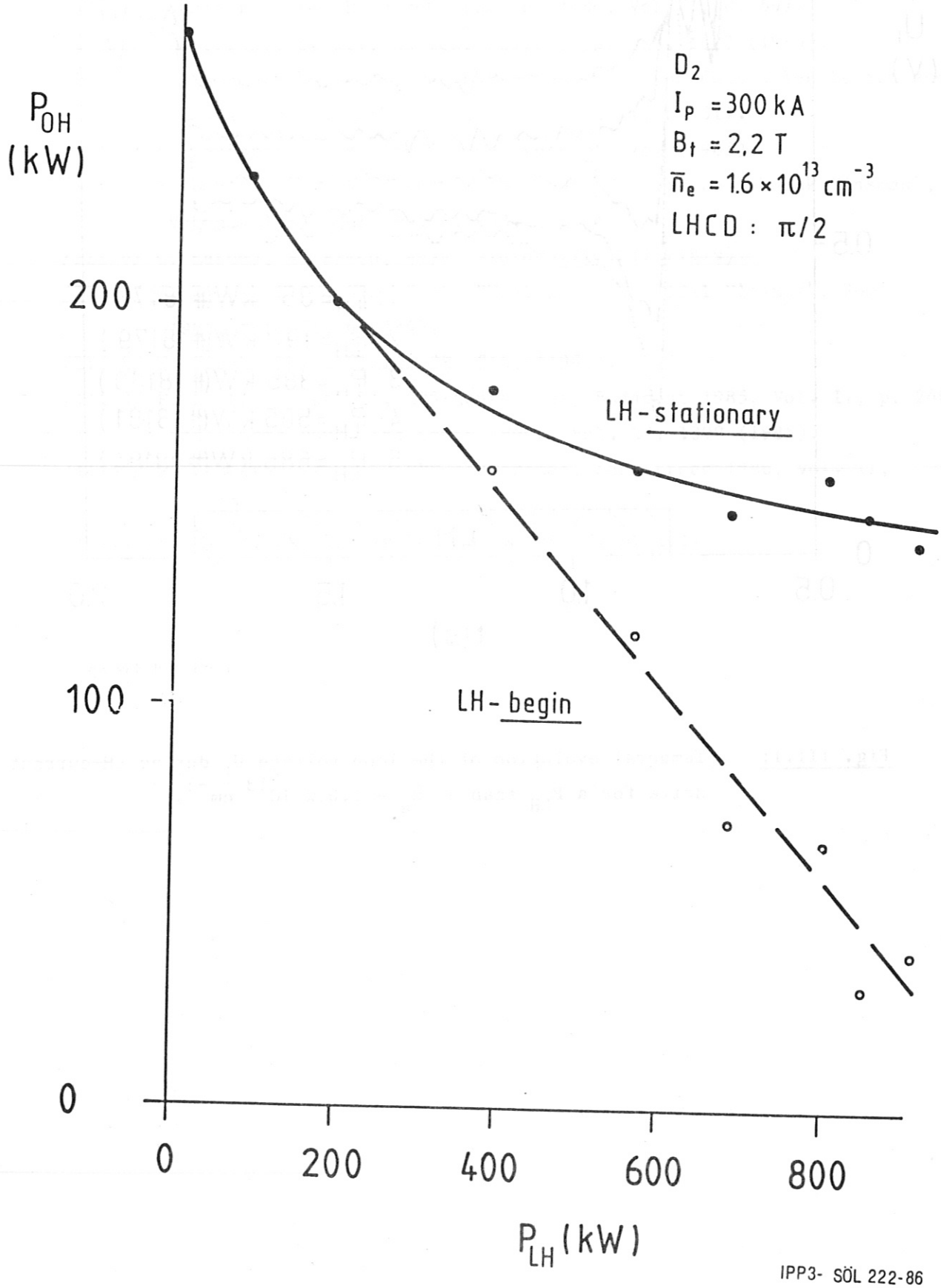

Fig. III.2: Initial and stationary reduction of Ohmic power input with LH-current drive at $\bar{n}_e = 10^{13}$ cm^{-3}.

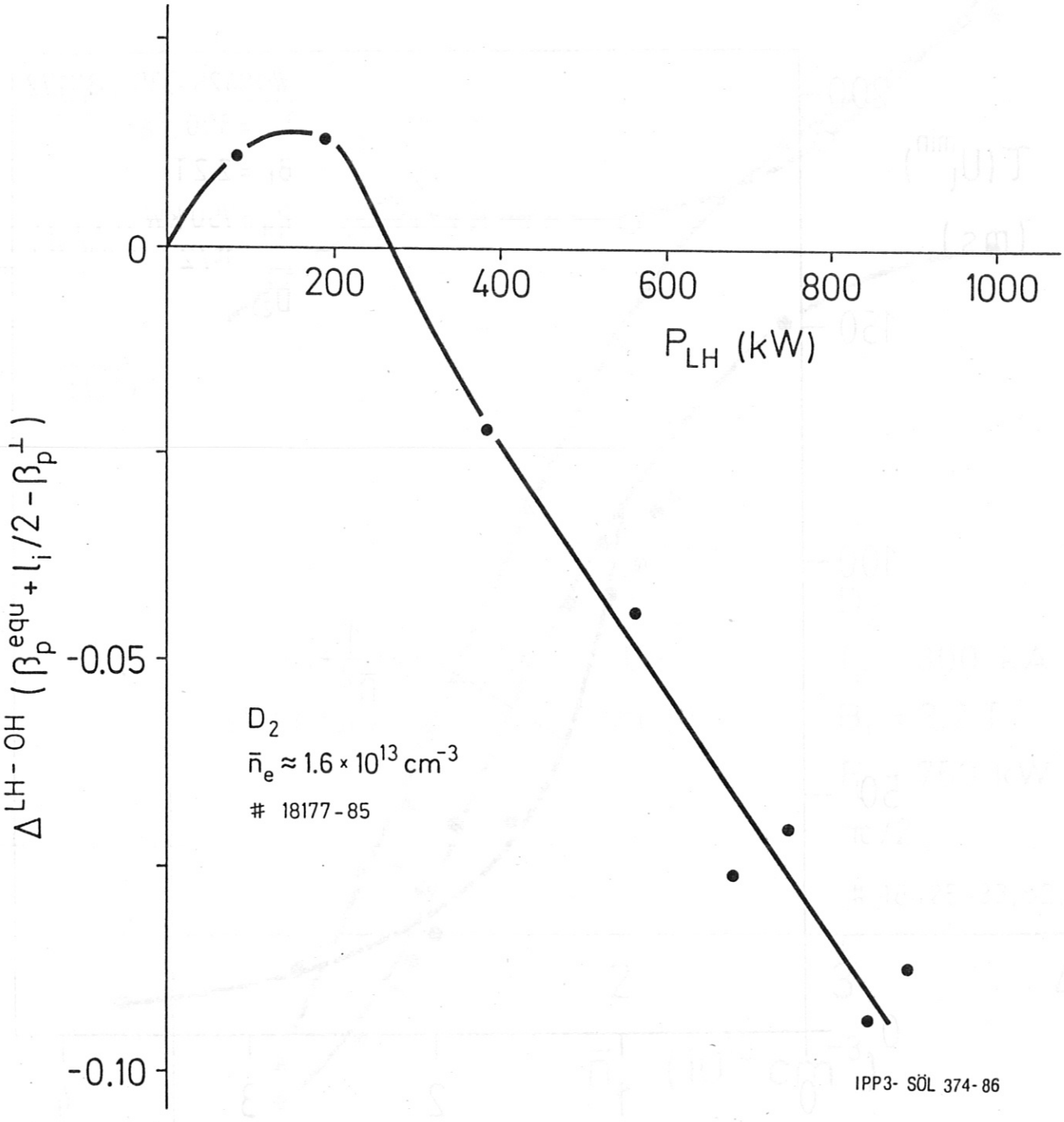

Fig. III.3: Change of the internal inductance l_i, derived from magnetic measurements, as function of P_{LH} for LH-current drive.

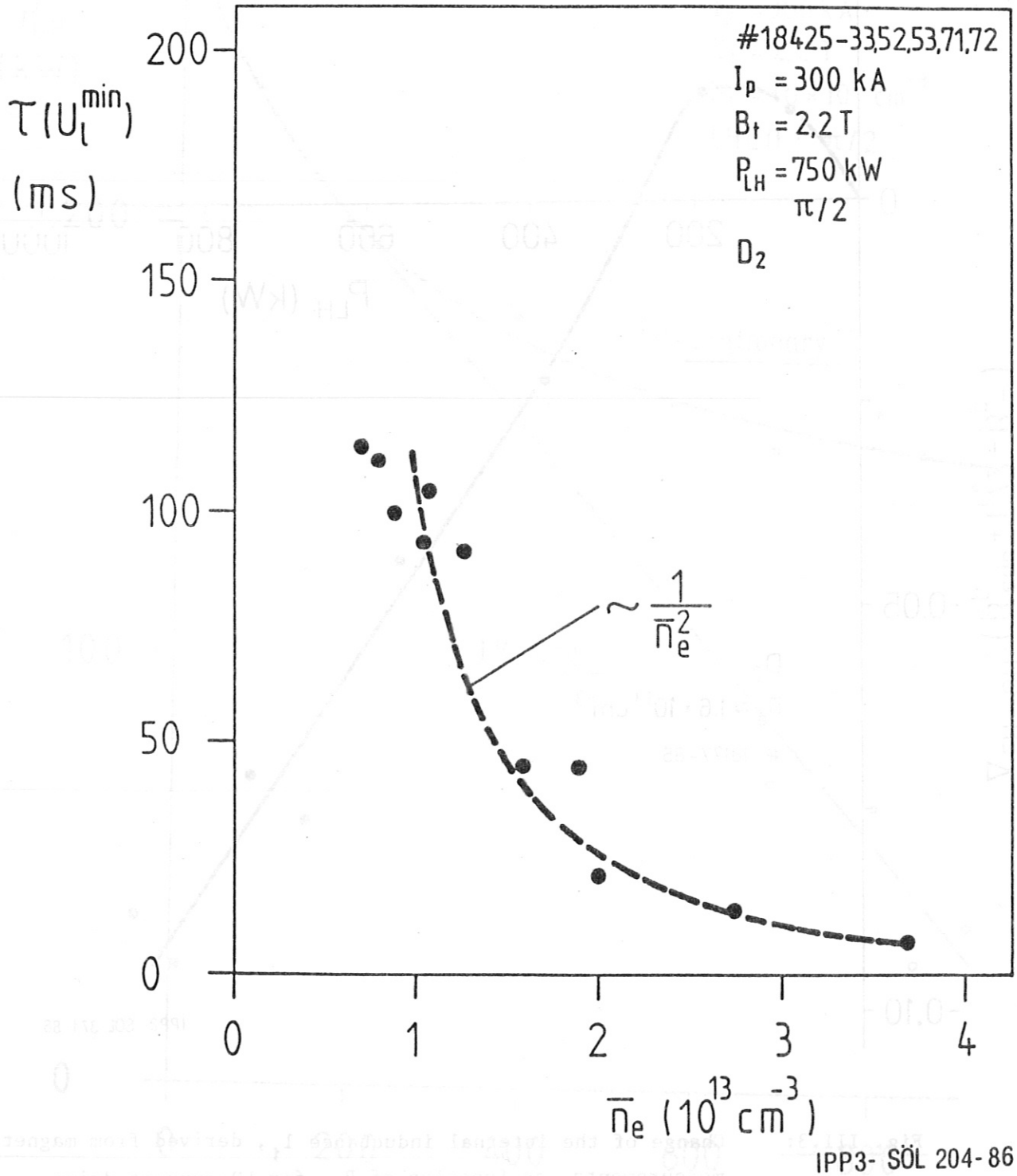

Fig. III.4: Time of maximum drop of the loop voltage U_1 in the initial phase of LH-current drive.

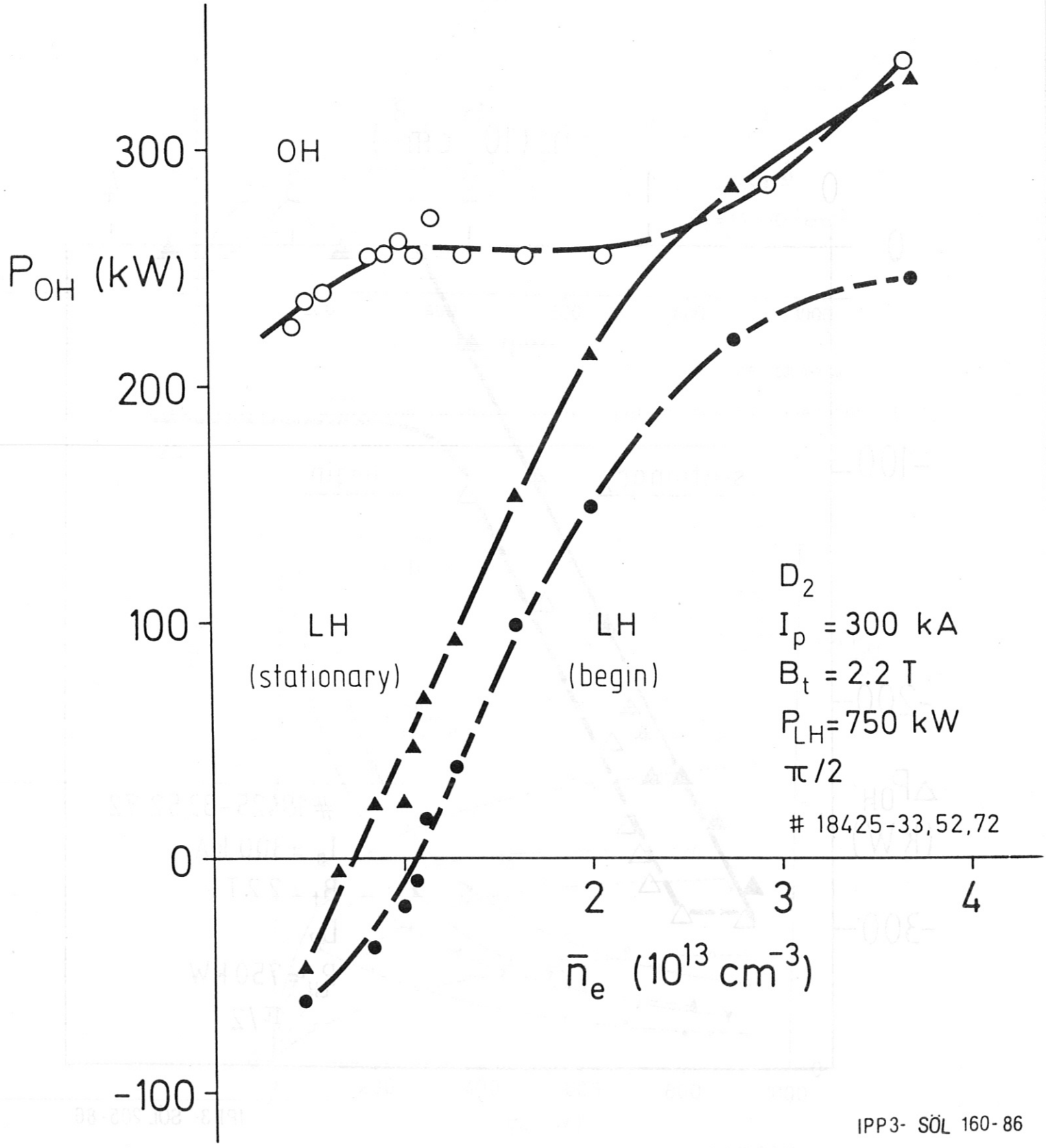

Fig. III.5: Ohmic power input with OH and LH-current drive.

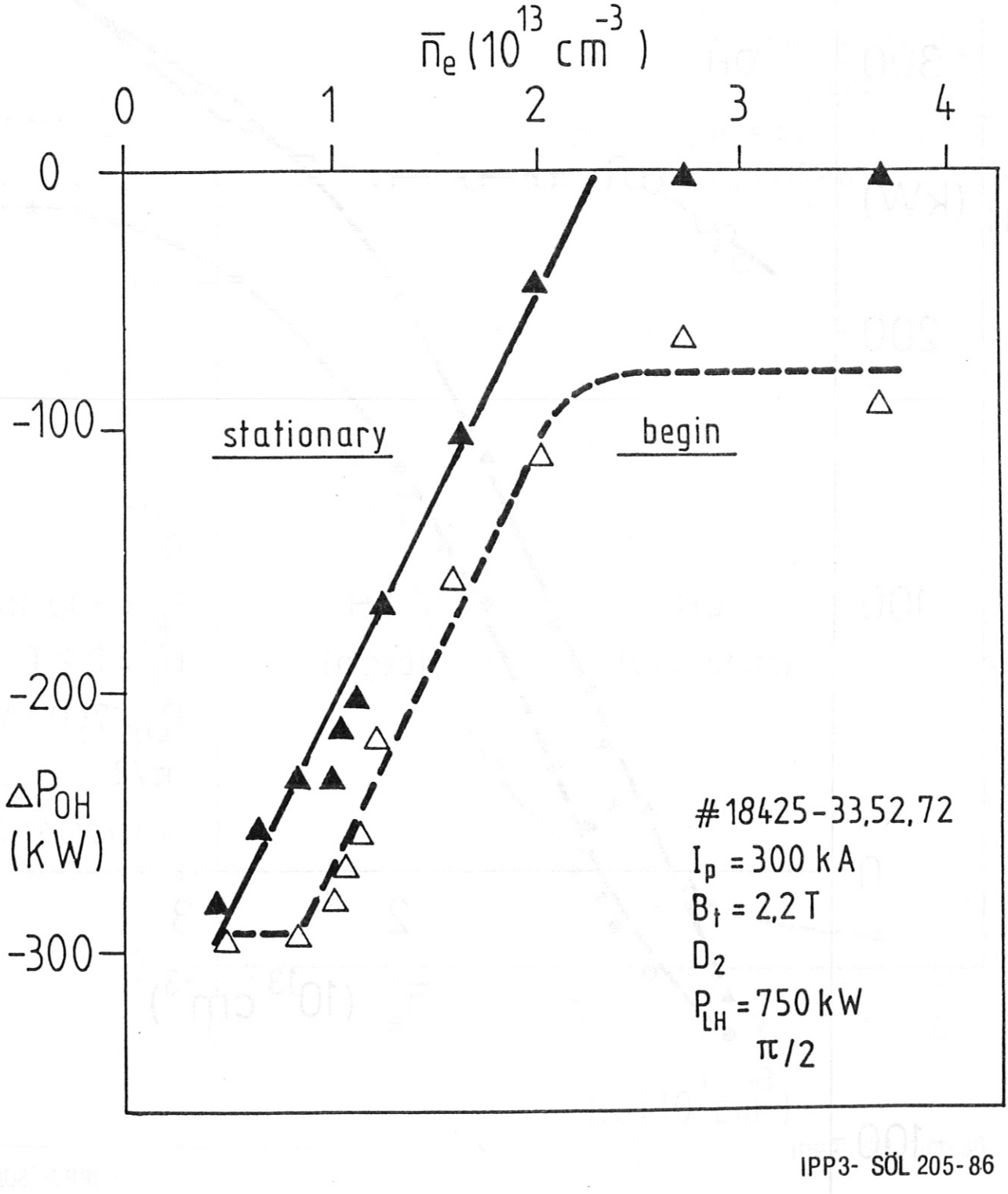

Fig. III.6: Reduction of Ohmic power input during LH-current drive in the initial and in the stationary phase.

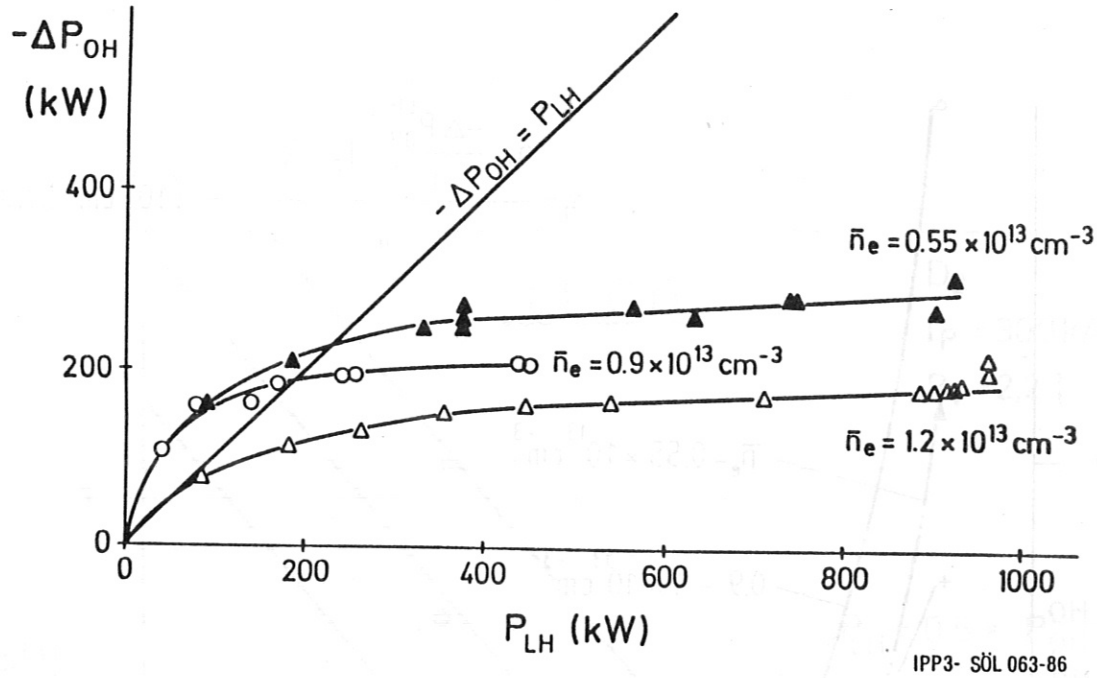

Fig. III.7: Reduction in Ohmic power input versus LH-power for LH-current drive.

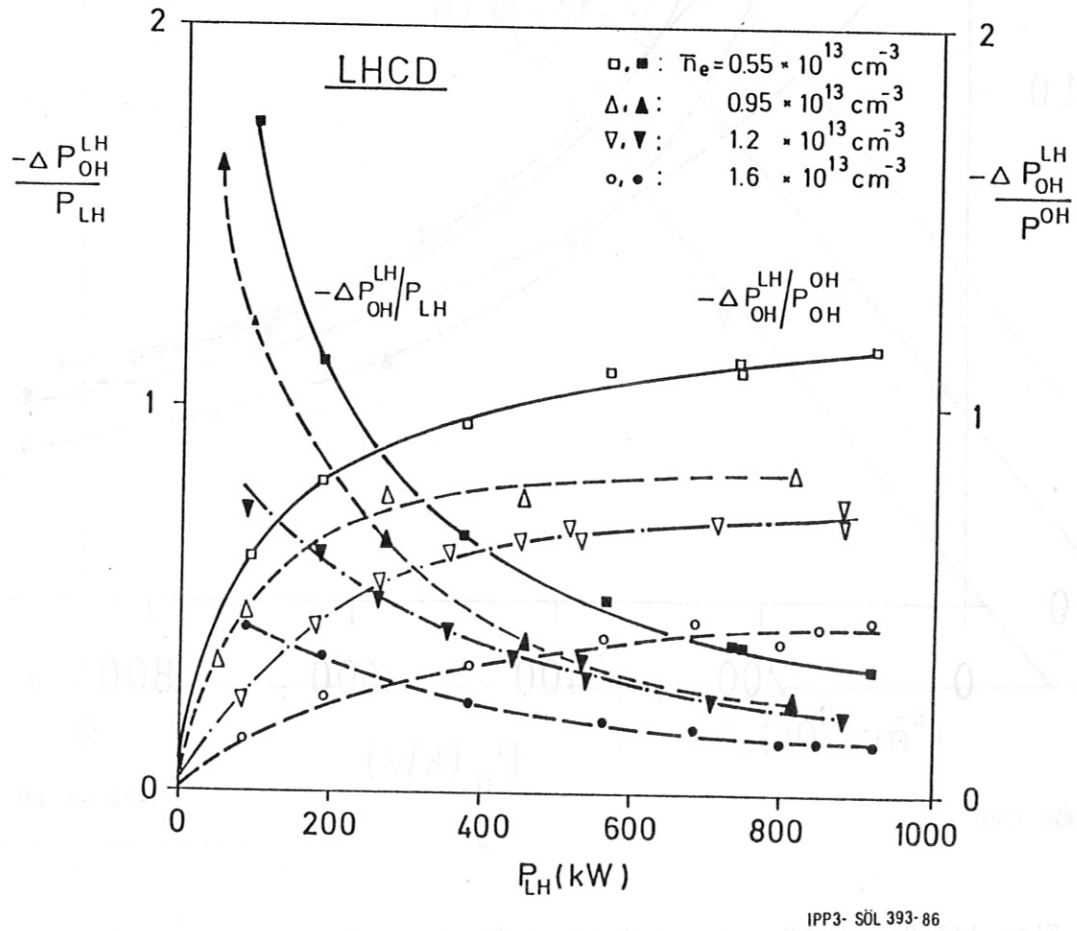

Fig. III.8: Power conversion rates $-\Delta P_{OH}^{LH}/P_{LH}$ and relative drop in OH-input $-\Delta P_{OH}^{LH}/P_{OH}$ for LH-current drive.

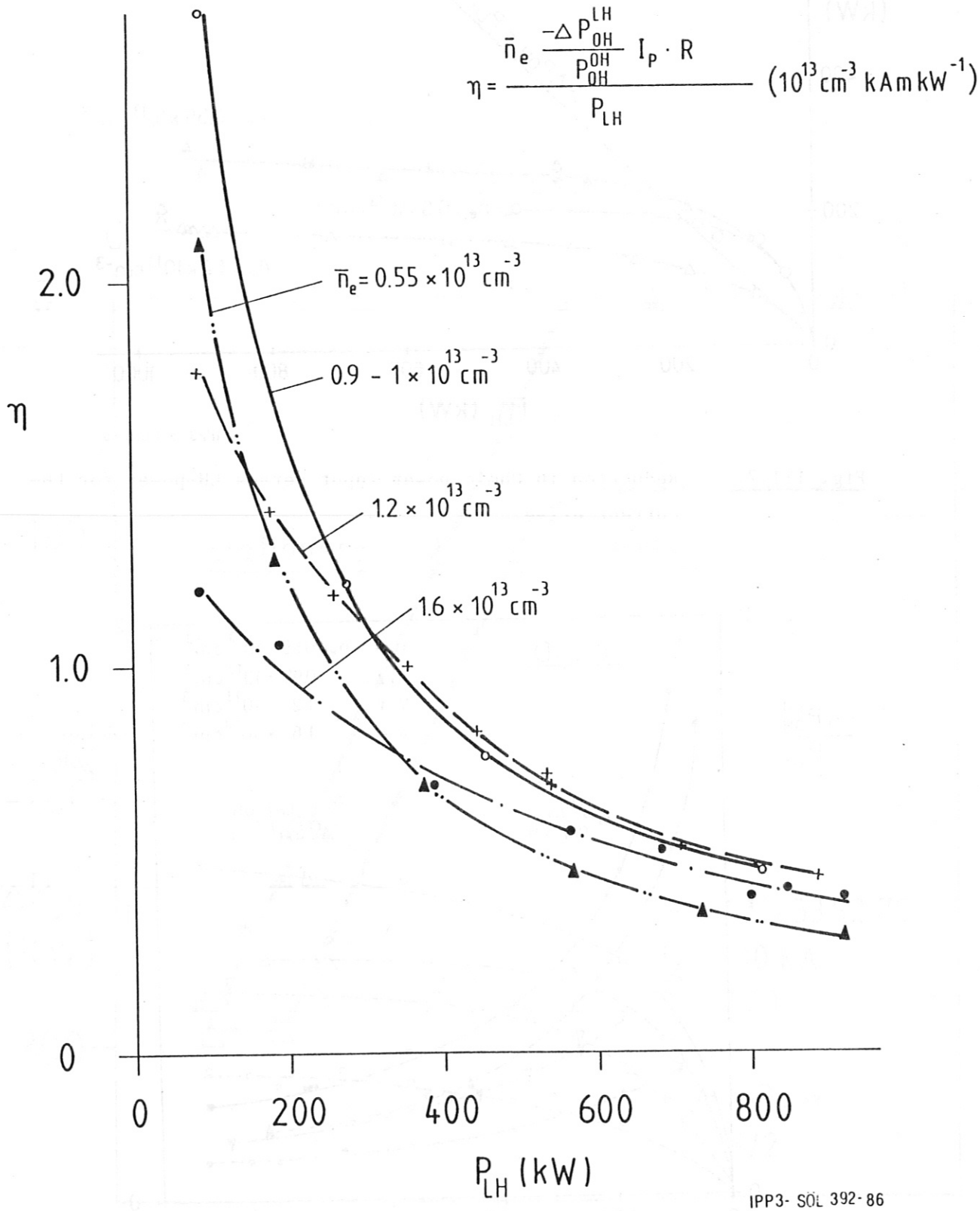

Fig. III.9: LH-current drive efficiency for combined OH/LH-current drive.

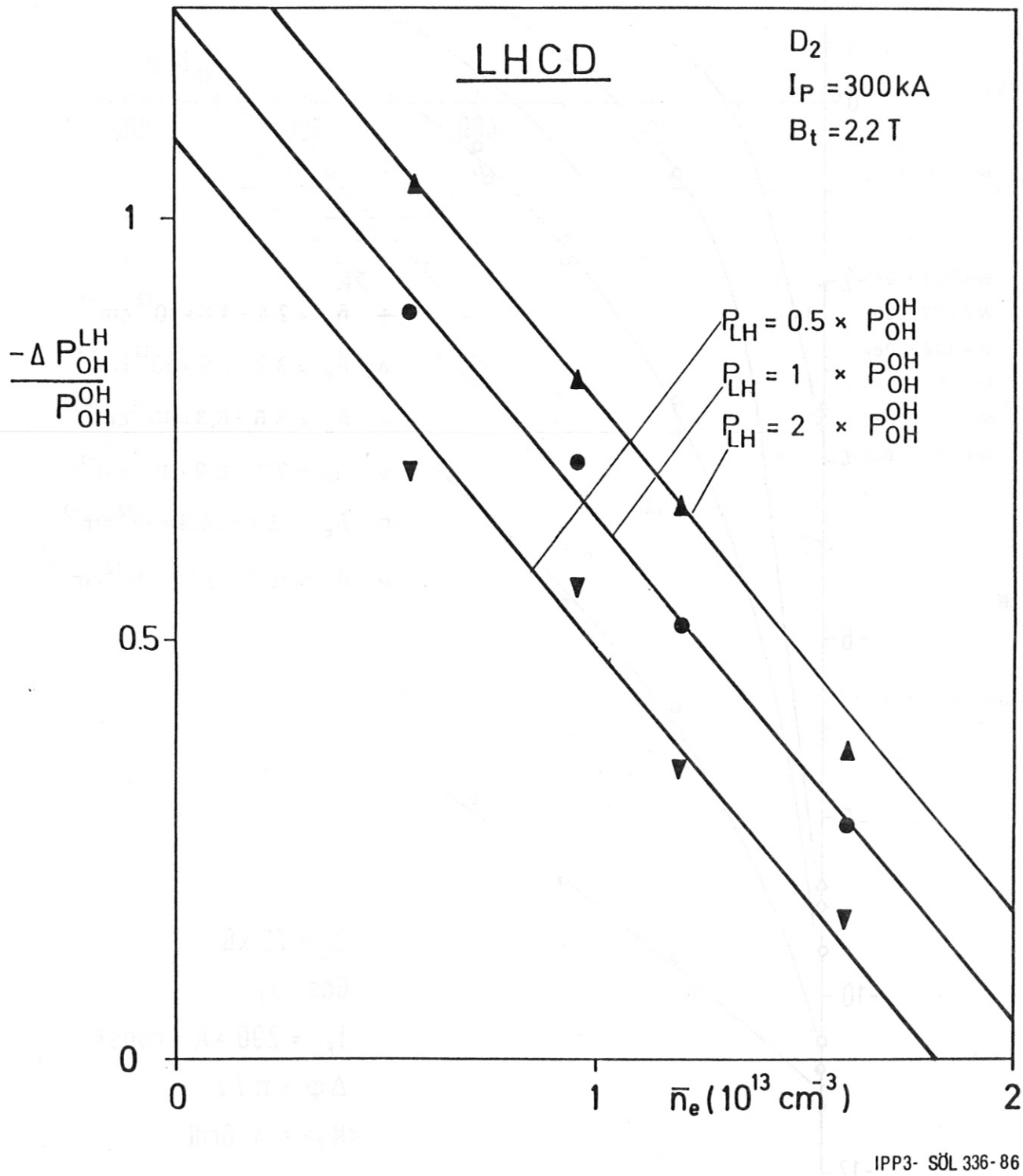

Fig. III.10: Relative reduction in Ohmic power input $-\Delta P_{OH}^{LH}/P_{OH}^{OH}$ with LH-current drive.

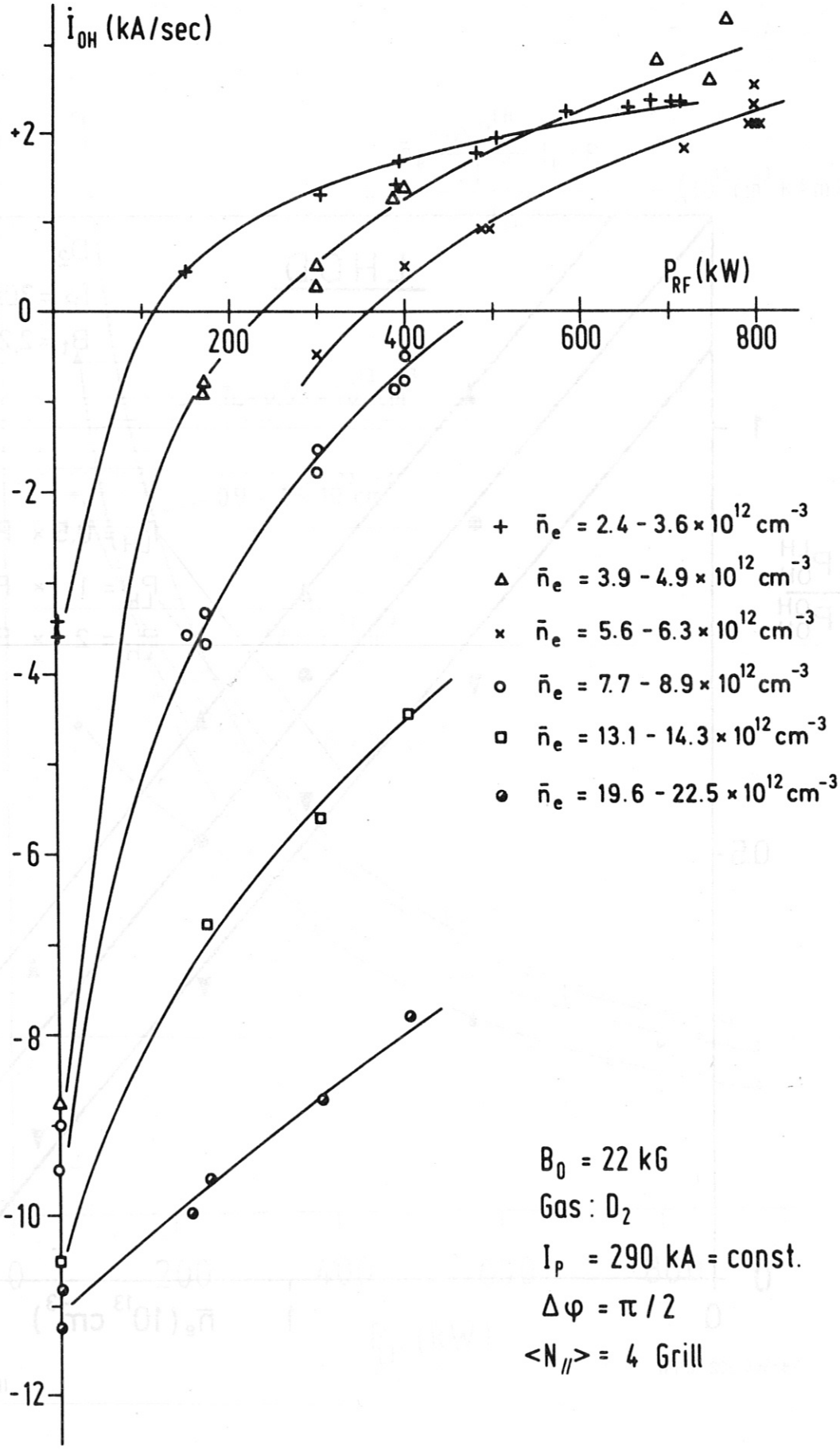

Fig. III.11: Primary current rate of change, $\dot{I}_{OH}$, as a function of power (ASDEX).

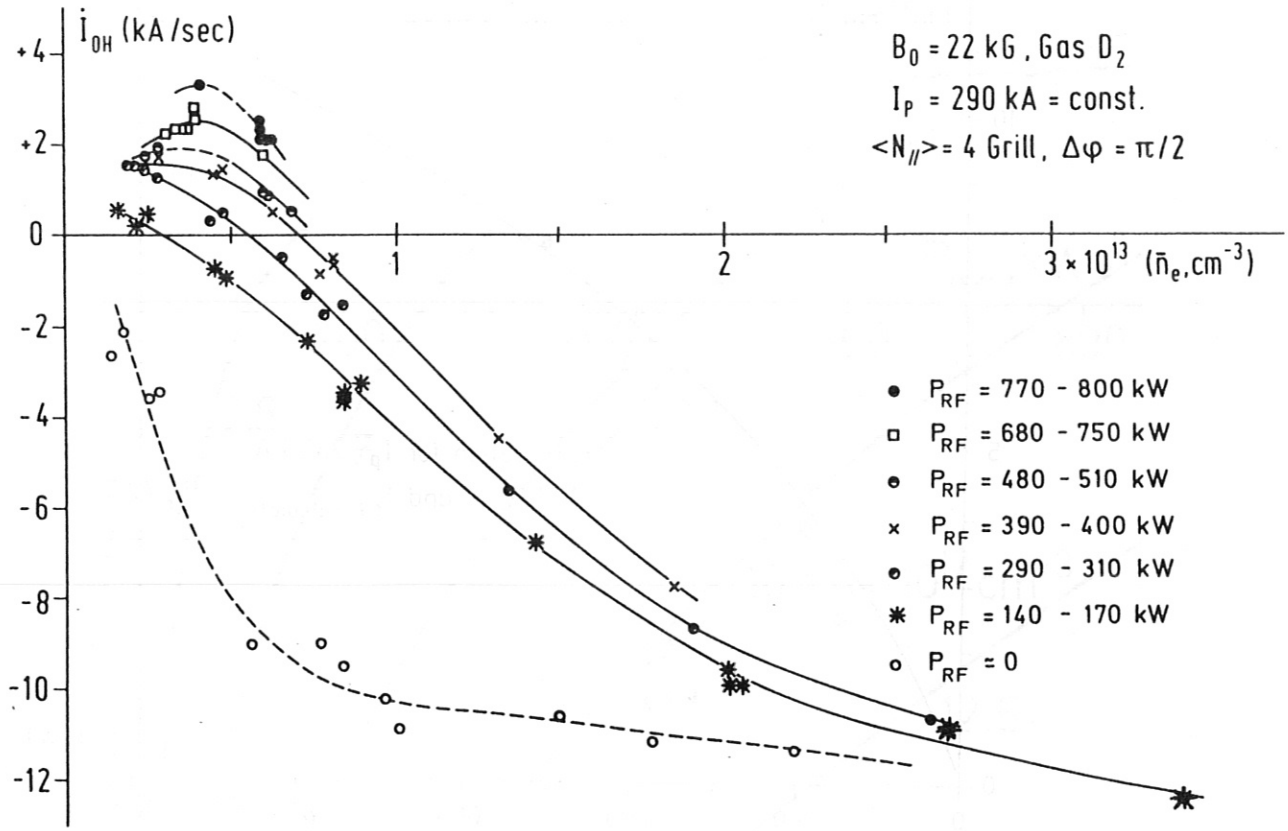

Fig. III.12: Primary current rate of change, $\dot{I}_{OH}$, as a function of density (ASDEX).

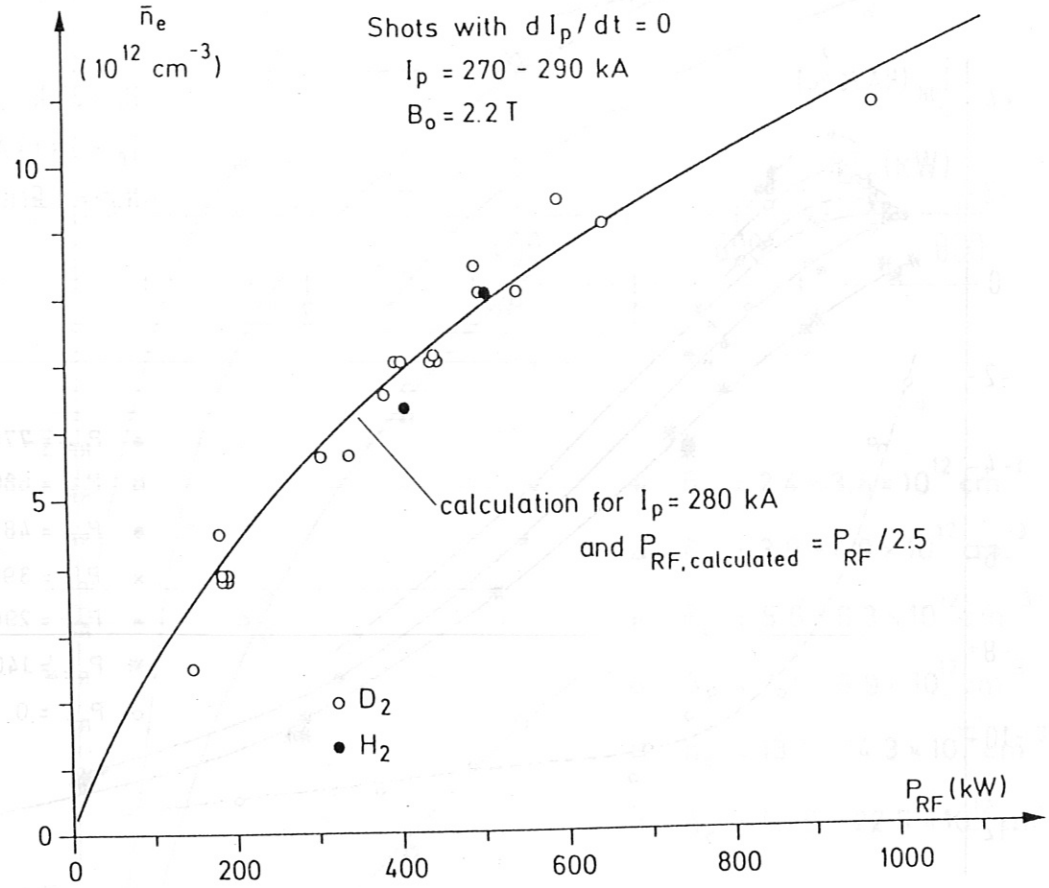

Fig. III.13: Electron density $\bar{n}_e$ versus applied LH-power P_{LH} at which the total plasma current of $I_p \approx 280$ kA can be driven in ASDEX with zero electric field. Experimental points (circles) and comparison with theory (solid line).

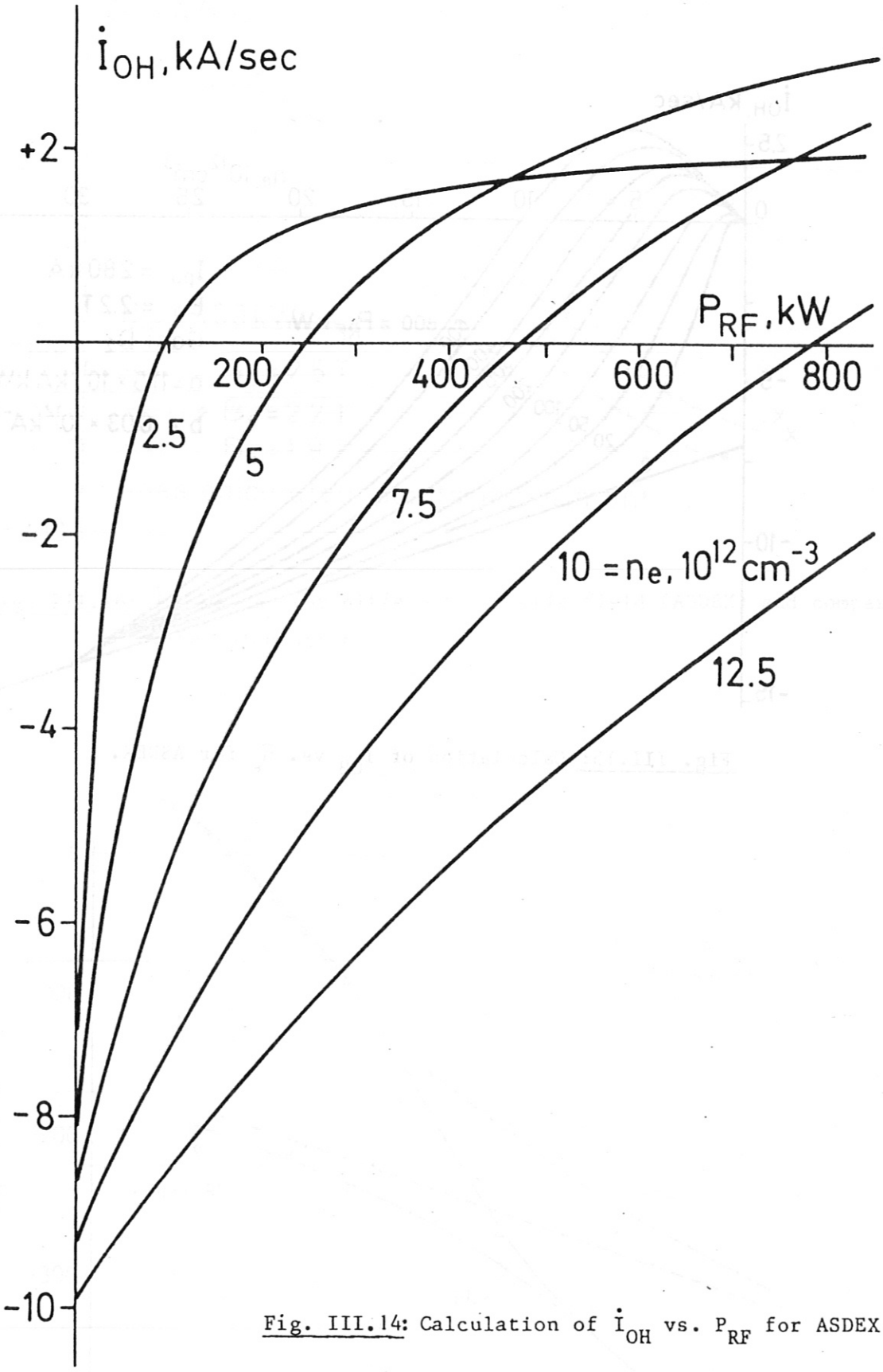

Fig. III.14: Calculation of $\dot{I}_{OH}$ vs. P_{RF} for ASDEX.

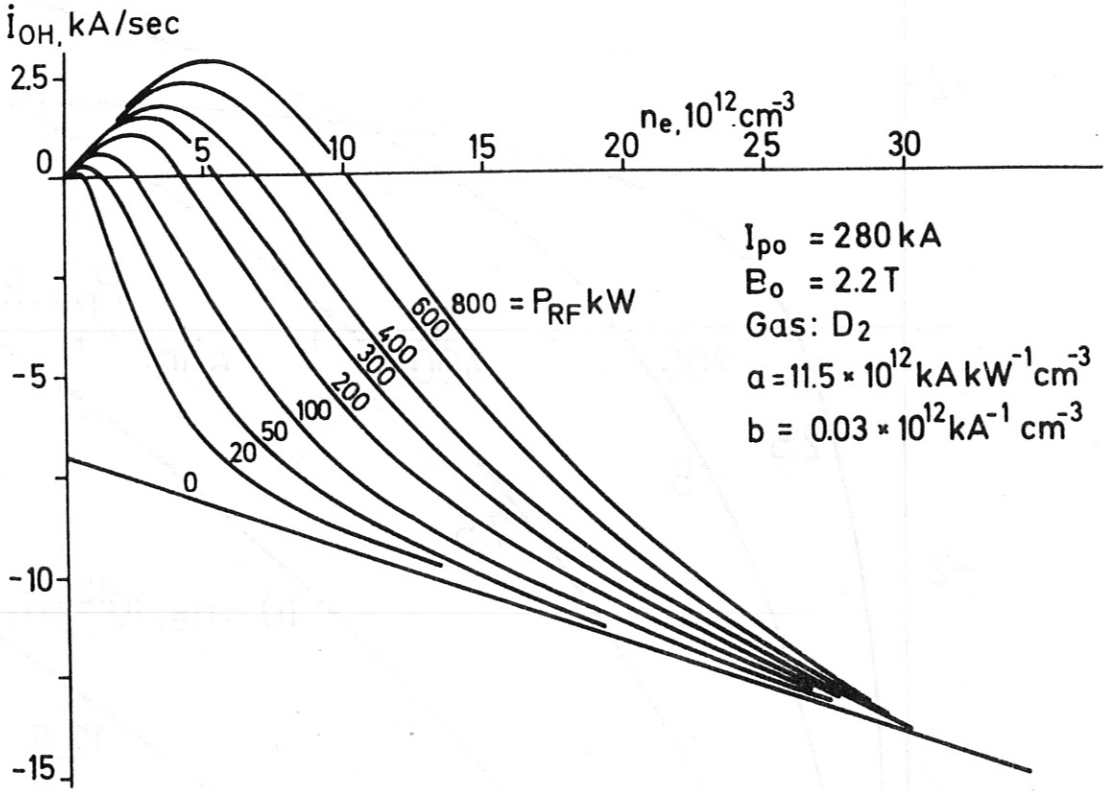

Fig. III.15: Calculation of $\dot{I}_{OH}$ vs. $\bar{n}_e$ for ASDEX.

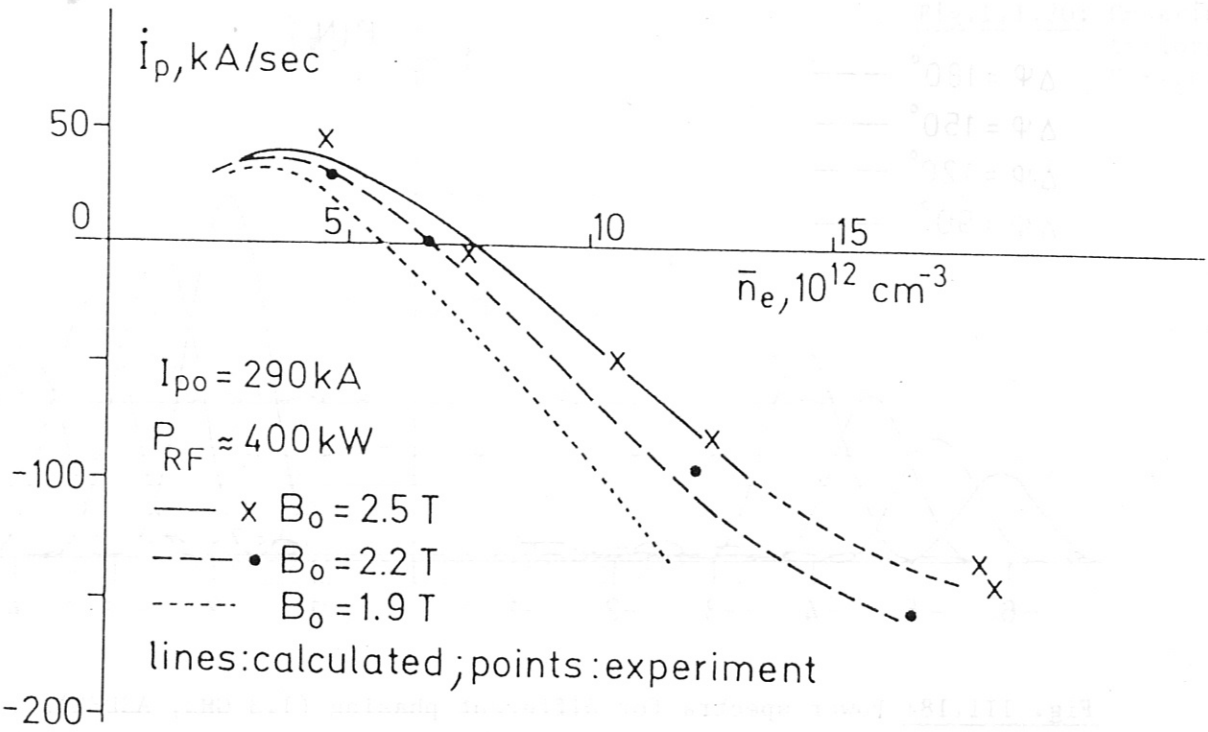

Fig. III.16: $\dot{I}_{OH}$ **vs.** $\bar{n}_e$ **for different magnetic field (ASDEX) and comparison with calculation.**

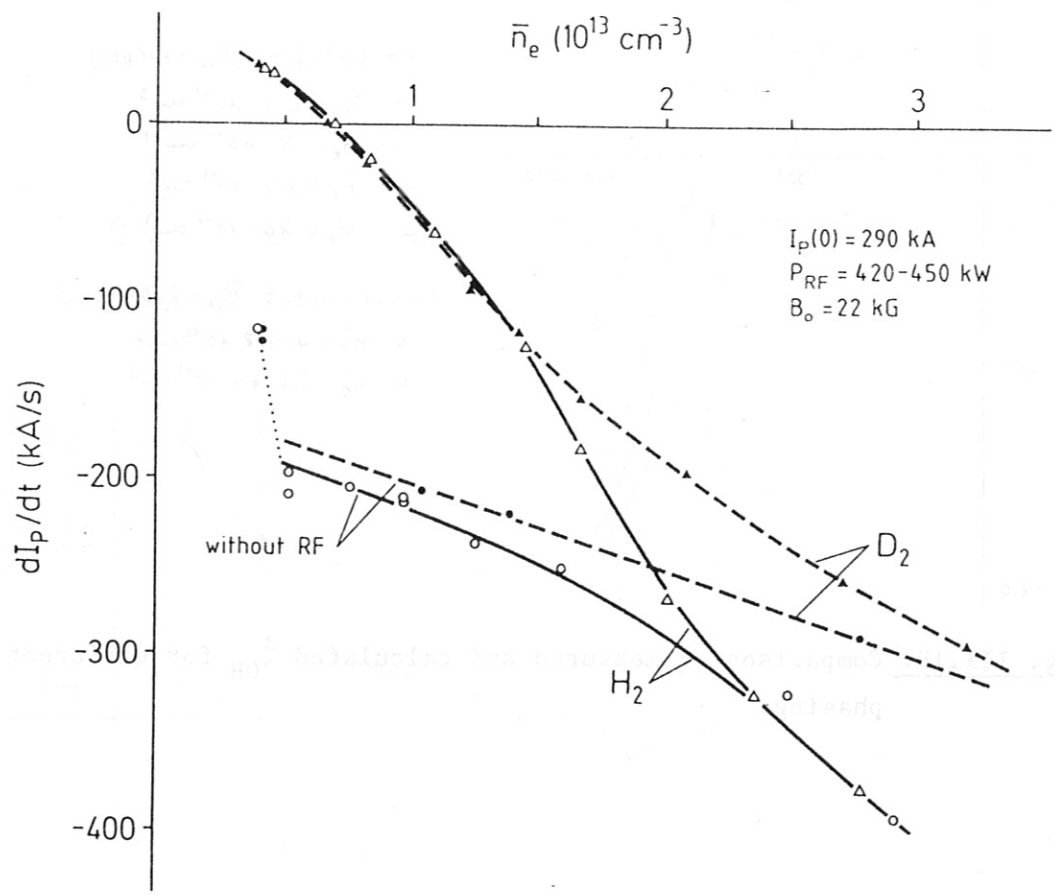

Fig. III.17: $\dot{I}_{OH}$ **vs.** $\bar{n}_e$ **in hydrogen and deuterium plasmas (ASDEX).**

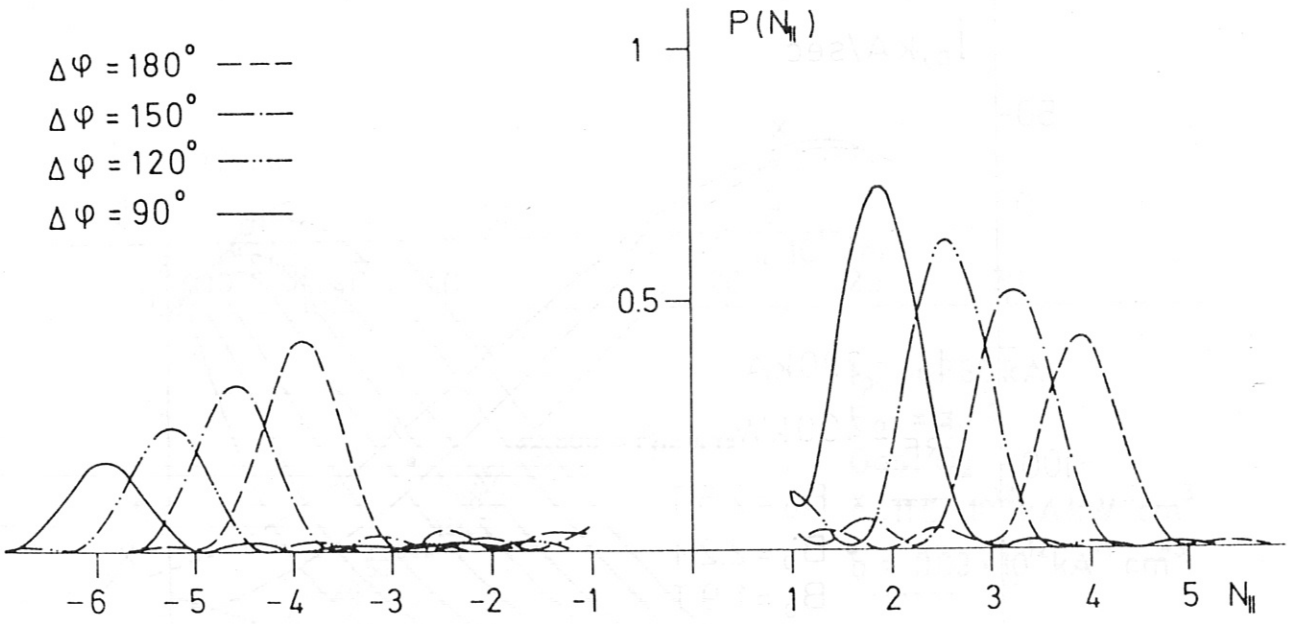

Fig. III.18: Power spectra for different phasing (1.3 GHz, ASDEX).

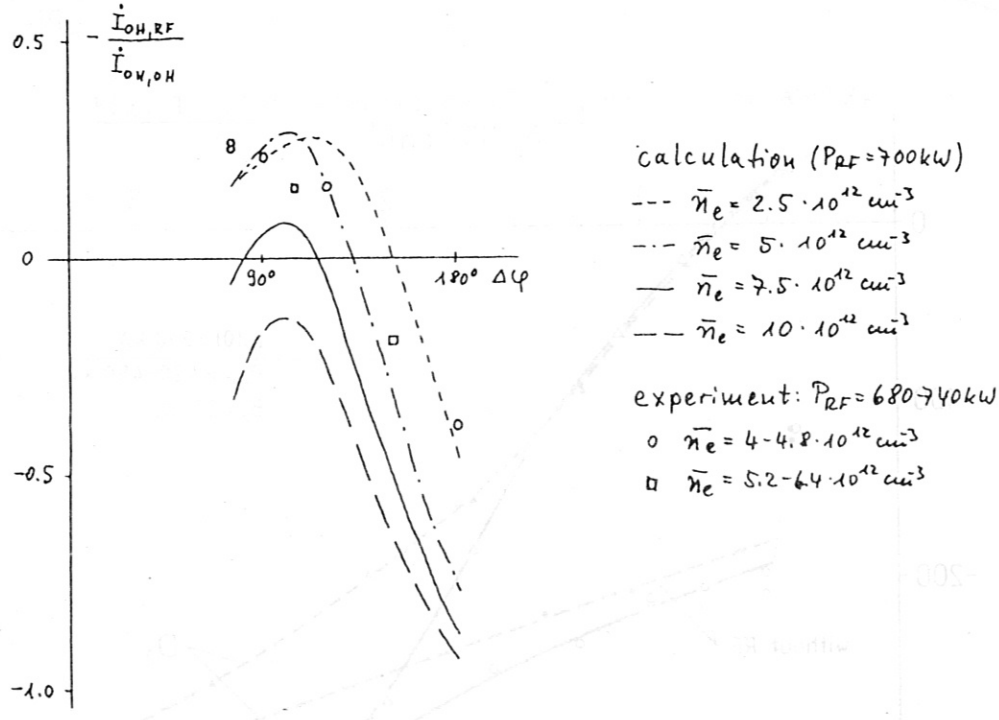

Fig. III.19: Comparison of measured and calculated $\dot{I}_{OH}$ for different grill phasing.

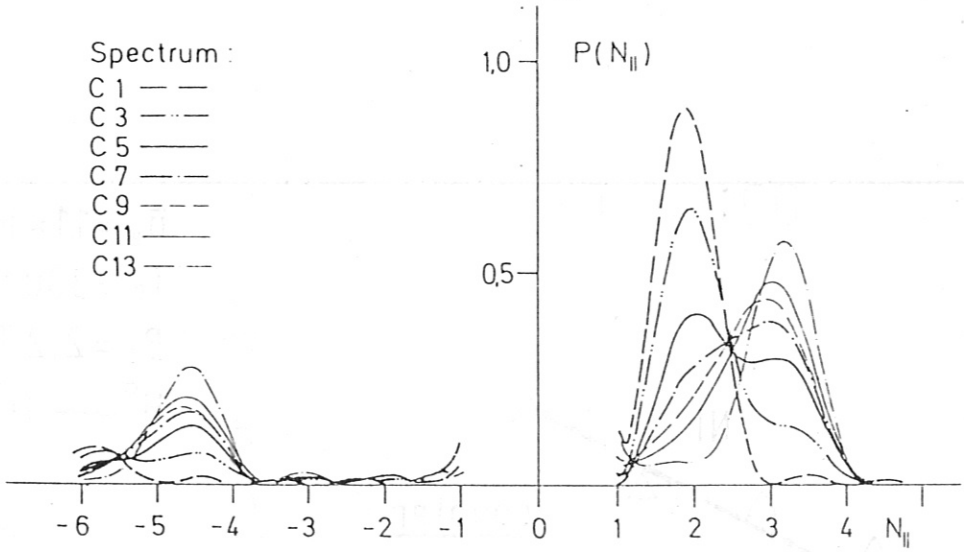

Fig.III.20: C-series of tailored N -spectra.
"

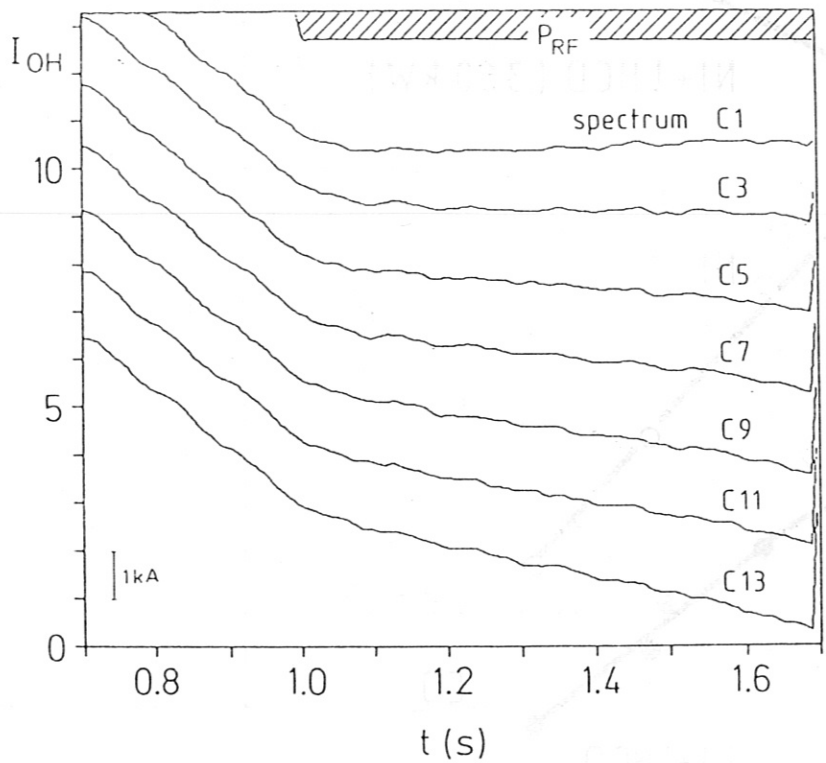

Fig.III.21: $I_{OH}(t)$ for experiments with tailored spectra.

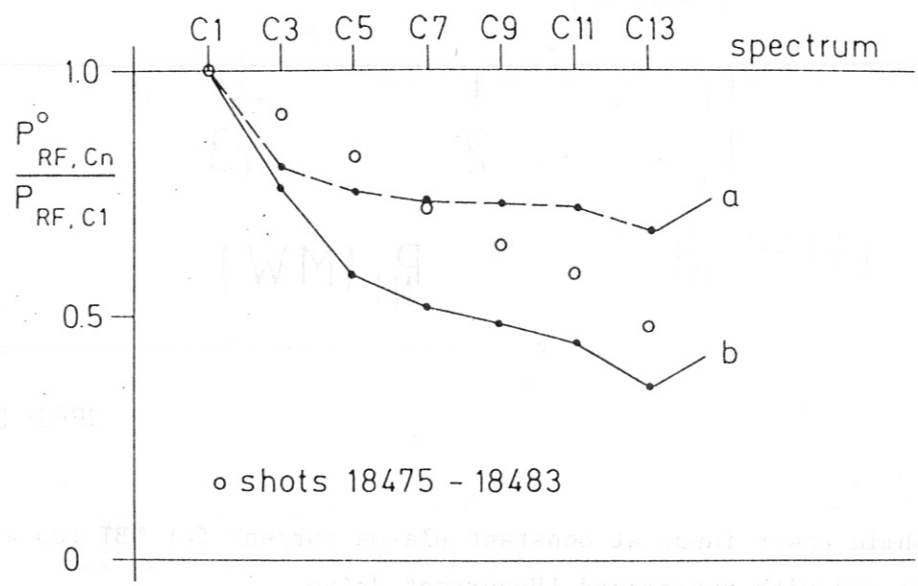

Fig. III.22: Reduction of current drive efficiency with tailored spectra.

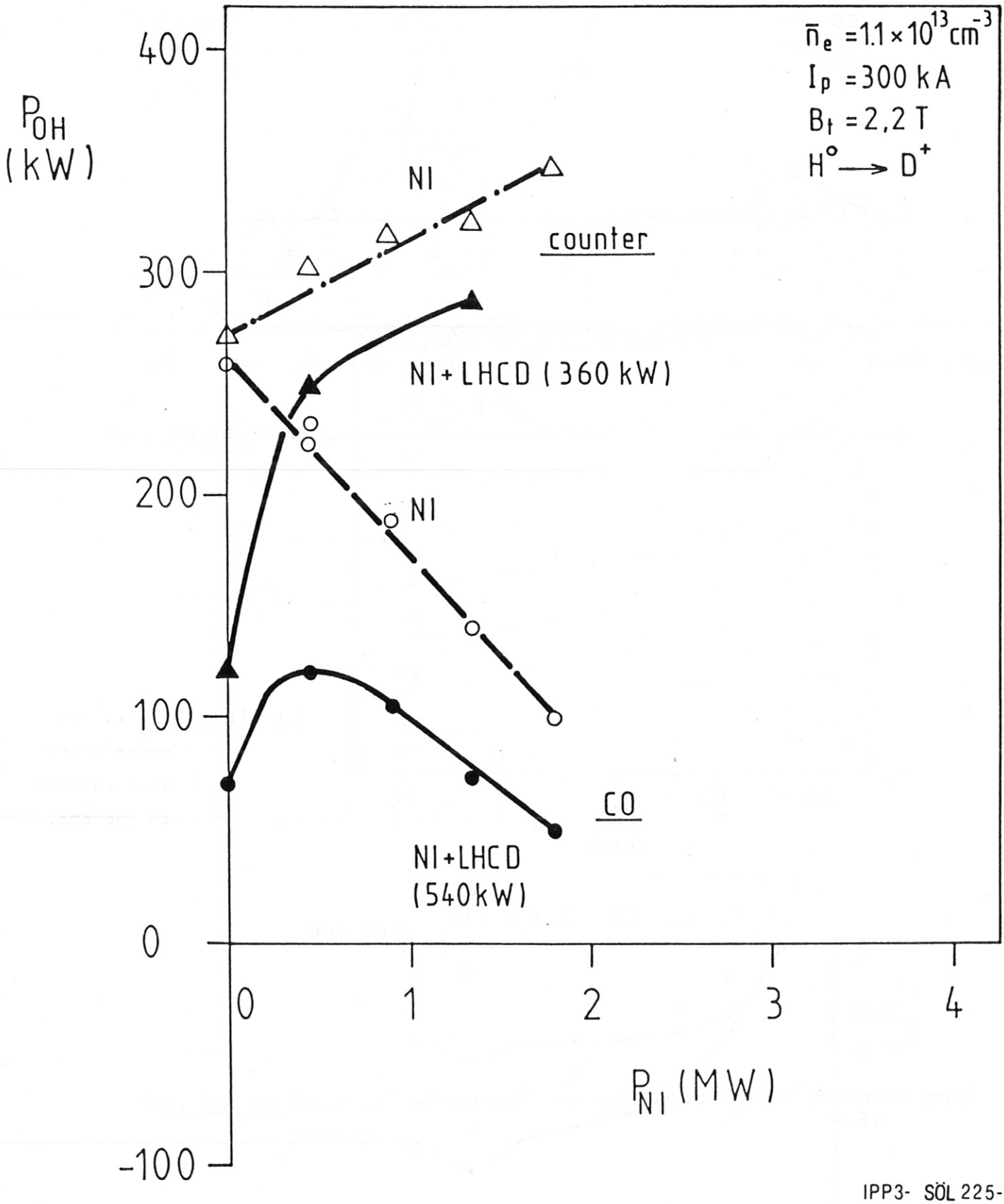

Fig. III.23: Ohmic power input at constant plasma current for NBI (co and counter) alone and with superposed LH-current drive.

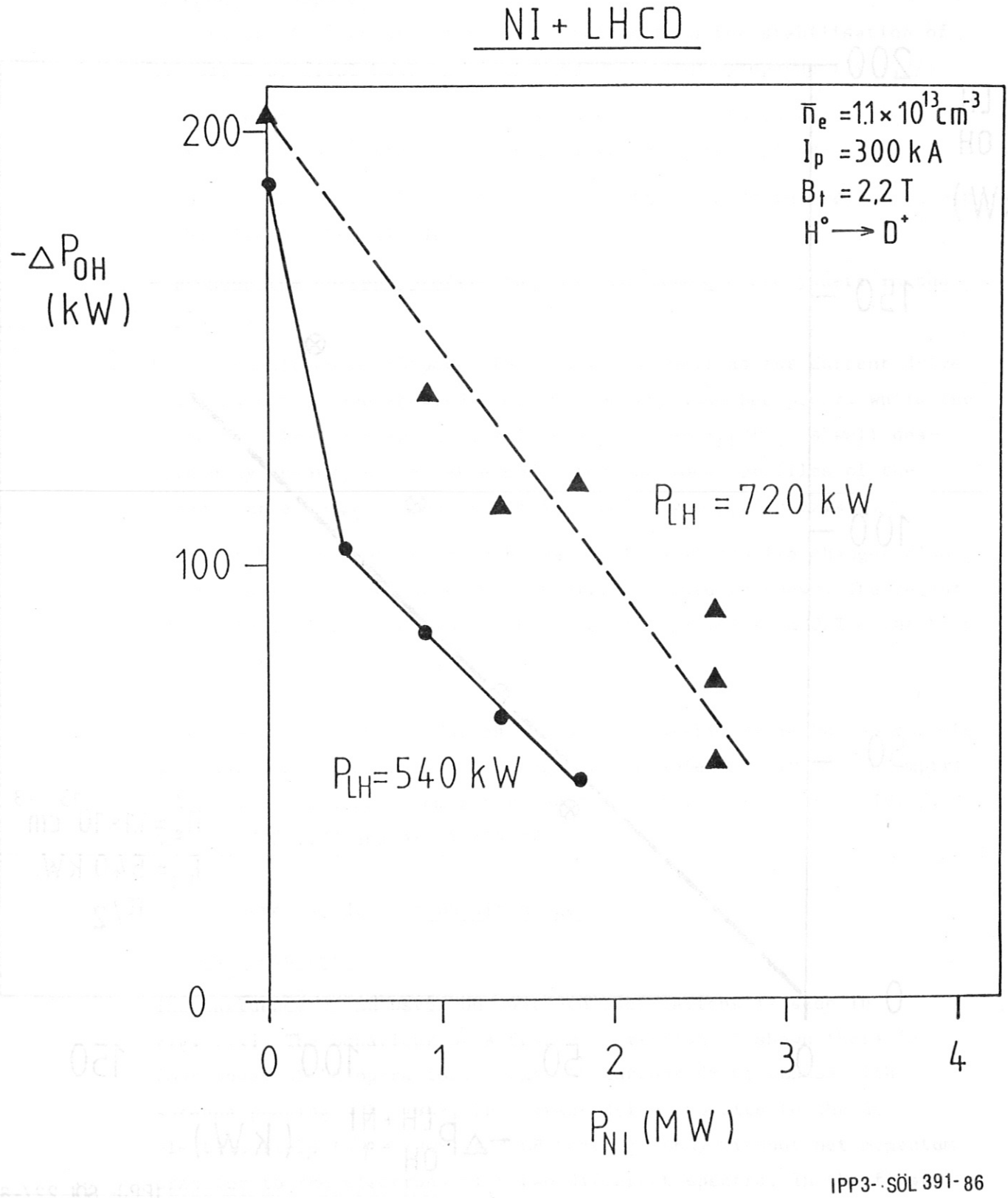

Fig. III.24: Reduction in Ohmic power for LH-current drive combined with NBI-heating versus beam power.

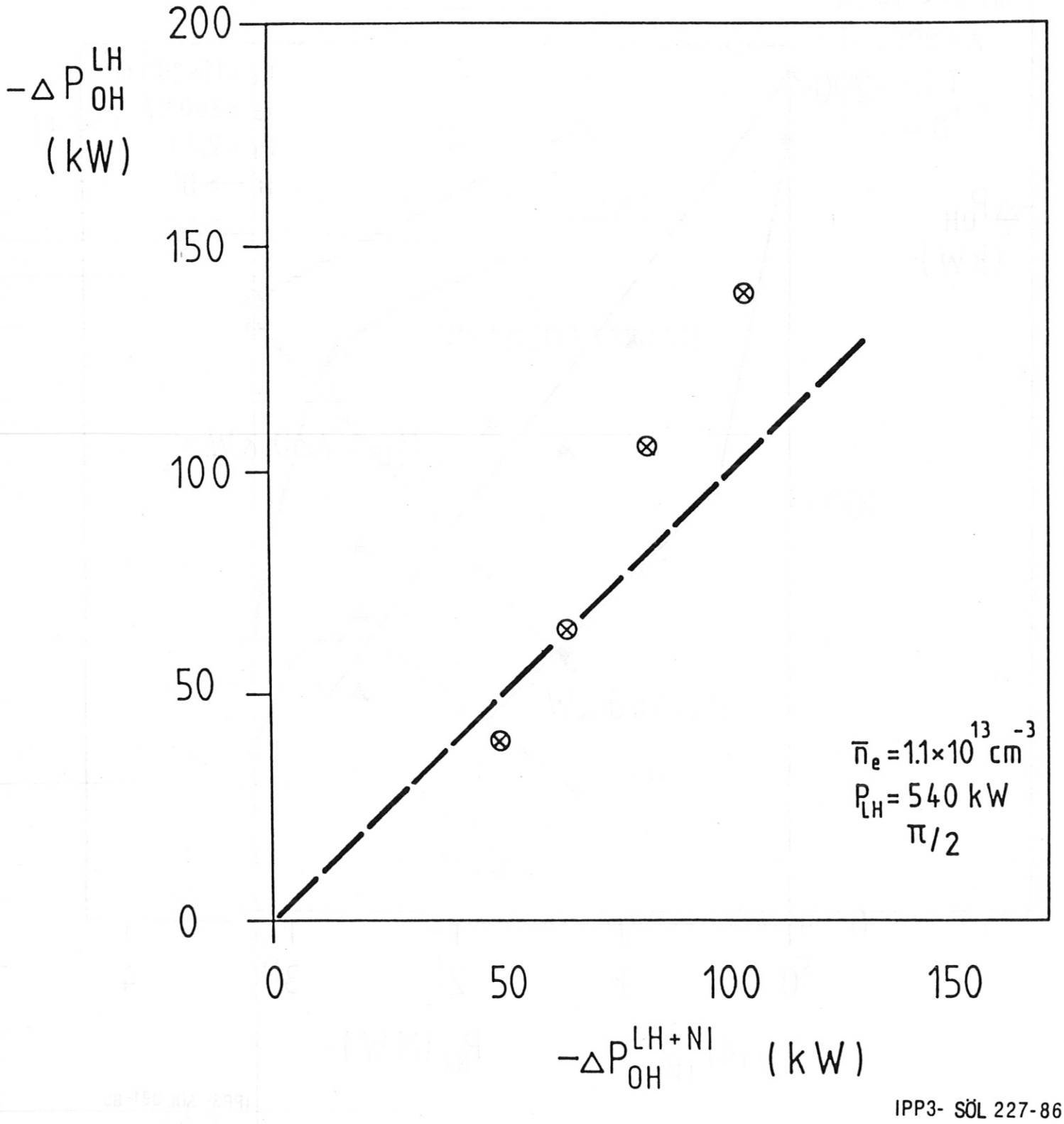

Fig. III.25: Calculated drop in Ohmic power from LH-current drive in a preheated OH-plasma $-\Delta P_{OH}^{LH}$ versus measured drop $-\Delta P_{OH}^{LH+NI}$ in combined operation LHCD/NBI.

IV. Sawtooth Stabilisation with Lower Hybrid Waves

1. General overview

From theoretical considerations several methods for stabilisation of MHD modes by local heating or current drive were proposed /IV.1,2/:

- Local heating in the magnetic islands in order to increase the electrical conductivity and thereby suppress the islands.
- Local rf-current drive within the magnetic islands in order to limit the size of the islands.
- Broaden the current profile in order to have $q > 1$ everywhere in the plasma.

Local deposition of LH-power for heating as well as for current drive requires a thorough knowledge of the locally absorbed power. While the ratio of driven current to dissipated rf power I_{rf}/P_{rf} is well described by theory, no reliable model for the local profiles of the driven current $j_{rf}(r)$ and of the absorbed power $p_{rf}(r)$ exists.

For stabilisation of sawteeth by means of local profile changes also the mechanism of the sawtooth instability should be known. The recent theoretical /IV.3/ and experimental results /IV.4/ from JET might help to clarify the situation.

With the present uncertainties about the instability mechanism and the LH power deposition profile it seems preferable to rely on the empirical scaling obtained from experiments in Petula /IV.5/, PLT /IV.6/, Alcator C /IV.7/ and ASDEX /IV.8/.

2. Parameter studies in OH discharges

2.1 Sawtooth period

The influence of LH waves on sawtooth oscillations is seen in Fig. IV.1. The behaviour of soft X-ray emission is shown there for four modes of LH operation: normal LH-current drive (LHCD) with antenna phasing $\Delta\varphi = +90^{\circ}$, LH-current drive opposite to the dc electric field ($\Delta\varphi = -90^{\circ}$) and LH heating (LHH) without net momentum transfer to the electrons with two different spectra. In the first three cases the wave spectrum covers the same range of phase velocities, with $\bar{N}_{\parallel} = 2$ (c.f. Fig. II.1, b, c), in the last case a spectrum with lower phase velocity waves is launched, with $\bar{N}_{\parallel} = 4$ (c.f. Fig. II.1, a). The total X-ray intensity rises due to the radiation from suprathermal electrons generated by the LH waves. The sawtooth period increases immediately after the start of the rf for

normal LH-current drive and for LH heating with low $\bar{N}_{\parallel}$. No change is seen with opposite current drive and with LH heating at the higher $\bar{N}_{\parallel}$. The dependence of the change in sawtooth period on the phase velocity of the LH waves was studied for the whole range available with various antenna phasings: $1.7 < \bar{N}_{\parallel} \leq 4$ ($75^{o} \leq \Delta\varphi \leq 180^{o}$). It is found that the sawtooth period during LH application closely correlates with the observed drop in loop voltage $-\Delta U_1^{LH}$ Fig. IV.2. A similar correlation between τ_{ST}^{LH} and $-\Delta U_1^{LH}$ is found when varying the rf power in the LH-heating mode. The drop in loop voltage in the latter case may be explained by an increase only of the electrical conductivity. This occurs rapidly after switch-on of the rf within the time scale of generation of a suprathermal electron population.

In the case of LH-current drive τ_{st} continues to change during the rf pulse. The values for the first sawtooth after start of the LH and for the saturated state are shown in Fig. IV.3 for a power scan at $\bar{n}_e = 1.6 \times 10^{13} cm^{-3}$. At low power the sawtooth period rises continuously until the end of the rf. For $P_{LH} > 400$ kW the period τ_{st} first increases and then decreases, at high rf power even below the Ohmic value.

The increment of the sawtooth period during LH decreases with increasing density, as shown in Fig. IV, 4 for the current drive mode. Below a density threshold of $\bar{n}_e = 1.2 \times 10^{13}$ cm^{-3} the sawteeth are suppressed by the LH. The time delay $_d$ between start of the LH and the last sawtooth collapse decreases with increasing rf power, as seen from the waveforms of soft X-ray emission for a P_{LH}-scan at $\bar{n}_e$ = 1.2×10^{13} cm^{-3} (Fig. IV.5). In this case sawteeth are stabilized for powers $P_{LH} \geq 445$ kW. The delay τ_d also depends strongly on the density and it increases with increasing density as shown in Fig. IV.6.

2.2 Mechanism of sawtooth stabilisation

Suppression of sawteeth could be attained only with current drive spectra. It is not related to the generation of suprathermal electrons, as revealed by rf power scans in LH heating or LH-current drive mode. With the same amount of rf power the drop in loop voltage $-\Delta U_1^{LH}$ is slightly larger in the current drive mode, but a much larger populationof high-energy electrons is produced in the heating mode /IV.9/. Sawteeth, however, persist during LH heating up to the maximum

applied power of P_{LH} = 1 MW, while they are suppressed in LH-current drive with much lower power, e.g. with P_{LH} = 400 kW at $\bar{n}_e = 1.1 \times 10^{13}$ cm^{-3}, I_p = 300 kA, B_t = 2.2 T. The increase of the electrical conductivity during LH is not decisive for stabilisation either. With LH heating, sawteeth were still present at a drop of the loop voltage $-\Delta U_1^{LH}/U_1^{OH} = 0.8$, while stabilisation could be achieved with LH-current drive at $-\Delta U_1^{LH}/U_1^{OH} \approx 0.5$. A correlation between the disappearance of sawteeth and the increase of the electrical conductivity or the generation of suprathermal electrons also seems to be ruled out by the different time scales. The drop in loop voltage and the build-up of the fast electron population occur within typically 25 ms, while the time delay between the start of rf and stabilisation of sawteeth is of the order of 50 - 500 ms, depending on $\bar{n}_e$ and P_{rf}.

A crucial parameter for suppression of sawteeth seems to be the total amount of rf-driven current. About half of the power necessary for full LH-current drive had to be applied in the density range 0.5×10^{13} $cm^{-3} \leq \bar{n}_e \leq 1.6 \times 10^{13}$ cm^{-3}, where sawteeth could be stabilised with the rf power available. The current distribution during LH differs from the OH current profile, as indicated by a change in the internal inductance l_i. This may be derived from measurements of the quantities $\beta_p^{equ} + l_i/2$ and $\beta_p^{\perp}$. Magnetic measurements allow one to determine only the sum of the pressure anisotropy and internal inductance: $(\beta_p'' - \beta_p^{\perp}) + l_i$. In the case of the LH power scan at $\bar{n}_e = 1.6 \times 10^{13}$ cm^{-3} (Figs. IV. 3,6) the pressure anisotropy remains small and the stationary value of $(\beta_p^{equ} + l_i/2) - \beta_p^{\perp}$ then gives l_i. At low rf power the internal inductance l_i increases while it drops during LH current drive with $P_{LH} > 400$ kW as seen from Fig. IV.7. Consequently, the current profile is peaking during low power LH-current drive, and the increase of the sawtooth period τ_{st} at low LH power in Fig. IV.3 might then be explained by an expansion of the sawtooth-unstable region within r(q=1). The drop in l_i at higher power indicates a flattening of j(r) and the reduction in τ_{st} could be explained in like manner by a shrinking of the q=1-surface.

Direct measurements of j(r) are made on ASDEX using a neutral Li-beam probe /IV.10/. In Fig. IV.8 the current profiles j(r) and the corresponding profiles of q(r) are shown during the Ohmic phase and during the stationary sawtooth-free phase of LH-current drive with P_{LH} = 540 kW ($\Delta\varphi = 90^{o}$) at $\bar{n}_e = 1.2 \times 10^{13}$ cm^{-3}, I_p = 300 kA, B_t = 2.2 T,

$-\Delta U_1^{LH}/U_1^{OH} \approx 0.7$. The current profile during LH-current drive is flatter than during the Ohmic phase. The q is slightly below 1 in the central plasma region during inductive current drive and above 1 in the whole plasma region during the LH-current drive. The time behaviour of the internal inductance l_i is seen in Fig. IV.9. It decreases with a time constant comparable to the delay τ_d for sawtooth stabilisation (Fig. IV.6). The suppression of sawteeth is therefore achieved by flattening the current profile j(r) in the central part of the plasma such that $q > 1$ everywhere. Consistently, no changes of the current profile are found in the cases of opposite current drive and of LH heating with low $\bar{N}_{\parallel}$ that are shown in Fig. IV.1 where sawteeth remain during the LH phase /IV.11/. The interpretation of magnetic signals alone would have been misleading in the case of opposite current drive as shown in Fig. IV.10. If the quantity $(\beta_p^{equ} + l_i/2)-\beta_p^{i}$ plotted there, would be interpreted as $l_i/2$, then an increase of l_i and a peaking of the current profile would be concluded. In fact, l_i stays constant while the anisotropy increases continuously due to acceleration of fast LH generated electrons by the large toroidal electric field to runaway energies.

The electron temperature profile during LH heating and LH-current drive peaks with a strong increase of the central temperatures. This demonstrates clearly the decoupling of electron temperature and current profiles during LH-current drive.

2.3 LH power requirements

In the parameter range where sawteeth were suppressed, about half of the rf power necessary for complete LH-current drive was required for stabilisation. For discharges with $q(a) = 3.5$ this can be seen from Fig. IV.11 where the relative reduction in Ohmic input $-\Delta P_{OH}^*/P_{OH}$ due to LH current drive at the stability margin with $P_{LH} = P_{LH}^*$ is plotted versus $\bar{n}_e$ together with the threshold power P_{LH}^* and the absorbable fraction $P_{LH,acc}^*$ of the rf power launched in these cases. Because of the uncertainty in the deposition profile two cases have been considered, for accessibility of the LH waves to r = 30 cm and to r = 10 cm (a = 40 cm) /IV.12/.

2.4 Control of the LH deposition profile

The lower hybrid driven current does not show the same current density profile as the inductively driven current. This is plausible since in

the LH-case the current is carried by suprathermal electrons while in the Ohmic case these are thermal electrons.

It has been shown that LH-current drive leads to a wider profile and that consequently q(0) can be greater than 1. The results of the Li-beam measurements agree reasonably with magnetic measurements, if ananisotropy of the electron velocity distribution is taken into account.

In Fig. IV.12 we show the time behaviour of the signal $(\beta_p^{equ} + l_i/2) - \beta_p^{\perp}$. The first part is taken from the equilibrium field while $\beta_p^{\perp}$ is from the diamagnetic loop. This signal thus contains contributions from an anisotropy $(\beta_p'' - \beta_p^{\perp})$ due to fast LH-generated electrons and from a slowly changing internal inductance l_i, as sketched in Fig. IV.12. In Fig. IV.13 we show Δl_i as a function of RF-power and we see that the drop $-\Delta l_i$ increases about linearly with power. At low power Δl_i may be slightly positive. In Fig. IV.14 we show the density variation of $-\Delta l_i$, which scales like $-\Delta l_i \sim 1/\bar{n}_e$. These measurements are all related to the normal current drive spectrum with $\Delta\varphi = \pi/2$.

By varying the form of the launched LH wave spectrum, we observed that Δl_i depends remarkably upon the applied spectrum /IV.8/. The dependence of Δl_i as a function of the applied spectrum is shown in Fig. IV.16 for the set of spectra shown in Fig. IV.15. We see that $-\Delta l_i$ increases with increasing power in the high $N_{\parallel}$-part of the spectrum. This has also been observed in a phase scan where the shape of the spectrum remains roughly constant but the mean value $\bar{N}_{\parallel}$ is shifted gradually from 2 to 4 with the directivity dropping to zero. The change in l_i is thus not only related to the amount of rf-driven current, but also to the shape of the spectrum, and the maximum Δl_i is not obtained under conditions for maximum current drive efficiency. The experimental results suggest that the higher $N_{\parallel}$-part of the spectrum is absorbed further radially outward than the low $N_{\parallel}$-part. Therefore stronger broadening of the current profile j(r) may in fact be achieved by peripheral LH-current drive. The LH-generated current density profile thus clearly depends on the form of the spectrum, and it may be determined not only by the direct rf-driven current, but also by an rf-modified conductivity profile due to bulk heating or suprathermal electrons. Presently we do, however, not know whether the

density and power dependence of Δl_i in the case of a wide spectrum extending to high $N_{\parallel}$ scales as it has been found in the scaling studies with a narrow current drive spectrum.

3. Sawtooth suppression during NBI-heating

3.1 Sawtooth period

The sawtooth period τ_{st} during NBI increases with increasing beam power P_{NI} in divertor discharges (Fig. IV.17). No similar power dependence is observed in limiter discharges. In divertor plasmas the sawteeth disappear above a threshold in P_{NI} which increases with higher $\bar{n}_e$ and lower q_a. This threshold is indicated by vertical bars at the upper ends of the curves for τ_{st} in Fig. IV.17.

Also in the combined operation of ICRH and NBI sawteeth disappear above a threshold in total heating power (Fig. IV.18). There is, however, a marked difference in power requirements for the two heating methods. For lowering the power threshold P_{NI}^* above which sawteeth are stabilised by additional ICRH heating, the amount ΔP_{NI}^* indicated by the arrows in Fig. IV.18 has to be replaced by about three times that ICRH power. The reason could be a more peaked heat deposition profile of ICRH and therefore less broadening of j(r) which on the other hand might be responsible for stabilisation with NBI heating alone.

3.2 LH power requirements

LH-current drive was combined with NBI at low density, where the current drive efficiency is high. In sawtoothing discharges with NBI τ_{st} rises upon injection of LH power both in heating and current drive mode. Suppression of sawteeth is possible with LH current drive only. Magnetic measurements again indicate a drop of the internal inductance l_i during the LH phase and therefore a flattening of j(r). The drop in l_i does not depend on P_{NI} as shown in Fig.IV.19 but only on P_{LH} and on the wave spectrum. With the LH power above a critical value, which depends on the beam heating power, the sawteeth could be stabilised in the whole range of beam heating powers where they were observed. In Fig. IV.20 the sawteeth on the line-averaged density $\bar{n}_e$ are shown for discharges with different injection powers. They disappear after the

beginning of the LH, the time delay being reduced with increasing beam power.

The minimum rf power required for stabilisation of sawteeth, P_{LH}^{*} is reduced with increasing P_{NI} as seen from Fig. IV.21. This suggests that the current profile is flattened in the central plasma region already by NBI alone and less LH-power is therefore required for higher P_{NI} to remove the q=1 surface from the plasma.

3.3 Comparison co-/counter-NBI

With counter-NBI the threshold power P_{LH}^{*} is even further reduced as seen in Fig. IV.21. Also with NBI alone sawteeth disappear already at lower power in this case. This seems to be mainly due to the broad $T_e(r)$ profiles which are observed with counter-NBI. The shorter sawtooth period might be also explained by this fact. A contribution from a counter-driven beam current reducing the net plasma current in the centre and thereby flattening j(r) as proposed in a scenario for sawtooth suppression /IV.13/ cannot be ruled out.

3.4 Energy confinement

In sawtooth-free discharges with NBI, higher central electron temperatures can be obtained. The $T_e(r)$ profiles are plotted in Fig. IV.22 for the Ohmic phase, NBI alone and for NBI combined with LH current drive. With P_{LH} = 540 kW which is below P_{LH}^{*}, the $T_e(r)$ profiles still resemble the profiles with NBI alone. The additional LH power replaces mainly the drop in P_{OH} in this case. With $P_{LH} > P_{LH}^{*}$ (P_{LH} = 720 kW) sawteeth are suppressed and the central temperatures increase. The resulting increase in total energy content in this case is small because of the small volume where sawteeth dominate the power loss.

With lower q_a the sawtooth-unstable region is larger and a larger gain for global plasma heating can be obtained. At q_a = 2.75 (I_p = 380 kA, B_t = 2.2 T) sawteeth during NBI with 1.35 MW and 1.8 MW were suppressed by LHCD with P_{LH} = 550 kW. In Fig. IV.23 the time evolution of $\bar{n}_e$, P_{rad} and $\beta_p^{\perp}$ is shown for a sawtoothing discharge with NBI alone and for a sawtooth-free discharge with NBI and LHCD combined. The $\beta_p^{\perp}$ values during NBI in the sawtooth-free case are up to 30 % higher than in presence of sawtooth oscillations.

In Fig. IV.24 the sawtooth amplitude $\Delta\tilde{W}_p$ of the total energy content is plotted together with the gain ΔW_p^* after stabilisation at the begin and at the end of 300 ms long stationary sawtooth-free phases. ΔW_p^* is the difference of the average energy content in the sawtoothing NBI heated discharge and the total energy content in the sawtooth-free discharge. The gain ΔW_p^* reaches up to 30 % of the total increase in energy content with NBI in the sawtoothing discharge. The increase ΔW_p^* at the beginning comes essentially from additional LH heating. The higher energy content at the end of a 300-ms-long sawtooth-free phase indicates an improvement in global energy confinement after suppression of sawteeth. It should be noted that stabilisation of sawteeth in this case does not lead to increased radiation losses.

LH-current drive has proven its ability to stabilise the sawteeth also under conditions of high-power neutral beam heating by driving $q(0) > 1$. The decoupling of current and temperature profiles in this case allows for an independent external control of the current profile and heat deposition. Improvement of the central confinement by stabilisation of the sawteeth results also in an improvement of the global confinement.

References:

/IV.1/ Y. Yoshioka, S. Kinoshita, T. Kobayashi, Nuclear Fusion, Vol. 24, No. 5 (1984), p. 565.

/IV.2/ D.W. Ignat, P.H. Rutherford, H. Hsuan, Course and Workshopn on Basic Physical Processes of Toroidal Fusion Plasmas, Varenna (Italy), (1985), Vol. I, p. 525.

/IV.3/ J.A. Wesson, Plasma Physics and Controlled Fusion, Vol. 28, No. 1A, (1986), p. 243.

/IV.4/ D.J. Campbell, et al., to be published in Nuclear Fusion.

/IV.5/ F. Parlange, et al., 12th European Conference on Controlled Fusion and Plamsa Physics, Budapest, 1985, Vol. II, p. 172.

/IV.6/ J. Stevens, et al., in Ref. /5/, p. 192.

/IV.7/ M. Porkolab, et al., 13th European Conference on Controlled Fusion and Plasma Physics, Schliersee, 1986, Vol. II, p. 445.

/IV.8/ F.X. Söldner, et al., in Ref. /7/, Vol. II, p. 319.

/IV.9/ R. Bartiromo, et al., in Ref. /7/, Vol. II, p. 335.

/IV.10/ K. McCormick, et al., in Ref. /5/, Vol. I, p. 199.

/IV.11/ K. McCormick, et al., in Ref. /7/, Vol. II, p. 323.

/IV.12/ F. Söldner, et al., in Ref. /5/, Vol. II, p. 244.

/IV.13/ J. Jacquinot, private communication.

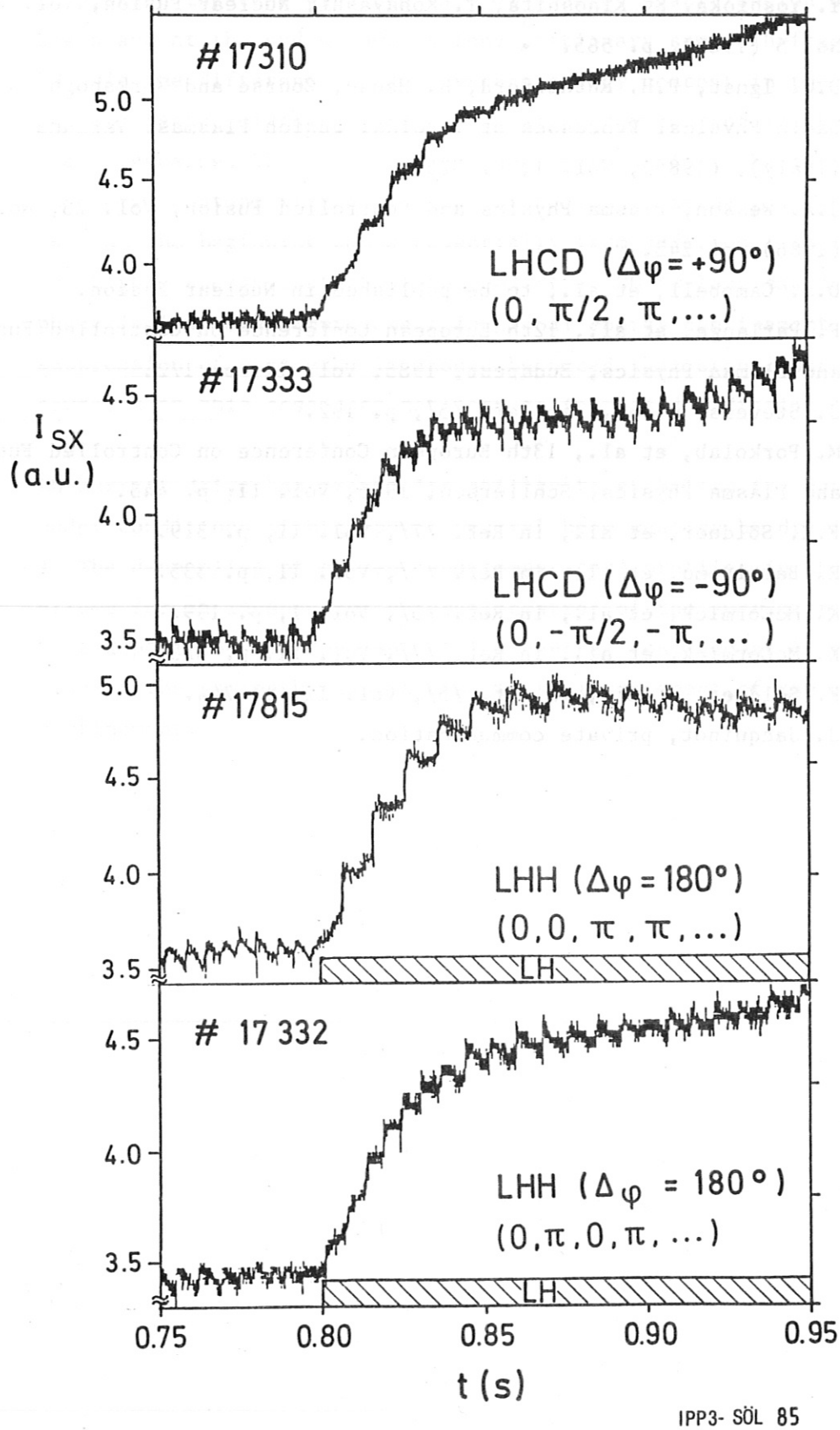

Fig. IV.1: Soft X-ray emission from a central chord for four different LH spectra. $\bar{n}_e = 1.2 \times 10^{13}$ cm^{-3}, $P_{LH} \approx 520$ kW.

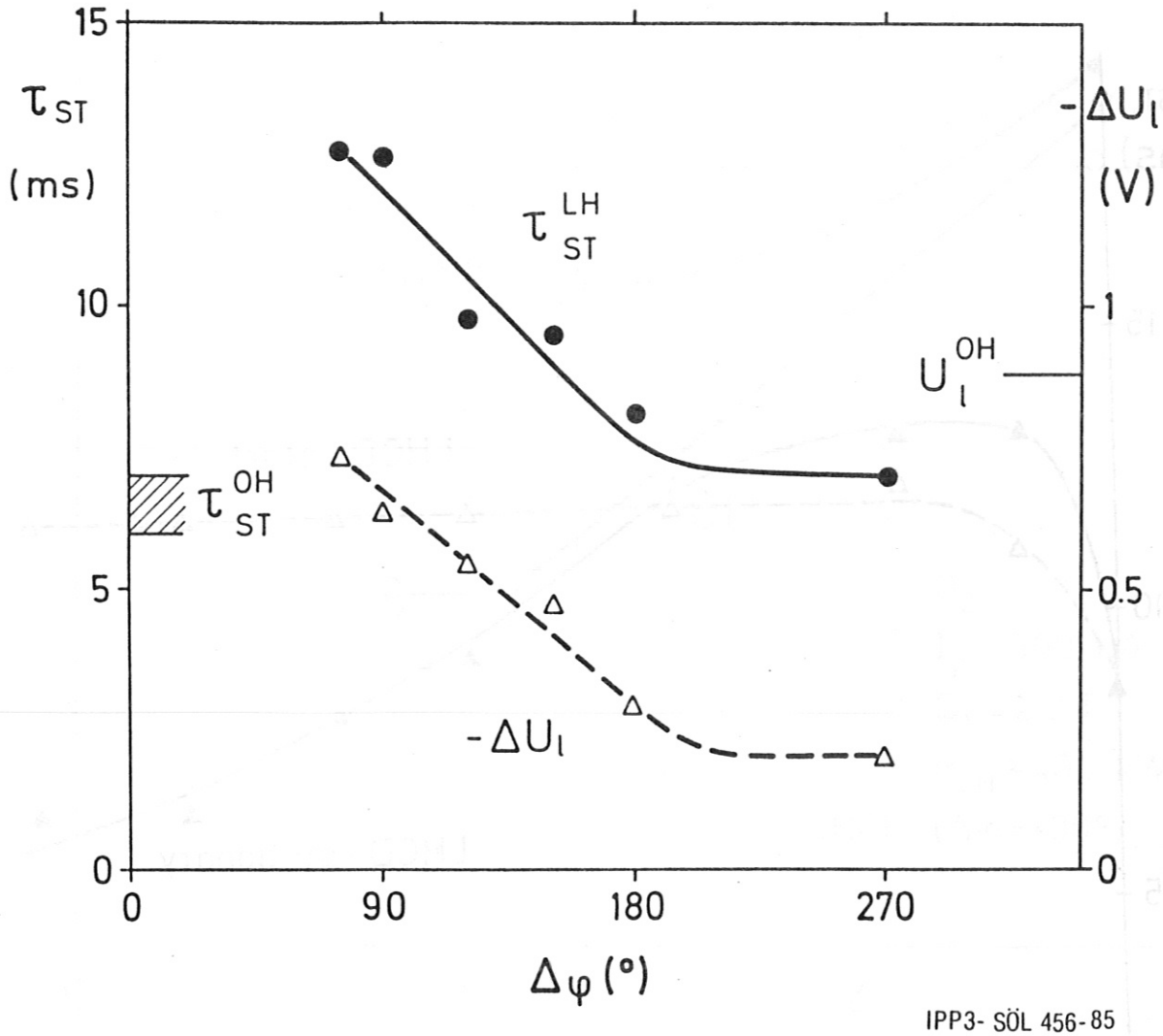

Fig. IV.2: Sawtooth period τ_{st} and drop in loop voltage $-\Delta U_l$ during LH application with various antenna phasings. $\bar{n}_e = 1.2 \times 10^{13}$ cm^{-3}, $P_{LH} \approx 510$ kW, $I_p = 300$ kA, $B_t = 2.17$ T.

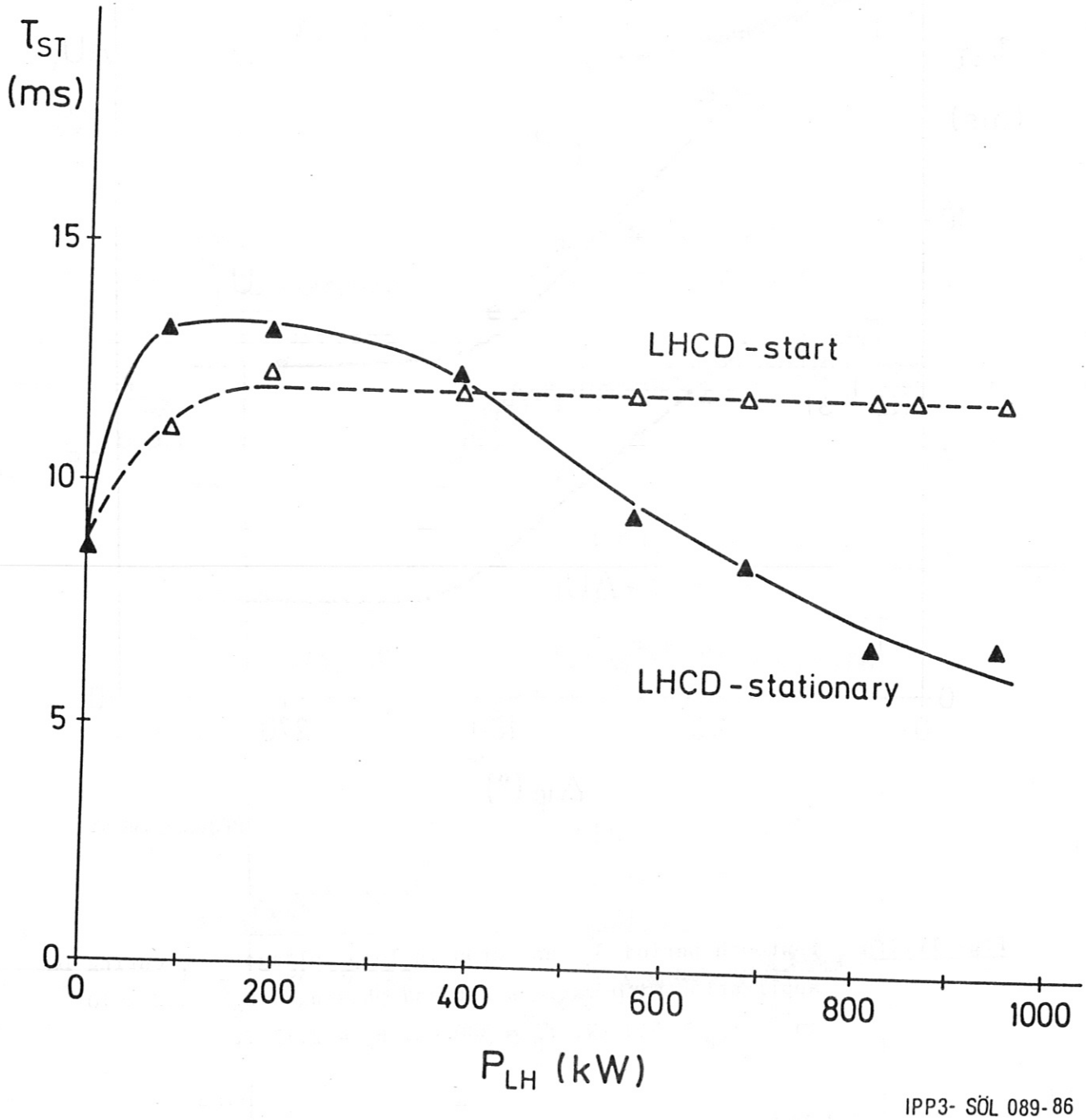

Fig. IV.3: Sawtooth period τ_{st} versus LH-power during the initial and the stationary phase of LH-current drive. $\bar{n}_e = 1.6 \times 10^{13}$ cm^{-3}, $I_P = 300$ kA, $B_t = 2.17$ T.

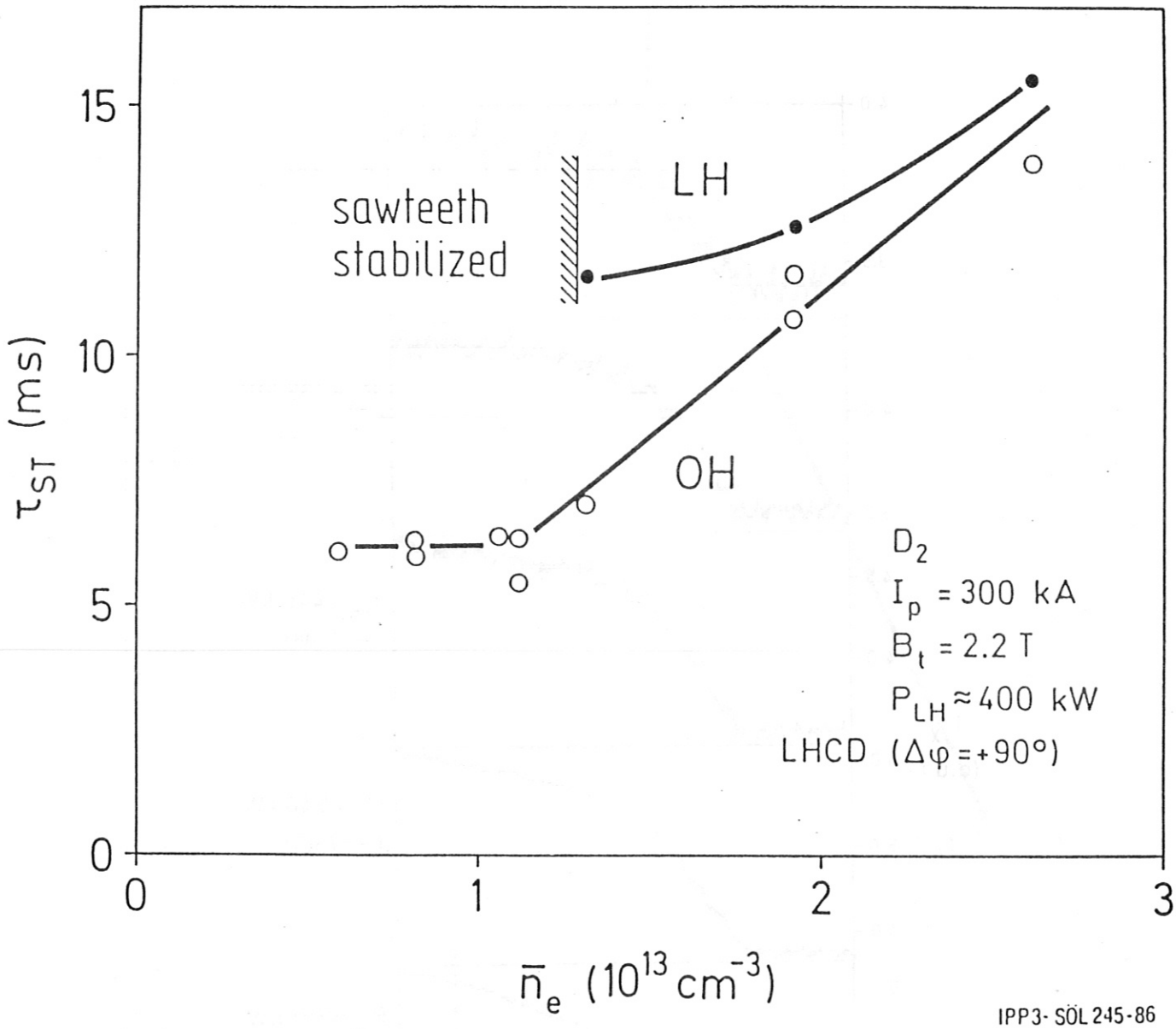

Fig. IV.4: Density dependence of the sawtooth period τ_{st} with OH- and LH-current drive.

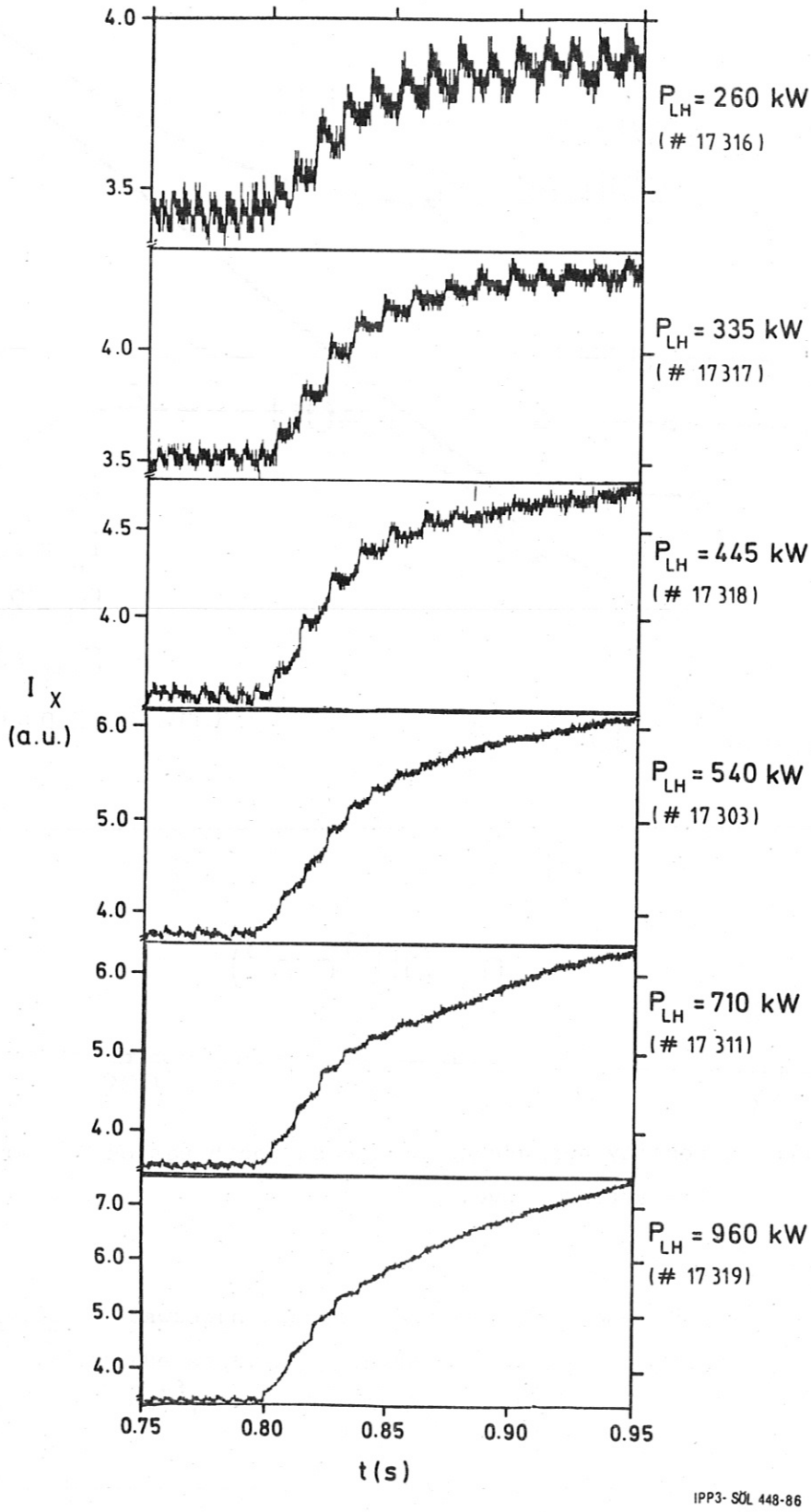

Fig. IV.5: Sawtooth oscillations on the soft X-ray emission during LH-current drive (LH starts at t = 0.8 s). $\bar{n}_e = 1.2 \times 10^{13}$ cm^{-3}, I_p = 300 kA, B_t = 2.17 T.

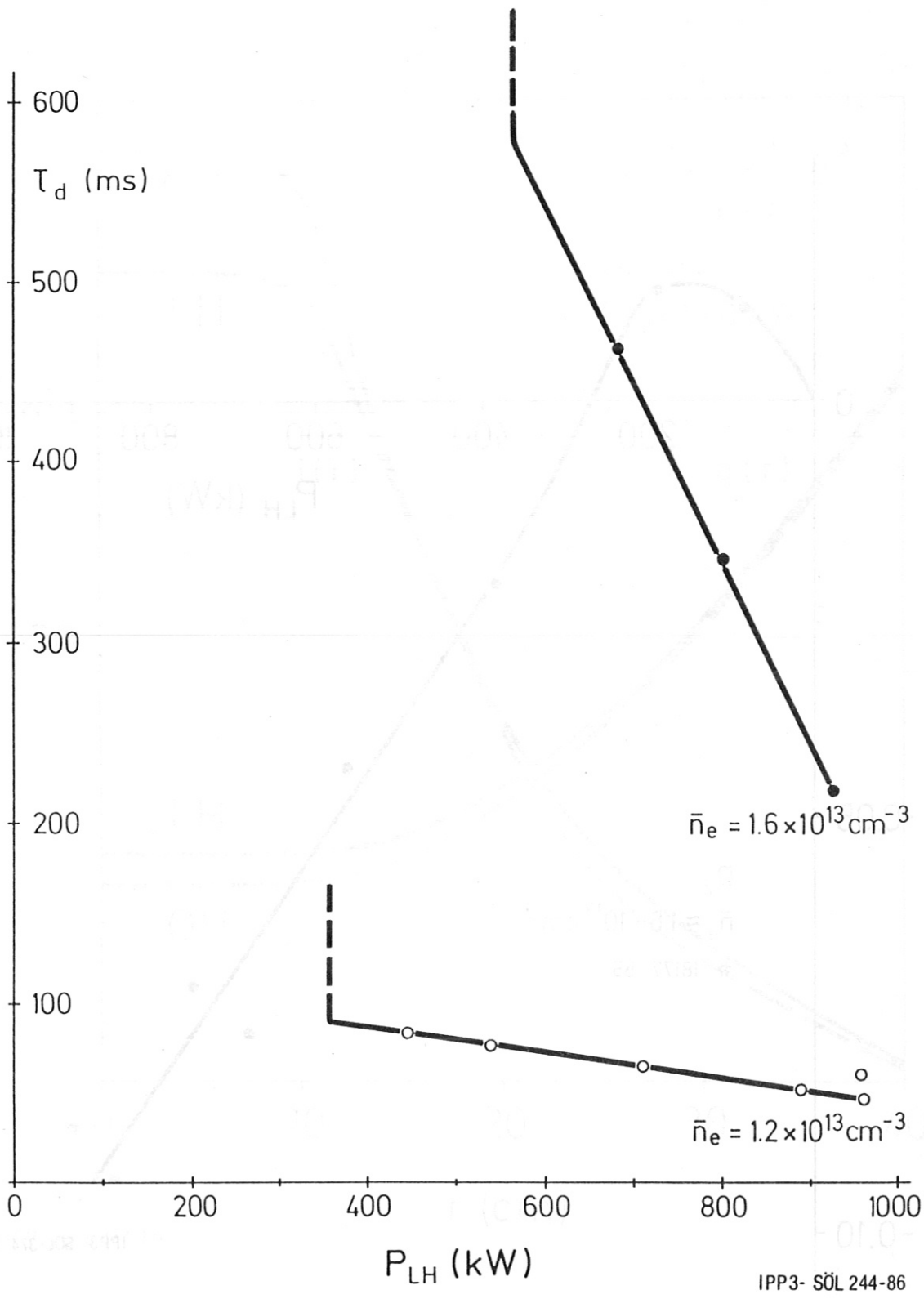

Fig. IV.6: Time delay τ_d between start of LH-current drive and stabilisation of the sawteeth. The threshold power P_{LH}^* for stabilisation is marked by dashed lines.

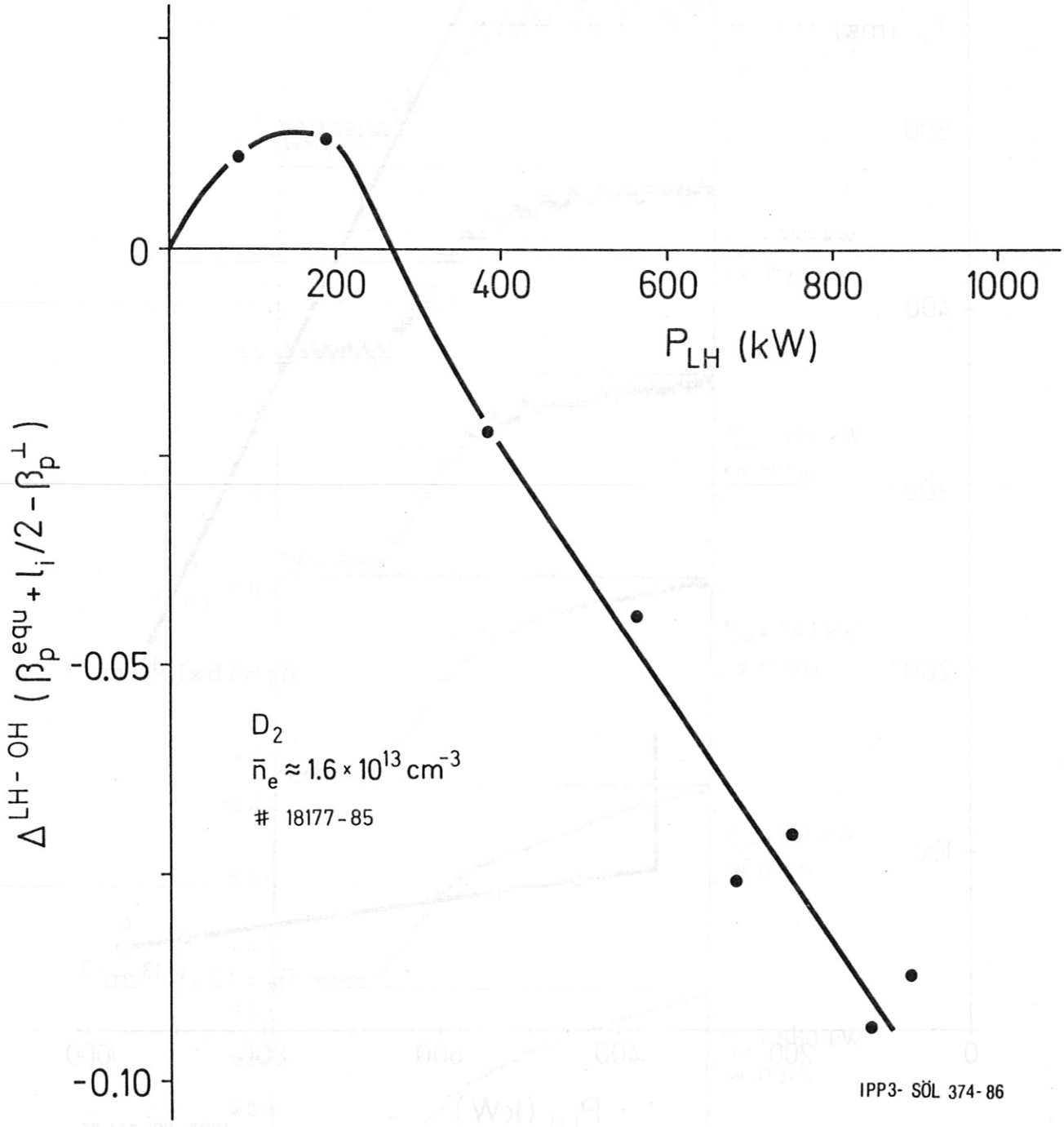

Fig. IV.7: Change of the internal inductance l_i with P_{LH} as derived from magnetic measurements.

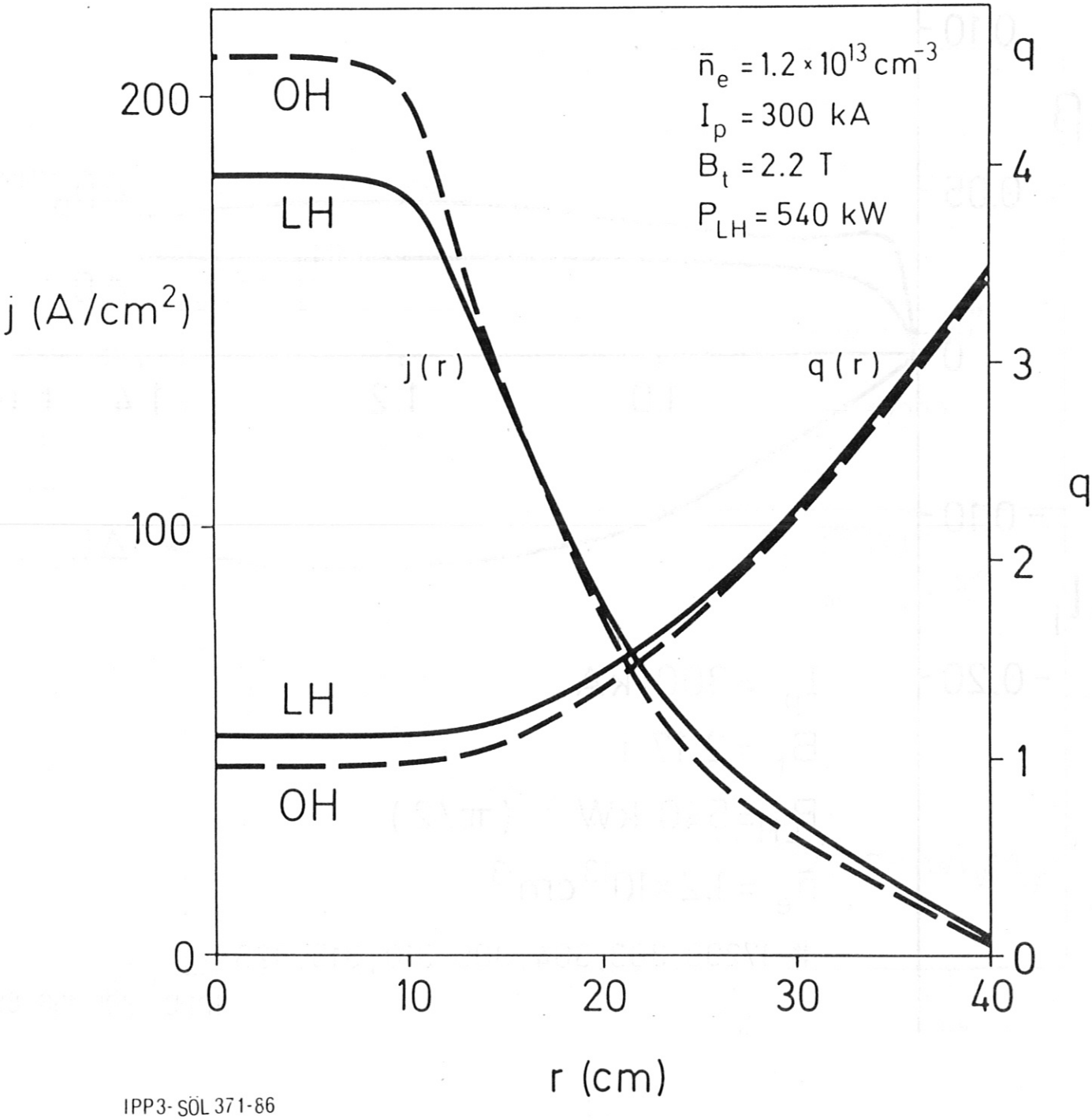

Fig. IV.8: Current profile j(r) and q(r) profiles during OH- and stationary LH-current drive.

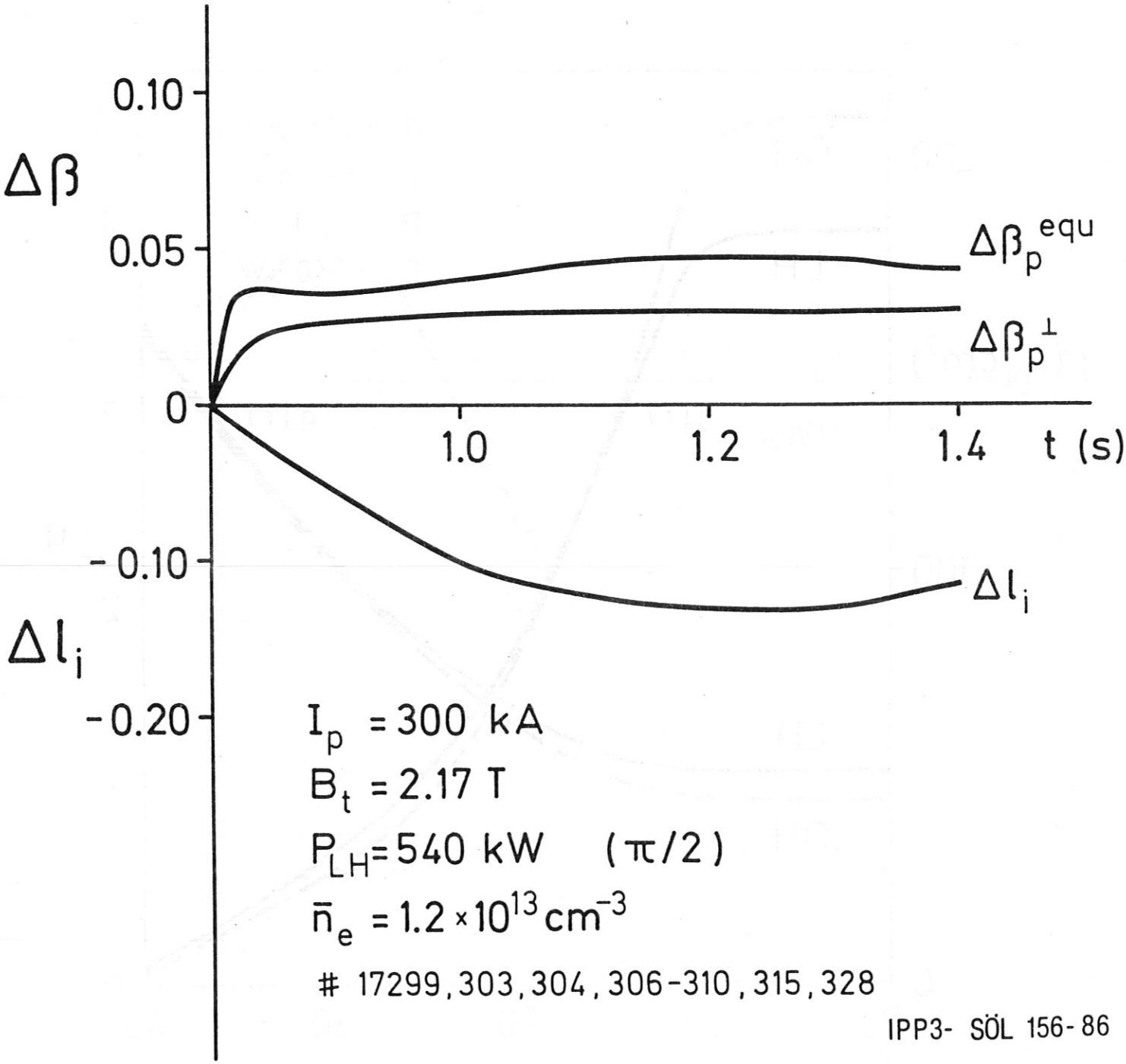

Fig. IV.9: Time behaviour of Δl_i from local current profile measurements during LHCD and of $\Delta\beta_p^{\perp}$ and $\Delta\beta_p^{equ}$, as derived from magnetic measurements.

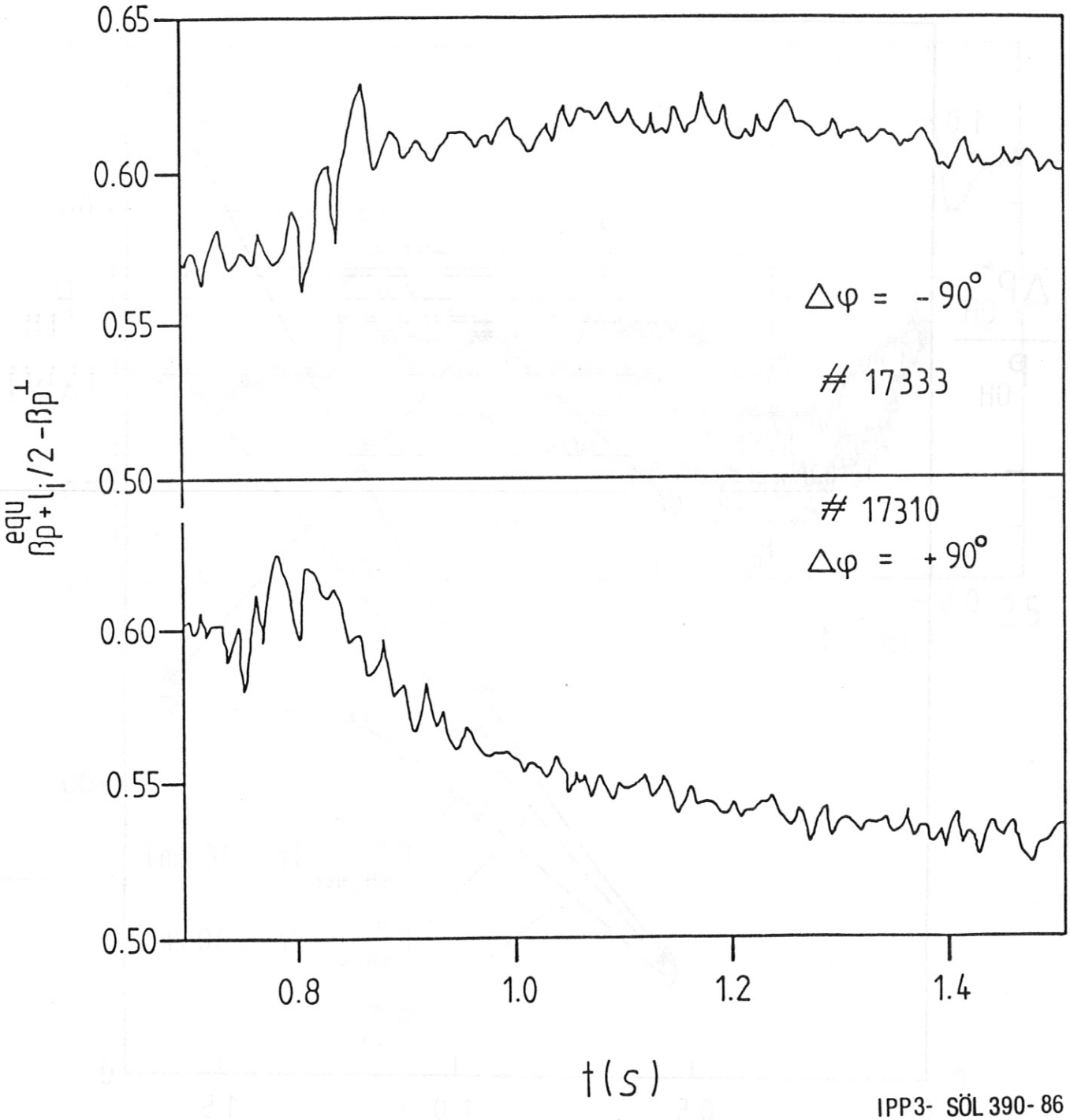

Fig. IV.10: Temporal evolution of the quantity $(\beta_p^{equ} + l_i/2) - \beta_p^{\perp}$ during opposite ($\Delta\varphi = -90^{\circ}$) and normal ($\Delta\varphi = +90^{\circ}$) LH-current drive. $\bar{n}_e = 1.2 \times 10^{13}$ cm^{-3}, $P_{LH} \approx 540$ kW, $I_p = 300$ kA, $B_t = 2.17$ T.

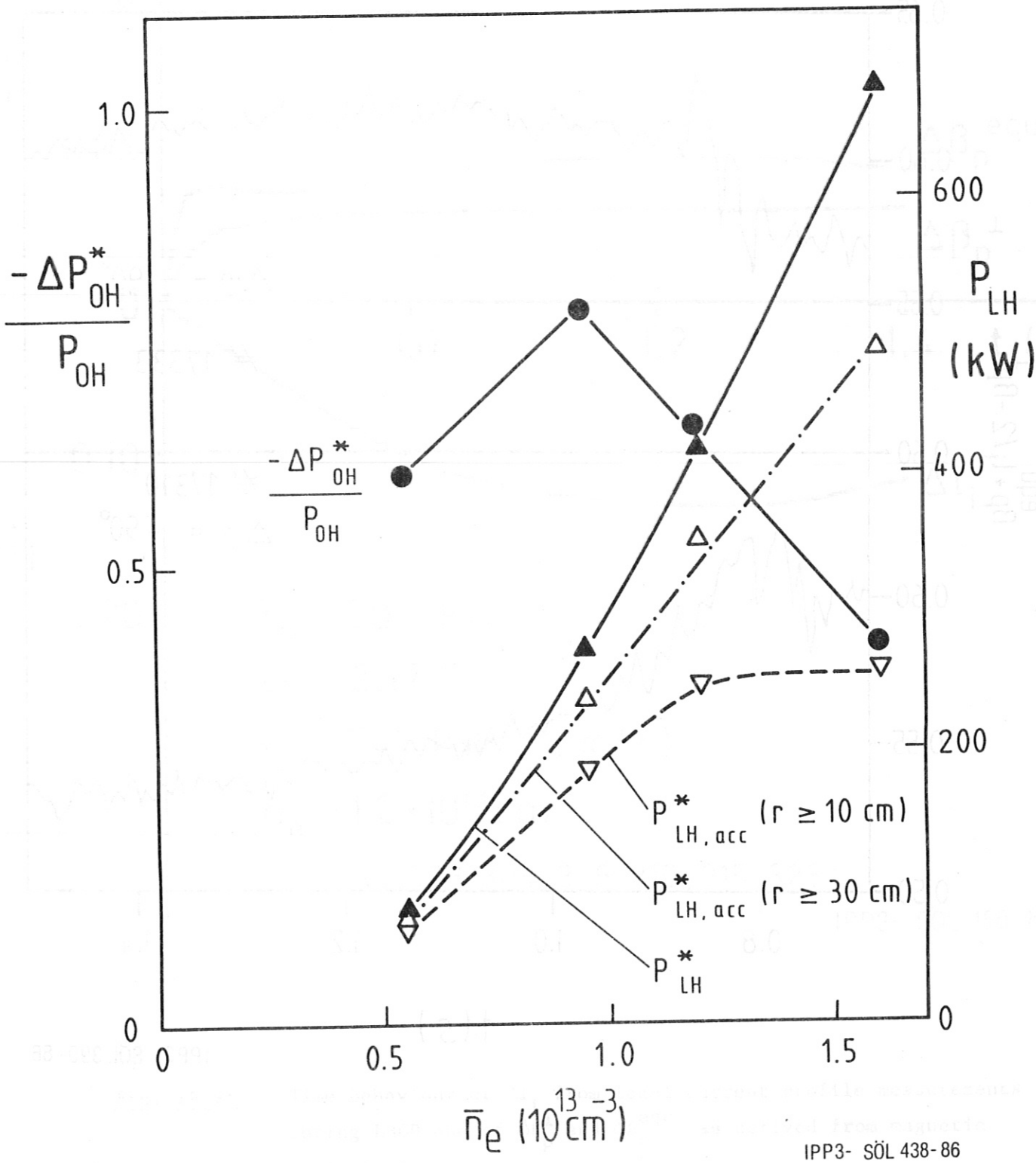

Fig. IV.11: LH-power P_{LH}^* required for sawtooth stabilisation by LHCD together with the fraction of P_{LH}^* accessible to regions inside r = 30 cm or r = 10 cm. Drop of OH-power for LHCD with P_{LH}^* (I_p = 300 kA, B_t = 2.2 T).

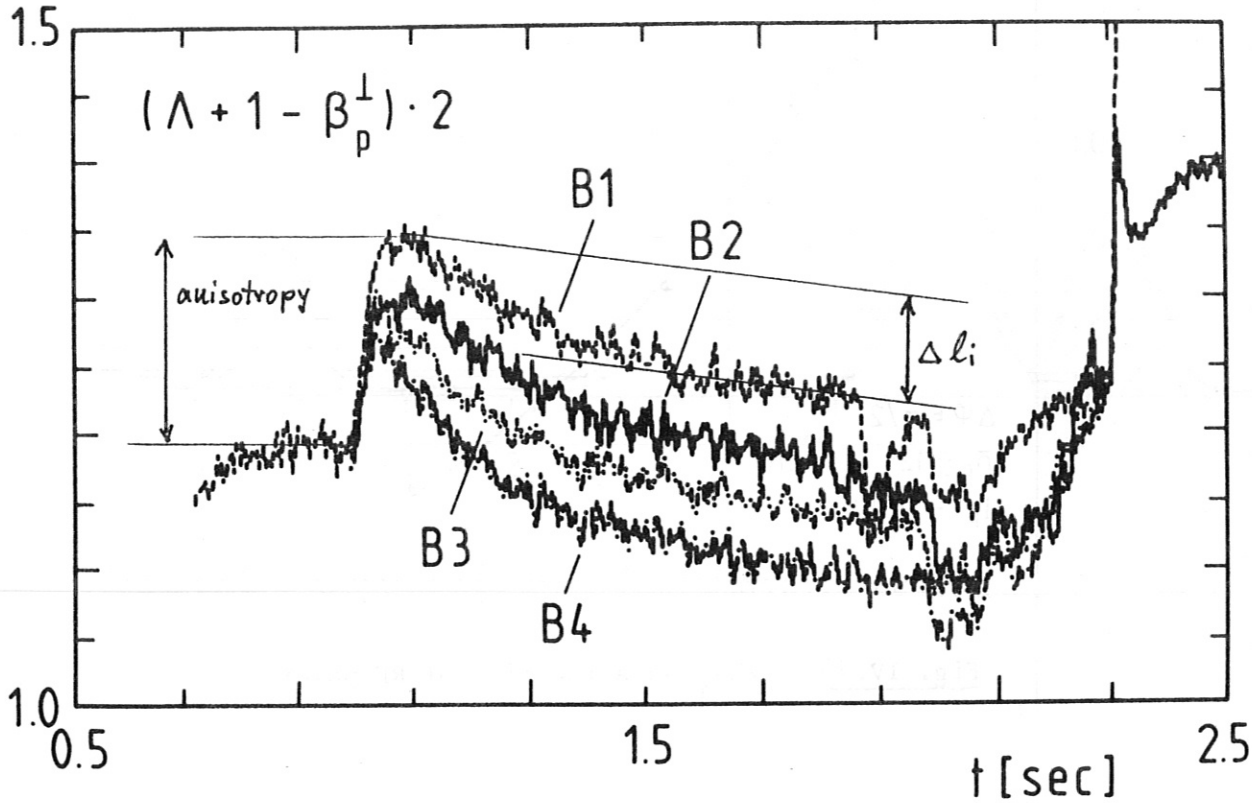

Fig. IV.12: $(\beta_p^{equ} + l_i/2) - \beta_p^{\perp}$ as a function of time.

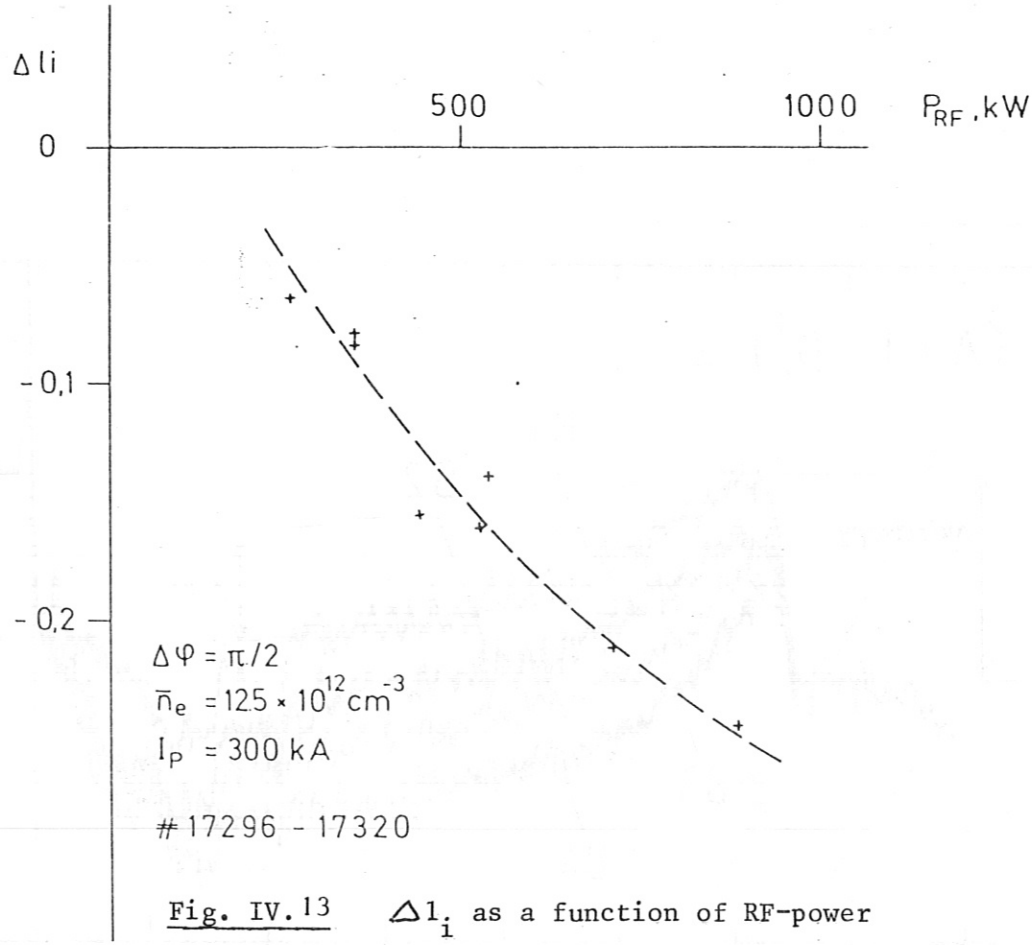

Fig. IV.13 Δl_i as a function of RF-power

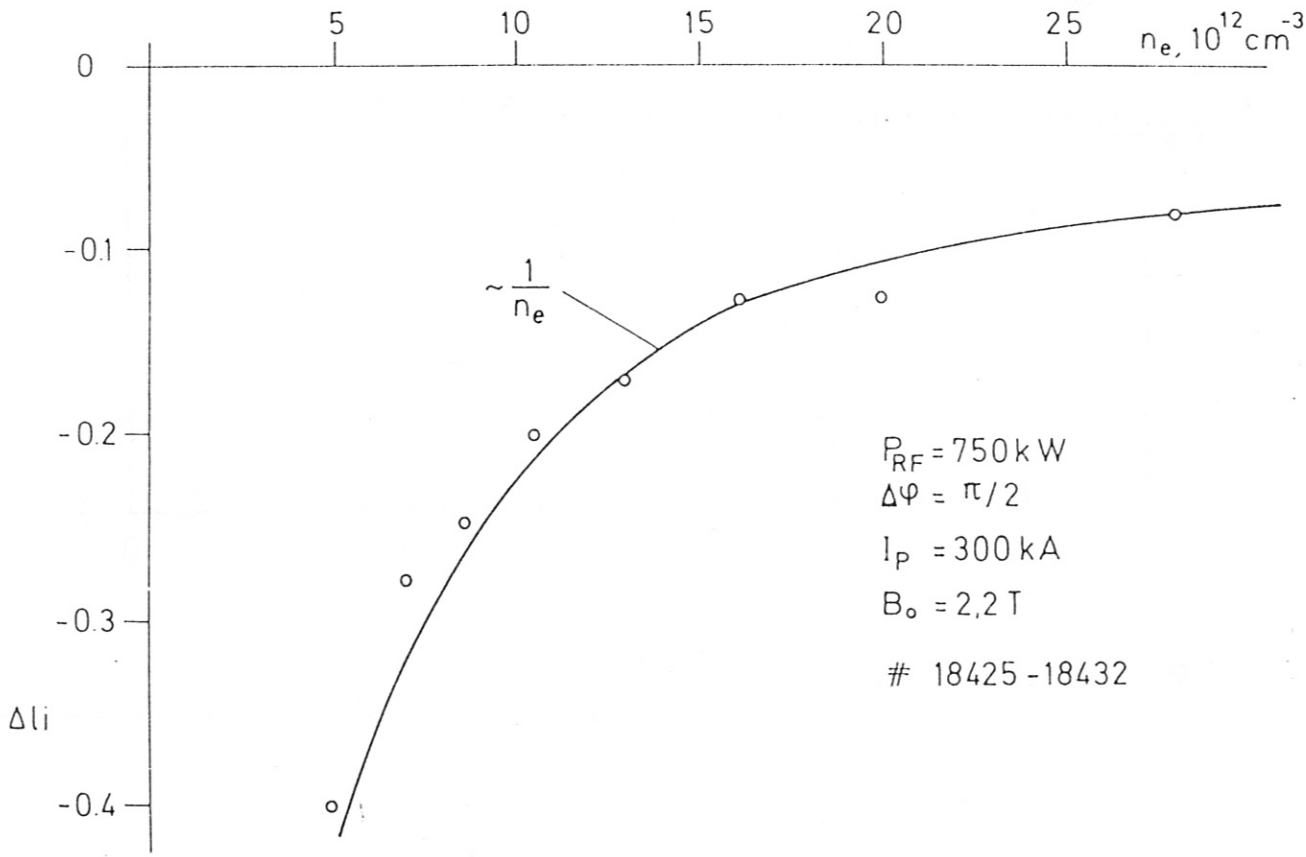

Fig. IV.14 Δl_i as a function of density

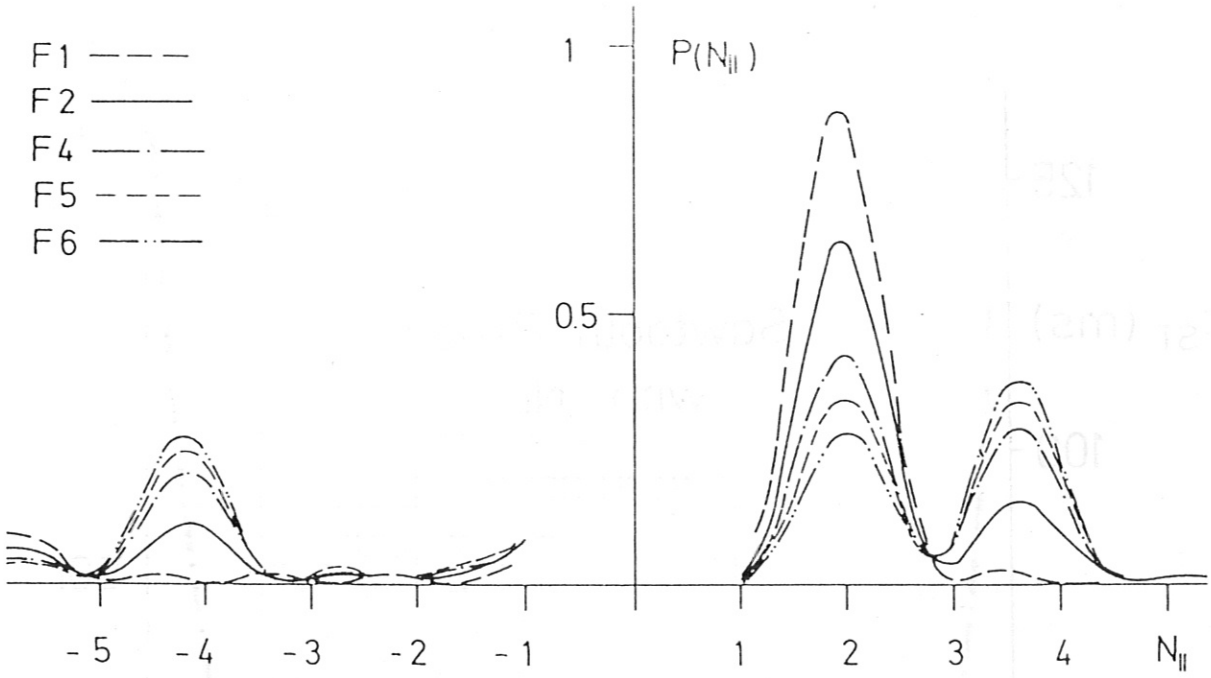

Fig. IV.15 F-series of tailored spectra.

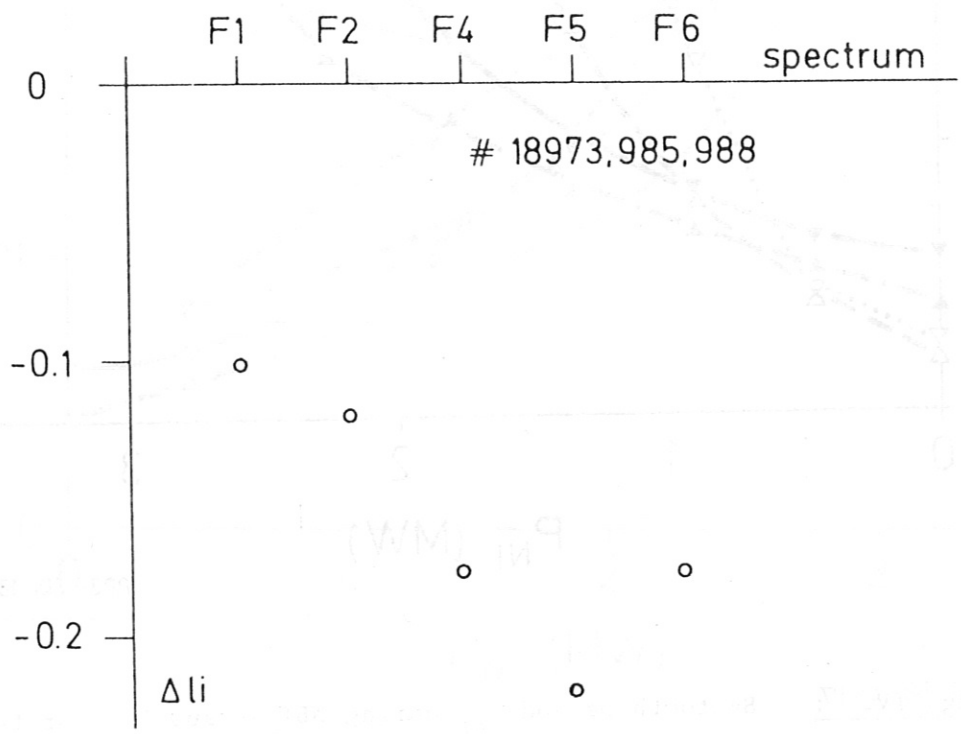

Fig. IV.16 Δl_i as a function of spectrum.

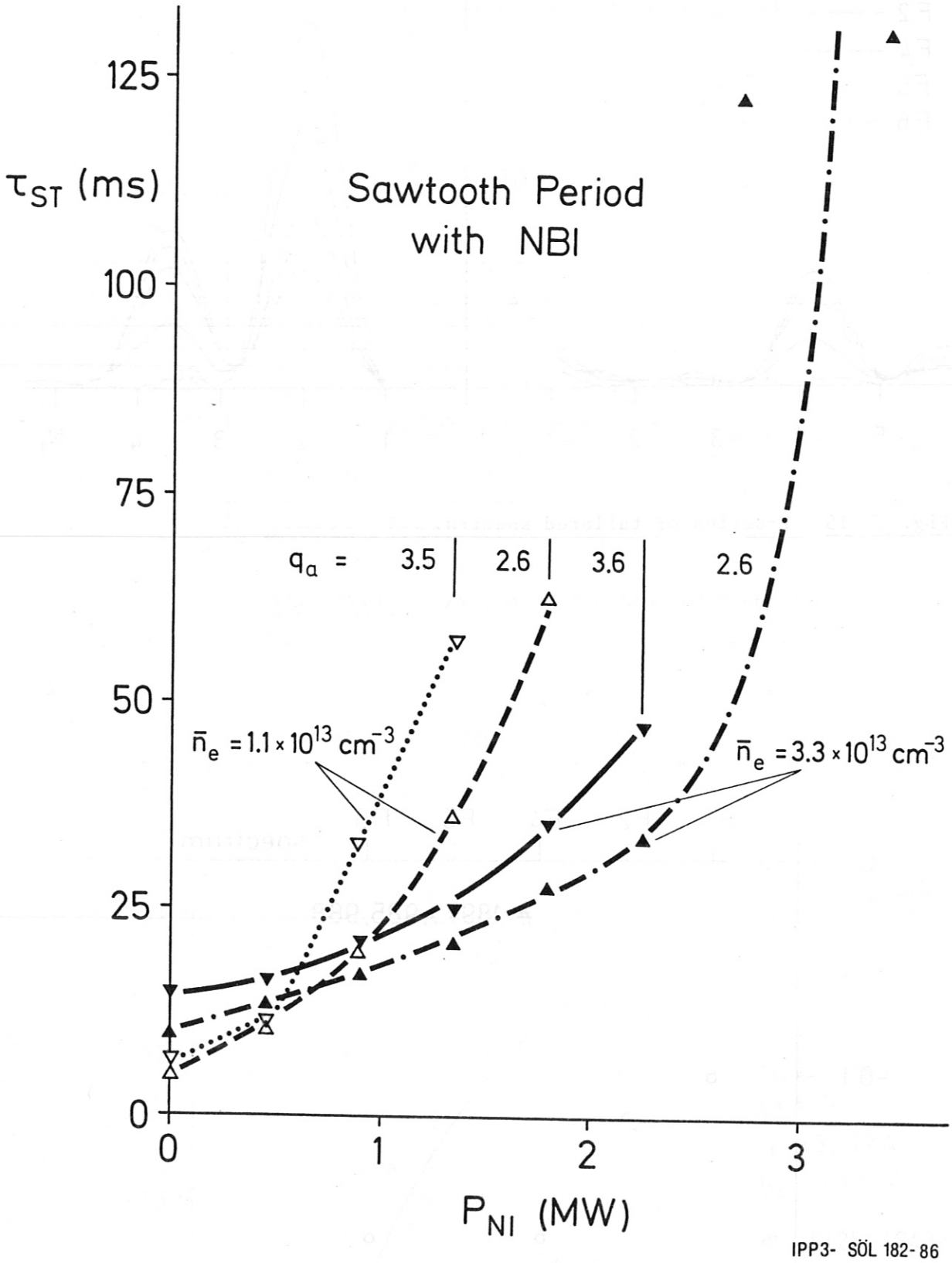

Fig. IV. 17: Sawtooth period τ_{st} during NBI versus P_{NI} for two different densities and two values of q_a.

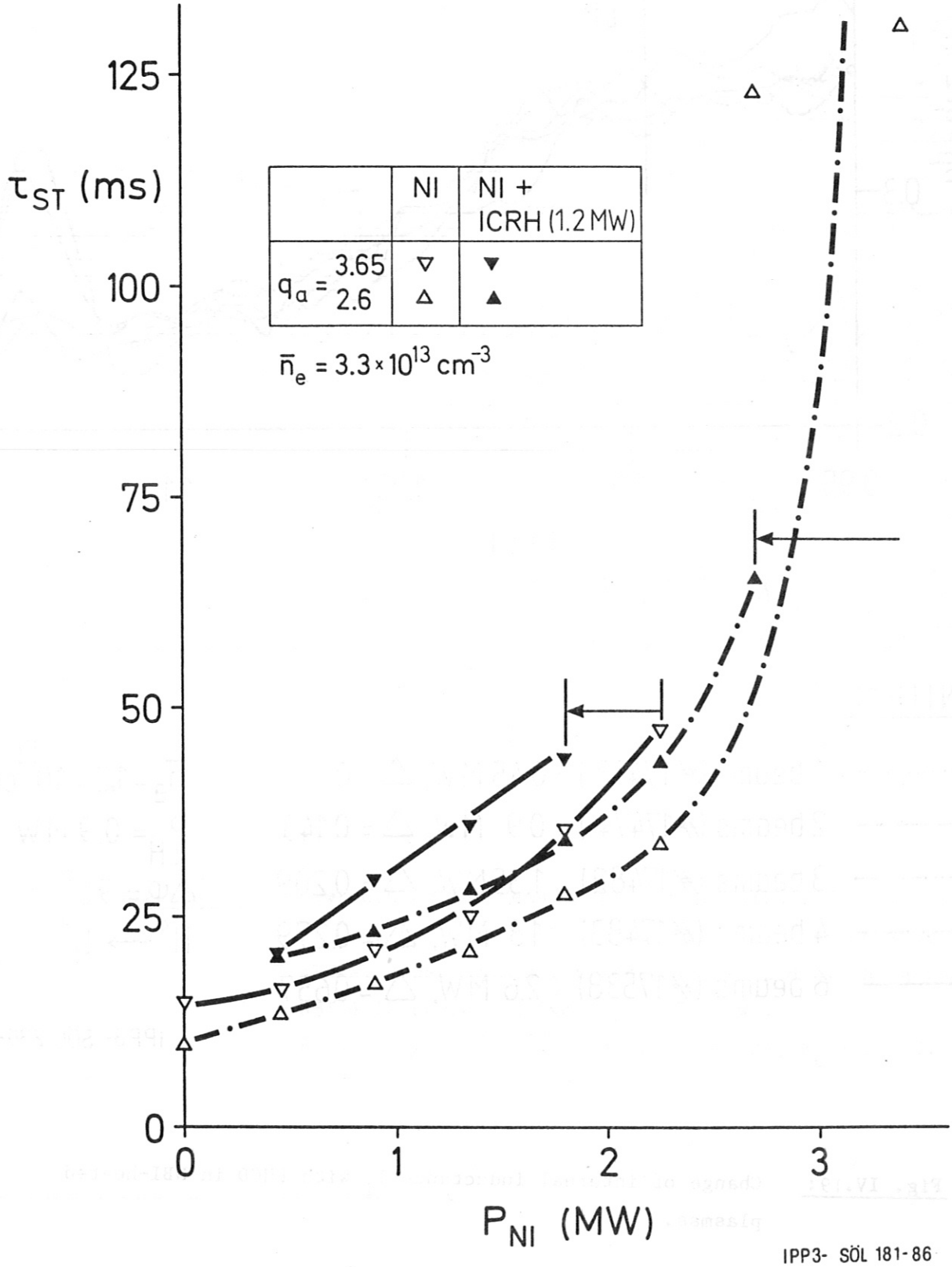

Fig. IV.18: Sawtooth period for combined operation of ICRH + NBI.

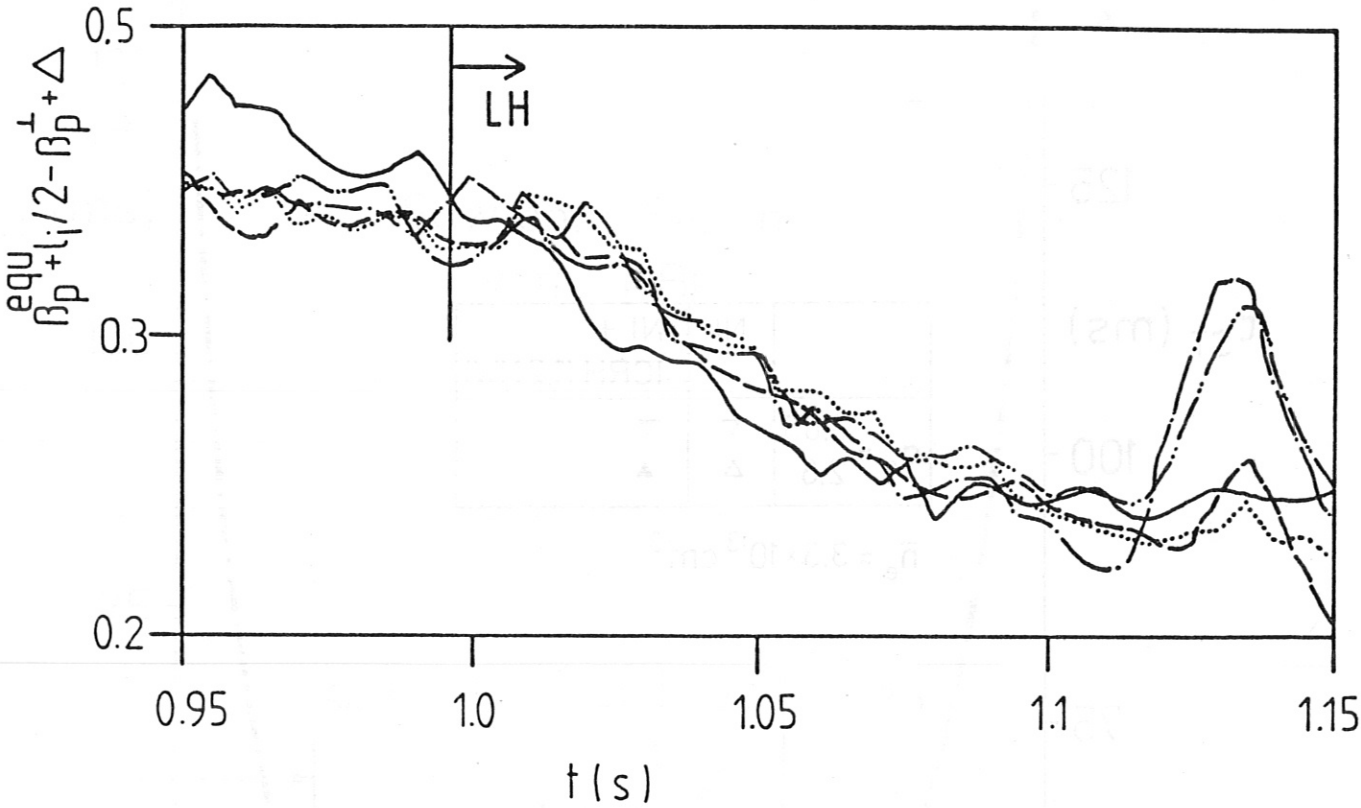

NI (H°)

·····	1 beam (#17473) : 0.45 MW, $\Delta = 0$	$\bar{n}_e = 1.2 \times 10^{13}$ cm^{-3}
— — —	2 beams (#17474) : 0.9 MW, $\Delta = 0.143$	$P_{LH} = 0.9$ MW
—··—··—	3 beams (#17482) : 1.35 MW, $\Delta = 0.209$	$\Delta\varphi = 90°$
—·—·—	4 beams (#17483) : 1.8 MW, $\Delta = 0.279$	$H^\circ \longrightarrow D^+$
———	6 beams (#17538) : 2.6 MW, $\Delta = 0.657$	

IPP3- SÖL 230-86

Fig. IV.19: Change of internal inductance l_i with LHCD in NBI-heated plasmas.

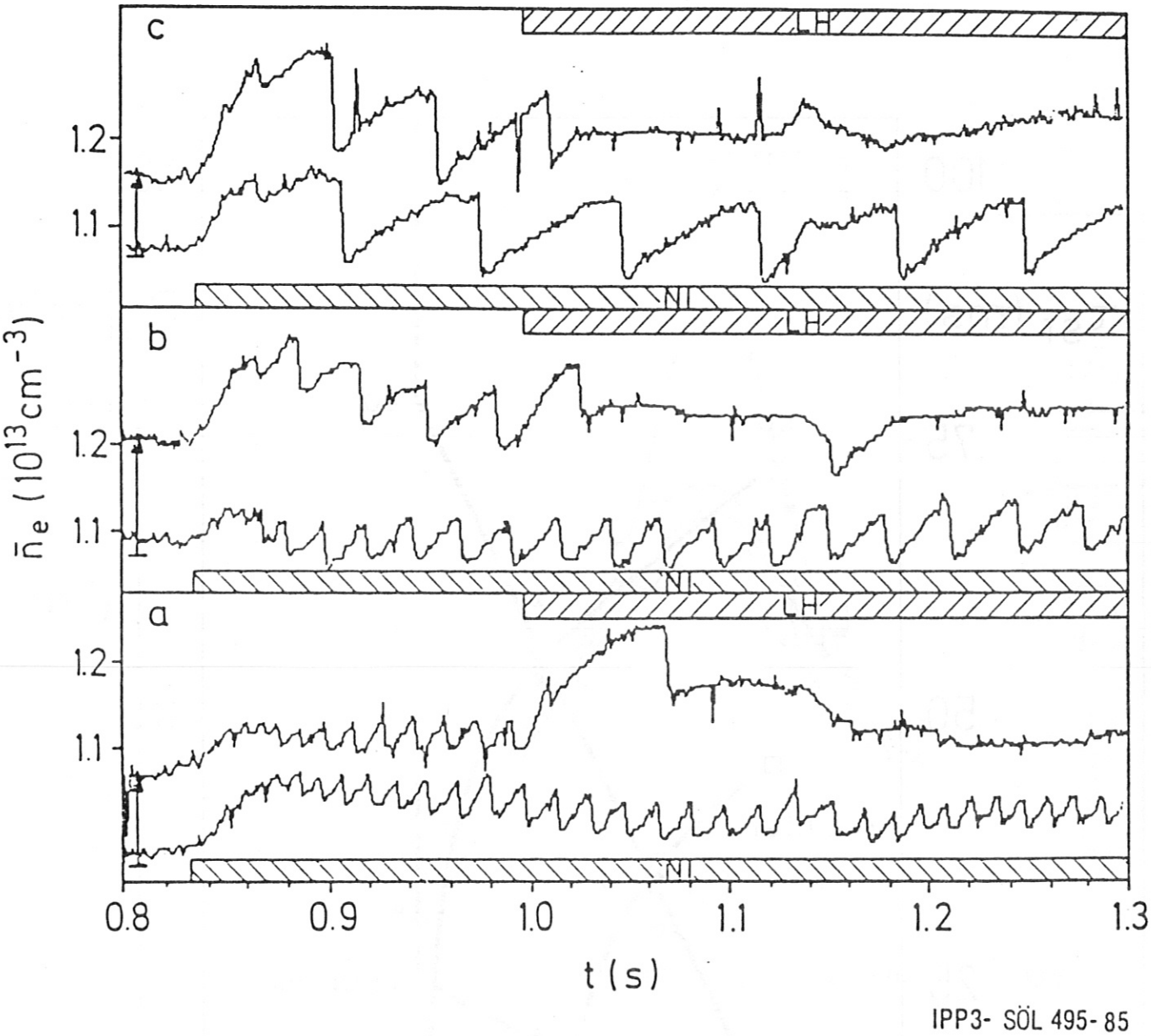

Fig. IV.20: Sawteeth on the density $\bar{n}_e$ for NBI with different powers: a) 0.45 MW, b) 0.9 MW, c) 1.35 MW. Lower traces for NBI alone, upper traces (offset as indicated by the arrows) for NBI + LH-current drive ($P_{LH} \approx$ 720 kW).
$\bar{n}_e = 1.1 \times 10^{13}$ cm^{-3} (D_2), I_p = 300 kA, B_t = 2.2 T.

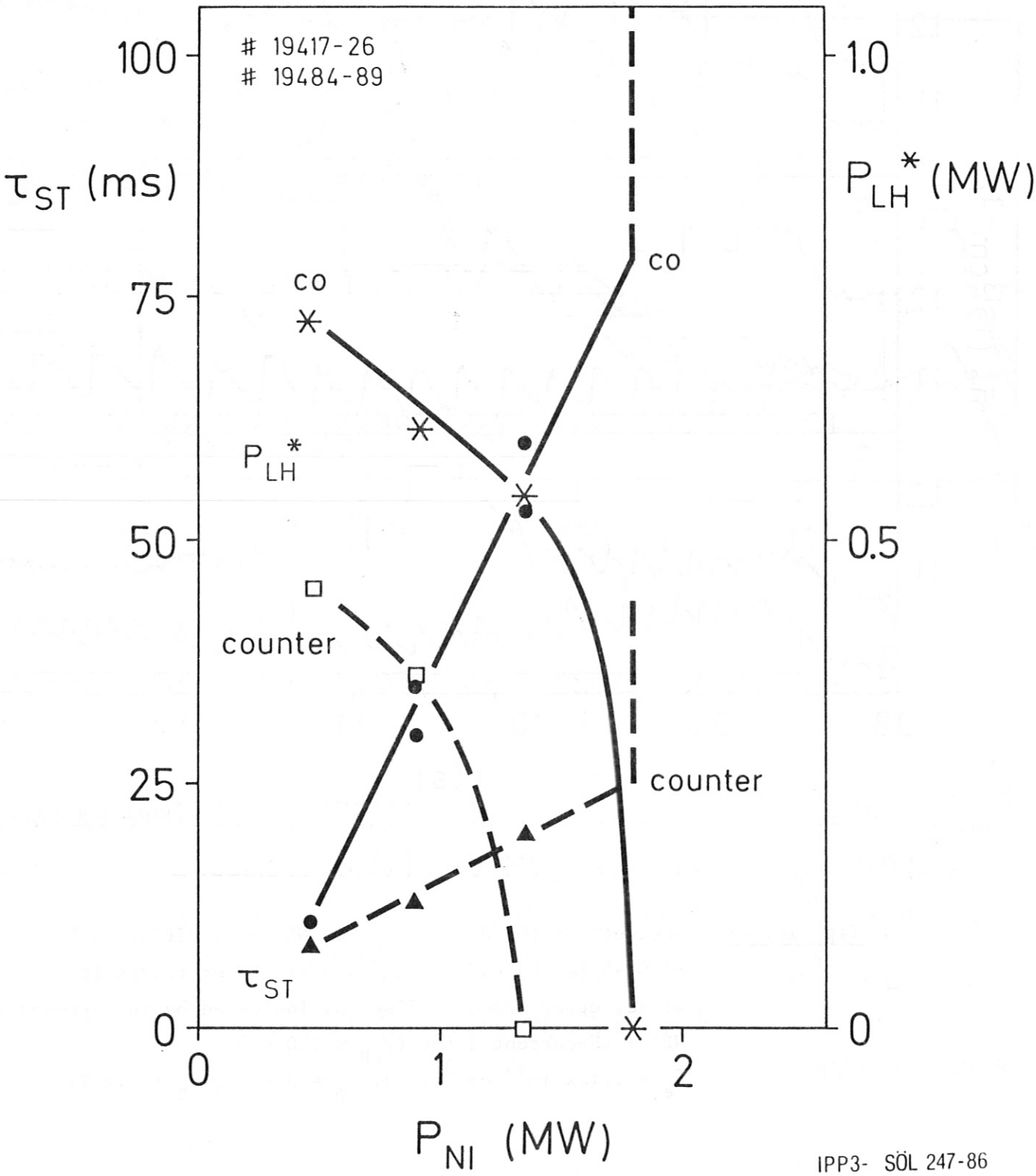

Fig. IV.21: Sawtooth period τ_{st} for NBI and threshold power P_{LH}^* for sawtooth stabilization by LH during NBI for co- and counter-injection as function of P_{NI}. $\bar{n}_e \approx 1.1 \times 10^{13}$ cm^{-3}, I_p = 300 kA, B_t = 2.17 T.

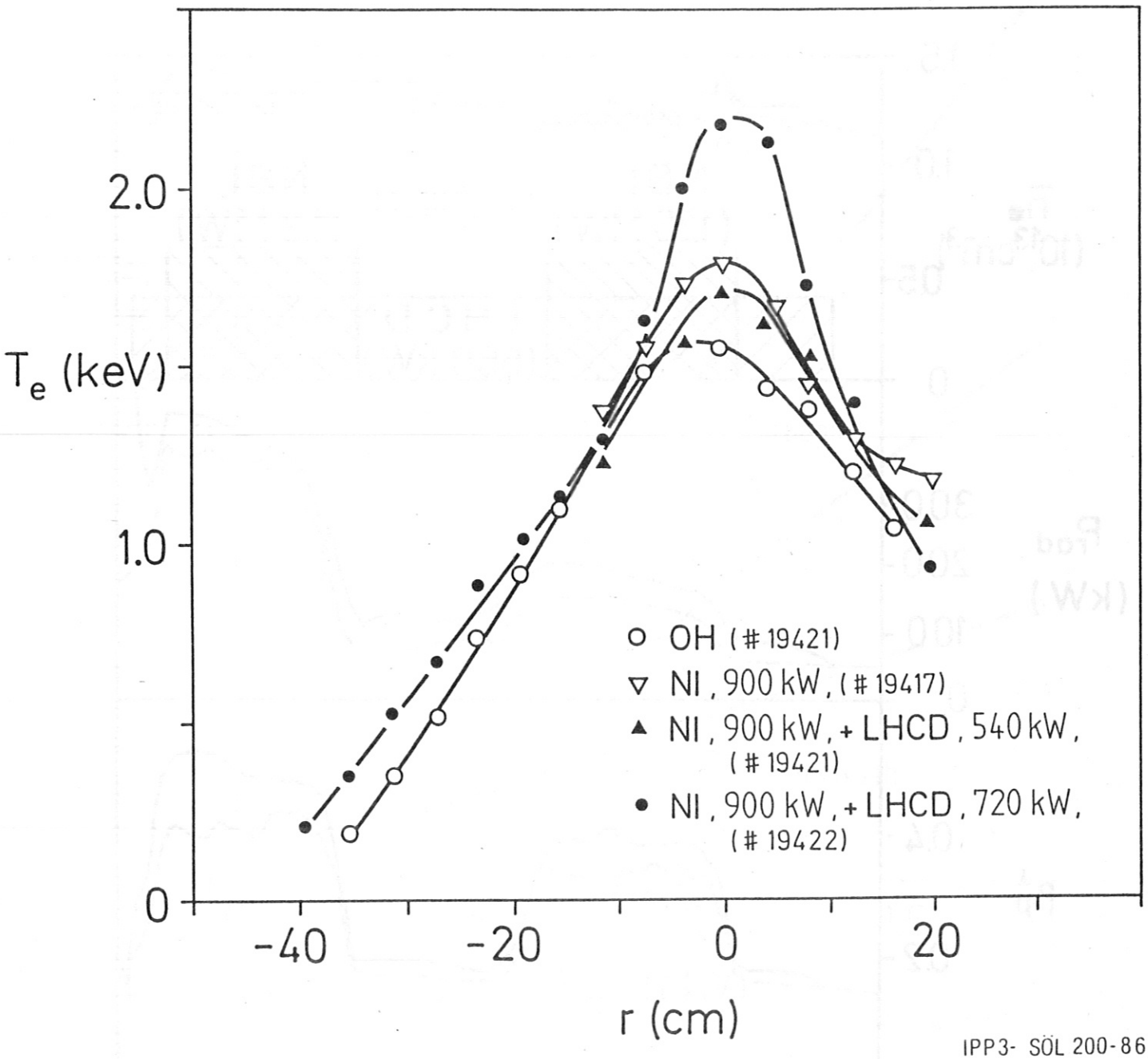

Fig. IV.22: $T_e(r)$ profiles during OH- and NBI-heating and for the saw tooth-free phase of NBI + LHCD (P_{LH} = 720 kW). $\bar{n}_e \approx 1.1 \times 10^{13}$ cm^{-3}.

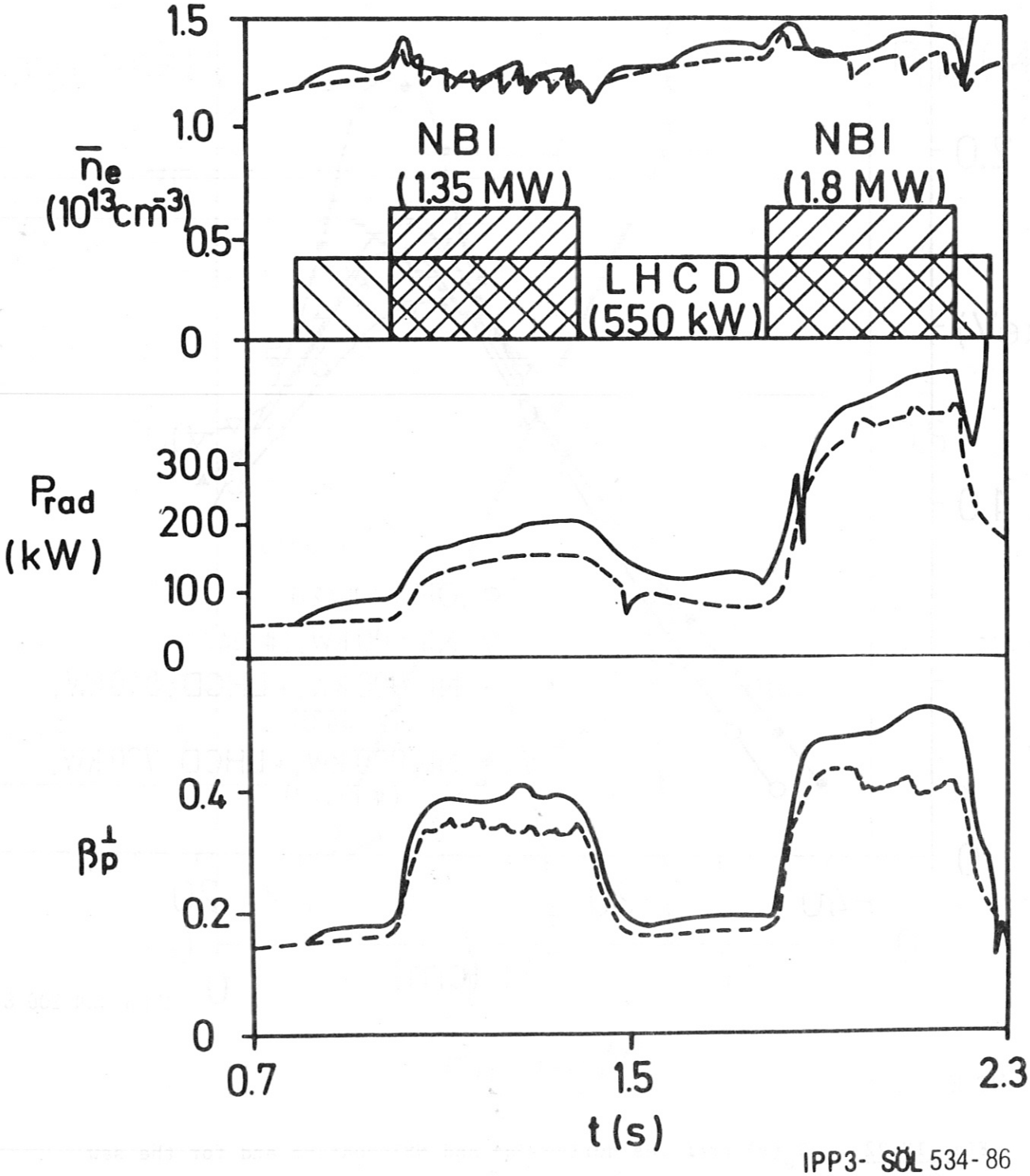

Fig. IV.23: Temporal evolution of n_e, P_{rad} and β_p during a sawtoothing discharge with NBI (dashed lines) and a sawtooth-free discharge with LHCD + NBI (solid lines).

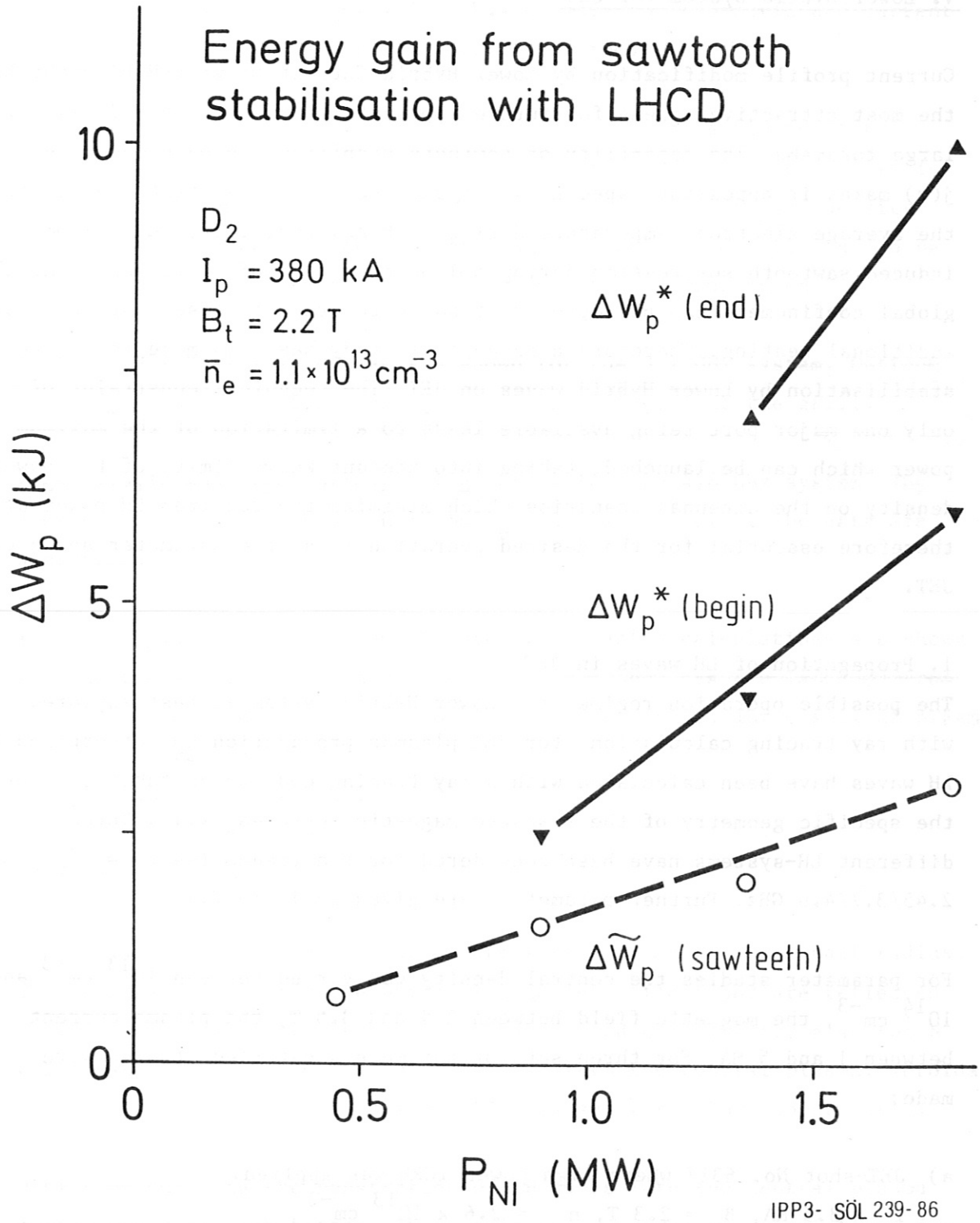

Fig. IV.24: Sawtooth amplitude of total energy content $\tilde{\Delta W_p}$ and gain ΔW_p^* after stabilisation at the beginning and end of the sawtooth-free phase versus beam power. P_{LH} = 550 kW.

V. Lower Hybrid System for JET

Current profile modification by Lower Hybrid Current Drive (LHCD) might be the most attractive scheme for future application of Lower Hybrid waves to large tokamaks. The capability of sawtooth stabilisation by broadening of j(r) makes it appealing especially for JET where giant sawteeth level off the average electron temperature during ICRF heating. The results from LHCD induced sawtooth suppression during NBI heating on ASDEX give hope that the global confinement can be improved if sawteeth are stabilised during strong additional heating. Therefore a conceptual study has been made for sawtooth stabilisation by Lower Hybrid waves on JET. The technical constraint of only one major port being available leads to a limitation of the maximum power which can be launched, taking into account known limits of the power density on the antenna. Scenarios which minimize the required LH power are therefore essential for the desired operation in a wide parameter space on JET.

1. Propagation of LH waves in JET

The possible operation regime of a Lower Hybrid System is best explored with ray tracing calculation. For JET plasmas propagation and absorption of LH waves have been calculated with a ray tracing code which takes care of the specific geometry of the D-shaped magnetic surfaces /V.1/. Three different LH-systems have been considered for the frequecies f_o = 2.45/3.7/4.6 GHz. Further parameters are given in Table V.1.

For parameter studies the central density was varied between 10^{13} cm^{-3} and 10^{14} cm^{-3}, the magnetic field between 2 T and 3.5 T, the plasma current between 1 and 5 MA. For three sets of parameters detailed studies were made:

a) JET-shot No. 6317 where high power ICRH was applied:
   I_p = 3.5 MA, B_t = 2.3 T, n_{eo} = 2.6 x 10^{13} cm^{-3}
b) optimum parameters for LH wave penetration:
   I_p = 3.5 MA, B_t = 3.4 T, n_{eo} = 4 x 10^{13} cm^{-3}, $T_{eo} = T_{io}$ = 2.5 keV
c) Full performance of JET:
   I_p = 5 MA, B_t = 3.4 T, n_{eo} = 10^{14} cm^{-3}, $T_{eo} \leq$ 12 keV

Finally the influence of a high energy ion minority on wave absorption was investigated.

The LH wave spectra are calculated with a spectrum code which takes reflection into account. In Figs. V.1 to V.4 examples of symmetric and current drive spectra are given for the 2.45 GHz system.

The mean reflection coefficient for the same system is plotted for different densities versus grill phasing in Fig. V.5, in Fig. V.6 it is shown for phasings $\Delta\varphi = 90^{o}$ and $\Delta\varphi = 180^{o}$ versus density and density gradient at the grill mouth. For minimum reflection the grill has to be positioned at densities $n_e = 0.9 - 2 \times 10^{12}$ cm^{-3} depending on Δ .

In Figs. V.7,8 similar curves are shown for the 3.7 GHz system. Optimum matching is here obtained for $n_e = 2 - 7 \times 10^{12}$ cm^{-3} at the grill.

Figs. V.9,10 show the corresponding curves for the 4.6 GHz system. The density at the grill should here be $n_e = 5\text{-}8 \times 10^{12}$ cm^{-3}. The data are summarized in Table V.2.

In Figs. V.11 to V.16 the results from ray tracing calculations are shown for the transmitter frequency $f_o = 2.45$ GHz. The waves are launched from the plasma edge in the midplane on the low field side. Three sets of plasma parameters are used:

a) $I_p = 3.5$ MA, $B_{to} = 2.3$ T
b) $I_p = 3.5$ MA, $B_{to} = 3.4$ T
c) $I_p = 5$ MA, $B_{to} = 3.4$ T

In all cases LH-waves do not penetrate further than to about half radius. Then all rays encounter the whispering gallery effect and are reflected back to the plasma periphery. The $N_{||}$ values and consequently also the N values are strongly modified on their way into the central plasma. Toroidal effects play an important role in JET because of the low aspect ratio.

With top-launching the penetration of LH waves into the central plasma region would be much better. The results of ray-tracing calculations for the three frequencies $f_o = 2.45$ GHz, $f_o = 3.7$ GHz, $f_o = 4.6$ GHz are shown in Figs. V.17 to V.19. The launching point in these cases is located at the position of a vertical ppart on JET. The plasma parameters for the cases shown are:

$I_P = 3.5$ MA, $B_{to} = 3.4$ T, $n_{eo} = 5 \times 10^{13}$ cm^{-3}, $T_{eo} = T_{io} = 2$ keV.

Variation of the plasma parameters shows that even at the lowest frequency of f_o = 2.45 GHz the LH waves can still reach the central region inside r_f/a = 0.5 for densities up to $n_{eo} = 1 \times 10^{14}$ cm^{-3}. With top-launching the radial variation of $N_{\parallel}$ is much smaller as seen from the plots in Figs. V.17,b) to V.19,b). This is due to the smaller variation of the magnetic field along the path of the rays from the antenna to the absorption zone in the central plasma region. Similar results are obtained from ray tracing calculations for slightly different geometry with another code at MIT /V.2/. The difference between the ray propagation in the cases of side-launch and top-launch is clearly seen from Figs. V.13 and V.17 where two different launching points are chosen for similar plasma conditions. Good penetration of waves into the central region is obtained only with top-launching. Top-launch in JET, however, seems nearly excluded because of the difficult access to the vertical port. It might be possible for the highest frequency of f_o = 4.6 GHz where sufficient high power could be launched through the small port size available.

The results on wave penetration for side-launching from an antenna in a main port of JET are summarized in Figs. V.20-22 for 2.45 GHz, in Fig. V.23 for 3.7 GHz and in Fig. V.24 for 4.6 GHz. From the results of the ray-tracing calculations it seems to be excluded that LH waves can reach the plasma centre at least for launching from the low field side as considered here. Even penetration to half radius seems to be only possible at moderate densities: waves with $\Delta\varphi = 90^o$ (LHCD) can reach r_f/a = 0.5 for :

$$n_{eo} \leq 2 \times 10^{13} \text{ cm}^{-3} : \quad f_o = 2.45 \text{ GHz}$$
$$n_{eo} \leq 3.5 \times 10^{13} \text{ cm}^{-3} : \quad f_o = 3.7 \text{ GHz}$$
$$n_{eo} \leq 4.5 \times 10^{13} \text{ cm}^{-3} : \quad f_o = 4.6 \text{ GHz}$$

Waves with slow phase velocities (large $\Delta\varphi$) are absorbed in the central plasma by thermal electrons through Electron Landau Damping (ELD). This can be seen for Δ = 180° at f_o = 3.7 GHz and for $\Delta\varphi$ = 150° and 180° at f_o = 4.6 GHz. The influence of ELD on wave penetration has been studied by varying the electron temperature in a wide range. The result is shown in Fig. V.25 for 2.45 GHz for various T_e-profiles with constant density profile ($n_e(0) = 6 \times 10^{13}$ cm^{-3}). Only the spectrum with $\Delta\varphi = 90^o$ is not affected by LHCD up to $T_e(0)$ = 10 keV. All other spectra with larger and therefore larger $\bar{N}_{\parallel}$ would be absorbed by ELD already outside $r_f/a \approx 0.8$ in JET plasmas with high additional heating. The waves with higher frequency would be even stronger affected by ELD than the waves at 2.45 GHz.

In the presence of fast ions from ICRH minority heating or NBI part of the Lower Hybrid power could be absorbed by these high energy ions. This has been investigated for ion energies up to 100 keV with a fractional population of the high energy minority of 5 %. Figure V.26 shows the result for the 2.45 GHz system. Only waves with $\Delta\varphi \geq 135^{o}$ might be depleted by absorption on fast ions. Current drive spectra would not be affected up to the highest energy of 100 keV. The density dependence of ion absorption was studied for 5 % of 100 keV H^{+} in D^{+}. Figure V.27 shows that wave spectra with $\Delta\varphi \leq 105^{o}$ would not be affected.

The results of the ray tracing calculations lead to the conclusion that penetration of LH waves to the central plasma region in JET seems to be unlikely due to

- decrease of launched $N_{\parallel}$ in the plasma interior
- absorption by ELD outside r/a = 0.8 at high central T_e values
- absorption by fast ions in regions of high density.

With the broad density profiles observed at high plasma current in JET, wave penetration becomes even more difficult. Figure V.28b shows a density profile of JET shot #5350 with $I_p \approx 5$ MA which is considerably broader than the profiles used for the ray tracing calculations. The profiles used in these calculations resemble the profiles at medium plasma current as in JET shot #6317 with $I_p = 3.5$ MA (Fig. V.28a). Therefore no scheme of profile control should be envisaged which requires central deposition of LH-power, e.g. deposition at the q = 1 surface.

2. Specification of the parameters of the LH-system

From considerations on LH-current drive efficiency and in view of the results of ray tracing calculations a scheme of peripheral LH-power deposition for control of the current profile seems to be obligatory for JET. The parameters of the LH systems are therefore fixed for this appplication.

2.1 Choice of the frequency

For operation in the suprathermal electron regime the critical density for onset of ion absorption should be above the maximum density in the LH deposition region. With realistic profiles of JET plasmas, deposition of LH waves would take place in zones where $n_e < 5 \times 10^{13}$ cm^{-3}. For existing frequencies, $f_o = 2.45$ GHz would be the closest with the critical density

higher than the supposed limit. Experiments with this frequency were performed on FT and PLT. On FT the onset for ion interaction was at $\bar{n}_e = 5.5 \times 10^{13}$ cm^{-3} and in PLT up to $\bar{n}_e = 4.6 \times 10^{13}$ cm^{-3} no indications of an approach to the ion regime are yet seen. Therefore 2.45 GHz seems to be appropriate for the parameter range envisageable in JET.

Several arguments would strongly suggest not to go higher in frequency than just necessary to stay in the electron regime:

a) Optimum coupling of the grill requires higher local densities for higher frequencies. For $f_o > 2.45$ GHz the grill must be positioned nearly at the limiter radius as inferred from Table 2. In expanded boundary operation on JET this might be difficult. In limiter operation the power load on the grill will be very high.

b) The sensitivity of grill coupling to changes in the edge density increases with frequency. The possible variation of the grill position is typically ± 1 cm for 1.3 GHz (ASDEX), ± 0.5 cm for 2.45 GHz (FT, PLT) and 0.1 cm for 4.6 GHz (Alcator C). Excursions of the density in front of the grill due to additional heating or to nonlinear effects of the LH itself could be better handled with a LH system at a frequency as low as possible.

c) The resistive losses in the waveguides increase with frequency.

Therefore a system at the commercially available frequency of $f_o = 2.45$ GHz is proposed.

2.2 LH-power requirements

To estimate the power requirements for an application to JET we first examine the case of full current drive by using equ. (2) (Section III.3), which we rewrite as

$$\frac{P_{RF,MW}}{I_{RF,MA}} = \frac{\bar{n}_{e,13} \cdot R_m \cdot \gamma}{\eta \cdot \mu \cdot g} \qquad (5)$$

For η we use the experimental value obtained in ASDEX. The parameters of the particular shot we use are $\bar{n}_e = 0.9 \times 10^{13}$ cm^{-3}, $P_{RF,net} = 650$ kW,

I_p = 280 kA, B_o = 2.2 T, D_2, f = 1.3 GHz, R = 1.65 m, γ = 1.25. From accessibility and spectrum codes we calculate μ = 0.58 and g = 0.5. We then obtain η = 2.75 $MA \cdot MW^{-1} \cdot 10^{13} cm^{-3} \cdot m$.

For application to JET we assume a similar density profile as in ASDEX, i.e. γ = 1.25, and we calculate μ and g for a 2.45 GHz grill with 30 waveguides (12+2 mm) and for different magnetic fields. We furthermore assume that the technical set up allows to vary the phasing of the grill so that always a "matched spectrum" may be generated, i.e. a spectrum which is above, but as near as possible at the accessibility boundary to get maximum efficiency. The grill design is assumed such that $N_{\parallel}$ for $\Delta\varphi = \pi$ is large enough ($\bar{N}_{\parallel} \approx 4.5$) so that within the range of variation of $\bar{N}_{\parallel}$ with the phasing we do not change the grill directivity appreciably. We thus assume for μ a value of μ = 0.7 which is the maximum directivity due to calculations with the Brambilla spectrum code. For the spectrum width (between the first zero power points) we use $\Delta N_{\parallel}$ = 0.6 (corresponding to the proposed grill at 2.45 GHz). For the accessibility we take plane wave propagation (Fig.V.29). With these assumptions we can calculate the ratio of launched LH power to rf driven plasma current as a function of density and magnetic field with equ. (2). The results are shown in Fig. V.30.

For complete rf current drive in JET the required LH power is excessively large. At $\bar{n}_e = 5 \times 10^{13}$ cm^{-3}, B_o = 3 T, I_p = 5 MA e.g., we would need about 130 MW. In a recent paper relativistic effects have been included in the current drive theory, predicting a favourable electron temperature dependence of the current drive efficiency /V.3/. However, for a temperature of 10 keV only an improvement by a factor of about 1.3 may be expected, which does not significantly reduce the required power for JET. If we would manage to drive the current only in the central region we would need for $\bar{n}_e = 5 \times 10^{13}$ and B_o = 3 T, a power of 25 MW/MA.

Therefore, with a power of 10 - 15 MW available at the coupler, appreciable central current drive has to be ruled out for central densities higher than 5×10^{13} cm^{-3}.

For the purpose of sawtooth stabilisation, however, we do not need to drive the full plasma current by means of rf. In addition, for a change in the current distribution, the power needs not to be deposited in the central region. Current drive in the outer region of the plasma may be more effective in achieving q(0) > 1. We note that the ratio P_{RF}/I_{RF} does not

directly depend on the plasma cross section. If we manage to drive the current only within the region of the plasma with $r/a > 0.5$, we may operate at a lower density and thus lower $\bar{N}_{\parallel}$. Fig. V.27 shows that with 10 MW we may then drive a current of about 1 MA in the density range of $\bar{n}_e = 2 - 3 \times 10^{13}$ cm^{-3}. In addition we should remember that according to the observations in ASDEX a maximum decrease of the internal inductance l_i does not necessarily coincide with the conditions of maximum current drive efficiency. With careful shaping of the $N_{\parallel}$-spectrum the region of LH current drive could be well localized thereby enhancing the efficiency for current profile modifications.

For this purpose flexibility in the $N_{\parallel}$-spectrum is needed. In Fig. V.31a the local values of $N_{\parallel acc}$ along a major radius are plotted for a central toroidal magnetic field of $B(0) = 3.4$ T and for the experimental density profile shown in Fig. V.31b. The curves are calculated with different values of the peak density. In lack of a reliable theory for local power deposition, we rely on the experimental results from ASDEX and propose a similar way for shifting the LH absorption zone by varying the $N_{\parallel}$-spectrum. From Fig. V.31a then a range of $1.5 \leq \bar{N}_{\parallel} \leq 2.5$ would be required. However, one has to be cautious in applying such a scheme of fractional current drive to JET. The enhancement of the conductivity used in equ. (3) is described by the

$$\text{factor } b = \frac{\alpha(Z_{eff}) \cdot 0.24 \cdot 10^{12}}{N_{\parallel}^{2}\ q\ m^{2}\ T_e^{3/2}\ \text{kV}} \quad \text{kA}^{-1}\ \text{cm}^{-3}$$

where α is a function of Z_{eff}, q is the cross-section and T_e the electron temperature. In table V.3 the relative enhancement of the conductivity, $b \cdot I_{RF}/\bar{n}_e$, is given for various sets of parameters. It turns out that for current drive in the outer half to third of the plasma this enhancement (or an improvement of the efficiency with a co-acting electric field) is negligible except for current drive at the very edge at very low density. But not only this: the electric field required to drive inductively the major fraction of the plasma current may generate runaway electrons near the plasma surface, if the rf produces fast electrons at sufficient high velocity. According to Fisch /V.4/ the runaway velocity is

$$v_R^2 = n\ q^3\ \ln\Lambda / 4\pi\varepsilon_o^3\ E\ m \quad \text{which for } \bar{n}_e = 2 \times 10^{13}\ \text{cm}^{-3} \text{ and}$$

E = 0.05 V/m gives 1.8×10^8 m/sec and thus corresponds to $N_{\parallel} \approx 1.7$. For this reason, fractional current drive within the outer region of the plasma should not be applied at too low $N_{\parallel}$.

2.3 LH-wave spectrum

The position of the main lobe in the LH spectrum is determined by the quite stringent accessibility condition. Nonaccessible rf power at low $N_{\parallel}$ may cause serious problems with arcing, ion sputtering due to a high plasma potential and a resulting increased influx of impurities. This was experienced on ASDEX each time when LH-spectra at low $N_{\parallel}$ with high nonaccessible power were launched. Therefore the optimum current drive spectrum should still be fully accessible at the highest density envisaged:

$$n_e < 5 \times 10^{13} \text{ cm}^{-3}.$$

Then with $B_t = 3$ T: $N_{\parallel,acc} \approx 2$ for $f_o = 2.45$ GHz. A consistent set of parameters is found with

$$\bar{N}_{\parallel} \ (\Delta\varphi = \pi) = 4.4$$
$$\Delta N_{\parallel} = 0.6$$
$$d = a+b = 1.4 \text{ cm}$$
$$n_{guides} = 30 \text{ (in 1 row)}$$

The narrow $N_{\parallel}$-spectrum of a multiwaveguide grill with only small power in secondary lobes might lead to problems with power absorption. In existing experiments the gap between the main lobe of the spectrum and the bulk eletrons could probably be bridged by secondary lobes in the $N_{\parallel}$-spectrum. A small amount of power should be already sufficient to pull out a tail of high energy electrons from the bulk if this mechanism is effective. With the narrow line produced by a multi-waveguide grill the power transferred to bulk electrons might be too low to start absorption. In this case power at higher $N_{\parallel}$ should be added. This should be provided by an independent grill in order not to limit the maximum power capability of the launcher (c.f. section III.3). Such flexible $N_{\parallel}$ shaping would be possible in JET if the power splitting for the vertical rows is not fixed internally but externally controlled. Then each independent horizontal row can produce another $N_{\parallel}$-spectrum.

Therefore a grill antenna with external power dividers is proposed in order to provide the highest possible flexibility for shaping of the $N_{\parallel}$-spectrum.

2.4 Summary

In summary we find for an application to JET:

- Central current drive requires too much power for $n_e(0) > 5 \times 10^{13}$ cm^{-3}

- For fractional current drive in the outer region of the plasma where $n_e \approx 2 - 3 \times 10^{13}$ cm^{-3} we may achieve a driven current of 1 MA with about 10 MW of launched power.

- Since maximum current drive and maximum broadening of j(r) are not obtained under the same conditions, $\bar{N}_{\parallel}$ should be variable in a range $1.5 < \bar{N}_{\parallel} < 2.5$ and the shape of the $N_{\parallel}$ spectrum should be externally controllable by independent phase setting of different parts of the grill.

- Appreciable current drive at $n_e > 5 \times 10^{13}$ cm^{-3} cannot be expected with the planned power. A frequency of 2.45 GHz is therefore sufficient, since the corresponding density limit for the onset of LH power absorption by the ions is still higher.

- Top launching might lead to better profile control because the LH waves would then be absorbed on the high field side where the density profiles are flatter and wave accessibility is better.

3. Technical Layout of the RF-System

3.1. Overview

Valuable technical information for the design of the system could be used from a previous conceptual study /V.5/. The characteristics of the proposed Lower Hybrid system for profile control on JET are summarized in table V.4. The transmitter has a power of 18 MW at a frequency of 2.45 GHz. The pulse length is 20 sec with one pulse every 10 min. The modular system consists of 30 klystrons each delivering 600 kW of RF power. Figure V.32 shows the block diagram of the RF system. Five high power klystron amplifiers are fed by one power supply followed by a crowbar protection. The power from each one of the klystrons is transmitted by a waveguide transmission line to a high power divider which feeds one vertical row of 6 or 8 waveguides of the grill antenna. The phasing between the 30 waveguides in one horizontal row of the grill antenna is adjusted electronically on the low power side of the klystrons. This concept has worked successfully on ASDEX /V.6, 7/. The central 4 waveguides of each vertical row are fed in phase while the two upper and lower waveguides in a vertical row can be set at different phasings by adjusting mechanical phase shifters in the high power divider. This arrangement provides a high flexibility for tailoring of the spectrum of the grill antenna. The klystron amplifiers are fed by a common RF exciter starting from a master oscillator at 2.45 GHz. The exciter contains the RF protection circuit, power divider, phase and amplitude control feedback system and the medium power amplifier to drive the klystron amplifiers.

The cooling system with heat exchanger must dissipate about 18 MW from the klystron amplifiers. Additional cooling requirements are necessary for water loads and waveguide components.

A RF diagnostic system measures the forward and reflected power at the entrance of the Grill antenna and feeds the phase and amplitude-control system.

This proposal has to be considered as a general layout. Specification of many components still needs a detailed technical study.

3.2. RF-Transmitter

3.2.1. RF-Exciter

The basic layout of the exciter is shown in Fig. V.33. A frequency stabilized master oscillator at 2.45 GHz feeds a low power divider with 32 output channels. Between the oscillator and the power dividers an inserted pin diode switch is necessary for the RF protection of the system. The master oscillator gives also the phase reference for the phase feedback loop as well as for the RF diagnostic measurement system. The amplitude and phase variation of the wave supplied at each klystron exit are adjusted and regulated electronically using a phase shifter and attenuator in front of each medium power amplifier which feeds one klystron. Measurements of incident and reflected power as well as that of the phase are given by directional couplers placed at the input of the Grill antenna before the step transformers and the vacuum windows. The amplitude and phase feedback system allow to regulate the output RF power of each klystron as well as the phase of the transmitted wave according to a power level and a phase reference against the RF master oscillator and high voltage power supply perturbations and also to modulate from an external signal these two parameters during the RF pulse. The range for the amplitude control is about 20 dB while the range for the phase regulation is 0 - 360°.

3.2.2. High Power Klystron Module

The klystron of one highpower module delivers 600 kW into a matched load. In Table V.5. the main characteristics of the klystron are shown. Preliminary contacts with klystron manufacturers revealed that tubes for long pulse operation (20 s pulse duration) at a power level of 600 kW per unit at a frequency of 2.45 GHz are developed and commercially available.

Figure V.34 shows the klystron module with a floating desk modulator, beam- and body current measurements, isolation transformer and the directional coupler at the RF output. All other standard protections necessary for klystron operation

like arc-detectors, temperature measurements, SWR, etc. are not shown in the diagram. The modulation anode for the klystron is necessary to reduce the collector dissipation at low power operation and gives also low phase variation through the klystron when the beam current is modulated.

3.3. Transmission line

Figure V.35 shows the arrangement of the transmission line. At the output of the klystron a waveguide switch transfers the RF power either to the transmission line or to a high power dummy load for tests of the RF system. The transmission lines on the klystron gallery are of the rectangular type WR 430. After a waveguide transition from rectangular WR 430 to circular WC 451 the long transmission line (40-50 m) goes down to the basement and through the concrete wall of the torus hall. At the entry from the basement to the torus hall a transition from WC 451 to WR 430 connects to a flexible waveguide. This feeds after an E-bend the first part of the High Power Divider which distributes the RF power to the corresponding vertical rows of the grill antenna. The flexible waveguide allows the horizontal displacement of the grill antenna. The total loss of the transmission line system is 0.56 dB.

3.4. High Power Divider

Two types of High Power Dividers are used to feed each vertical row of the grill antenna. As shown in Fig. V.36 a series of 3 dB power splitters provides the RF partition into 8 waveguides of the same vertical row of the grill antenna. Half of the reflected power will be dissipated in the matched load of port 4 of each 3 dB divider. The 4 outputs of the inner 3 dB dividers go through a fixed phase correction waveguide, a directional coupler to the step transformer input of the grill antenna. The two upper and lower waveguides of each vertical row have adjustable phase-shifters for flexible spectrum control of the grill antenna. As shown in Fig. V.37 the same arangement is used to split the RF power up to 6 waveguides in the 6 vertical rows at both sides of the grill assembly. The power output at the horizontal rows 1 and 8 is recycled through an adjustable phase-shifter and is fed to port 4 of the preceding 3 dB divider.

At the input of the High Power Divider, which is electrically on the potential of the grill antenna and the vacuum vessel, a DC break isolates this system from the transmitter. The RF losses of the High Power Divider are $\simeq$ 0.25 dB.

Figure V.38. shows the mechanical arrangement. It is not foreseen to use high power circulators. The 3 dB Power dividers in series reduce considerably the total reflected power towards the klystron. Also the insertion loss of the transmission line gives an additional return loss of 2 dB. The klystron withstands a standing wave ratio of 2 under all phases with a tube protection by an active feedback system to reduce RF output power during the mismatch but would result in some per cent less than the typical 53 per cent.

3.5. Grill Antenna

The grill antenna is built of 216 independent waveguides which form a phased array with 6 horizontal rows of 30 waveguides and 2 horizontal rows of 18 waveguides (Fig. V.39). Taking off waveguides in the corners of the array is required by the geometry of the available port on JET. This solution offers the advantage of modular construction, independently fed waveguides and easy RF tests during manufacturing. The waveguides with reduced height are made by coextruding of stainless steel and copper tubes. The copper on the inner walls reduces the RF losses and gives the optimum surface for additional galvanic surface coating which is applied in order to suppress multipactoring /V.8/. Each of the waveguides is ~3 m long. The inner dimensions are 110 x 12 mm^2. The wall thickness is 2 mm. A vacuum tank surrounds the waveguide structure and allows a thin wall waveguide construction, a good mechanical handling of the antenna and additional pumping if necessary. The 216 waveguides are mechanically assembled and welded together at the frontside of the vacuum tank and at the rear side of the vacuum tank flange. The space needed to locate 8 vertical and 30 horizontal waveguide flanges at the back side of the coupler leads to a ~3 m long pyramidal shaped grill antenna. The losses in the grill antenna are ~0.2 dB. The vacuum tightness is realized on each waveguide by a double reduced heigth waveguide window of alumina ($\lambda/2$ wavelength block window). Four

vertical windows form a multiple window block. Between two window blocks additional pumping is foreseen. Four symmetric 2 step transformers on the atmospheric pressure side form one transformer block which matches the reduced height waveguides to the standard waveguides WR 430.

A bellow located between the port of the JET vessel and the vacuum tank is designed in order to allow for a horizontal positioning of the grill antenna with respect to the plasma and to absorb movement between the grill antenna and the vacuum vessel during operation.

A hydraulic system will allow the movement of the grill antenna. The waveguides and the double window section have a rough gold coating to prevent multipacting and ω_{ce} breakdown and need no special additional methods for conditioning the grill antenna.

3.6. High Voltage Power Supply

Figure V.40 shows the diagram of two High Voltage Power Supply modules each feeding 5 klystrons connected in parallel. The modules can be run independently. The thyristor controller is used to compensate for the network voltage variations during the machine operation and to protect the module in case of a short-circuit. The high voltage transformers which feed two diode bridges are connected in series to construct a 12-phase rectifier. The capacitor bank filters out the 600 Hz voltage fluctuations and protect the bridges against over-voltage. The total installed power is ~ 34 MW.

Characteristics of one Module:

Voltage	70 kV
Current	80 A
Power	5.6 MW
Ripple	0.1 %
Rise Time	150 ms
Voltage Regulation	$\pm$ 1 %

A fast crowbar (Fig.V.41) which follows each module protects the 5 klystrons in case of a breakdown. The klystrons are

switched in parallel and decoupled by resistors. High voltage distribution switches allow an independent selection of each klystron for operation or grounding for safety protection.

3.7. Cooling System

The cooling system for the klystron amplifiers, the water dummy loads and cooled waveguide components will be realized by demineralized water flowing in several closed loops. The energy will be transfered by heat exchangers. No detailed solution of the cooling system is presented in this proposal.

3.8. Buildings

The klystrons with their control cabinets will be located in the Hall J1H on the gallery near the ICRH generators (Figs. V.42, 43). In the basement of J1H the high voltage protection and the heat exchangers are installed. The 30 transmission lines go through the basement to the Torus Hall at the shortest possible distance. The high voltage power supplies (6 modules) are located outdoors.

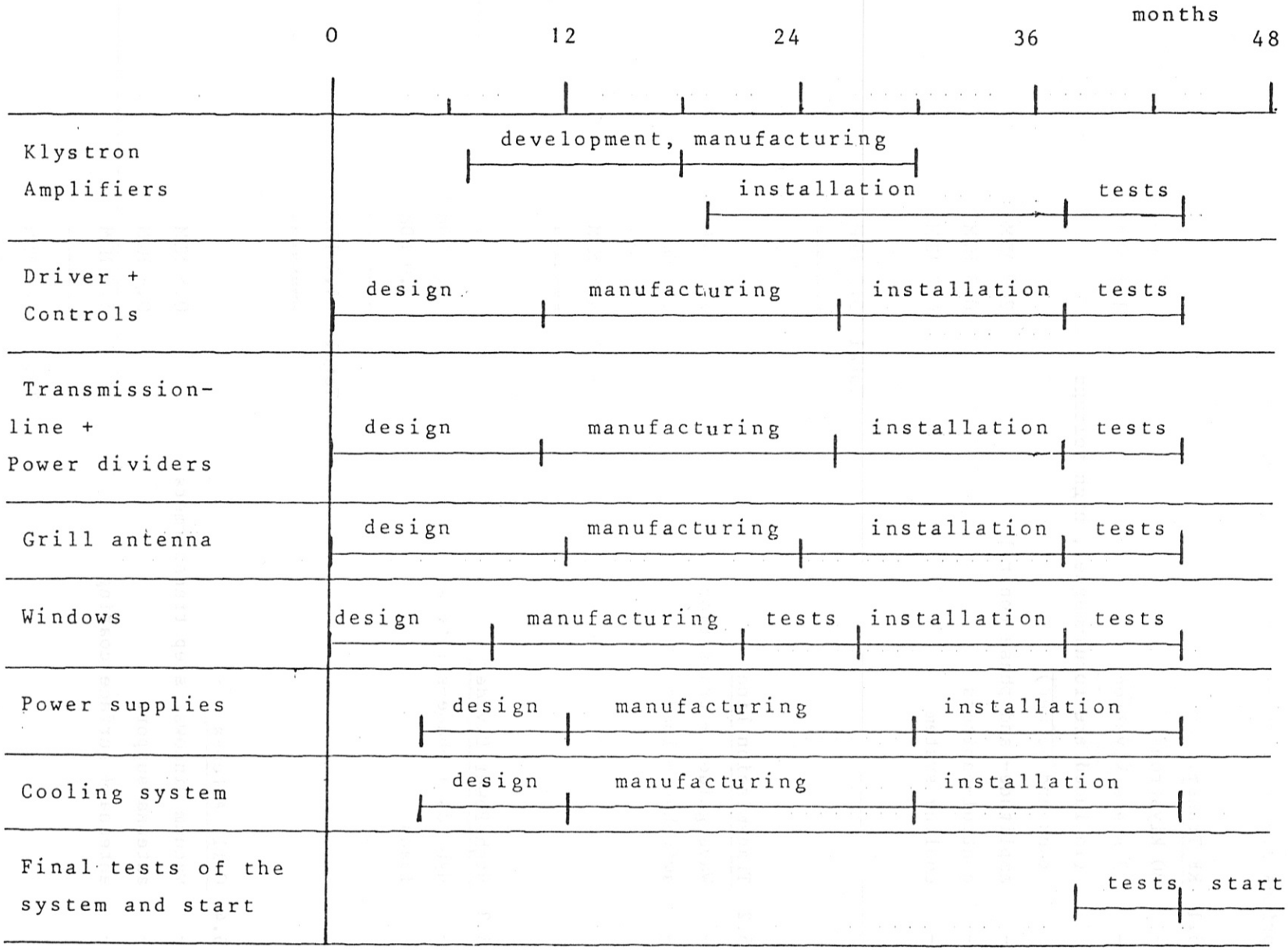
months
0
12
24
36
48
Klystron Amplifiers
development, manufacturing
installation
tests
Driver + Controls
design
manufacturing
installation
tests
Transmission-line + Power dividers
design
manufacturing
installation
tests
Grill antenna
design
manufacturing
installation
tests
Windows
design
manufacturing
tests
installation
tests
Power supplies
design
manufacturing
installation
Cooling system
design
manufacturing
installation
Final tests of the system and start
tests
start

5. Cost estimation

In the cost estimation for the JET Lower Hybrid System exact prices were specified only for klystrons, loads, phase-shifters, hybrids and the High Voltage Power Supply. Other prices are based on extrapotations from existing systems.

5.1 RF Transmitter

- 30 klystrons	10.9 MDM
- 3 spare klystrons (included are focus-magnet, high voltage tank and socket)	1.1 MDM
- amplitude- and phase control	2.0 MDM
- control-cabinets	0.5 MDM
- cooling system	0.7 MDM
Total	15.2 MDM

5.2 Transmission Line

- Wave guides + transition	2.6 MDM
- switches + loads	1.9 MDM
Total	4.5 MDM

5.3 High Power Divider

- Hybrids + phase-shifters	1.4 MDM
- loads	3.0 MDM
Total	4.4 MDM

5.4. Grill Antenna

- vacuum windows, step transformers	0.5 MDM
- antenna support	0.6 MDM
- antenna + surface coating	5.0 MDM
Total	6.1 MDM

5.5. High Voltage Power Supply

-	Protection	0.4 MDM
-	6 modules	7.5 MDM
	Total	7.9 MDM

Total cost of RF-System	38.1 MDM
In European Count Units:	17.8 MUC

References

/V.1/ M. Brambilla, Computer Physics Report 4 (1986), 71.

/V.2/ P. Bonoli, private communication.

/V.3/ C.F.F. Karney, N.J. Fisch, internal report PPPL-2128, Princeton (1984).

/V.4/ N.J. Fisch, C.F.F. Karney, Phys.Rev.Lett. 54, 897 (1985).

/V.5/ G. Tonon, et al., Conceptual Study of Lower Hybrid Frequency Heating of the JET Plasma, Report EUR-CEA-FC-1075 (April 1981).

/V.6/ M.J. Münich, et al., The Lower Hybrid RF Heating System for the ASDEX Tokamak; 4th Symposium on Heating in Toroidal Plasmas, Vd. II, p. 1183, Rome 1984.

/V.7/ M. Zouhar, Beschreibung des Niederleistungsteils des HF-Systems für die LH-Experimente an ASDEX, IPP 4/218 (Feb. 1984).

/V.8/ H. Derfler, J. Perchermeier, H. Spitzer, patent (11383), USA 4, 559, 281 (1985).

Table V.1:LH-parameters for ray-tracing calculations

f_o [GHz]	2.45	3.7	4.6
Number of waveguides in 1 horizontal row	30	40	60
Number of vertical rows	8	10	12
Periodicity Δ [cm]	1.4	0.9	0.7
$\bar{N}_{\parallel}$	4.4	4.5	4.7
$\Delta\bar{N}_{\parallel}$	0.6	0.45	0.3
S_{tot} [cm^2]	2400	1960	1980
P_t [MW]	12	12	12
p [kW/cm^2]	5	6.1	6.1

Table V.2: Grill coupling

f_o [GHz]	$n_{e,grill}$ for optimum coupling [cm^{-3}]		distance
	90°	180°	grill plasma [cm]
2.45	0.9×10^{12}	2×10^{12}	1 - 2.5
3.7	2×10^{12}	7×10^{12}	0 - 1.5
4.6	5×10^{12}	8×10^{12}	~ 0

Table V.3: Enhanced conductivity term (for $Z_{eff} = 3$)

$N_{\parallel}$	$\bar{n}_{e,13}$	q_m^2	$T_{e,kV}$	$I_{HF,MA}$	$b \cdot I_{HF}/\bar{n}_e$
1.5	2	5	1.5	1	1×10^{-1}
1.75	2	5	1.5	1	7×10^{-2}
2	2	5	1.5	1	6×10^{-2}
2	3	5	2.5	1	2×10^{-2}

Table V.4: Lower Hybrid system for JET (characteristics)

a) Transmitter		
Frequency	f_o	= 2.45 GHz
Number of klystrons	N_k	= 30
Power per klystron	P_k	= 600 kW
Total power	P_{tot}	= 18 MW
Pulse length	τ	= 20 s
b) Power transmission		
Length of transmission line (WR 430/WC 451)	L	$\approx$ 50 m
Losses in the transmission line	D_1	= 0.56 dB
Losses in the power divider	D_2	= 0.25 dB
Losses in the grill antenna	D_3	= 0.2 dB
Total power transmitted	P_t	= 14.3 MW
Reflection coefficient	R	$\lesssim$ 0.1
Total power radiated	P_t	= 12.8 MW
c) Grill antenna		
Number of horizontal rows, vertical stacked	N_v	= 10
Number of waveguides in 1 horizontal row: central part	N_g	= 30 (x 6)
top, bottom	N_g	= 18 (x 2)
Total number of waveguides	N_{tot}	= 216
Height of waveguides	h	= 10 cm
Vertical spacing between waveguides	d_v	= 1.5 cm
Width of waveguides	a	= 1.1 cm
Wall thickness	b	= 0.3 cm
Periodicity of waveguides d = a + b	d	= 1.4 cm
Surface per waveguide	s	= 11 cm^2
Total radiating surface	S_{tot}	= 2376 cm^2
Mean $\bar{N}_{\parallel}$	$\bar{N}_{\parallel}$	$(\Delta\varphi = \pi) = 4.4$
Width of spectrum	$\Delta N_{\parallel}$	= 0.6

Table V.5

JET LHPC

KLYSTRON CHARACTERISTICS

FREQUENCY (FIXED)	2,45	GHZ
BANDWIDTH (1 dB)	5	MHZ
POWER	600	KW
VSWR (min)	2	
PULSE LENGTH	20	s
REPETITION RATE	1:30	
GAIN	50 dB	
EFFICIENCY	53	%
OUTPUT	WAVEGUIDE	WR 430
BEAM VOLTAGE	65	KV
BEAM CURRENT	16,5	A
MOD. ANODE		

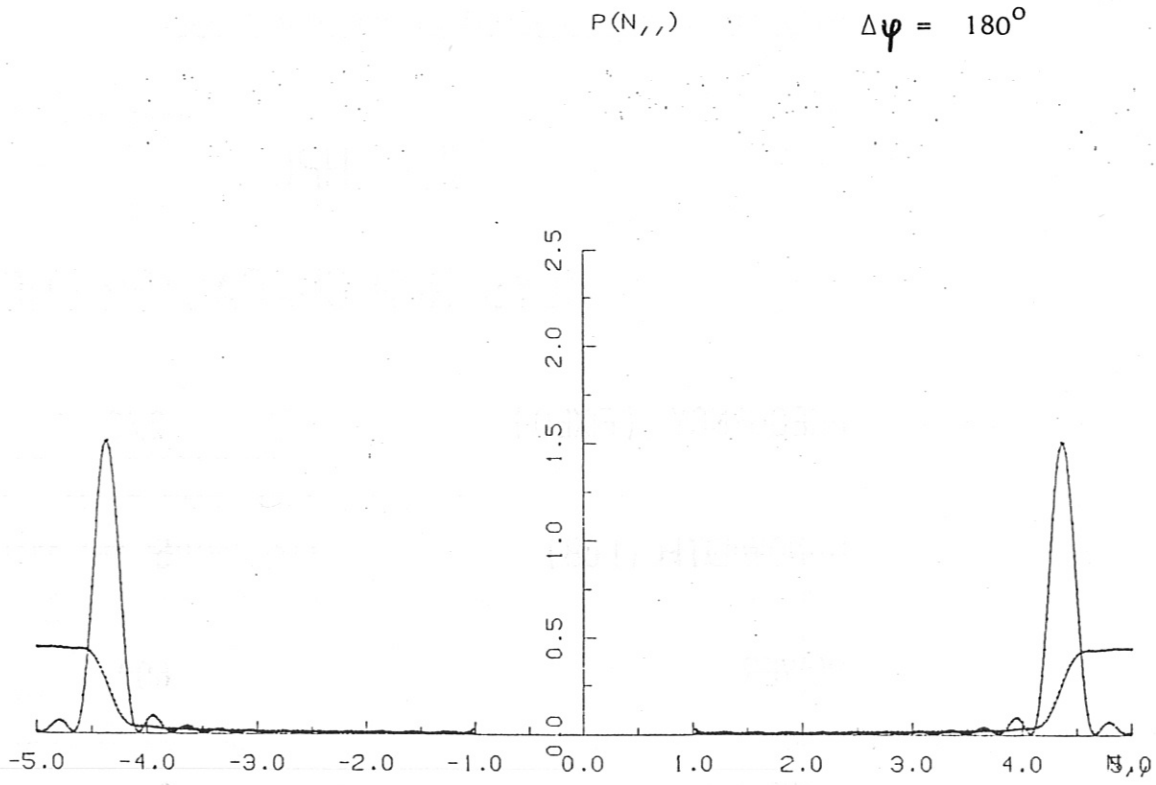

Fig. V.1: LH-wave spectrum for the 2.45 GHz system with $\Delta\varphi = 180^{\circ}$.

IPP-CRAY 06/03/86 09:19:55 MZB011 J2-03 10

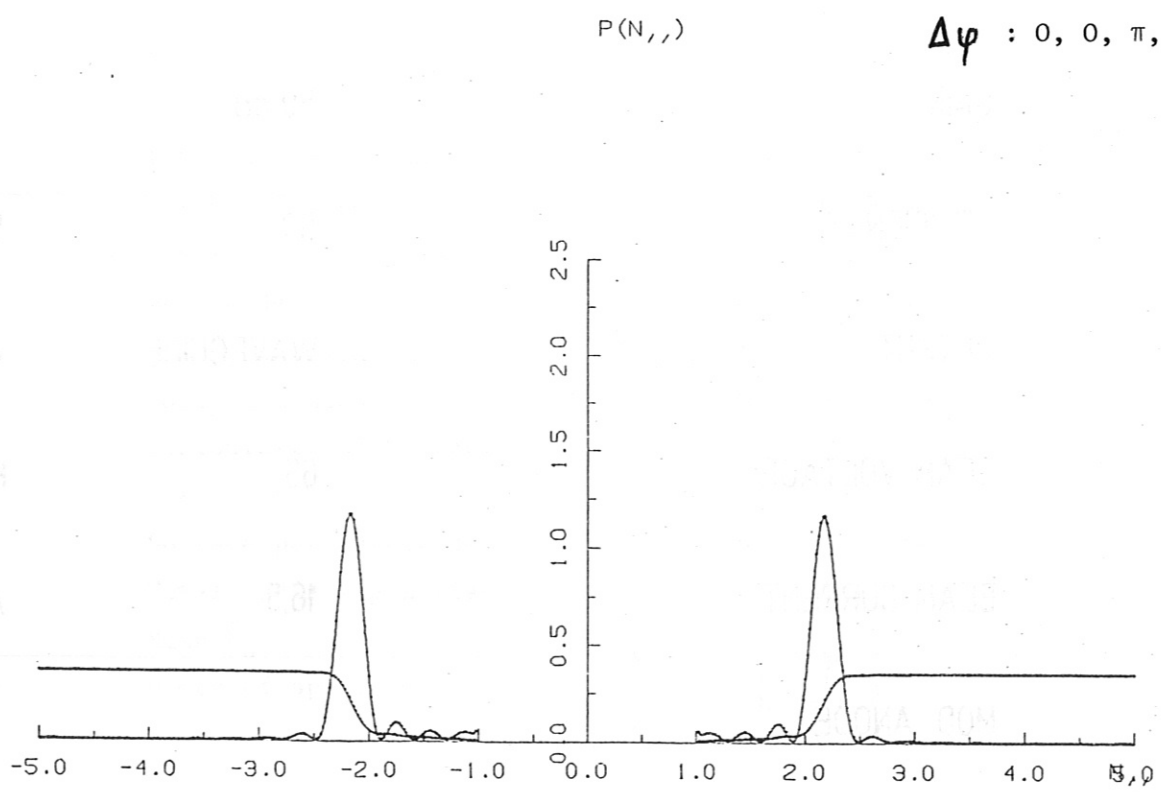

Fig. V.2: LH-wave spectrum for the 2.45 GHz system with phasing 0 0 π π ...

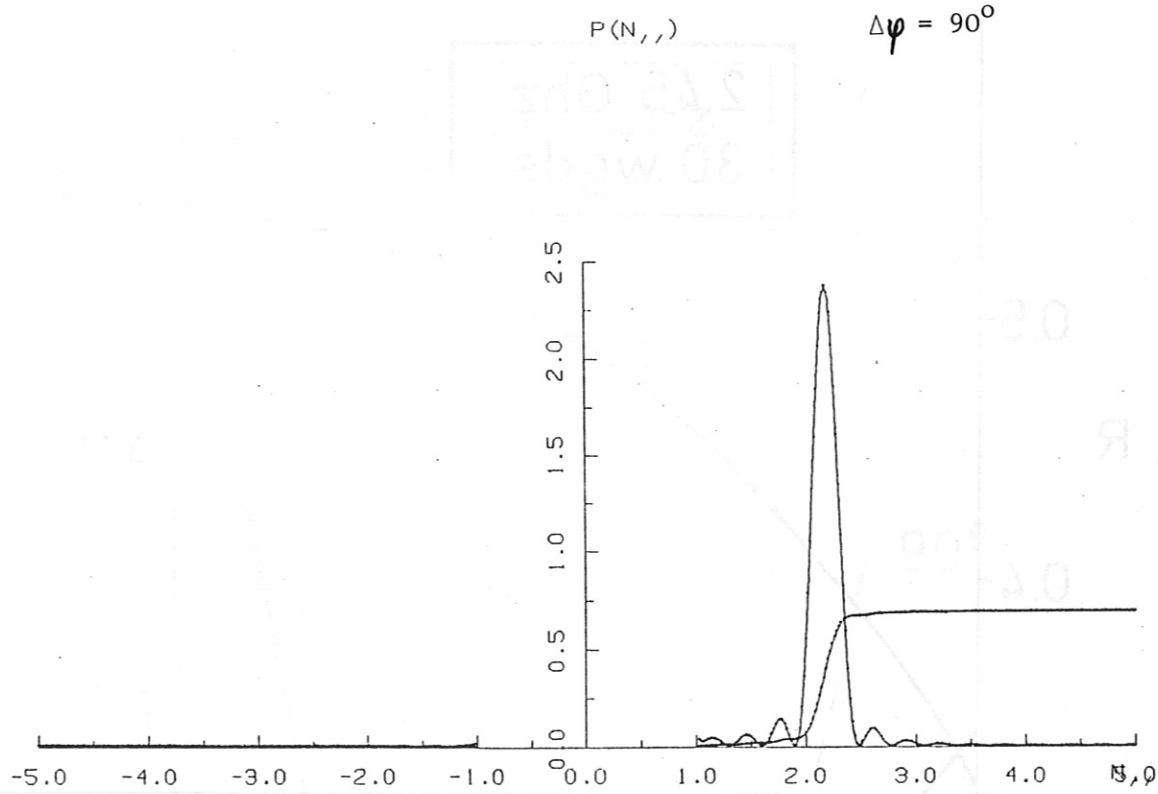

Fig. V.3: LH-wave spectrum for the 2.45 GHz system with $\Delta\varphi = 90^{\circ}$.

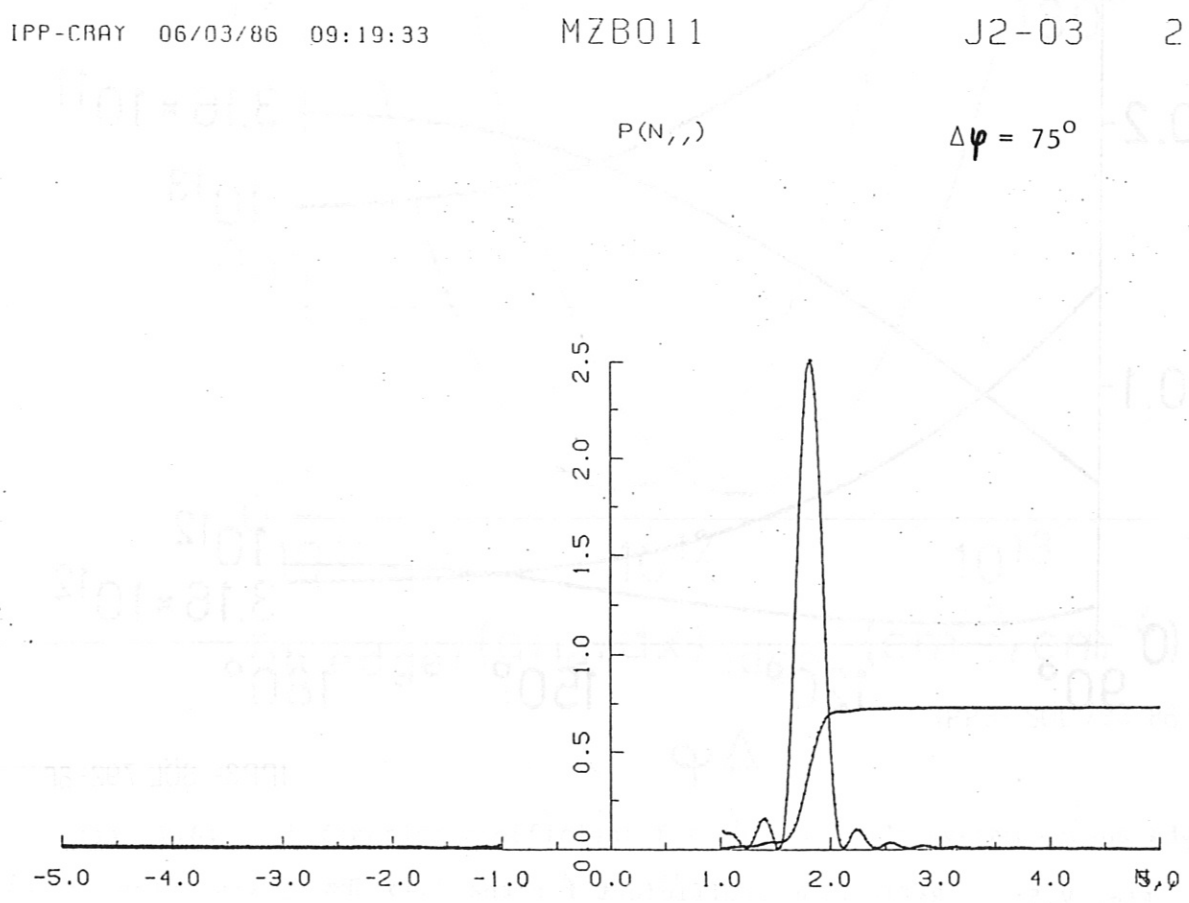

Fig. V.4: LH-wave spectrum for the 2.45 GHz system with $\Delta\varphi = 75^{\circ}$.

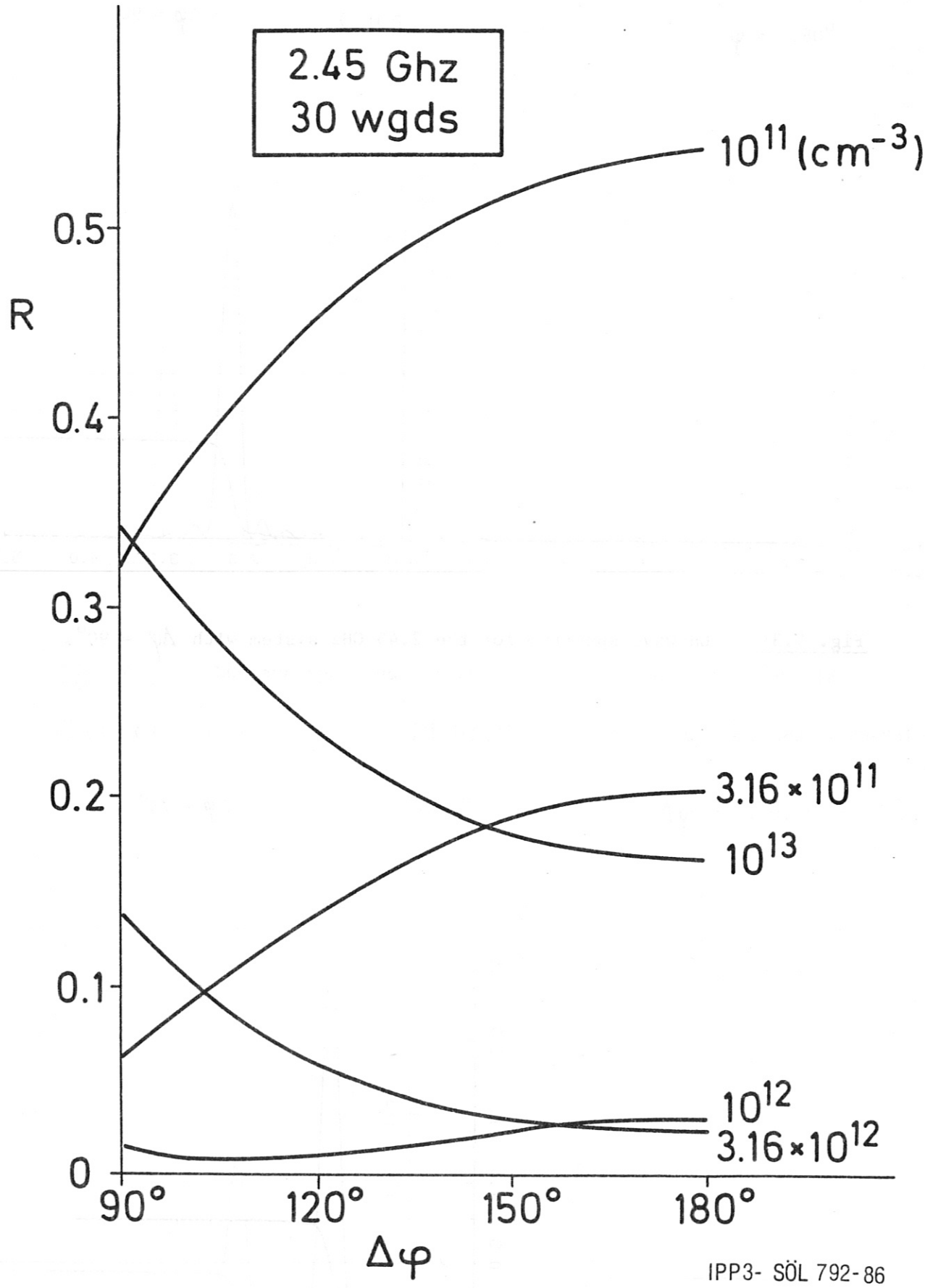

Fig. V.5: Reflection coefficient for the 2.45 GHz system versus grill phasing.

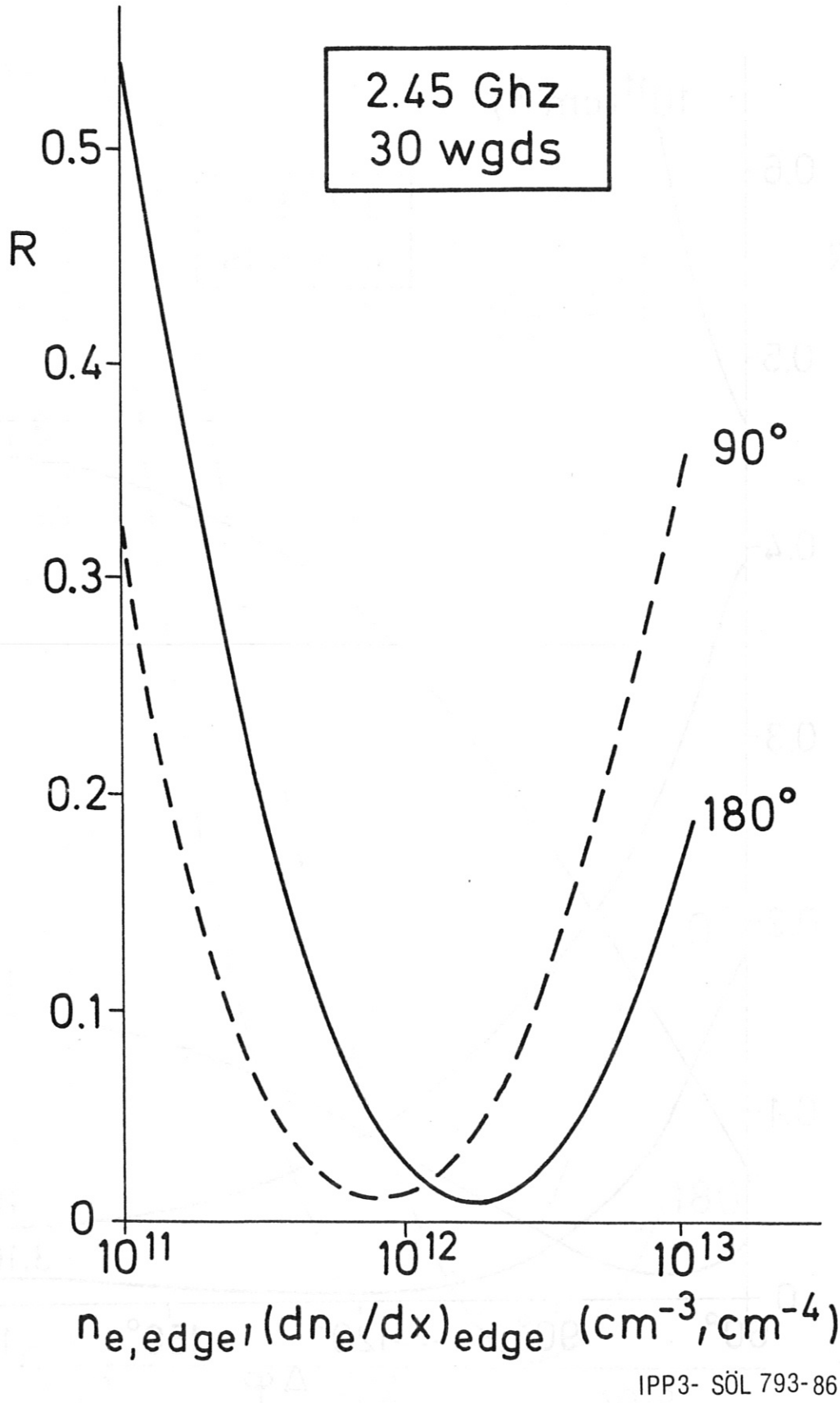

Fig. V.6: Reflection coefficient for the 2.45 GHz system versus edge density and density gradient.

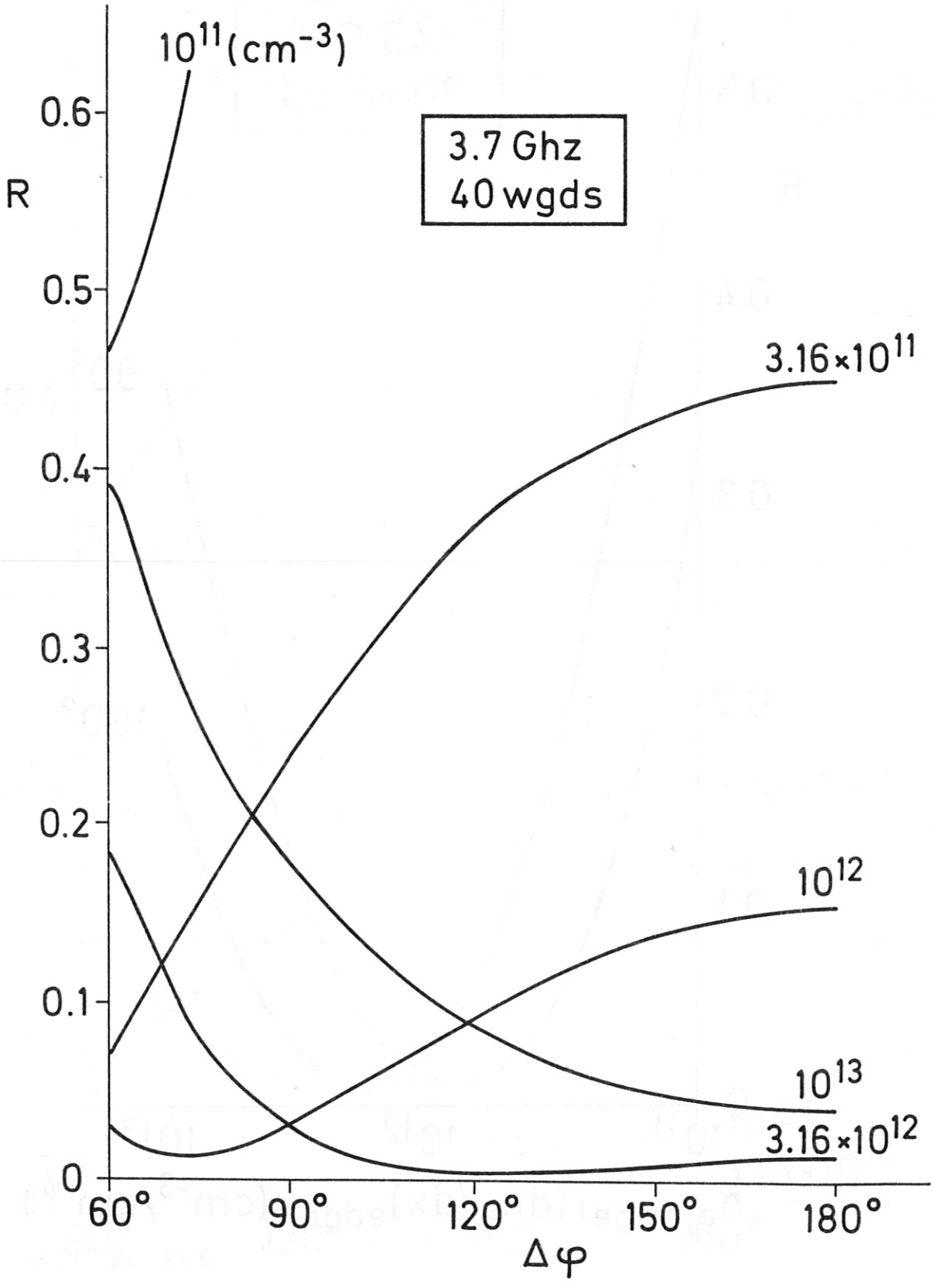

Fig. V.7: Reflection coefficient for the 3.7 GHz system versus grill phasing.

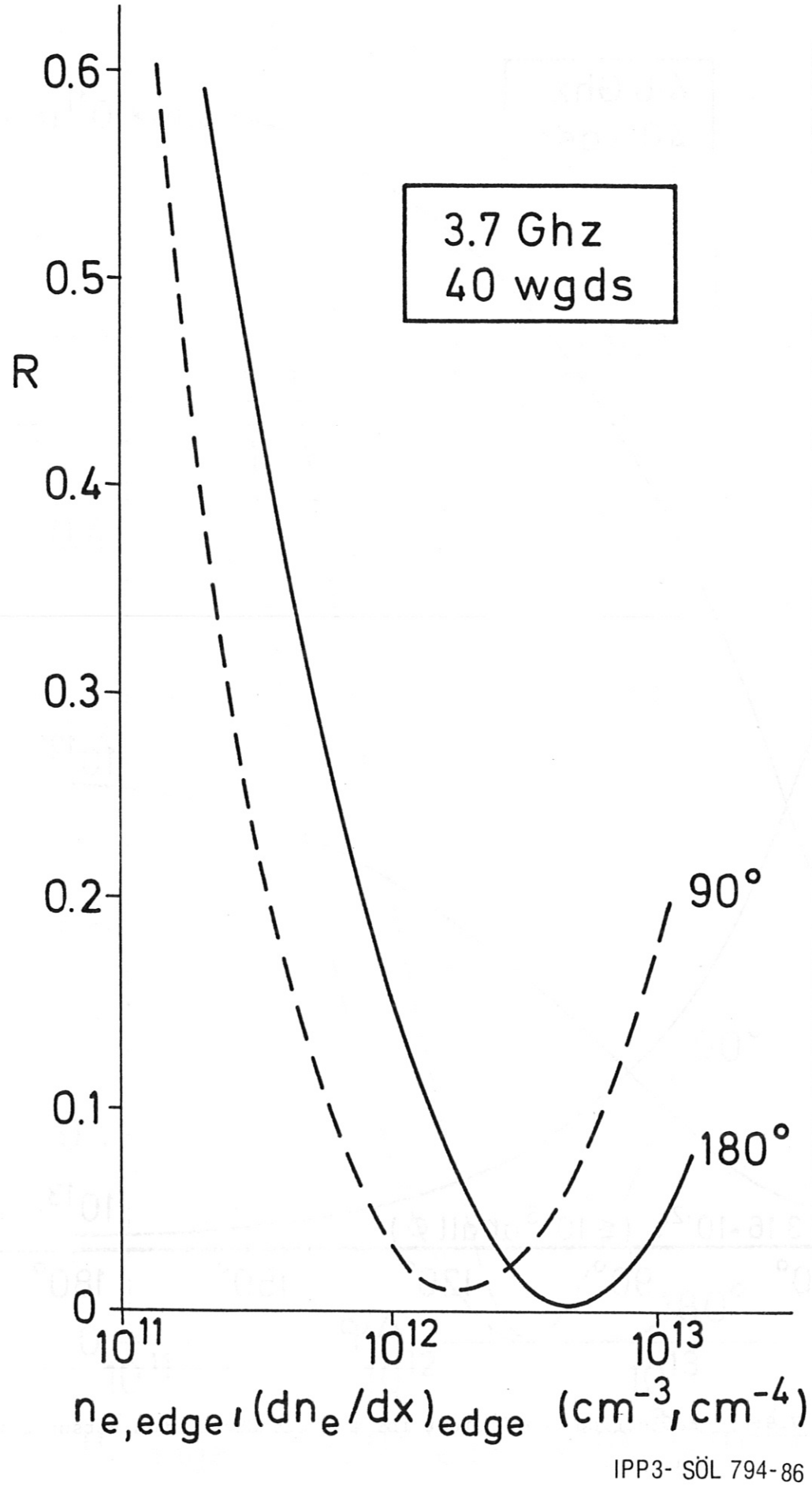

Fig. V.8: Reflection coefficient for the 3.7 GHz system versus edge density and density gradient.

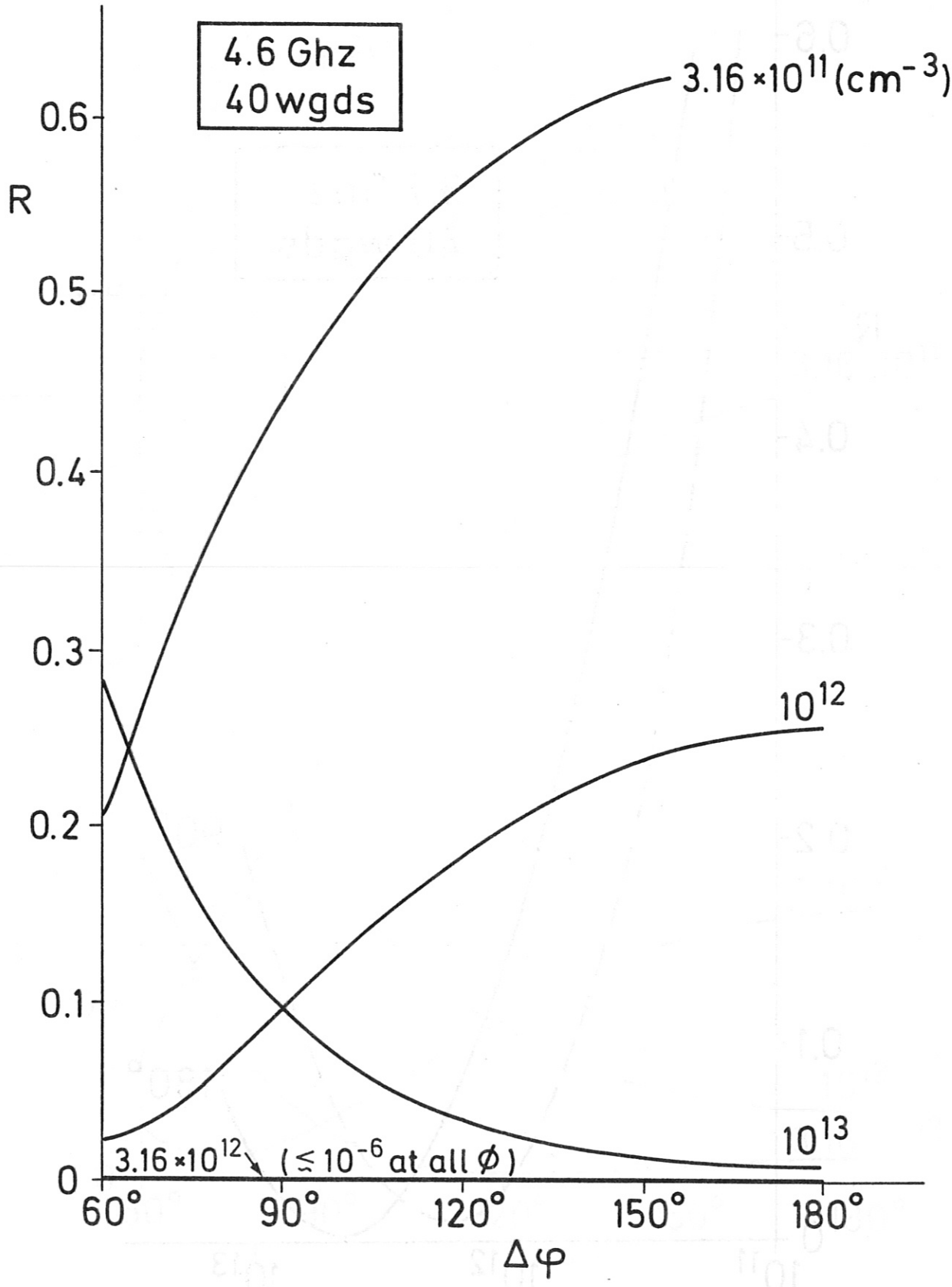

Fig. V.9: Reflection coefficient for the 4.6 GHz system versus grill phasing.

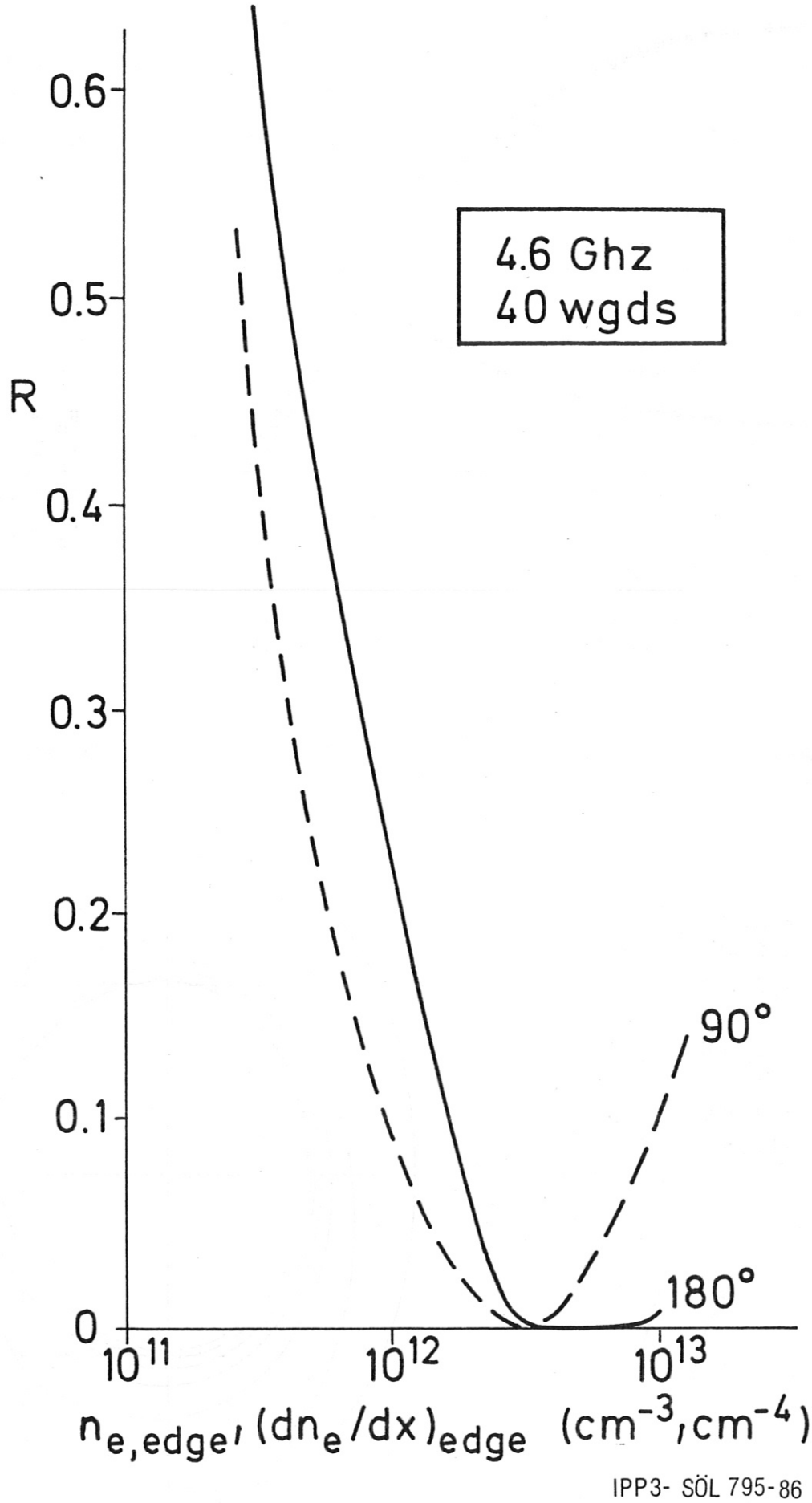

Fig. V.10: Reflection coefficient for the 4.6 GHz system versus edge density and density gradient.

IPP-CRAY MZB017 2 2-03 02.04.86 11:35:35

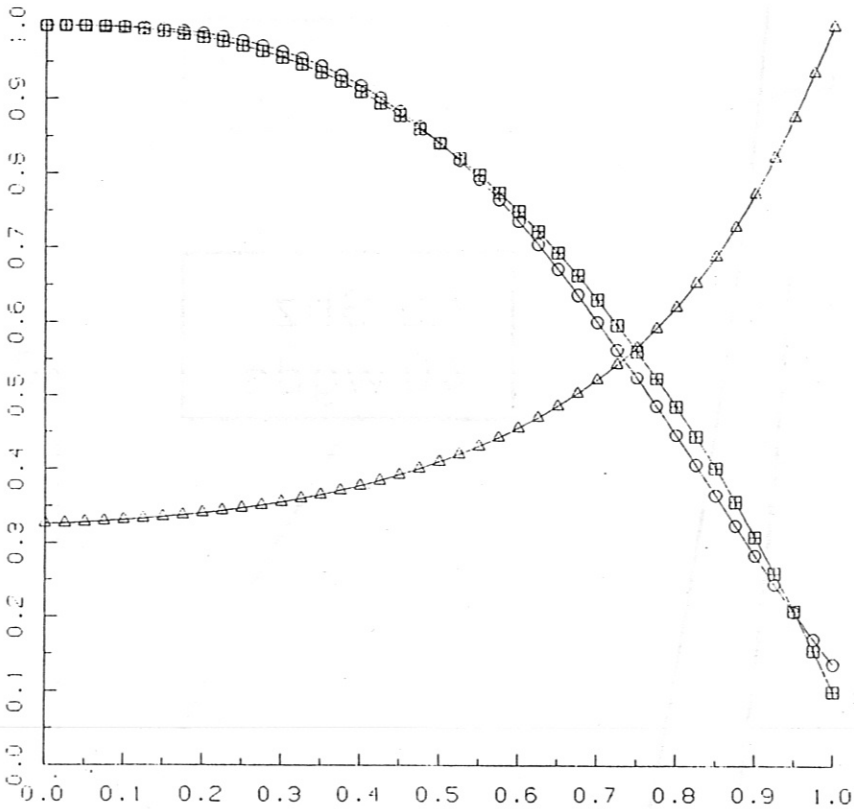

PROFILES

N_e

N_0 = 0.40 10^{14}

T_e

T_{e0} = 3.50 Kev

T_i

T_{i0} = 2.55 Kev

$\Omega(r)$

$\Omega(a)$ = 2.78

R_o = 2.95 m

I_P = 3.5 MA

B_t = 2.3 T

f_o = 2.45 GHz

IPP-CRAY MZB017 3 J2-03 02.04.86 11:35:35

N_z = 2.000
N_z = 2.400
N_z = 2.800
N_z = 3.200
N_z = 3.600
N_z = 4.000
N_z = 4.400
ΔS = 10.00

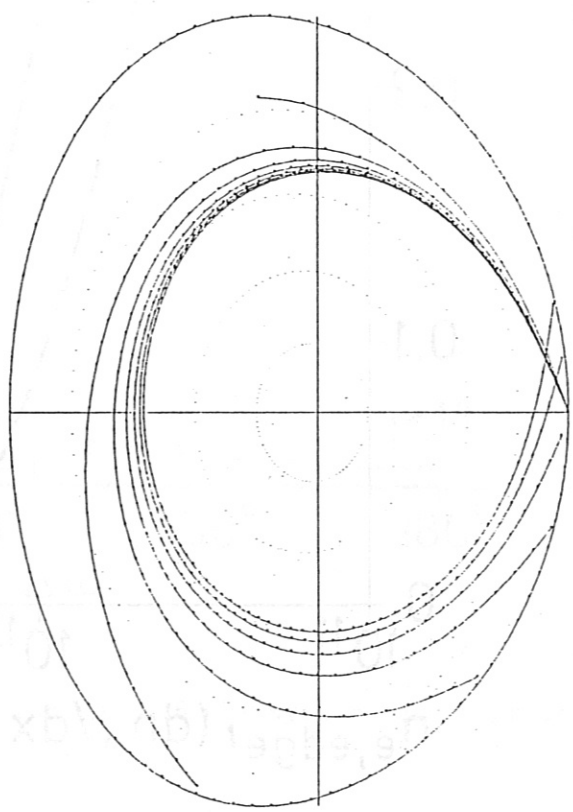

Fig. V.11: Plasma profiles and ray-tracing results for I_p = 3.5 MA, B_t = 2.3 T with f_o = 2.45 GHz, side launch.

IPP-CRAY M2B017 5 J2-03 02.04.86 11:35:37

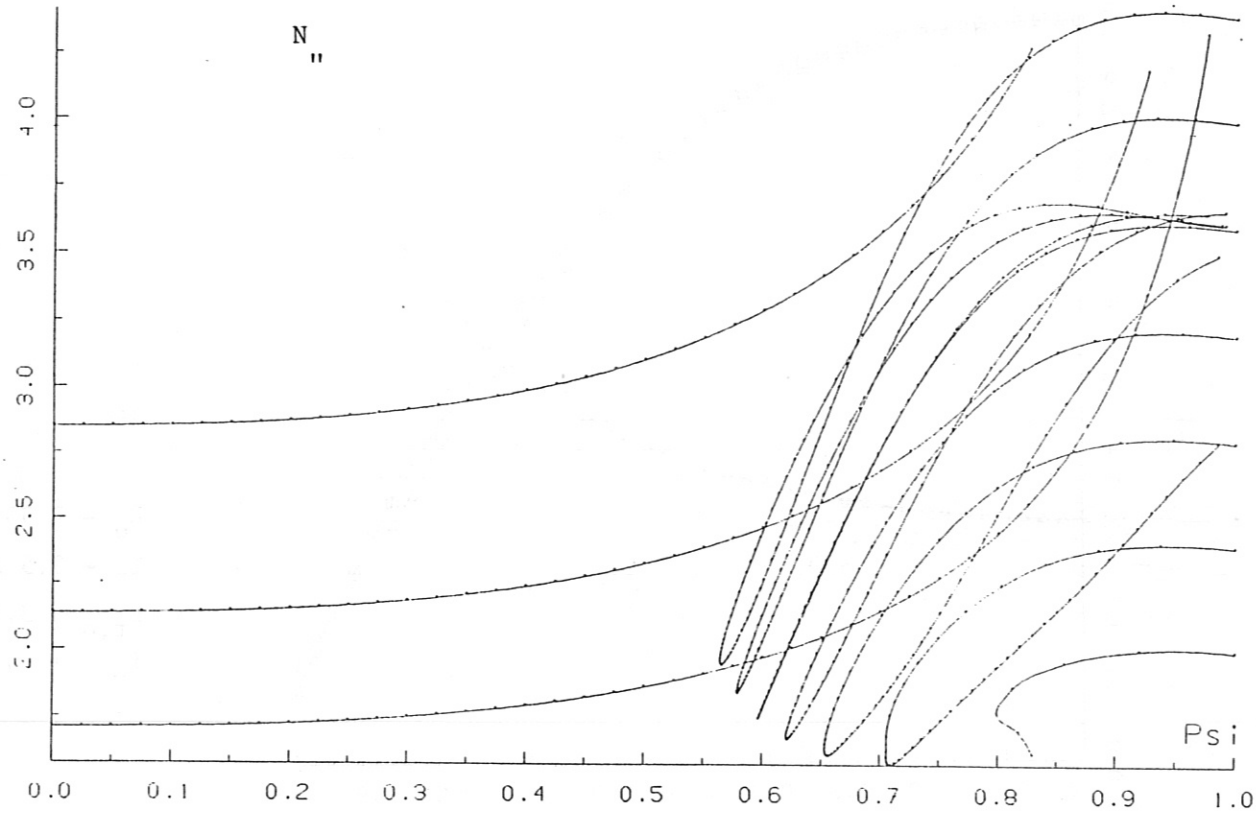

IPP-CRAY M2B017 4 J2-03 02.04.86 11:35:36

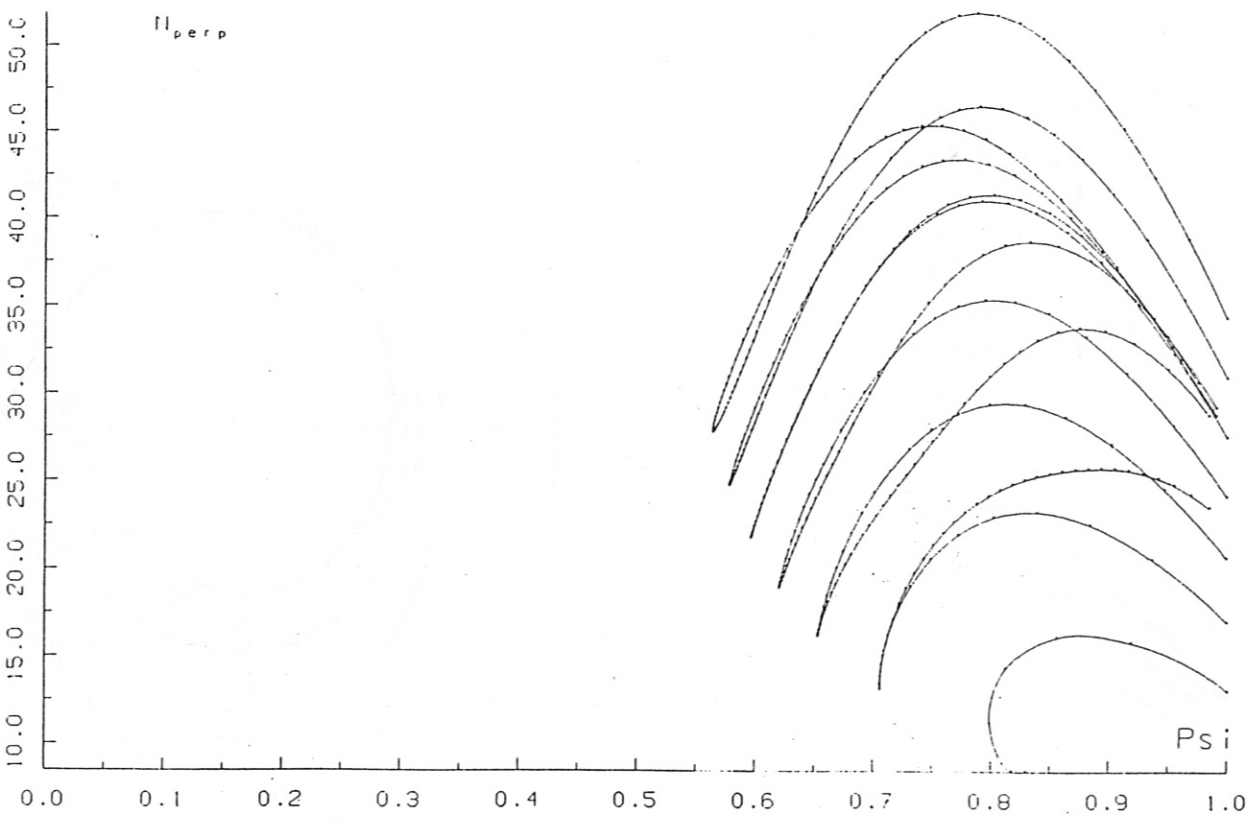

Fig. V.12: $N_{\parallel}$ and $N_{\perp}$ for parameters of Fig. V.11.

IPP-CRAY MZB036 2 J2-03 03.04.86 18:30:12

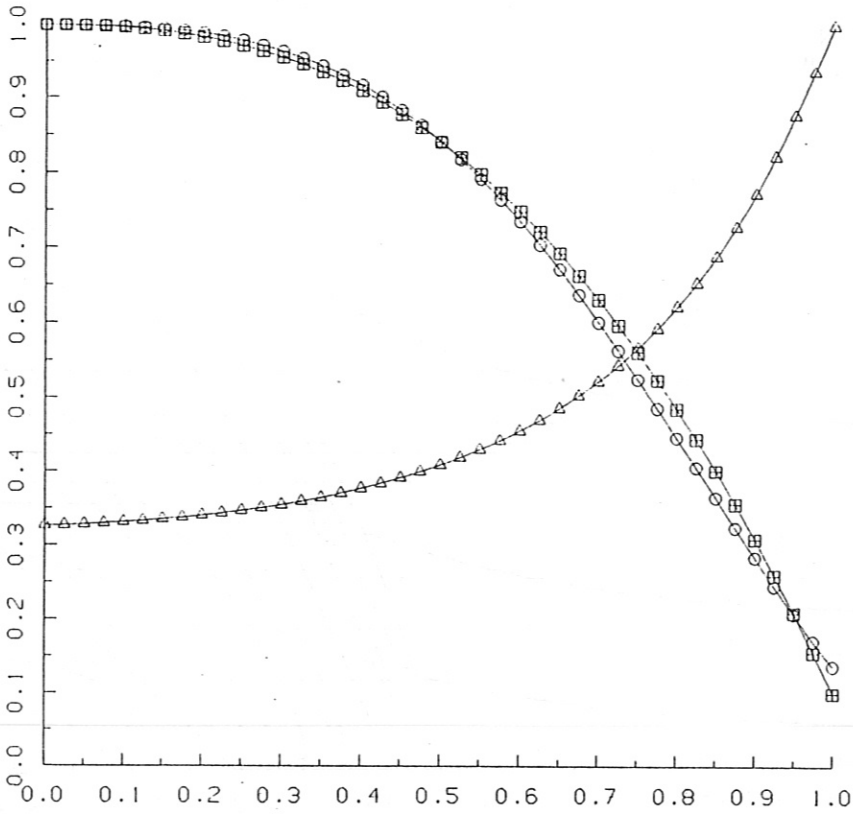

PROFILES

N_e

N_0 = 0.40 10^{14}

T_e

T_{e0} = 2.50 Kev

T_i

T_{i0} = 2.50 Kev

Q(r)

Q(a) = 4.10

R_o = 2.95 m

I_P = 3.5 MA

$B_{t,o}$ = 3.4 T

f_o = 2.45 GHz

IPP-CRAY MZB036 3 J2-03 03.04.86 18:30:12

N_z = 2.000
N_z = 2.400
N_z = 2.800
N_z = 3.200
N_z = 3.600
N_z = 4.000
N_z = 4.400
ΔS =10.00

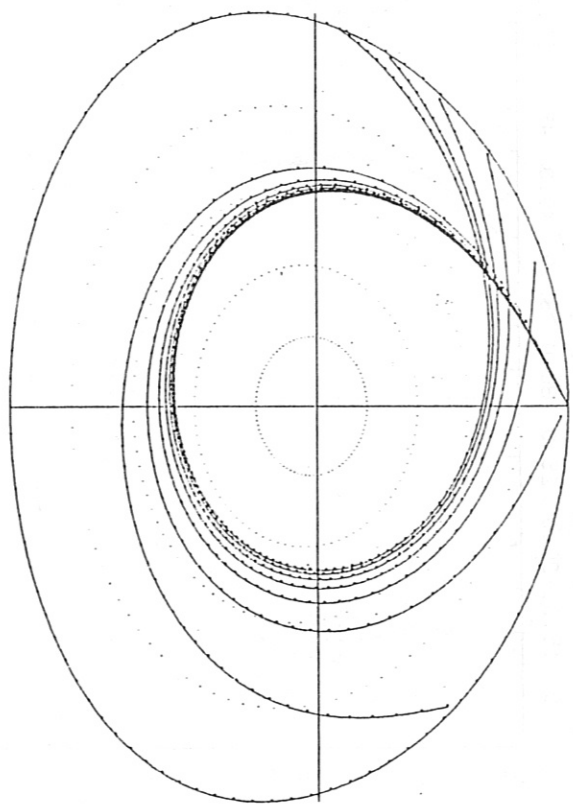

Fig. V.13: Plasma profiles and ray tracing results for I_p = 3.5 MA, B_{to} = 3.4 T with f_o = 2.45 GHz, side launch.

IPP-CRAY MZ6036 5 J2-03 03.04.86 18:30:27

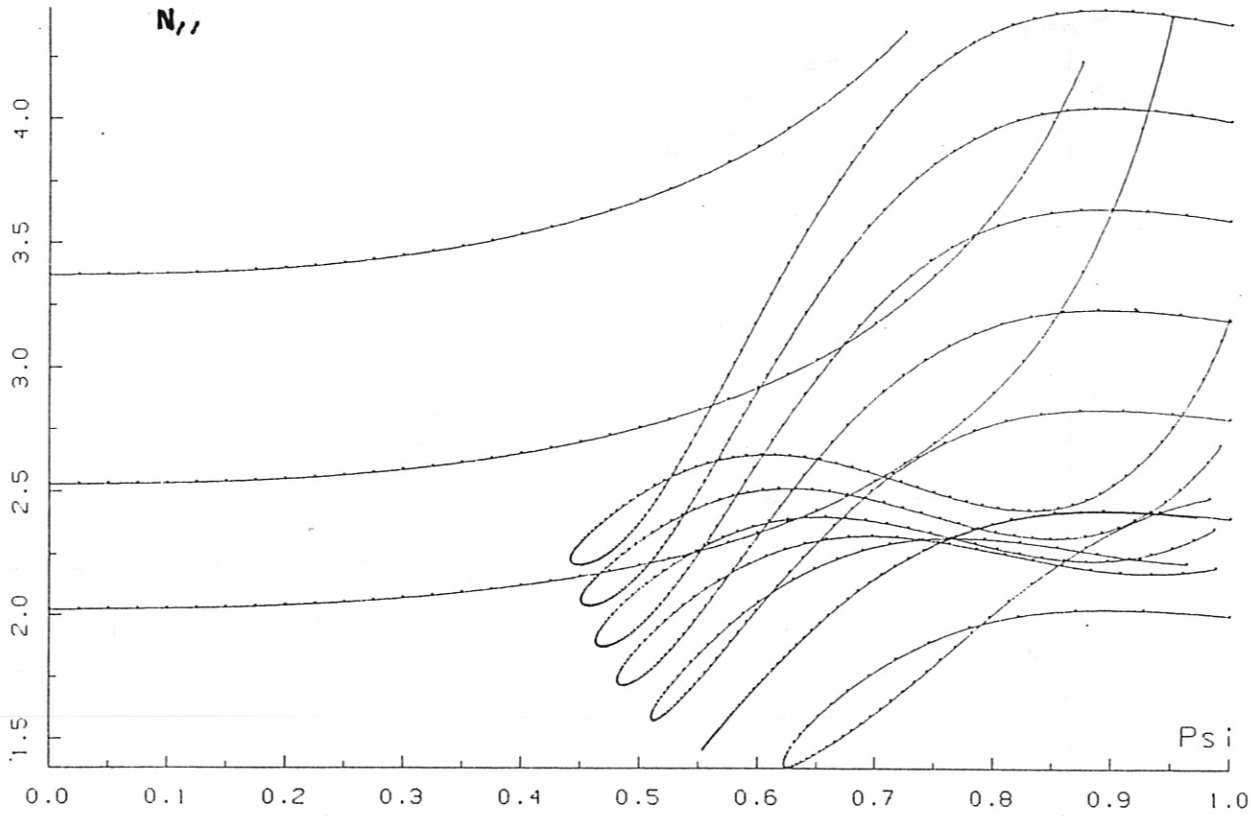

IPP-CRAY MZ6036 4 J2-03 03.04.86 18:30:13

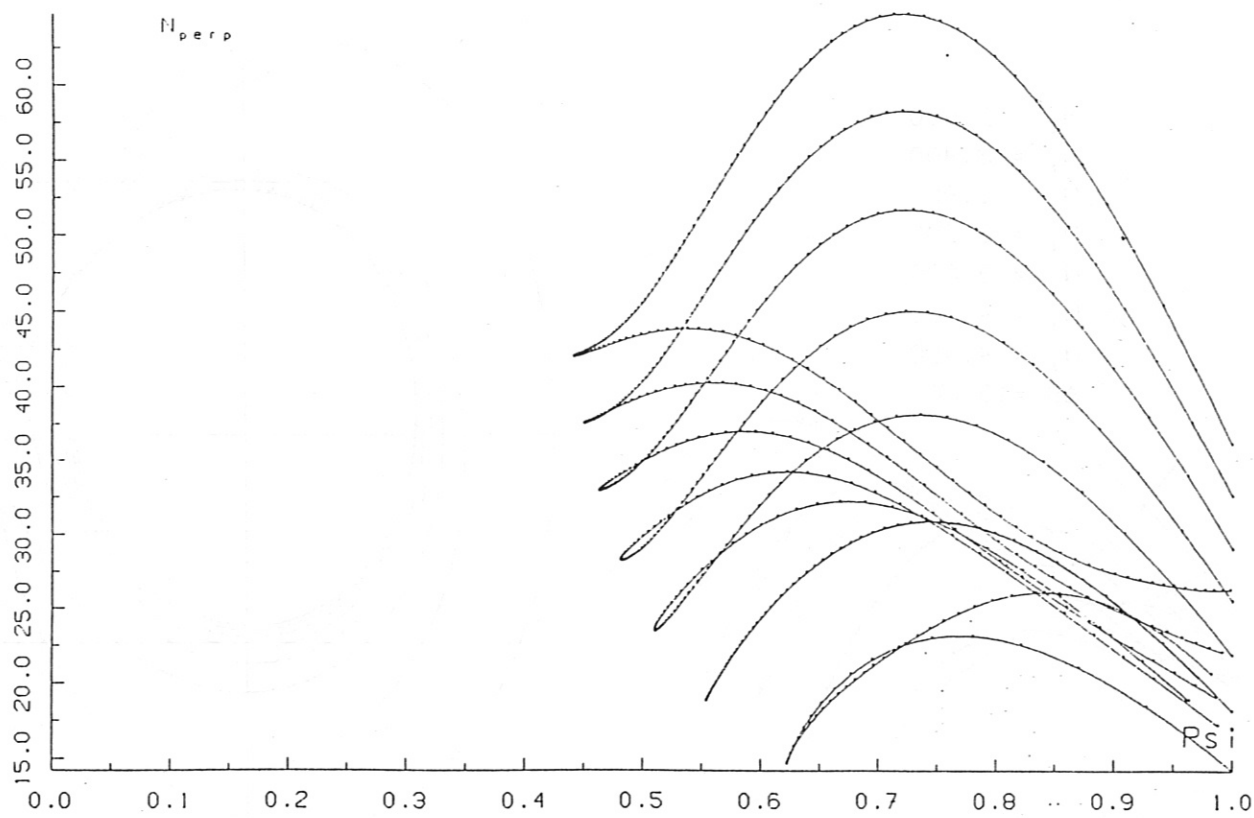

Fig. V.14: $N_{\parallel}$ and $N_{\perp}$ for parameters of Fig. V.13.

IPP-CRAY MZB037 2 J2-03 03.04.86 18:32:54

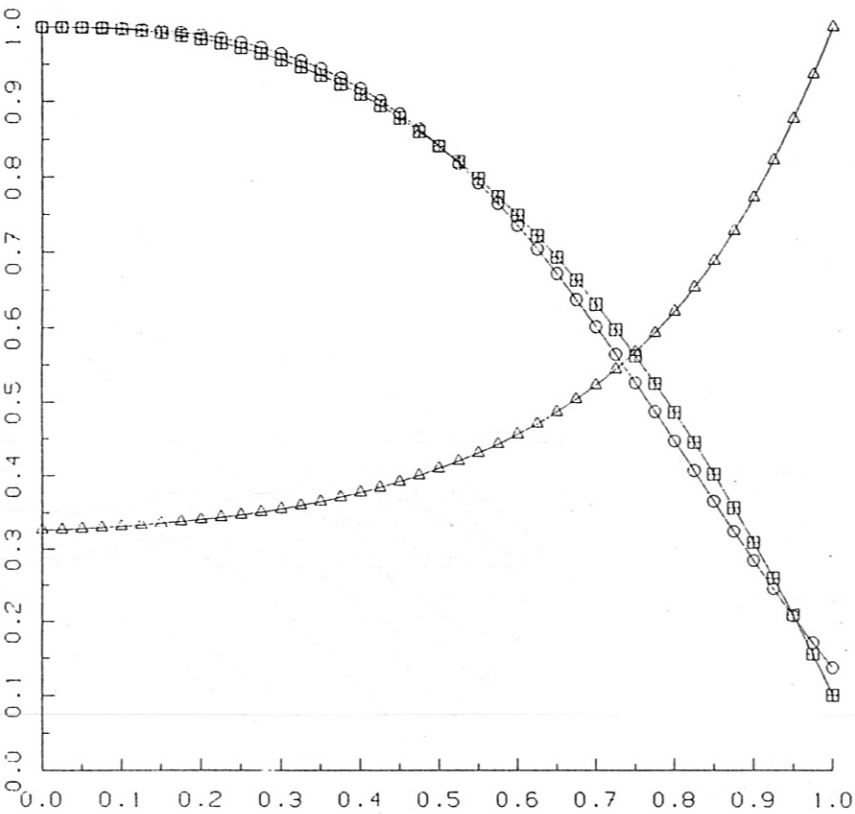

PROFILES

N_e

N_0 = 0.40 10^{14}

T_e

T_{e0} = 2.50 Kev

T_i

T_{i0} = 2.50 Kev

Q(r)

Q(a) = 2.87

R_o = 2.95 m

I_P = 5 MA

$B_{t,o}$ = 3.4 T

f_o = 2.45 GHz

IPP-CRAY MZB037 3 J2-03 03.04.86 18:32:54

N_z = 2.000
N_z = 2.400
N_z = 2.800
N_z = 3.200
N_z = 3.600
N_z = 4.000
N_z = 4.400
ΔS =10.00

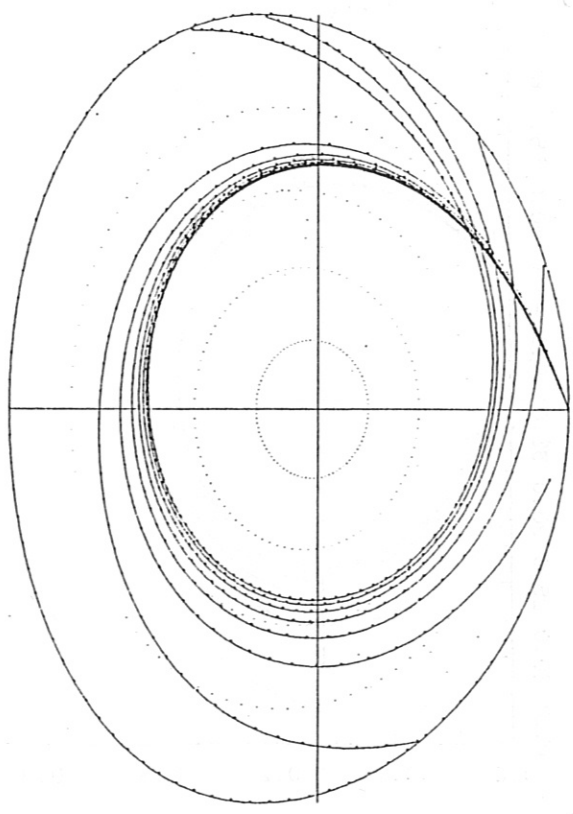

Fig. V.15: Plasma profiles and ray tracing results for I_p = 5 MA, B_{to} = 3.4 T with f_o = 2.45 GHz, side launch.

IPP-CRAY MZB037 5 J2-03 03.04.86 18:32:56

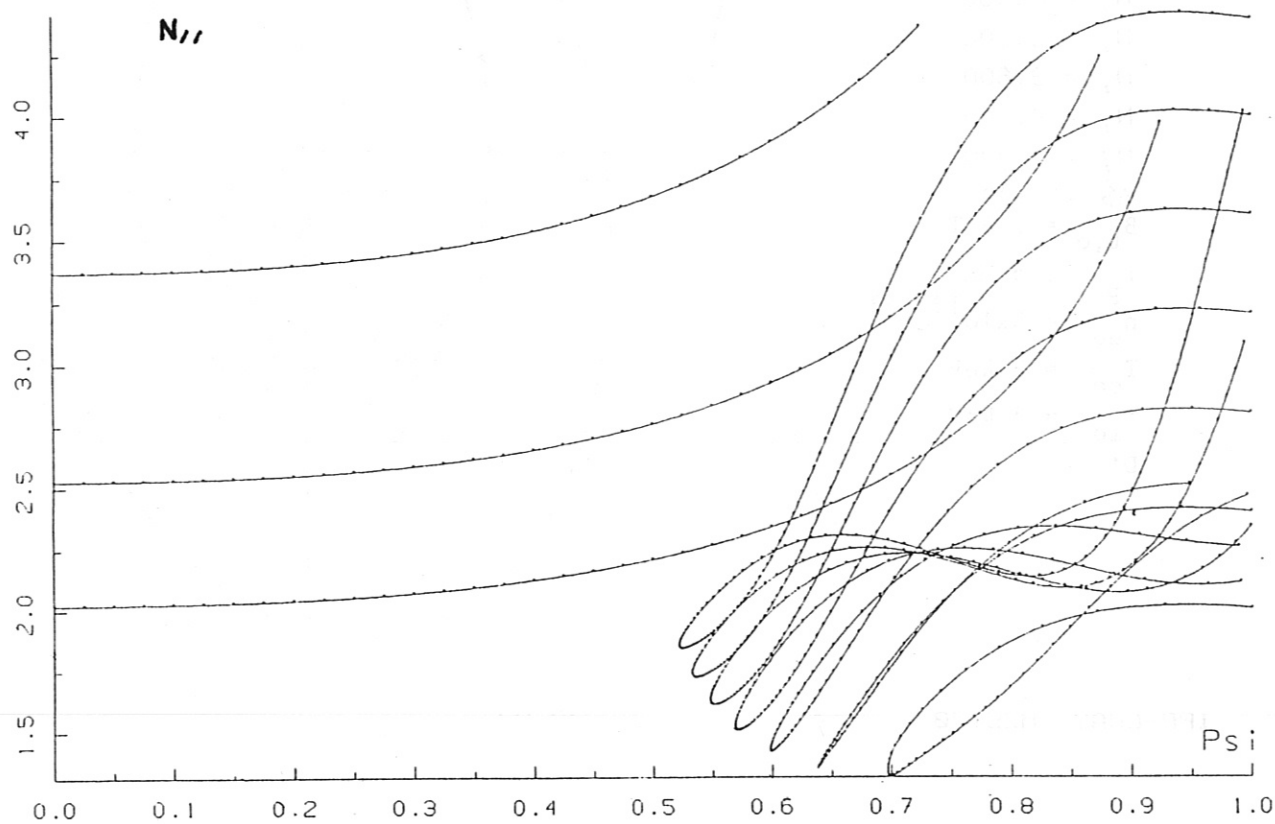

IPP-CRAY MZB037 4 J2-03 03.04.86 18:32:55

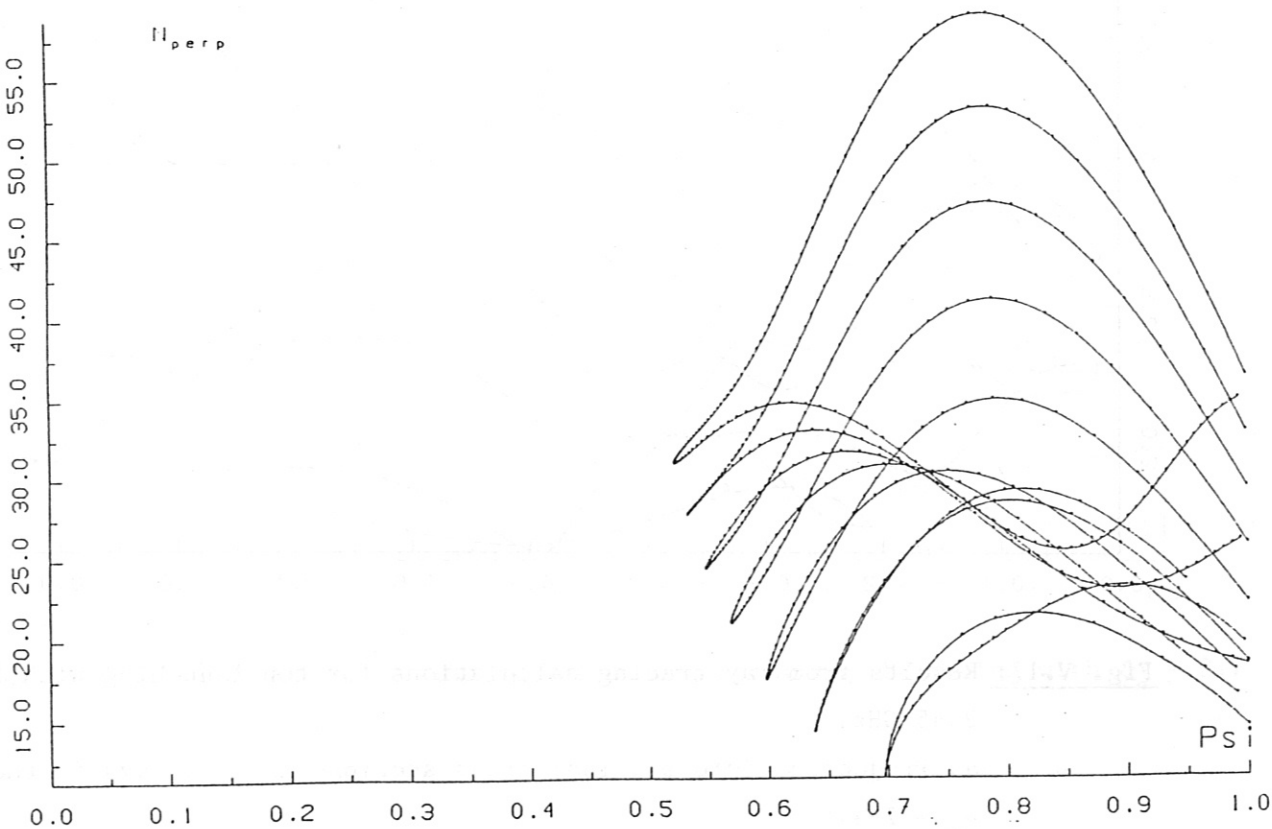

Fig. V.16: $N_{\parallel}$ and $N_{\perp}$ for parameters of Fig. V.15.

f_o = 2.45 GHz
N_z = 2.000
N_z = 2.400
N_z = 2.800
N_z = 3.200
N_z = 3.600
N_z = 4.000
N_z = 4.400
ΔS = 10.00
$B_{t,o}$ = 3.4 T
I_P 3.5 MA
n_{eo} = 5×10^{13} cm^{-3}
T_{eo} = 2 keV
T_{io} = 2 keV
D^+

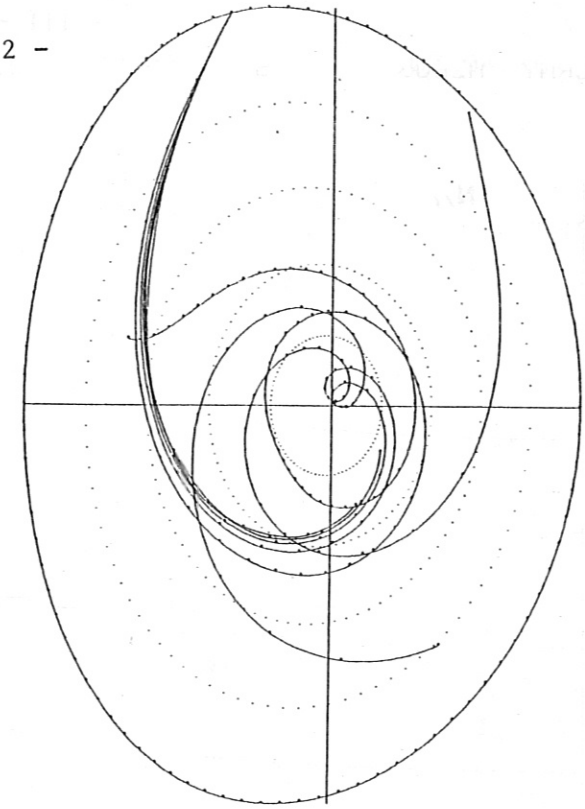

IPP-CRAY MZB170 4 J2-03

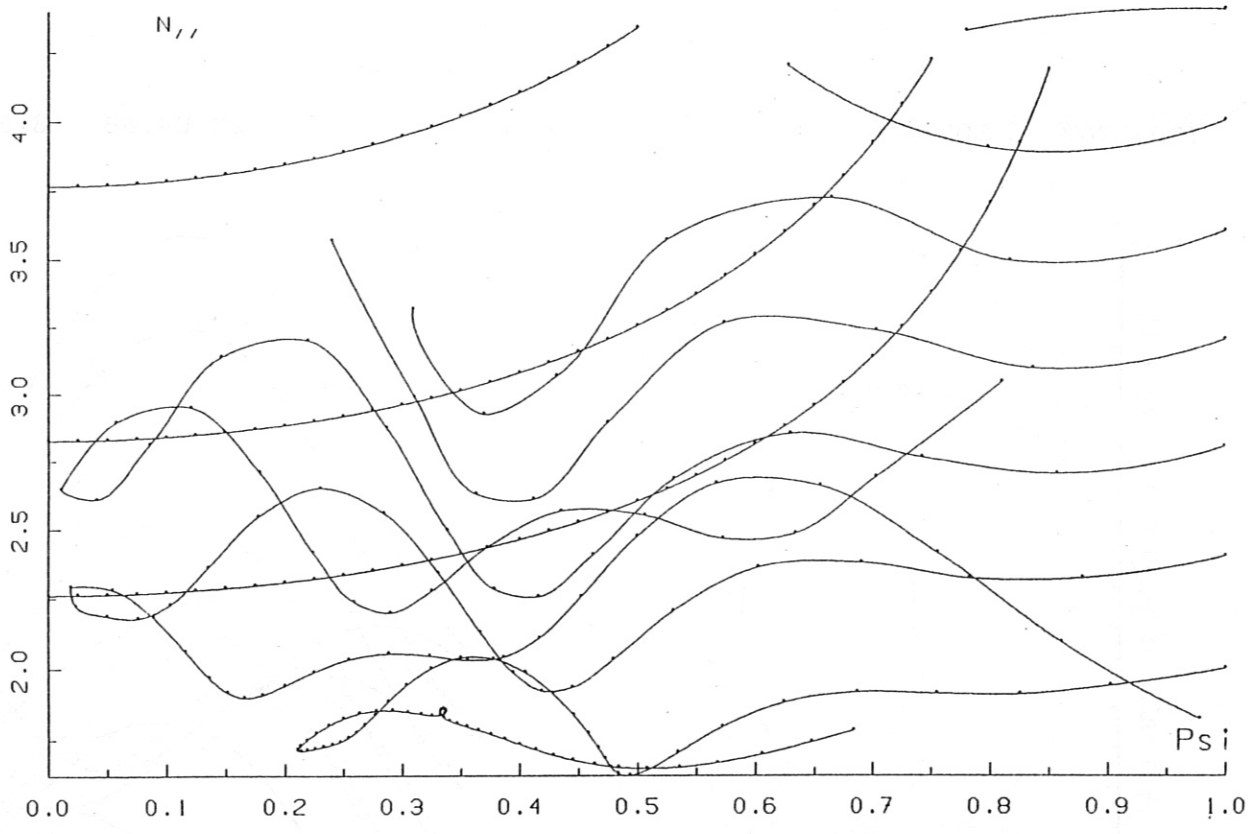

Fig. V.17: Results from ray tracing calculations for top launching with f_o = 2.45 GHz.

a) Projection into poloidal cross section plane of rays in the range $N_{||}$ = 2-4.4.

b) Radial variation of $N_{||}$.

f_o = 3.7 GHz
N_z = 2.000
N_z = 2.400
N_z = 2.800
N_z = 3.200
N_z = 3.600
N_z = 4.000
N_z = 4.400
ΔS = 10.00
$B_{t,o}$ = 3.4 T
I_P = 3.5 MA
n_{eo} = 5×10^{13} cm^{-3}
T_{eo} = 2 keV
T_{io} = 2 keV
D^+

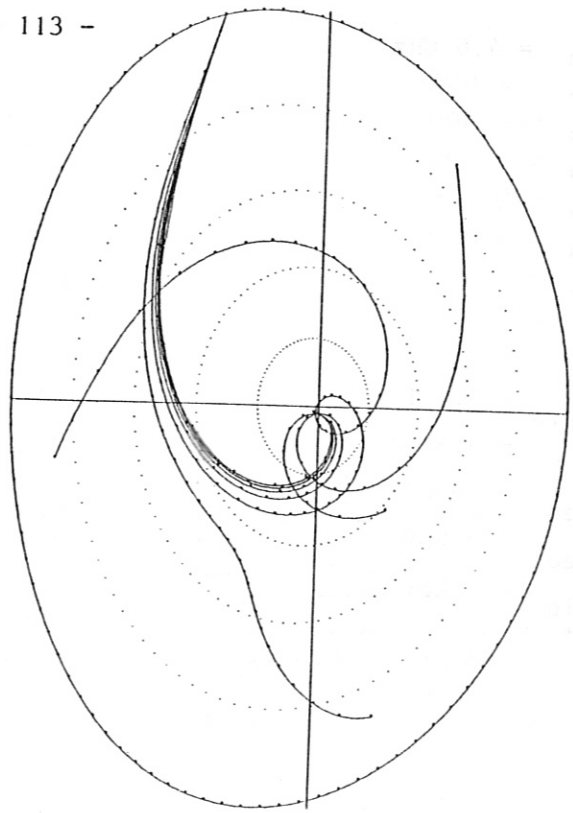

IPP-CRAY MZB163 4 J2-03

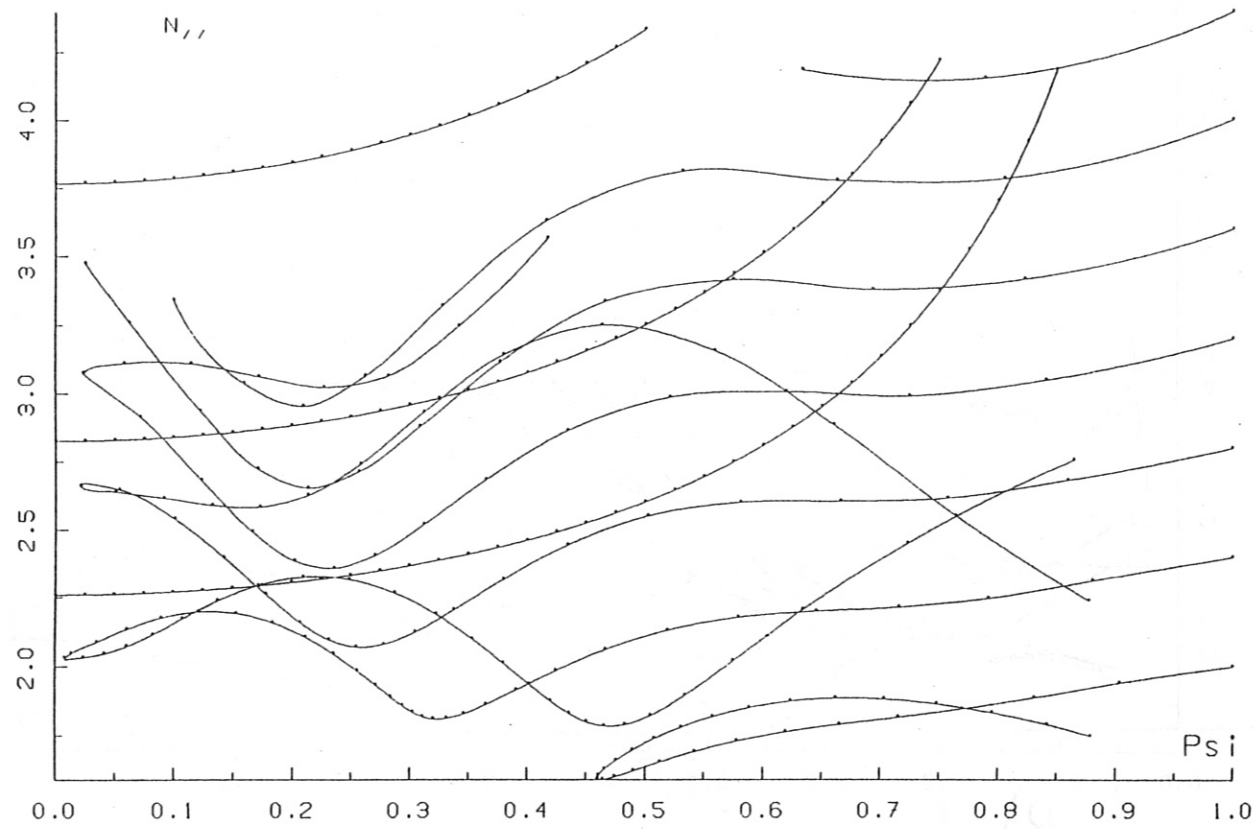

Fig. V.18: Results from ray tracing calculations for top launching with f_o = 3.7 GHz.

a) Projection into poloidal cross section plane of rays in the range $N_{//}$ = 2-4.4.

b) Radial variation of $N_{//}$.

f_o = 4.6 GHz
N_z = 2.000
N_z = 2.400
N_z = 2.800
N_z = 3.200
N_z = 3.600
N_z = 4.000
N_z = 4.400
ΔS = 10.00
$B_{t,o}$ = 3.4 T
I_P = 3.5 MA
n_{eo} = 5×10^{13} cm^{-3}
T_{eo} = 2 keV
T_{io} = 2 keV
D^+

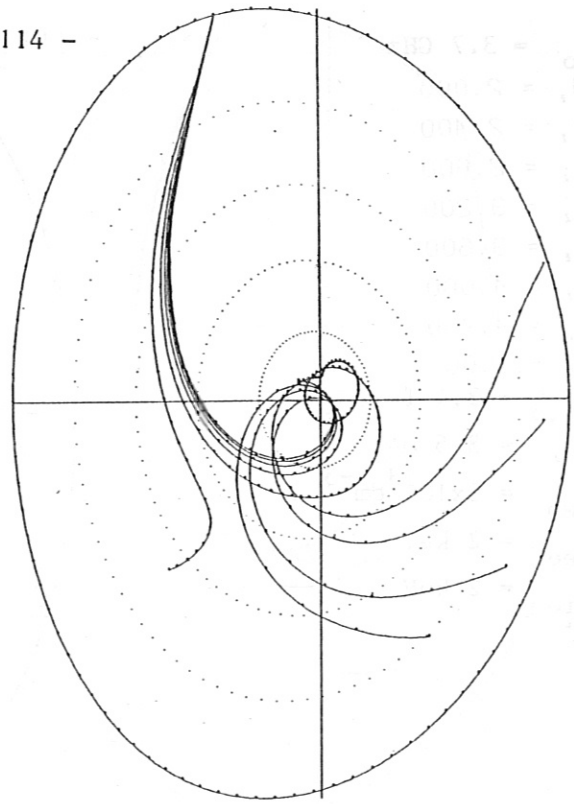

IPP-CRAY MZB160 4 J2-03

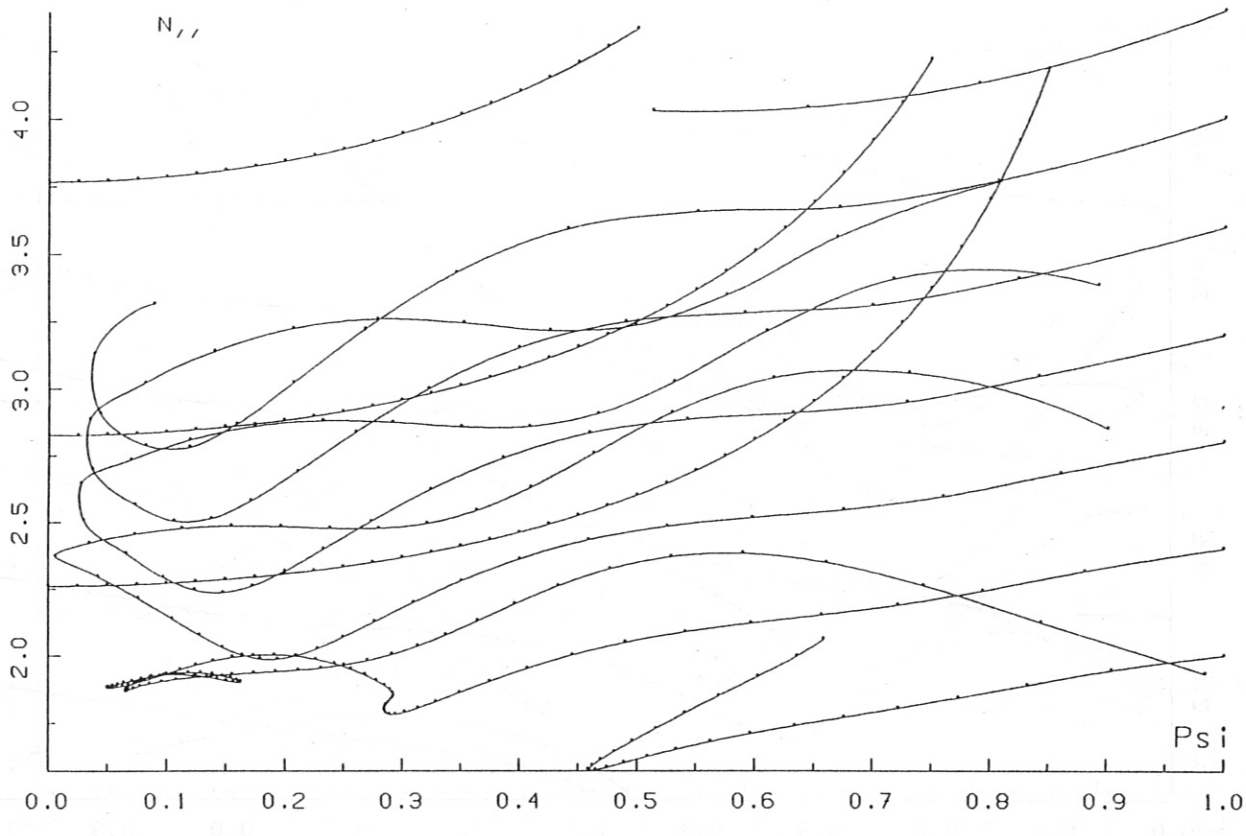

Fig. V.19: Results from ray tracing calculations for top launching with f_o = 4.6 GHz.

a) Projection into poloidal cross section plane of rays in the range $N_{||}$ = 2-4.4.

b) Radial variation of $N_{||}$.

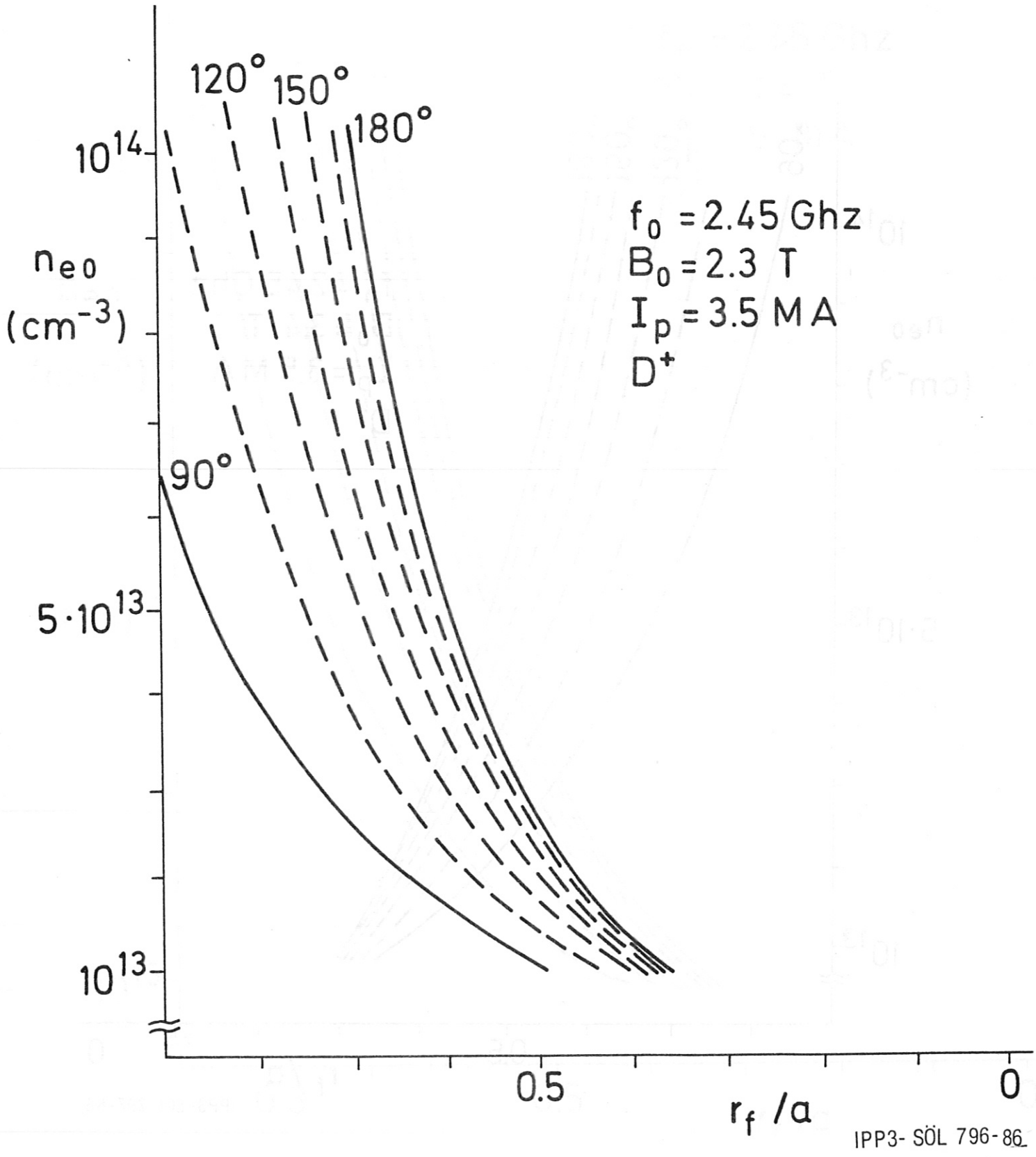

Fig. V.20: Relation between central density and innermost flux surface to which waves from with different spectra can penetrate.
f_o = 2.45 GHz, I_p = 3.5 MA, B_t = 2.3 T.

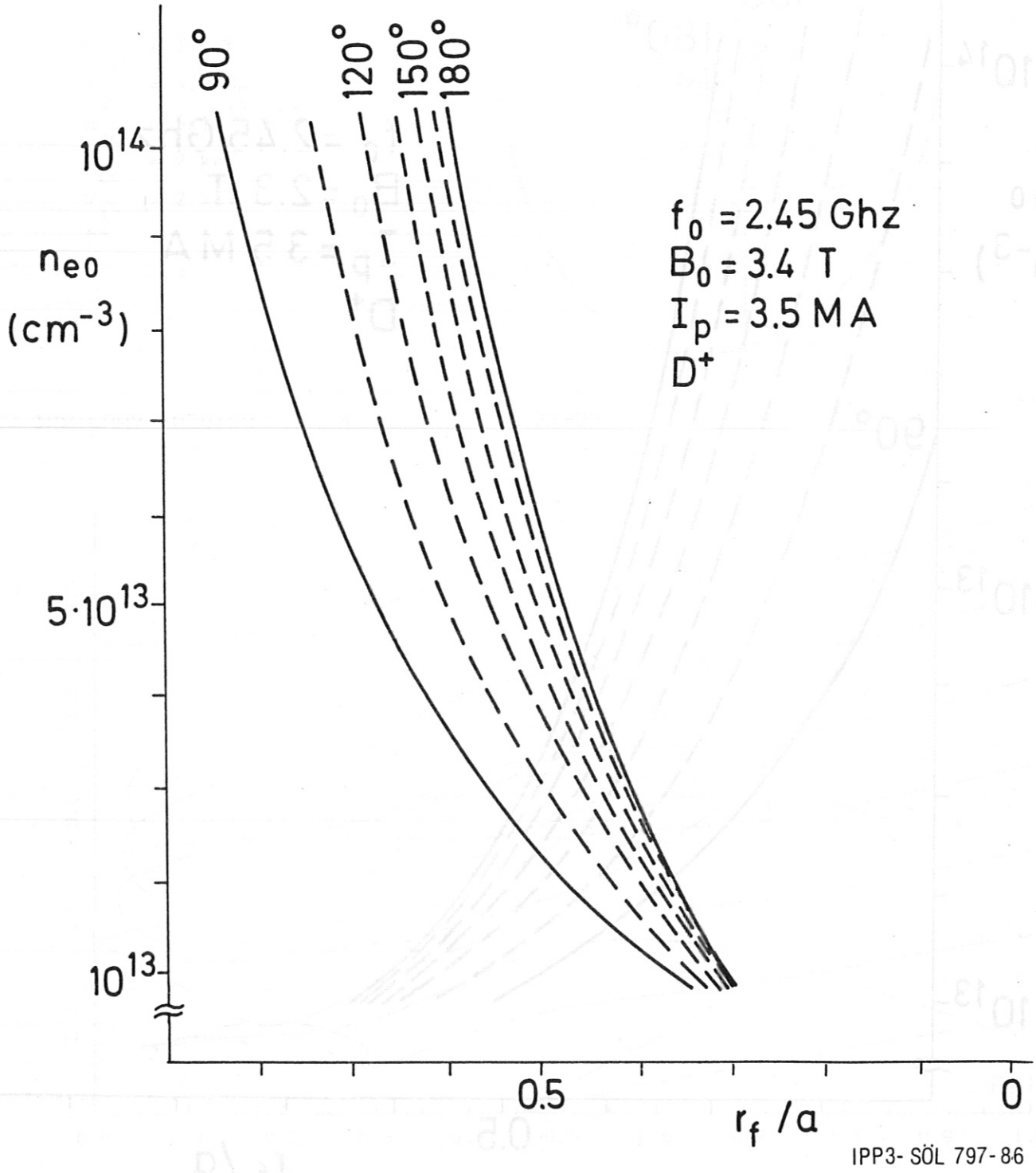

Fig. V.21: Curves as in Fig. V.17,
f_o = 2.45 GHz, I_p = 3.5 MA, B_t = 3.4 T.

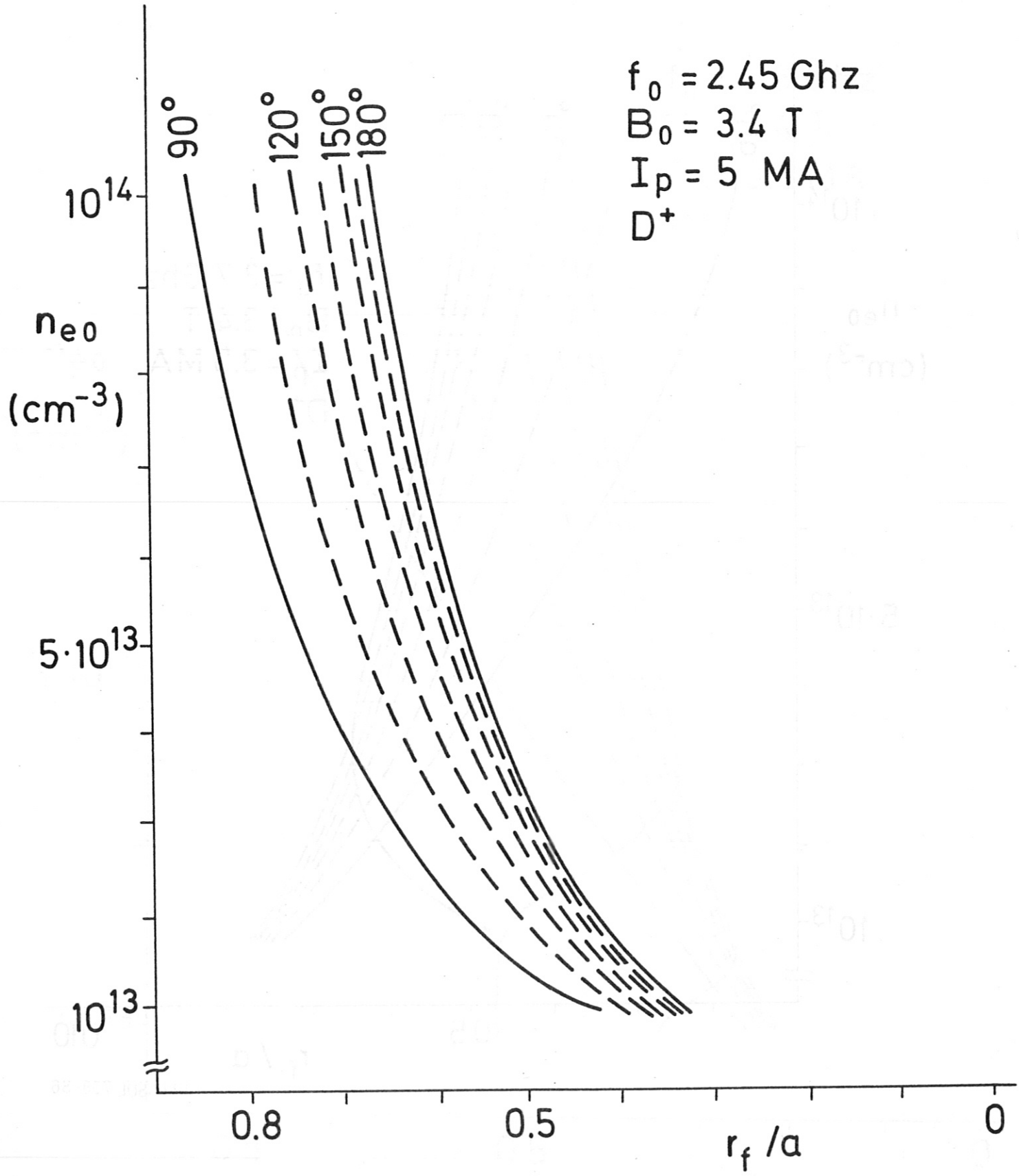

Fig. V.22: Curves as in Fig. V.17,
f_o = 2.45 GHz, I_p = 5 MA, B_t = 3.4 T.

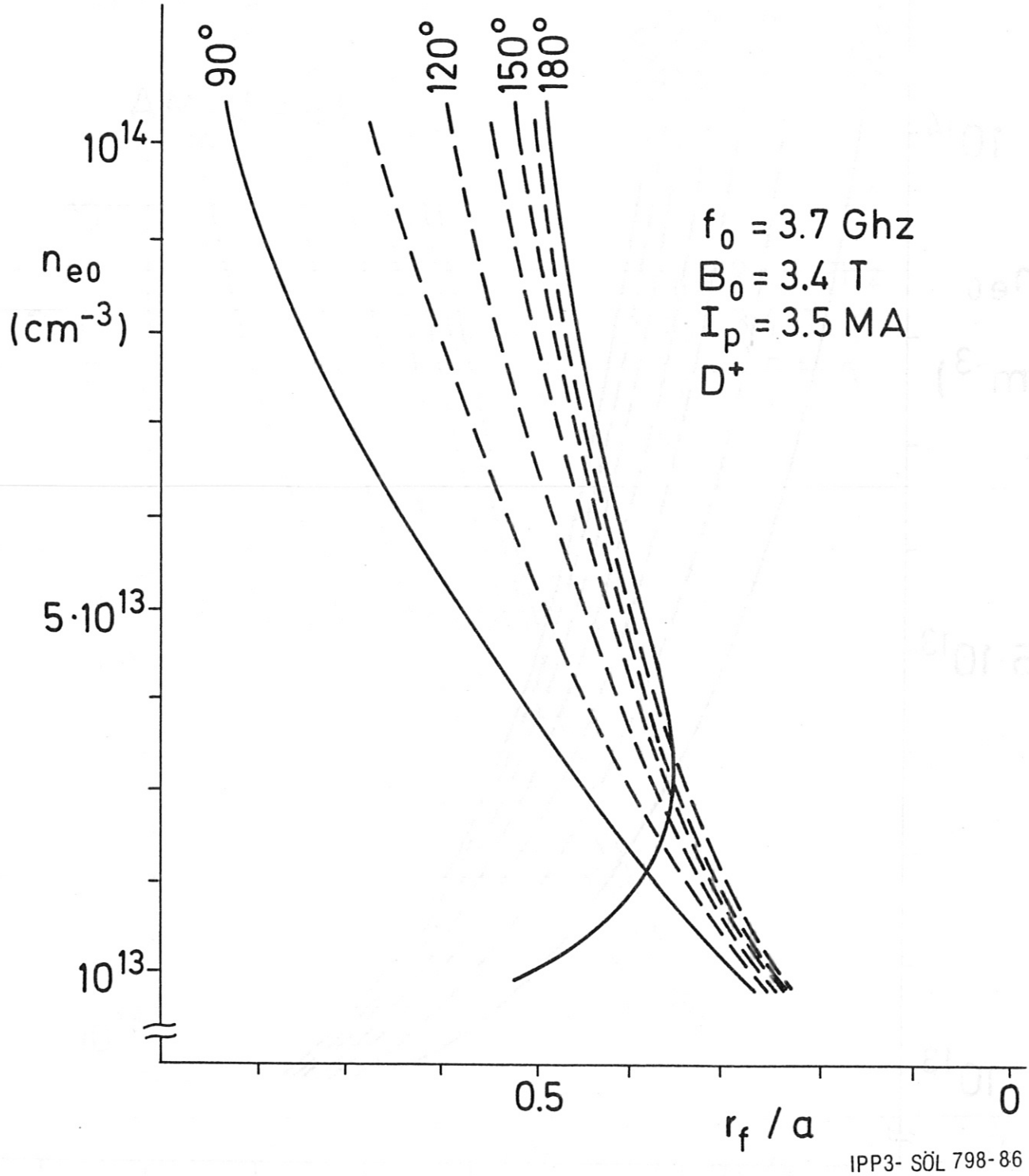

Fig. V.23: Curves as in Fig. V.17,
f_o = 3.7 GHz, I_p = 3.5 MA, B_t = 3.4 T.

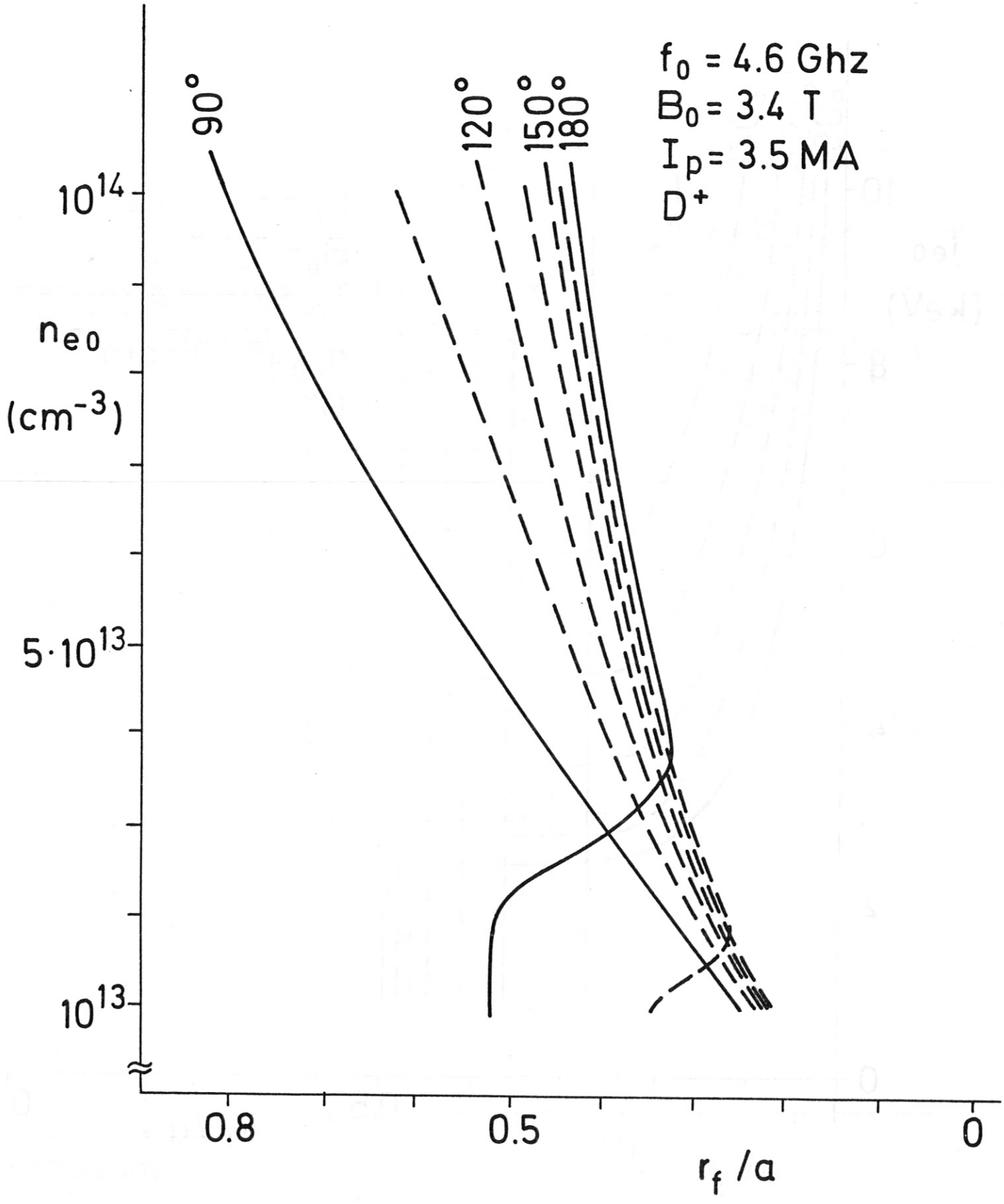

Fig. V.24: Curves as in Fig. V.17,
f_o = 4.6 GHz, I_p = 3.5 MA, B_t = 3.4 T.

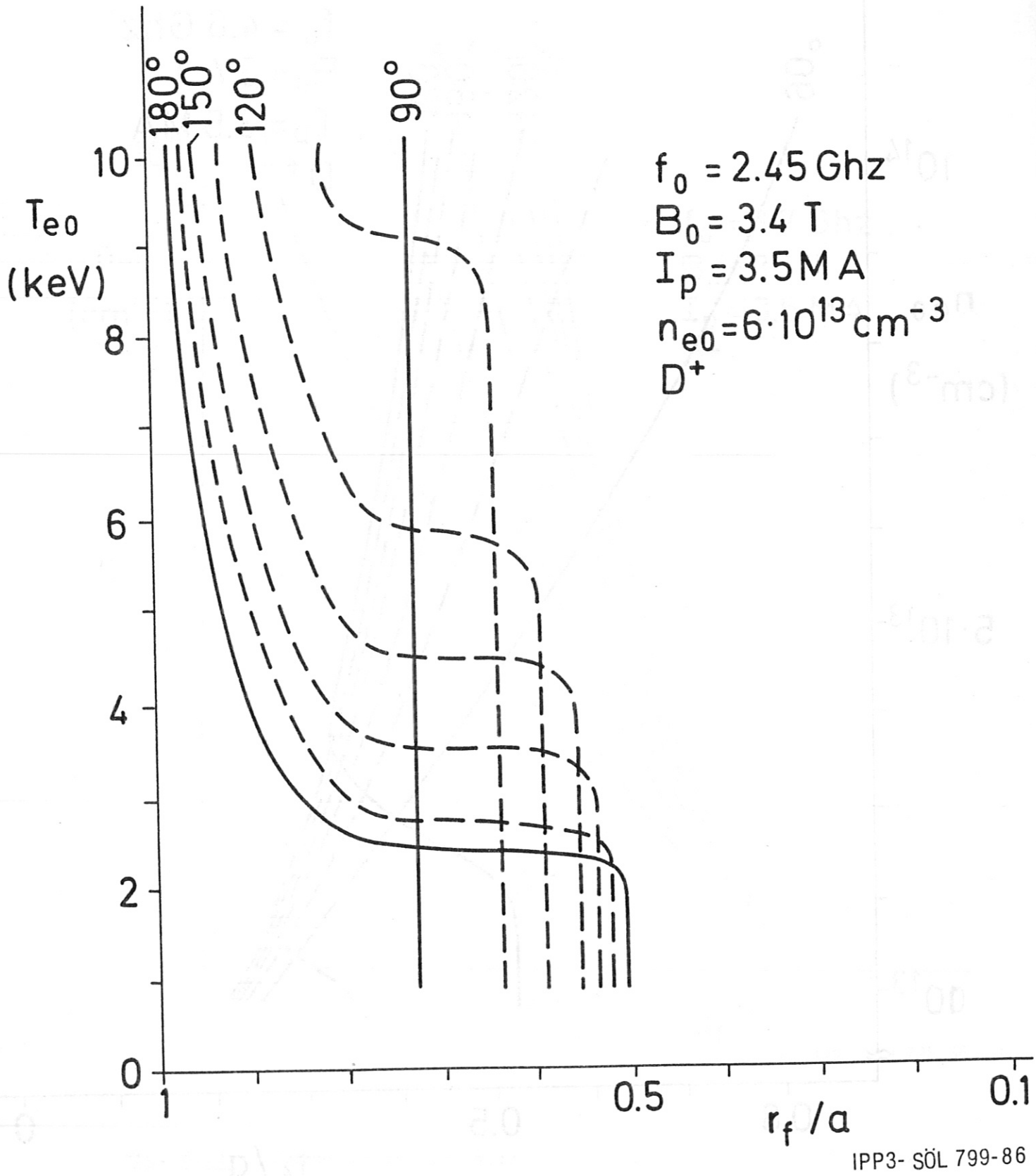

Fig. V.25: Relation between electron temperature and innermost flux surface to which waves from different spectra can penetrate. f_o = 2.45 GHz, I_p = 3.5 MA, B_t = 3.4 T.

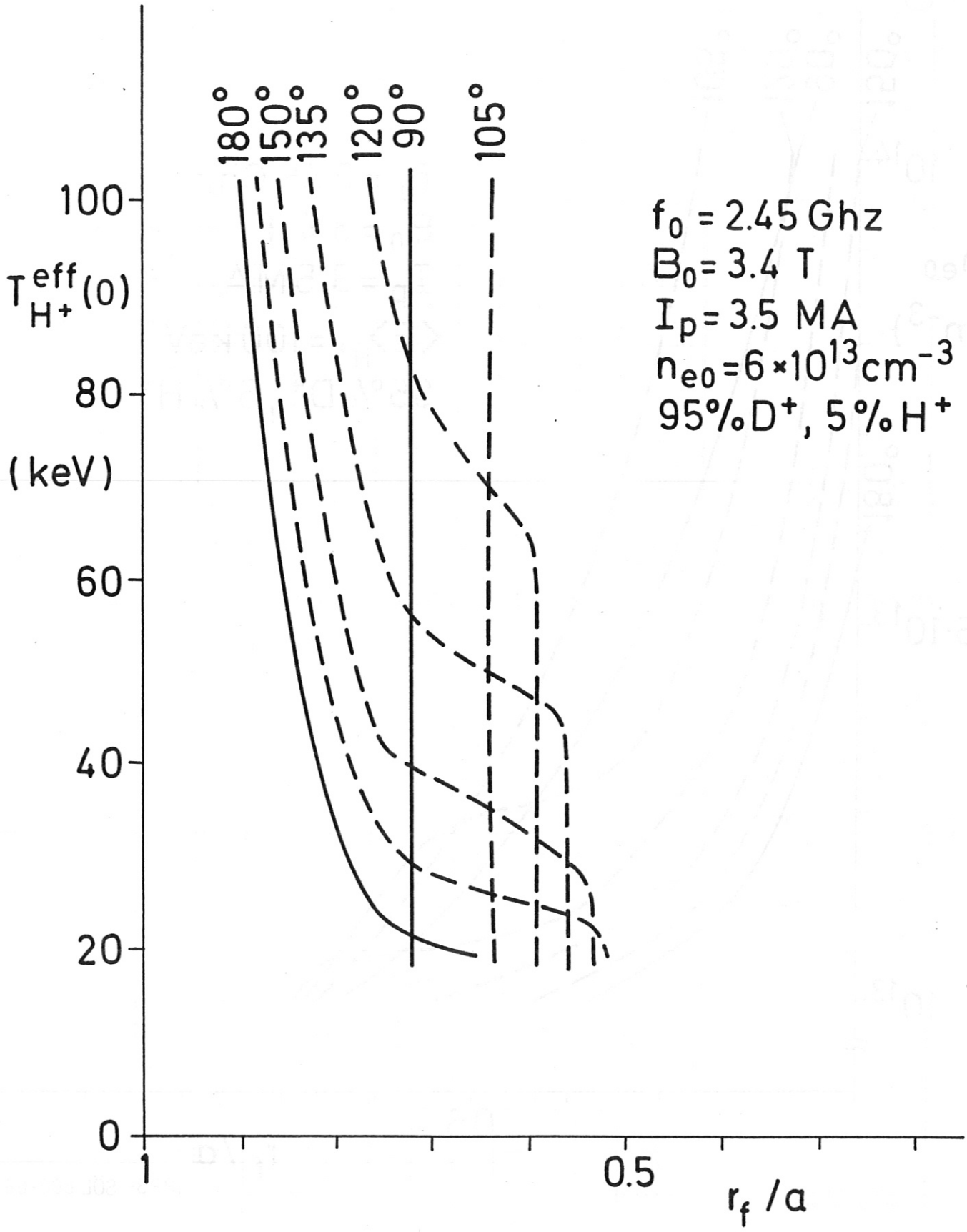

Fig. V.26: Influence of LH power absorption by a high energy ion minority with $T_{H^+}^{eff}$ on wave penetration.

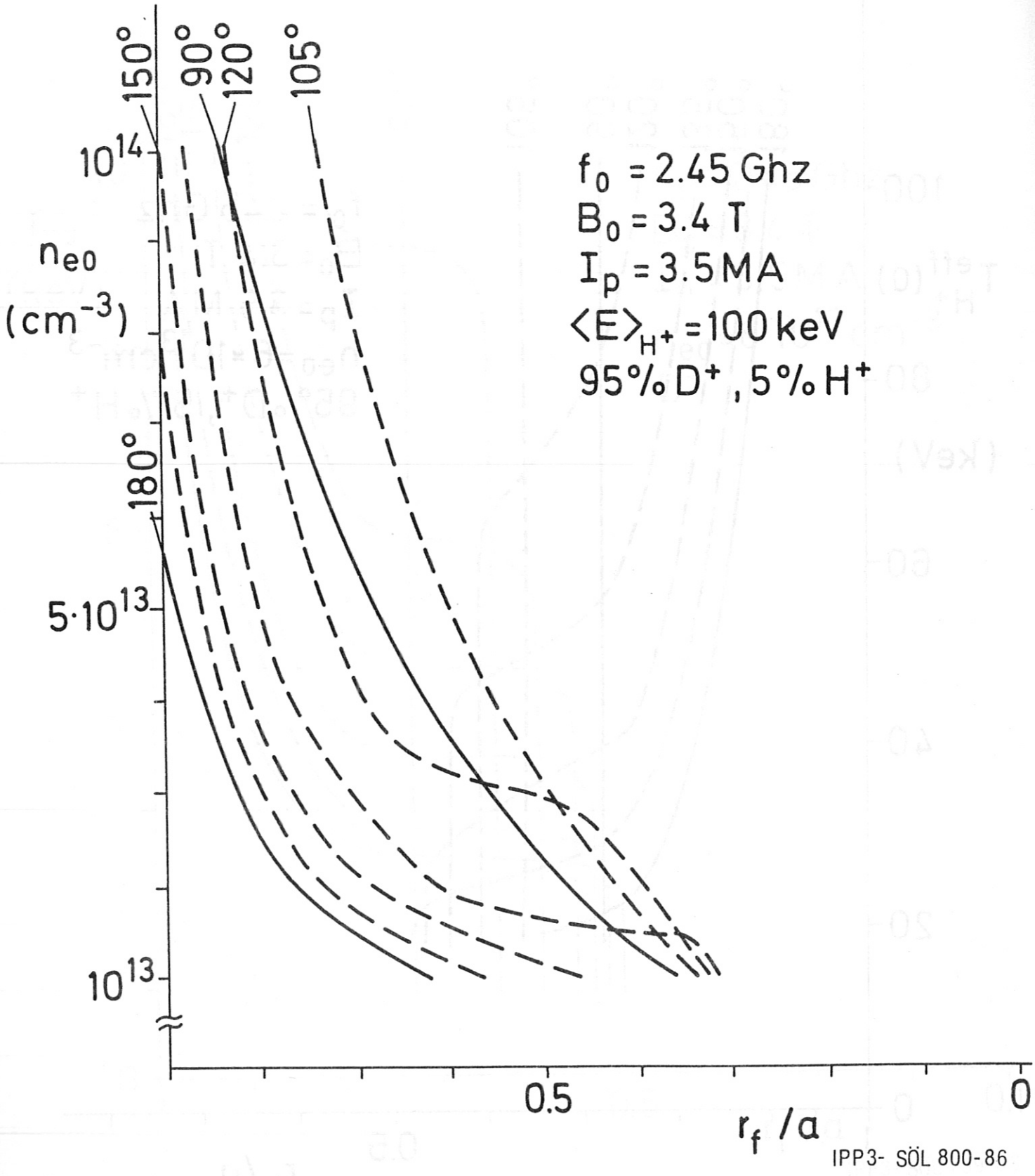

Fig. V.27: Density dependence of depletion of LH power by 100 keV H^+

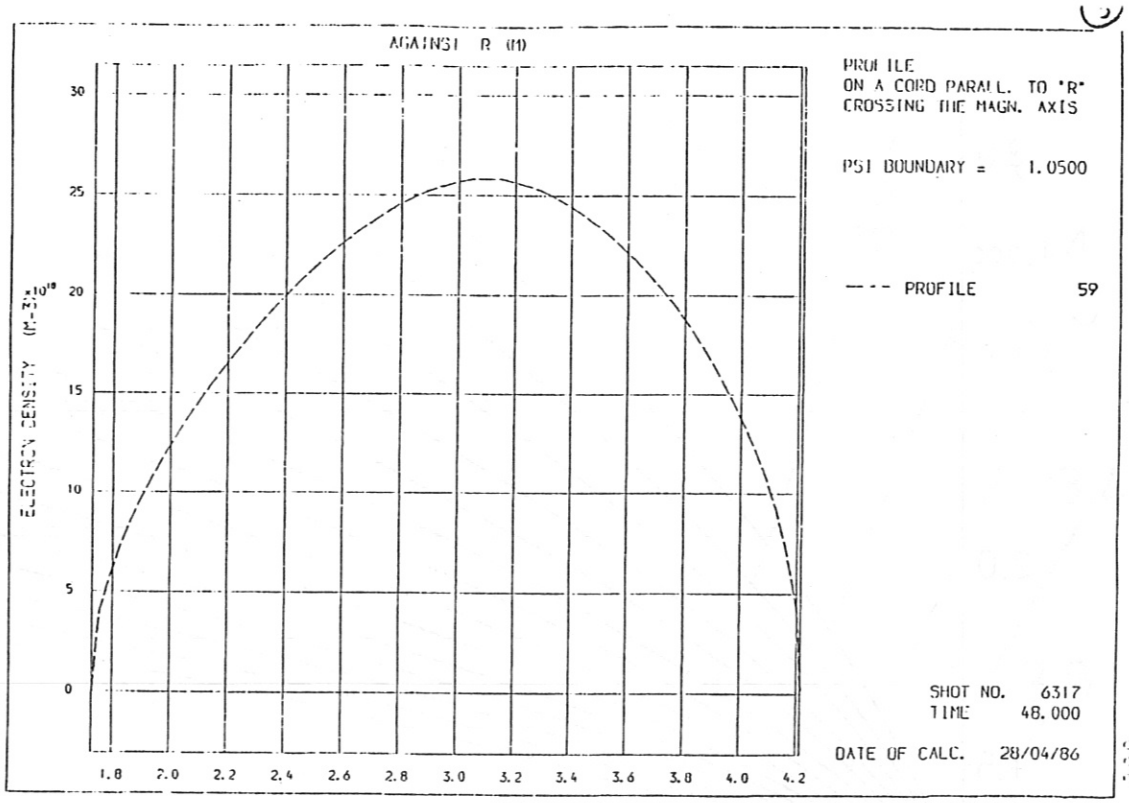

Fig.V.28a: Experimental density profile from JET shot 6317. I_p = 3.5 MA, B_t = 2.3 T.

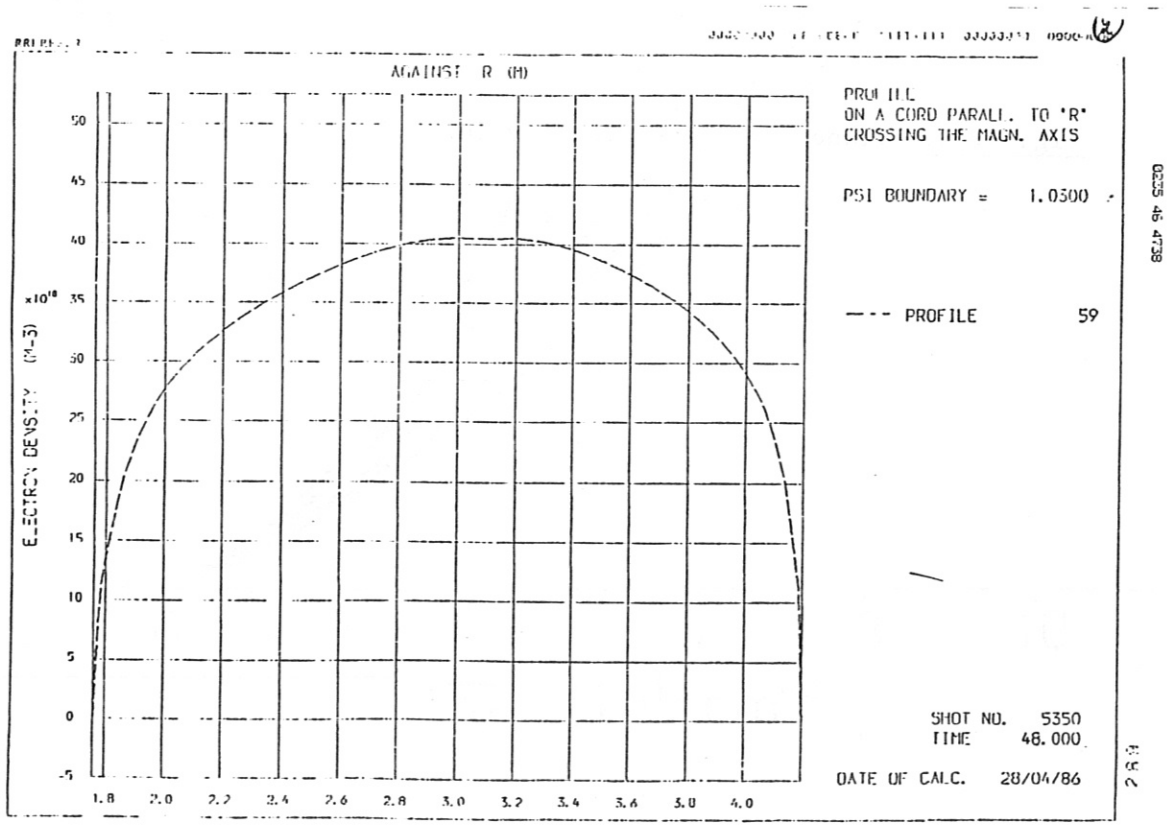

Fig.V.28b: Experimental density profile from JET shot 5350. I_p = 5 MA, B_t = 3.4 T.

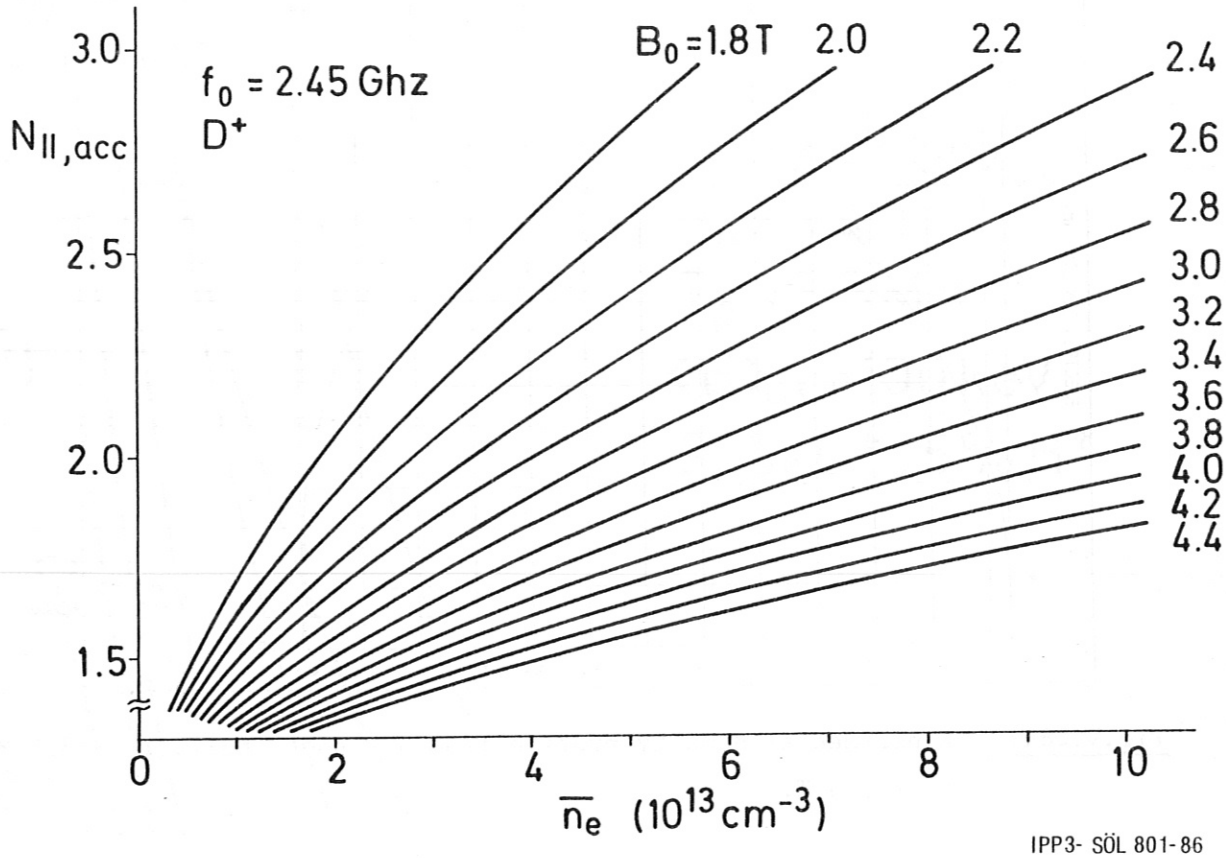

Fig. V.29: Plane wave accessibility for 2.45 GHz.

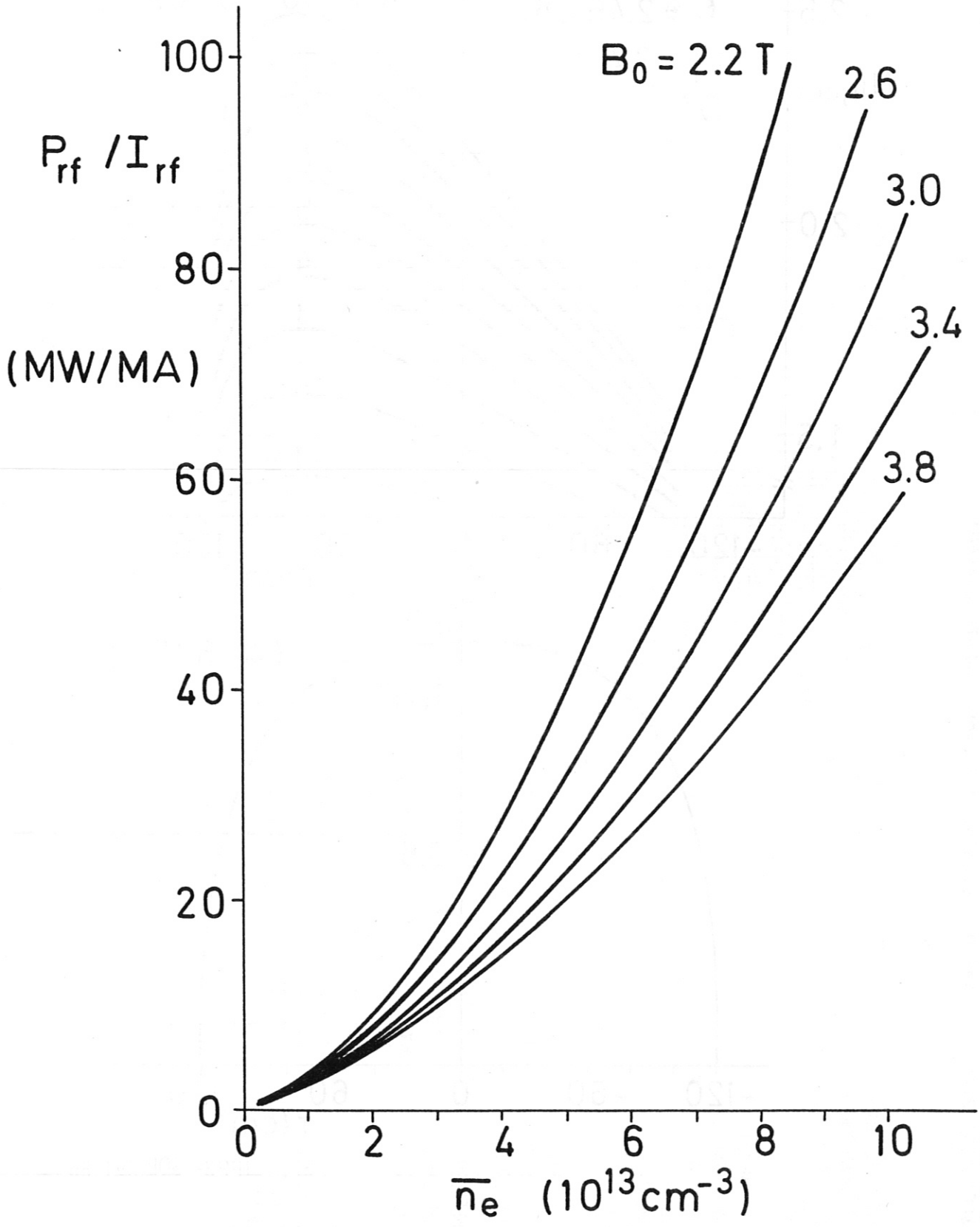

Fig. V.30: Calculated power required for complete current drive in JET. $P_{rf}/I_{rf} = (\bar{n}_e \cdot R \cdot \gamma)/(\eta \cdot \mu \cdot g)$. (MW, MA, 10^{13} cm^{-3}, m) with η = 2.75, μ = 0.7, γ = 1.25, R = 3 m, f = 2.45 GHz, $\Delta N_{\parallel}$ = 0.6, D_2, plane wave accessibility.

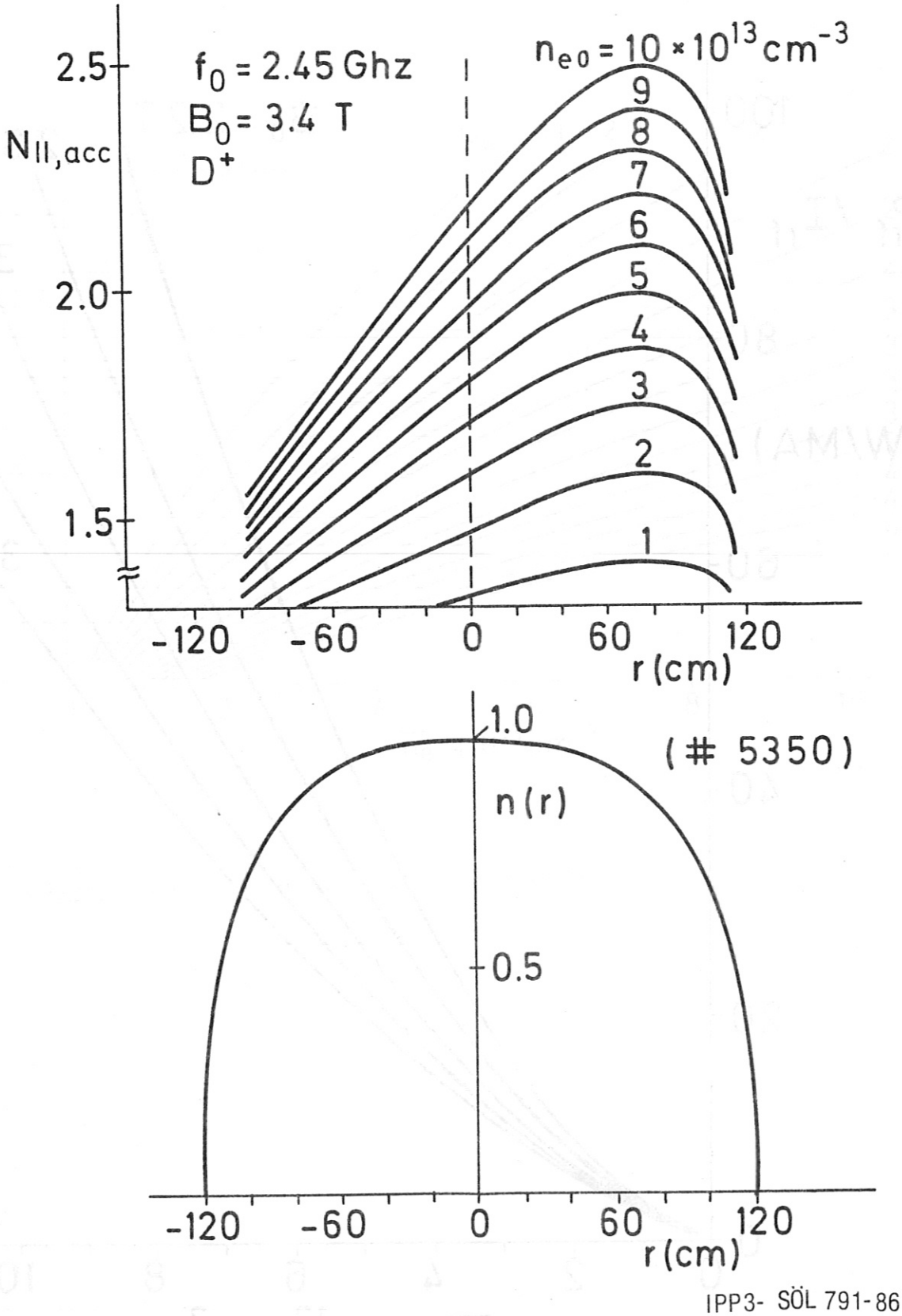

Fig. V.31: Local values of $N_{"acc}$ along a major radius for different peak plasma densities.

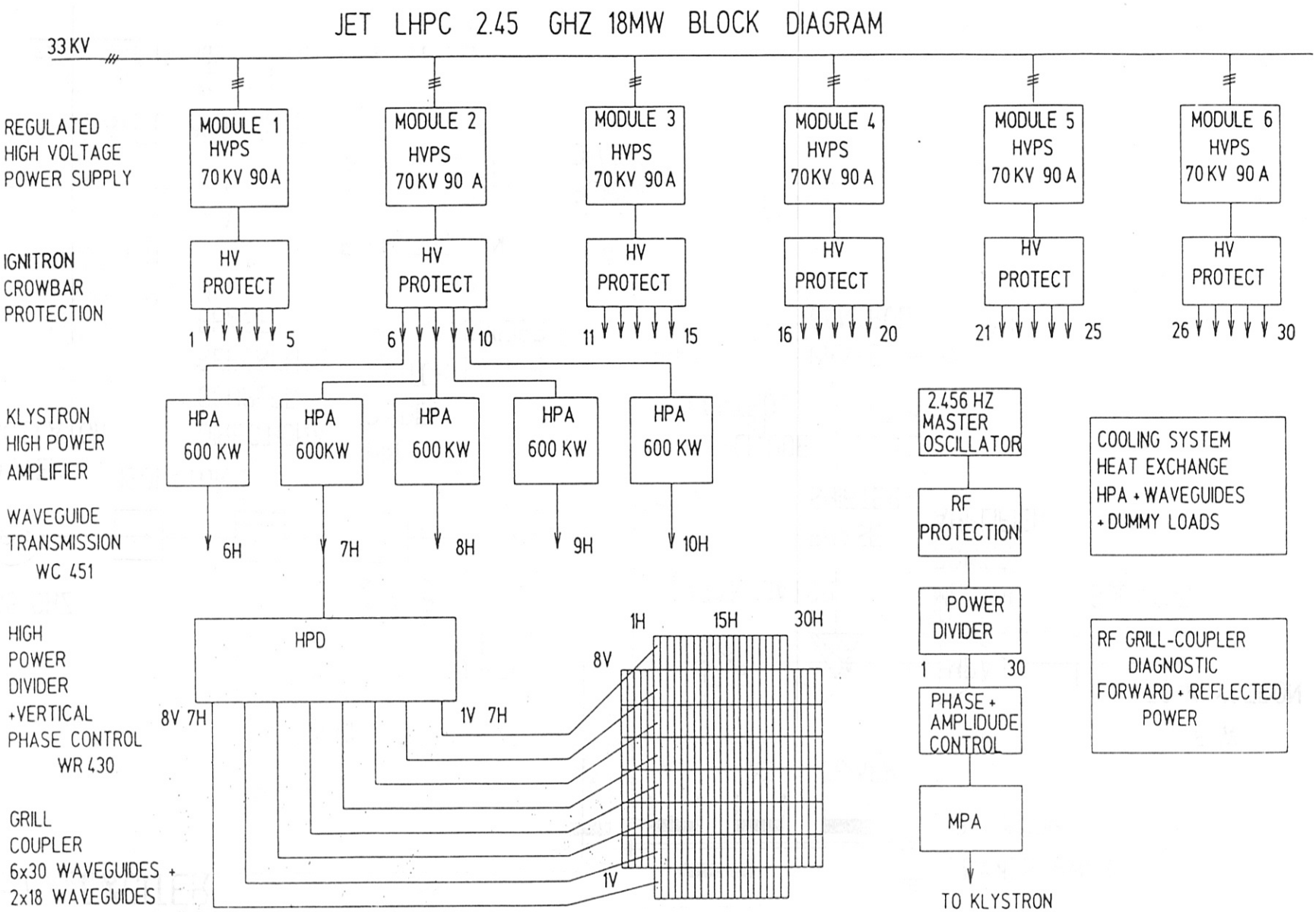

Fig.V.32: Block diagram of JET/2.45 GHz Lower Hybrid System.

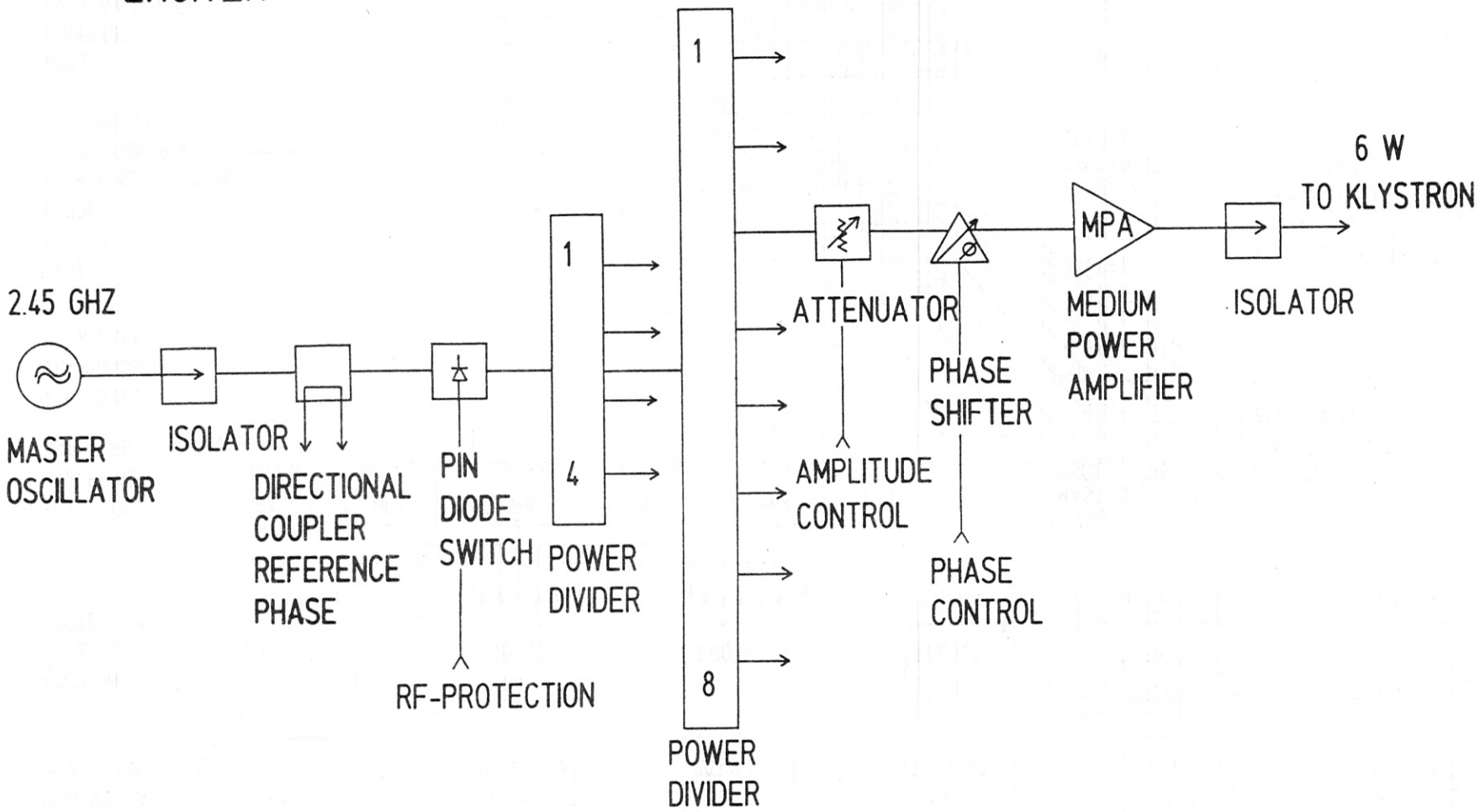

Fig.V.33: Layout of low power exciter.

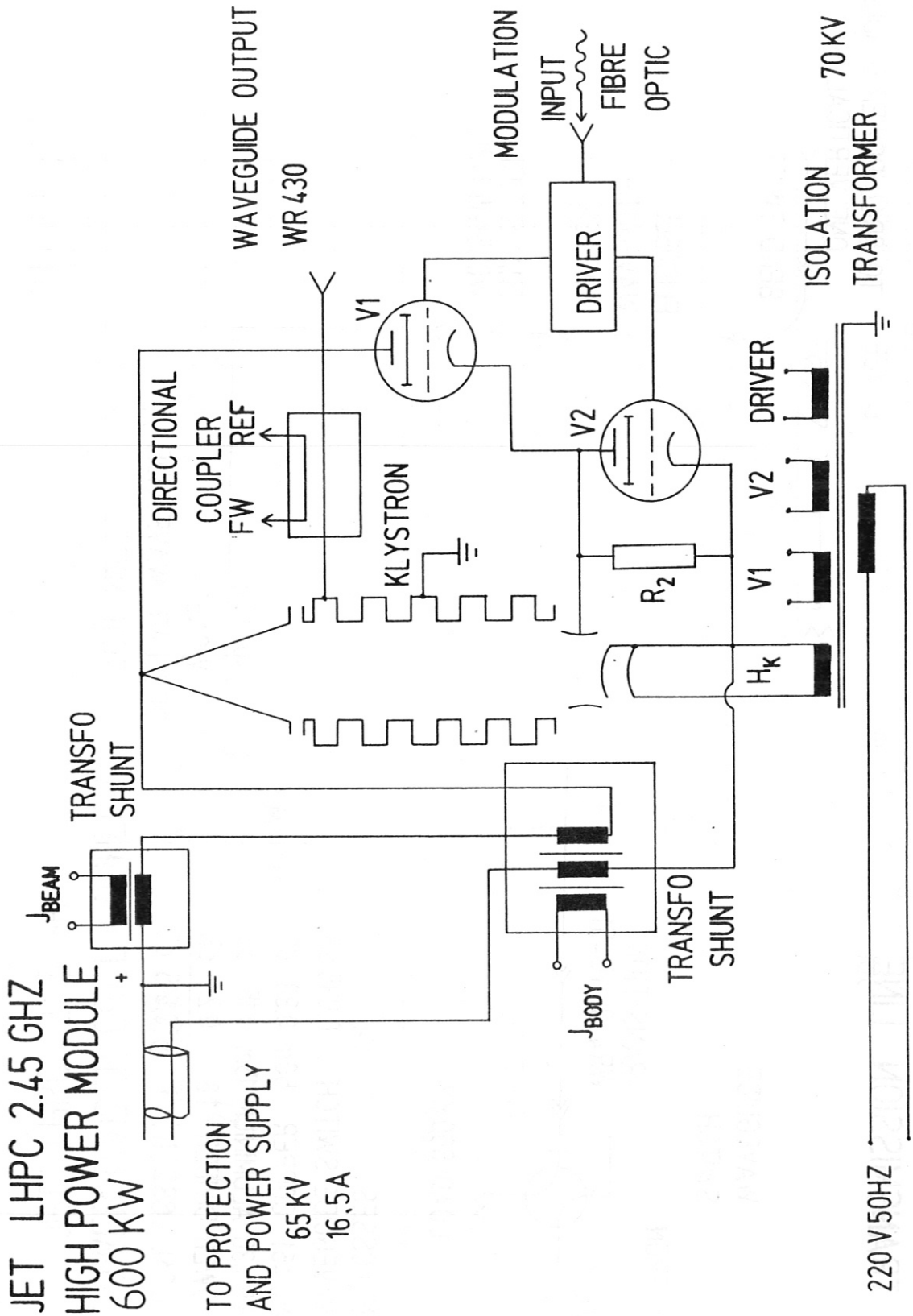

Fig.V.34: Schematic drawing of one klystron module.

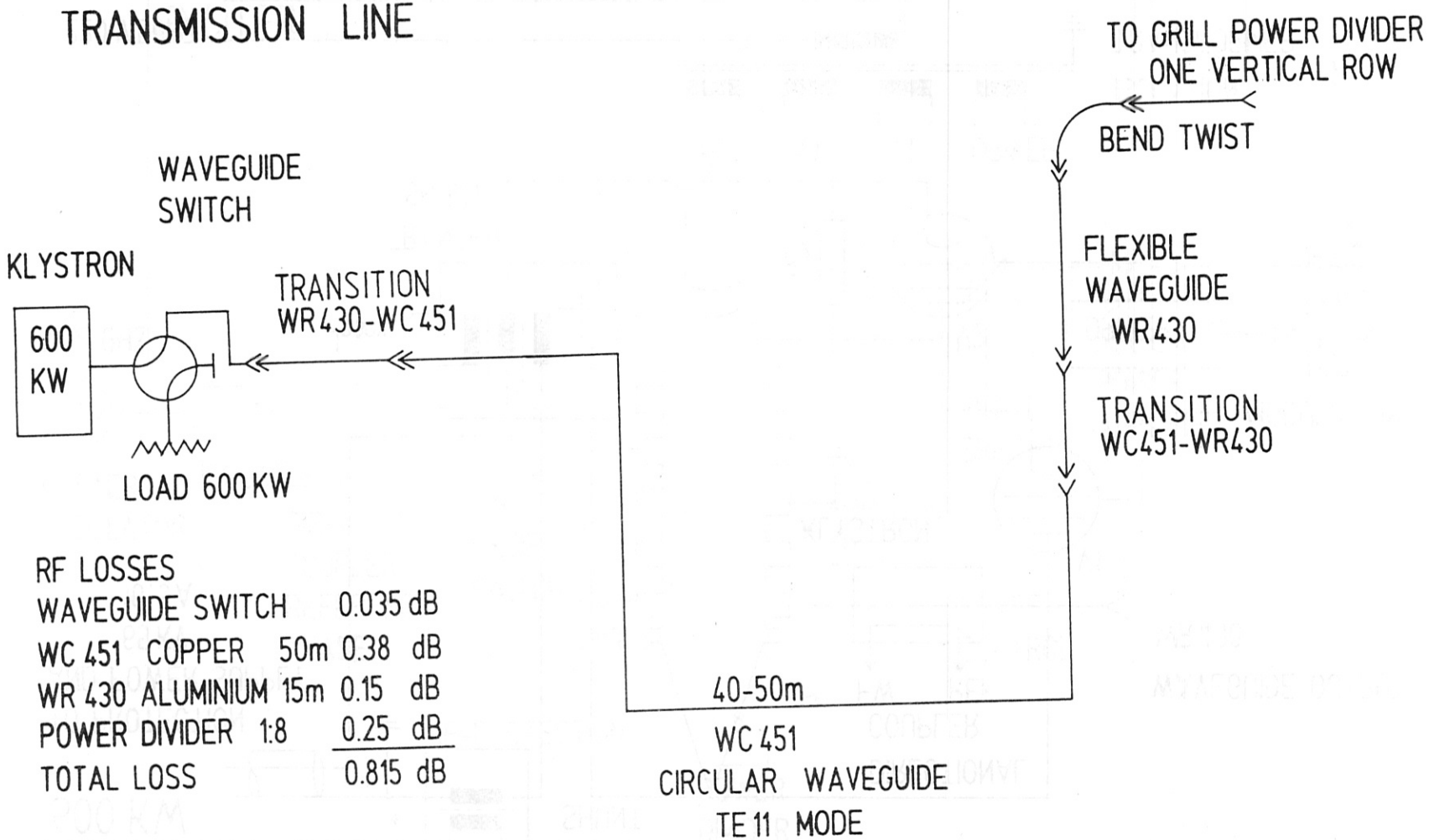

Fig.V.35: Layout of the transmission line.

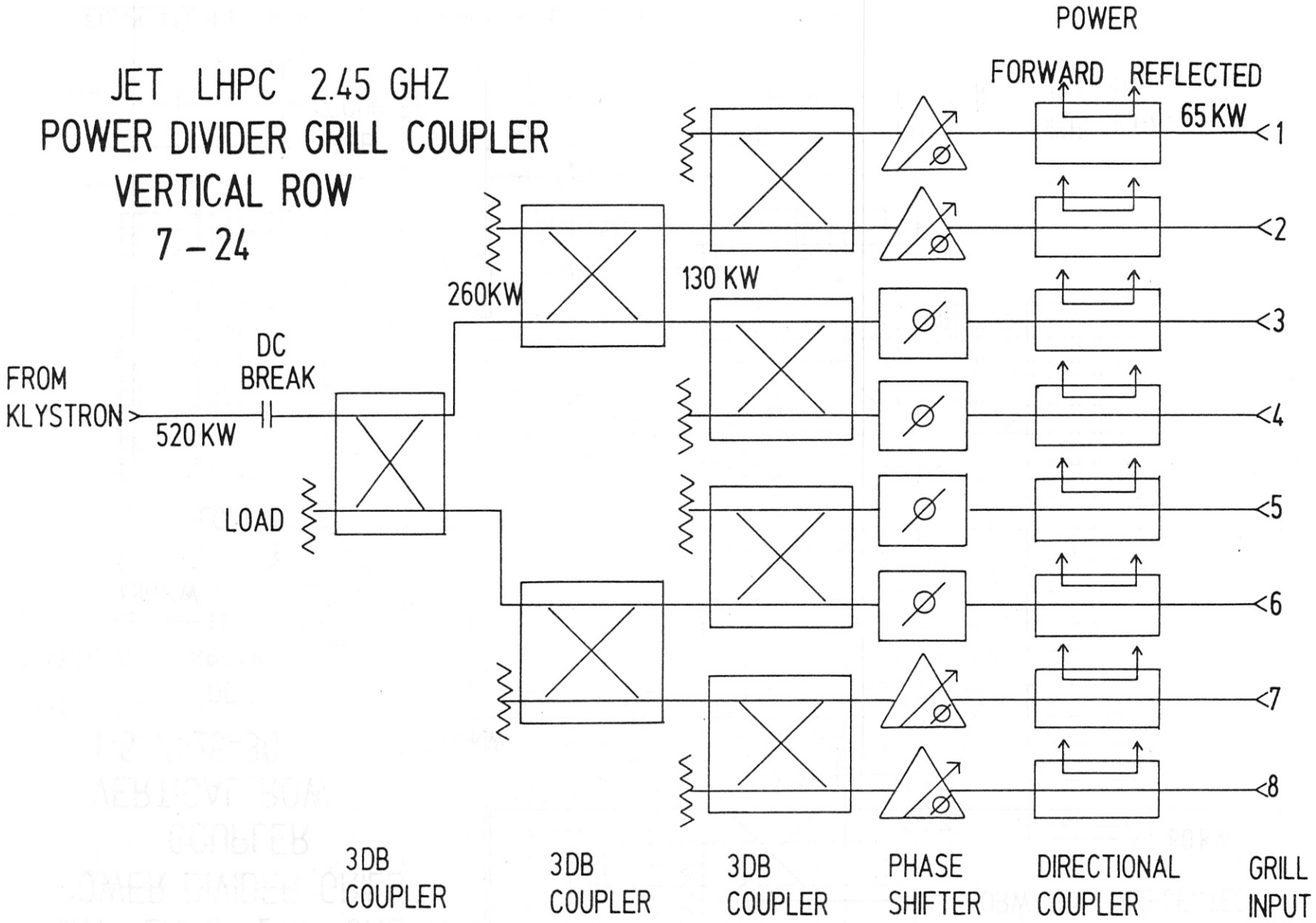

Fig.V.36: High power divider for the central 18 vertical rows (No. 7-24) of 30 of the JET grill.

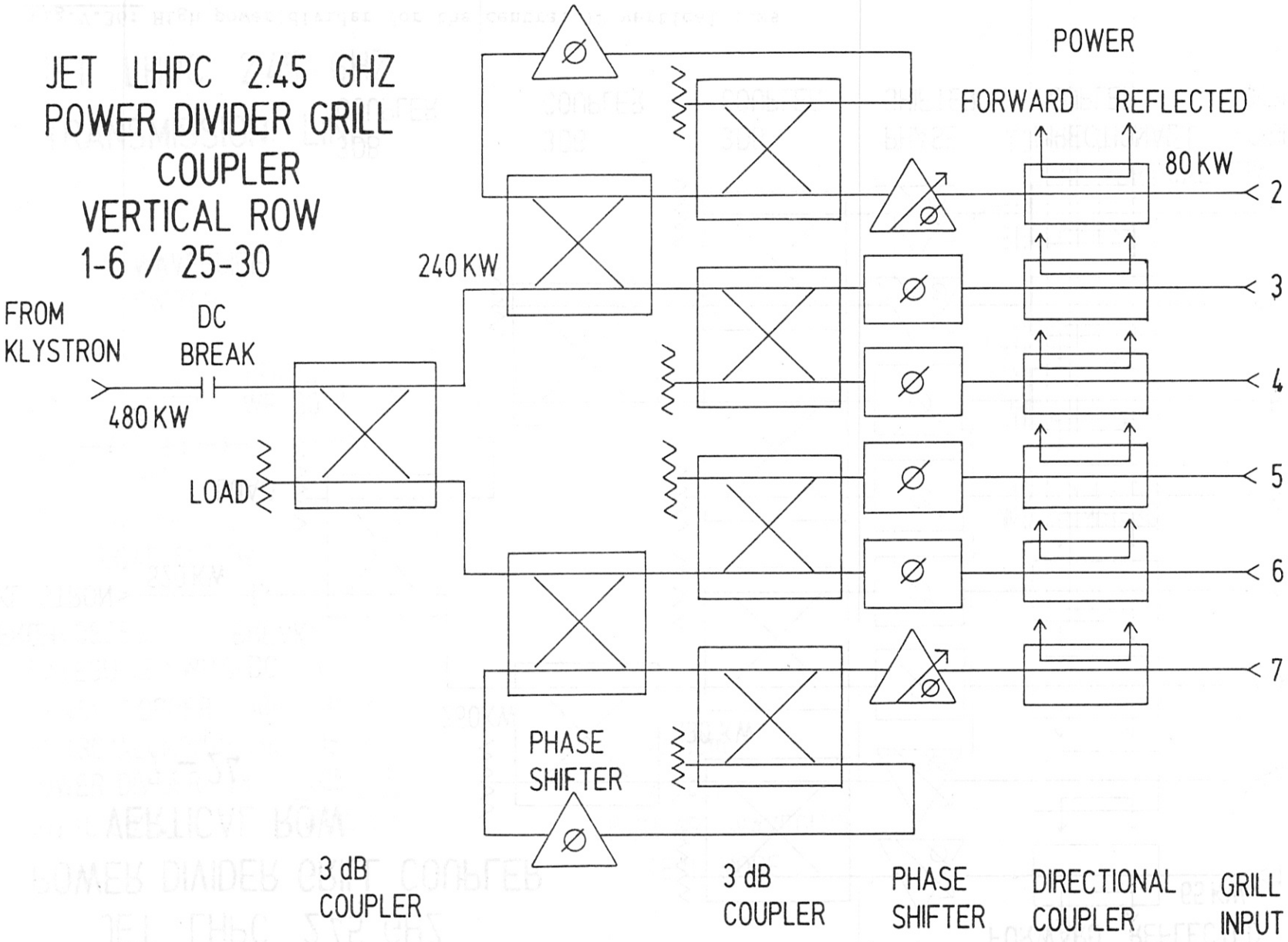

Fig.V.37: High power divider for 6 vertical rows on both sides (No. 1-6, 25-30) of the JET grill.

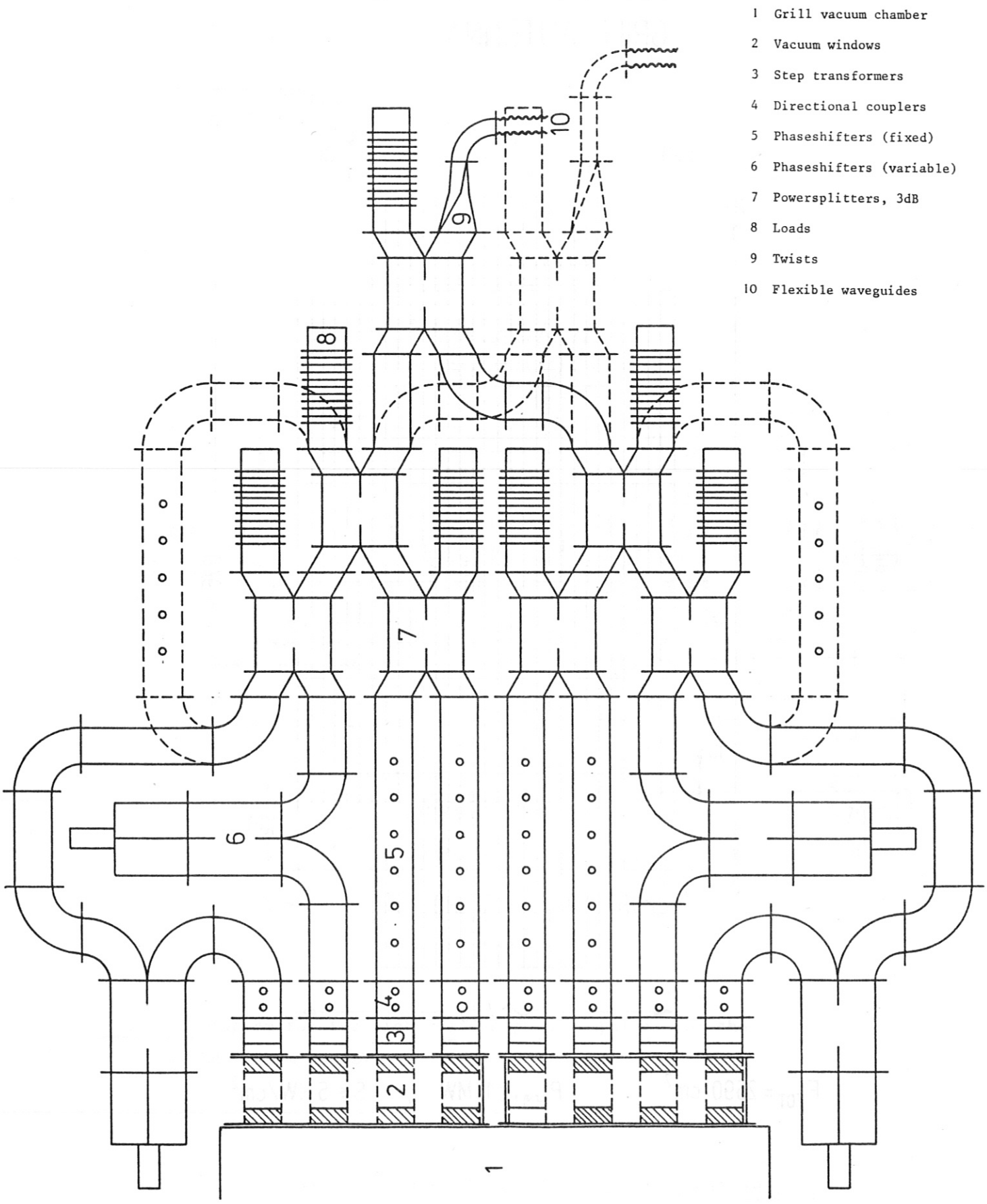

Fig.V.38: 2.45 GHz Power divider.

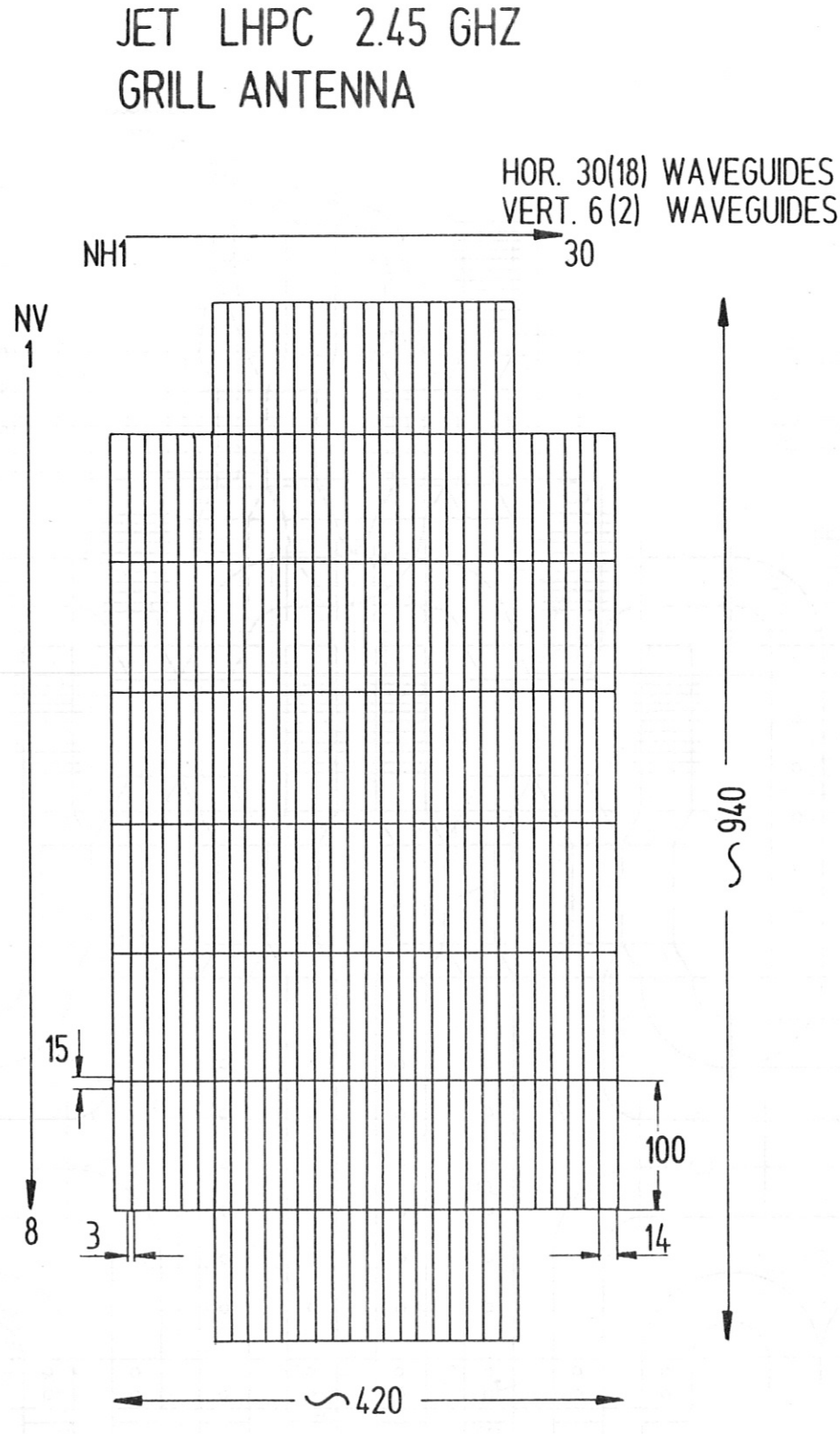

Fig.V.39: Waveguide array of the JET grill antenna.

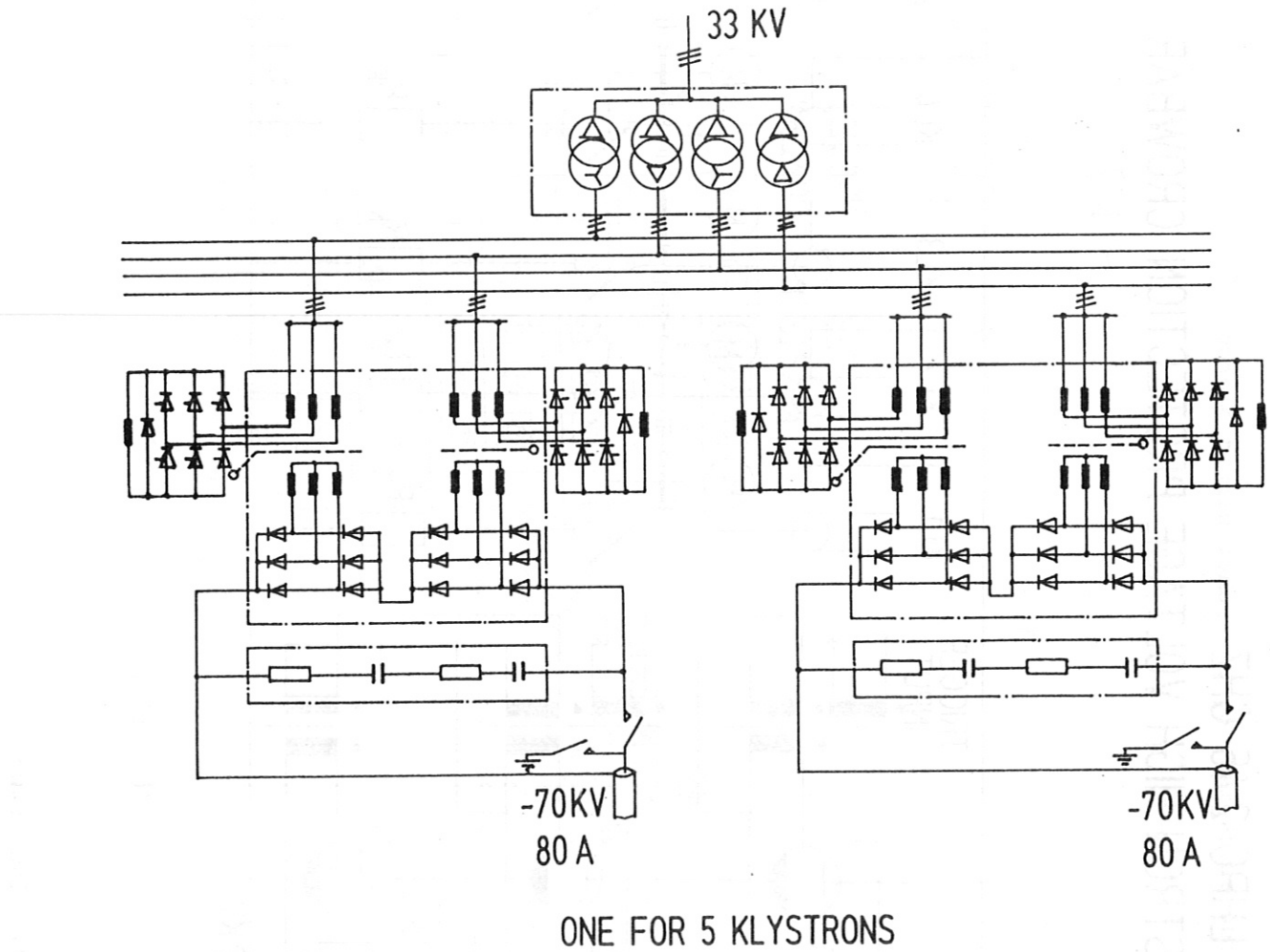

Fig.V.40: Diagram for two high voltage power supplies for the LH system on JET.

JET LHPC 2.45 GHZ
KLYSTRON HIGH VOLTAGE PROTECTION CROWBAR

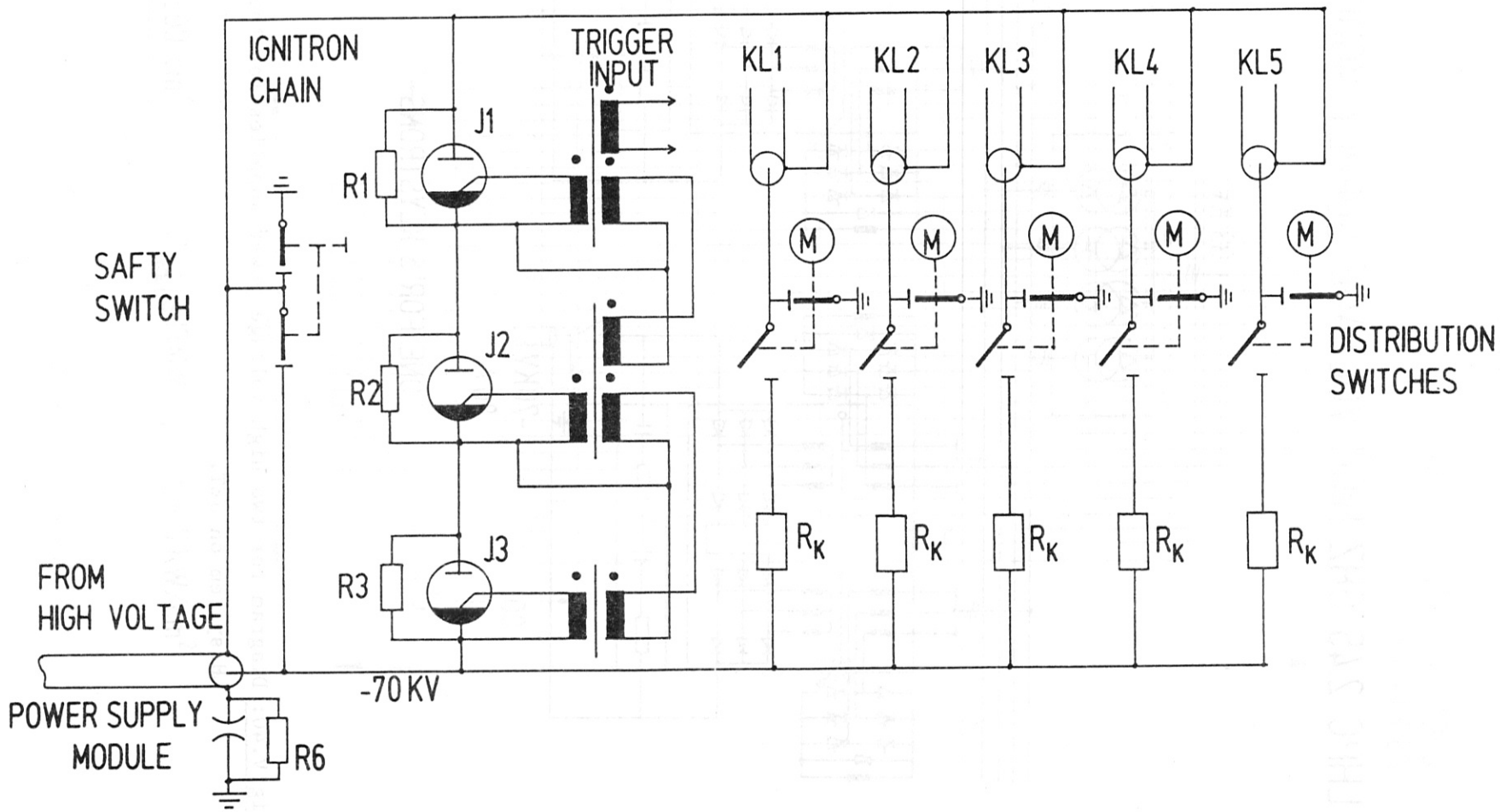

Fig.V.41: High voltage protection crowbar.

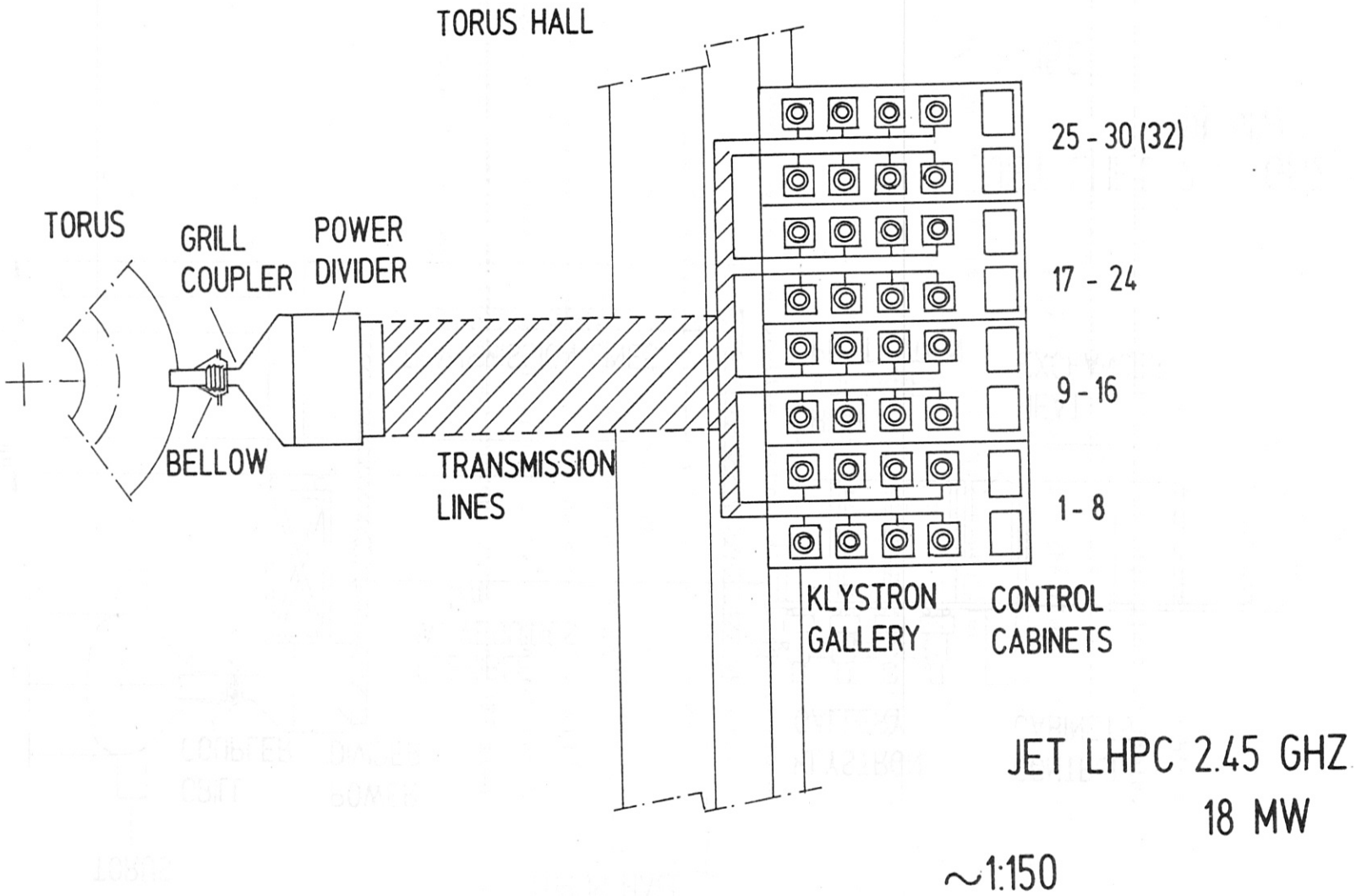

Fig.V.42: Top view of the arangement of the Lower Hybrid System on JET.

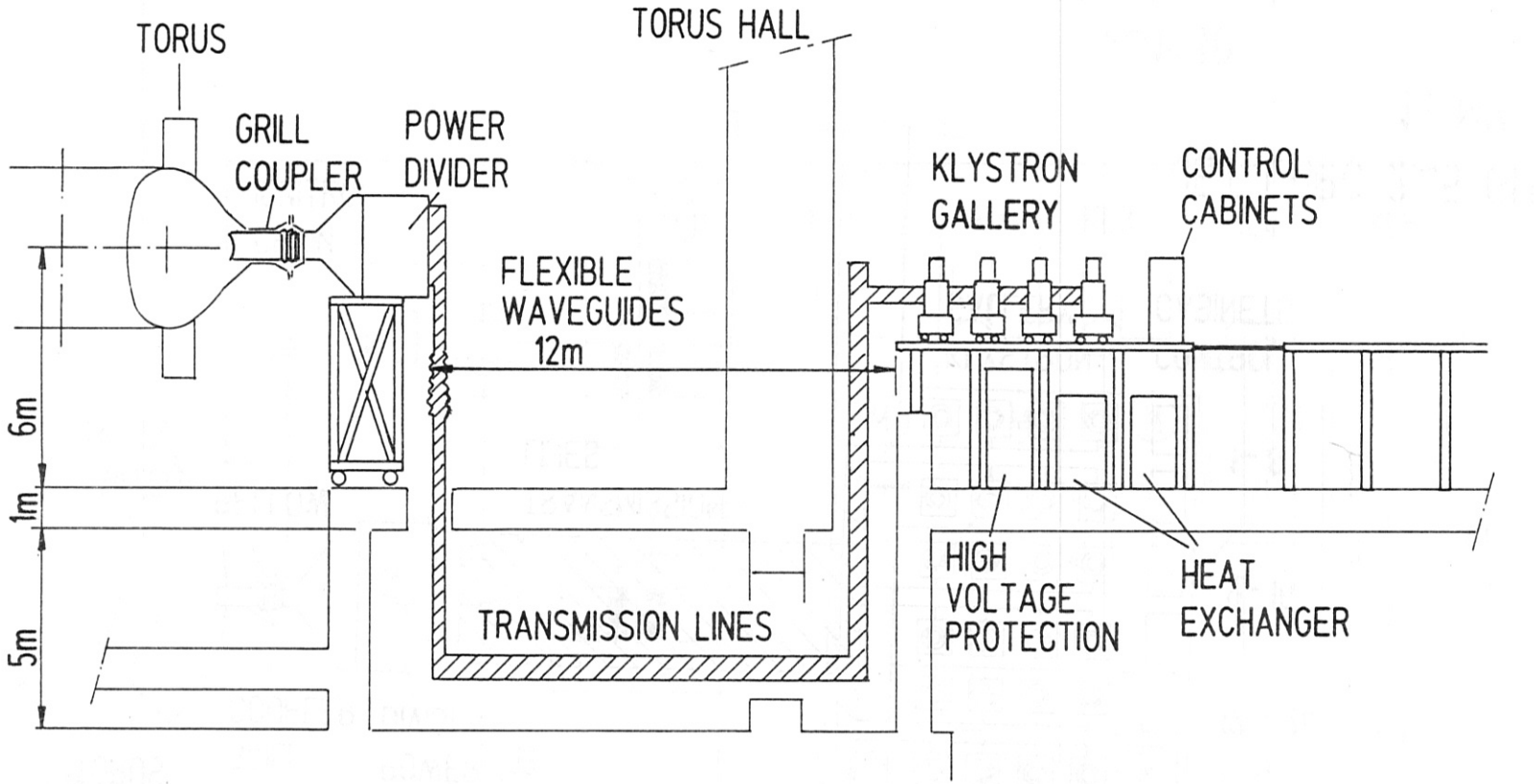

Fig.V.43: Side view of the arrangement of the Lower Hybrid System on JET.

VI. Summary

Lower Hybrid waves produce suprathermal electrons at densities below the onset of ion interaction. By appropriate choice of plasma and wave parameters the electron distribution function can be specifically influenced by producing a suprathermal tail or a runaway population. With improved local deposition of LH-power this provides a means of local modification of the electrical conductivity.

Lower Hybrid Current Drive has high efficiencies in a combined operation with inductive current drive at high electric field. The results of scaling studies on the LH-current drive efficiency are well explained by existing theories.

The decoupling of temperature and current profiles with LH-current drive can be used for external control of $j(r)$ independent of the heat deposition by additional heating. This allowed to stabilise sawteeth by increasing $q(o)$ above 1.

A Lower Hybrid System for profile control on JET should aim at power deposition at the plasma periphery. Problems with wave propagation due to toroidal effects and absorption of waves on thermal electrons and fast ions prevent penetration of LH waves into the central plasma region. Also the high power requirements for LH-current drive in the high density region would discard such a scheme. With LH current drive in the low density edge region control of the plasma current profile on JET might be attained at moderate LH-power.